The growth and characterisation of ordered arrays of zinc oxide nanostructures and optical studies of defects in zinc oxide

By

Daragh Byrne BSc. MSc.

School of Physical Sciences

Dublin City University

A dissertation submitted in fulfilment of the requirements for the degree of
Doctor of Philosophy

to

Ollscoil Chathair Bhaile Átha Cliath

Dublin City University

Research Supervisor

Dr. Enda McGlynn

March 2012

I hereby certify that this material, which I now submit for assessment on the programme of study leading to the award of Doctor of Philosophy is entirely my own work, that I have exercised reasonable care to ensure that the work is original, and does not to the best of my knowledge breach any law of copyright, and has not been taken from the work of others save and to the extent that such work has been cited and acknowledged within the text of my work.

Signed: _____ ID No.:___58100997 __ Date: _____

Acknowledgements

First and foremost I would like to thank Dr. Enda McGlynn, for taking a chance on me, giving me the opportunity to study at DCU and for all his help, advice and encouragement during my time at DCU. I don't think I could put into words how much this opportunity has meant to me or how much I have enjoyed my time at DCU. Without Enda's help and guidance this work would not have been possible. Thank you Enda, for everything that you have done for me.

I would also like to thank all the academic staff at DCU for their constant support and help and in particular, Prof. Martin Henry for giving me the chance to see big physics in action and for his help during this work; Prof. Greg Huges for his assistance and advice with the XPS measurements; Dr. Tony Cafolla for helping me with the AFM measurements; Dr. Brendan Twamley for his assistance with the FESEM measurements and Dr. Eilish McLoughlin for her advice on returning to education. I would also like to thank all the technical staff without whom, nothing would get done. Thanks to Henry Barry, for letting me pilfer the undergrad labs; Des Lavelle, for building anything that I could possible think of; Pat Wogan, for fixing everything that I managed to break; Alan Hughes, for support with getting things done and Lisa Peyton for all her help and administrative know how.

I would like to thank Science Foundation Ireland and the strategic research cluster "Functional Oxides and Related Materials for Electronics" (FORME) for their financial support, without which, this work would not have been possible. I would also like to thank Prof. Martyn Pemble, for his support and encouragement within the FORME group, for all his advice and help during the course of this work and in helping me apply for further funding going forward.

I would also like to thank my office and lab colleagues for all their support. In particular I'd like to thank Seamus Garry, Joe Cullen and Barry Foy for putting up with me for the last number of years and for their constant help and encouragement. A special thanks to Ruth Saunders for proof reading this thesis and for all her encouragements through out the years. I would also like to thank Dr. Conor McLoughlin, Dr. Mairead Hurley, Dr. Mahua Biswas and Dr. Patrick Kavanagh for all their help and guidance and for making me feel welcome during my first years at DCU and showing me how it's done.

To my brothers Brian and Ciaran and my sister Aelish, thank you for all the support patience and guidance, through some tough times. Without you, I never would have gotten this far. To Amanda, thank you for keeping me sane and tearing me away from the books from time to time. Your support and encouragement has been invaluable. Hopefully I will be able to do as much for you when your time comes! Finally I would like to thank my parents Roisin and Joseph, for everything that they have done for me and for helping and encouraging me every step of the way, in good times and in bad. For this I will forever be grateful.

Dedicated to my father

Joseph A. Byrne

Abstract

In this work the growth of *c*-axis aligned zinc oxide nanorods on non-epitaxially matched substrates is examined. Nanorod arrays were deposited on silicon by seeding and chemical bath deposition (CBD), carbothermal vapour phase transport (CTR-VPT) and a hybrid CBD / CTR-VPT method. The best optical quality nanorods were obtained by the hybrid CBD / CTR-VPT method. This hybrid method was extended further and a method was developed to deposit hexagonally close packed positioned *c*-axis aligned arrays using a facile nanosphere technique in conjunction with silica templating. The varying factors affecting the deposition process were examined, including the growth conditions, transformations in the CBD layer during high temperature CTR-VPT deposition and the formation of new interfaces between the substrates and nanorods. The optical properties of the nanorod arrays were examined by low temperature Fourier transform photoluminescence spectroscopy, where it was found that the quality of both the positioned and unpositioned nanorods was excellent. Work on an important deep level emission in ZnO (the structured green band) was also undertaken, both in nanostructures by deliberately introducing copper into the growth process and also by a soft Cu isotopically specific doping technique into highly perfect single crystals. These samples' properties were then studied by low temperature photoluminescence spectroscopy.

Contents

Declaration i

Acknowledgements ii

Abstract v

Contents vi

List of Acronyms ix

List of Figures x

List of tables xv

Publications xv

Conferences xvii

Chapter 1 Introduction

1.1 Introduction 1

1.2 Applications and motivation for this work 3

1.3.1 Material Properties: Crystal structure 6

1.3.2 Material Properties: Electronic bandgap 8

1.3.3 Growth techniques 10

1.4 References 14

Chapter 2 Experimental Techniques

2.1 Introduction 20

2.2 Substrate preparation 21

2.3 Buffer layer preparation 21

2.4 Chemical bath deposition 21

2.4.1 HMT based reaction 22

2.4.2 Acetate based reaction 23

2.4.3 NaOH based reaction 23

2.5 Carbothermal reduction vapour phase transport deposition 24

2.6 Nanosphere lithography 25

2.6.1 Generating colloidal monolayers 26

2.6.2 Direct template assisted nanorod growth 28

2.6.3 Inverted template assisted nanorod growth 29

2.7 Characterisation techniques 32
2.7.1 White light profilometry 33
2.7.2 Scanning electron microscopy 34
2.7.3 Atomic force microscopy 37
2.7.4 X-Ray diffraction 39
2.7.5 X-Ray photoelectron spectroscopy 41
2.7.6 Photoluminescence 42
2.7.7 Transmission electron microscopy 54
2.8 References 57

Chapter 3 Chemical Bath Growth

3.1 Introduction 60
3.2 Seed layer characterisation 60
3.3 Chemical origins of the ZnO seed layer 63
3.4 Seed layer morphology 71
3.5 Chemical Bath deposition 77
3.5.1 Growth of HMT CBD Nanorod arrays 81
3.5.2 The effects of surfactants on HMT CBD growth 85
3.5.3 Origin of *c*-axis alignment 89
3.5.4 NaOH and Acetate based CBD nanorod arrays 92
3.6 Conclusions 96
3.7 References 97

Chapter 4 Carbothermal Vapour Phase Transport Growth

4.1 Introduction 100
4.2 Carbothermal deposition on acetate derived seed layers 102
4.3 CTR-VPT deposition on CBD derived buffer layers 109
4.3.1 Effect of varying substrate height over source powder 111
4.3.2 Effect of varying the CBD buffer layer 114
4.3.3 Structural characterisation of the Nanorods 115
4.4 Growth and nucleation of nanorods: the influence of temperature and buffer layer 116
4.5 Effect of CTR-VPT on the substrate / nanorod interface 126
4.6 Conclusions 130

4.7 References 131

Chapter 5 Nanosphere Lithography

5.1 Introduction 133

5.2 Self-assembly of nanospheres 135

5.3 Spheres as templates for growth 137

5.4.1 Inverse nanosphere lithography: CuO and Carbon templates 141

5.4.2 Inverse nanosphere lithography: Silica templates 144

5.5.1 Inverse nanosphere lithography: CTR-VPT deposition 147

5.5 Conclusions 154

5.6 References 155

Chapter 6 Optical Characterisation

6.1 Introduction 157

6.2 CBD versus CTR-VPT 157

6.3 CTR-VPT deposited nanorods 161

6.4 The structured green band 167

6.5 Single crystal ZnO and isotopic doping 174

6.6 Conclusions 180

6.7 References 181

Chapter 7 Conclusions & Outlook

7.1 Conclusions 185

7.2 Outlook 188

List of Acronyms

Aluminium	Al
Atomic force microscopy	AFM
Argon	Ar
Bright field TEM	BF-TEM
Carbothermal reduction	CTR
Carbothermal reduction vapour phase transport	CTR-VPT
Chemical bath deposition	CBD
Copper	Cu
Conventional TEM	C-TEM
Dark field TEM	DF-TEM
Deionised water	DI-H_2O
Donor acceptor pair	DAP
Dublin City University	DCU
Dye sensitised solar cell	DSSC
Electron energy loss spectroscopy	EELs
Energy dispersive x-ray spectroscopy	EDX
Ethanol	etoh
Face-Centred Cubic configurations	FCC
Fast Fourier transform	FFT
Fast ramp temperature profile	FRTP
Field emission scanning electron microscopy	FESEM
Fourier transform	FT
Full width half max	FWHM
Gallium	Ga
Gallium nitride	GaN
Gold	Au
Hexagonal Close Packed	HCP
Hexamethylenetetramine / Hexamine	HMT
High angular annular dark field	HAADF
Hydrogen	H
Hydrochloric acid	HCl
Indium	In
Internal quantum efficiency	IQE
Layered basic zinc acetate	LBZA
Lithium	Li
Longitudinal optical	LO
Nanosphere lithography	NSL
Near band edge	NBE
Oxygen	O
Photoluminescence	PL
Polyethylenimine	PEI

Scanning electron microscopy	SEM
Scanning transmission electron microscopy	STEM
Scanning tunnel microscope	STM
Selected area diffraction	SAD
Silicon	Si
Silicon dioxide	SiO_2
Slow ramp temperature profile	SRTP
Sodium hydroxide	NaOH
Structured green band	SGB
Sulphuric acid	H_2SO_4
Tetraethyl orthosilicate	TEOS
Transmission election microscopy	TEM
Ultra high vacuum	UHV
Vapour liquid solid	VLS
Vapour phase transport	VPT
Vapour solid	VS
White light profilometry	WLP
X-ray diffraction	XRD
X-ray photoelectron spectroscopy	XPS
Zero phonon line	ZPL
Zinc	Zn
Zinc oxide	ZnO

List of Figures: Abbreviated titles

	Page
Figure 1.1: The Wurtzite crystal structure and unit cell of ZnO.	6
Figure 1.2: Hexagonal ZnO structure showing the various different planes.	7
Figure 1.3: Schematic diagram of ZnO band structure at the zone centre.	9
Figure 2.1: Equipment set up for chemical bath deposition of ZnO nanorods.	22
Figure 2.2: Equipment setup for CTR-VPT growth of ZnO nanorods	25
Figure 2.3: A schematic repsentation of the two approaches to positioning nanorod arrays using nanosphere lithography.	26
Figure 2.4: A schematic representation of the equipment and method to obtain nanosphere monolayers on silicon substrates.	28
Figure 2.5: Organisational chart showing the various different characterisation techniques used to examine the deposited nanorod arrays.	32

Page

Figure 2.6: Simplified schematic of a WLP instrument . 33
Figure 2.7: A schematic representation of a scanning electron microscope. 36
Figure 2.8: Schematic representations of a typical AFM instrument. 37
Figure 2.9: A representation of the Bragg diffraction condition used in XRD. 40
Figure 2.10: A schematic representation of the electron-hole recombination in direct & indirect band-gap semiconductors. 44
Figure 2.11: Schematic representation of the two different varieties of excitons. 45
Figure 2.12: Configurational coordinate diagram from showing the ground and excited state of a dopant atom and corresponding absorption and emission spectrum. 47
Figure 2.13: A schematic diagram of the various near band edge emission lines found at low temperature in ZnO. 49
Figure 2.14: Schematic representation of the photoluminescence experimental configuration. 50
Figure 2.15: Optical layout of a TEM instrument. 55
Figure 3.1: ZnO nanorods grown on a textured ZnO seed layer prepared by (a) drop-coating an alcoholic zinc acetate solution and (b) by evaporation of a ZnO sol. 62
Figure 3.2: Peak fitted XPS spectra of the C-1S region of the spectrum of a drop-coated seed layer. 64
Figure 3.3: Peak fitted XPS spectra of the O-1S region of the spectrum of a drop-coated seed layer. 66
Figure 3.4: Peak fitted XPS spectra of the Zn 2P3/2 region of the spectrum of a drop-coated seed layer. 67
Figure 3.5: Proposed chemical route to the formation of ZnO seed layers by drop-coating alcoholic solutions of zinc acetate. 69
Figure 3.6: AFM images of a drop-coated seed layer. 70
Figure 3.7: AFM cross sectional profile of ZnO seeds deposited by drop-coating. 71
Figure 3.8: WLP & FESEM image of a substrate surface drop-coated. 72
Figure 3.9: FESEM image of a substrate drop-coated 5 times. 73
Figure 3.10: Schematic representation of the drop-coating process. 74
Figure 3.11: Results of a computer simulated model of an evaporating sol droplet on a surface. 76

Page

Figure 3.12: Speciation diagram of a Zn^{2+} / hexamine solution. 78

Figure 3.13: FE-SEM images of a HMT CBD nanorod array 82

Figure 3.14: HRTEM and FFT image of HMT CBD grown nanorod showing the amorphous SiO_2 interface. 84

Figure: 3.15: XRD 2 θ / ω scan of HMT CBD grown nanorod array on Si (100). 84

Figure 3.16: SEM images of ZnO nanorods patterned during growth by trapped bubbles. 86

Figure 3.17: SEM images of Zno nanorods grown in two successive 45 minute, 25mM zinc nitrate / HMT baths. 87

Figure 3.18: SEM images of nanorods deposited for various times with and without surfactants. 88

Figure 3.19: HRTEM image and corresponding FFT or a ZnO CBD deposited nanorod growing with its' (10-10) axis perpendicular to the substrate normal 90

Figure 3.20: SEM images of CBD sample grown on substrates using varying numbers of drop-coating steps. 91

Figure 3.21: SEM image of a low density nanorod array, with a large mass of debris trapped on the surface of the substrate. 93

Figure 3.22: SEM and XRD data of ZnO nanorods grown by the NaOH method. 94

Figure 3.23: SEM and XRD data of ZnO nanorods grown by the zinc acetate method. 95

Figure 4.1: CTR-VPT growth on a thin acetate derived buffer layer at 925°C. 103

Figure 4.2: Temperature ramp profile of CTR furnace set to 900°C. 104

Figure 4.3: Carbothermal Reduction growth on a thick acetate derived buffer layer at 925°C. 105

Figure 4.4: AFM images of acetate derived seed layers. 106

Figure 4.5: 30° FESEM images of acetate derived seed layers. 107

Figure 4.6: HAADF-STEM image of a drop-coated seed layer post annealing. 108

Figure 4.7: SEM images of growth using hybrid CBD/CTR-VPT technique. 110

Figure 4.8: SEM images of growth using hybrid CBD/CTR technique using a smaller alumina boat during CTR-VPT step. 111

Figure 4.9: SEM images of growth using hybrid CBD/CTR-VPT technique using a smaller alumina boat and compressed source powder during CTR-VPT step. 113

Page

Figure 4.10: SEM images of growth using hybrid CBD/CTR-VPT technique on a NaOH CBD derived buffer layer. 114

Figure 4.11: FE-SEM, CTEM and HAADF-STEM image of CTR-VPT grown nanorods. 115

Figure 4.12: Furnace temperature profiles FRTP and SRTP used for the various CTR-VPT depositions on CBD buffer layers. 117

Figure 4.13: SEM images of growth using CBD/CTR-VPT technique using the SRTP. 118

Figure 4.14: Schematic representations of the various different conical base shapes 119

Figure 4.15: Plan view FESEM image of ZnO nanorod array deposited by CTR-VPT on a CBD buffer and on a PLD buffer layer. 120

Figure 4.16: FESEM images of a CBD buffer layer prior to annealing and post annealing using the SRTP. 121

Figure 4.17: SEM images of a cleaved edge of CBD grown sample after high temperature annealing. 122

Figure 4.18: HAADF-STEM images of CBD nanorods prior to CTR-VPT deposition and of a faceted void formed in an annealed CBD buffer layer. 125

Figure 4.19: HRTEM and FFT of a CTR-VPT grown sample at the SiO_2-ZnO interface. 126

Figure 4.20: Individual core loss EEL spectra from several points at the Si substrate/wires interface. 128

Figure 4.21: HAADF-STEM Images of Si / ZnO interface after different thermal treatments and growths. 129

Figure 5.1: Schematic representation of HCP packing and FCC packing and associated monolayer. 134

Figure 5.2: SEM images of (a) Plan view (b) higher magnification plan view of nanospheres deposited using various methods. 136

Figure 5.3: SEM images of ZnO HCP structure grown by CBD through a nanosphere monolayer. 137

Figure 5.4: 45° SEM image of ZnO HCP structure grown by the acetate CBD method through a nanosphere monolayer. 139

Figure 5.5: SEM images of a nanohole array and a schematic representation of the reaction vessel used for the deposition of the honeycomb nanohole array. 140

Page

Figure 5.6: Schematic representation of the various steps required for inverse nanosphere lithography. 141

Figure 5.7: SEM images of honeycomb templates deposited by various methods. 143

Figure 5.8: SEM images of honeycomb silica template on CBD derived from acid and base catalysed sols. 145

Figure 5.9: SEM images of nanorod array deposited through an acid and acid / base catalysed silica honeycomb template using the NaOH-CBD method 146

Figure 5.10: Schematic representations and associated SEM images of the effects of poor surface contact and surface roughness its effect on silica templates. 148

Figure 5.11: SEM image of a CBD buffer layer deposited by acetate method and HMT methods. 149

Figure 5.12: SEM images of a 1 μm and 500 nm spaced CTR-VPT grown ordered array. 150

Figure 5.13: SEM images a ZnO ordered array showing additional morphologies and crystal twinning. 151

Figure 5.14: SEM images of a 1 μm and 500 nm spaced VPT grown ordered array grown on a substrate where a second CBD step was performed. 152

Figure 5.15: XRD 2 θ / ω scan of CTR-VPT grown patterned arrays on CBD buffer layers. 154

Figure 6.1: PL spectra take at 19.8 K of the NBE region and visible spectral region of CBD and CTR-VPT nanorod arrays. 161

Figure 6.2: PL spectra take at 19.8 K of the NBE region and visible spectral region of various CTR-VPT nanorod array samples. 163

Figure 6.3: PL spectra taken at ~18-20 K of CTR-VPT grown 1 μm and 500 nm patterned nanorod array. 165

Figure 6.4: Cathode luminescence, absorption and emission spectra. 167

Figure 6.5: Low temperature PL showing the zero-phonon doublet reproduced from reference 28. 168

Figure 6.6: Low temperature (19.8 K) PL spectra of the ZPL region of the spectrum from CTR-VPT grown samples at various resolutions. 173

Figure 6.7: Low temperature PL spectra of the visible emission region for a Tokyo Denpa single crystal ZnO sample as received and after annealing at 900°C for ten minutes. 175

Page

Figure 6.8: Low temperate PL spectra of ZnO single crystals doped with various proportions of Cu isotopes. 177

Figure 6.9: Absorption measurements of the Cu related line in ZnO for undoped isotope specific Cu doped and Cu doubly doped samples 178

Figure: 6.10: (a)Low temperature PL spectrum of the ZPL region of a (i) ZnO sample co-doped twice and (ii) a ZnO sample co-doped once with ^{63}Cu and ^{65}Cu. 180

List of Tables

Page

Table 2.1: Nomenclature for low temperature PL spectra. 46

Table 3.1: Summary of the dimensions and aspect ratios for nanorods grown with or without the addition of PEI, keeping all other deposition parameters identical. 87

Table 4.1: The variation in conical base width and height for samples grown with varying conditions. 119

Table 6.1: A summary of the observed emission intensities for a range of Cu doped and undoped CTR-VPT grown ZnO nanorod arrays. 172

Table 6.2: The ratio of peak NBE intensity to peak green band intensity for Cu doped and undoped CTR-VPT nanorod arrays prior to annealing and post annealing at 900°C. 172

Publications

D. Byrne, E. McGlynn, M. Biswas, M.O. Henry, K. Kumar, G. Hughes, A study of drop-coated and chemical bath-deposited buffer layers for vapour phase deposition of large area, aligned, zinc oxide nanorod arrays, Crystal Growth and Design, 10 (2010) 2400–2408.

D. Byrne, E. McGlynn, M.O. Henry, K. Kumar, G. Hughes, A novel, substrate independent three step process for the growth of uniform ZnO nanorod arrays, Thin Solid Films, 518 (2010) 4489–4492.

S.K. Das, M. Biswas, D. Byrne, M. Bock, E. McGlynn, M. Breusing, R. Grunwald, Multiphoton-absorption induced ultraviolet luminescence of ZnO nanorods using low-energy femtosecond pulses, Journal of Applied Physics, 108 (2010) article # 043107.

D. Byrne, E. McGlynn, J. Cullen, M.O. Henry, A catalyst-free and facile route to periodically ordered and c-axis aligned ZnO nanorod arrays on diverse substrates, Nanoscale, 3 (2011) 1675–1682.

Daragh Byrne, Rabie Fath Allah, Teresa Ben, David Gonzalez Robledo, Brendan Twamley, Martin O. Henry, E. McGlynn, Study of morphological and chemical changes of aligned zinc oxide nanorods growth by vapour phase transport on chemical bath deposited buffer layers. Crystal Growth Design, 2011, 11 (12), 5378–5386

E. McCarthy, D. Byrne, S. Garry, E. McGlynn, J.P. Mosnier, Field emission in ordered arrays of ZnO nanowires prepared by nanosphere lithography and extended Fowler-Nordheim analyses. Journal of Applied Physics, 2011, 110, article# 124324

S. Yılmaz, E. McGlynn, E. Bacaksız, Ş. Özcan, D. Byrne, M.O. Henry, Effects of Cu diffusion-doping on structural, optical and magnetic properties of ZnO nanorod arrays grown by VPT. Journal of Applied Physics, 2012, 111, article# 013903

R. Fath, D. Byrne, T. Ben, D. González, E. McGlynn, R. García, Effect of high temperature VPT conditions on the development of aligned ZnO nanorod arrays grown by a three step catalyst-free method, Journal of Nanoscience Letters (in print).

Publications in preparation:

D. Byrne, F. Herklotz, M.O. Henry, E. McGlynn,Unambiguous identification of the role of a single Cu atom in the ZnO structured green band.

Conferences:

D. Byrne, E. McGlynn, M.O. Henry, K. Kumar, G. Hughes, A novel, substrate independent three step process for the growth of uniform ZnO nanorod arrays. Oral presentation (by E. McGlynn) at EMRS 2009 Conference, June 8th - June 12th 2009, Strasbourg, France.

S.K. Das, D. Byrne, E. McGlynn, M. Bock, R. Grunwald, Multi-photon excited UV luminescence of ZnO nanorods after irradiation with few-nJ femtosecond laser pulses. Poster presentation at Conference on Lasers and Electro-Optics and The Quantum Electronics and Laser Science Conference (CLEO/QELS) 2010, May 16th - May 21st 2010, San Jose CA, USA.

D. González, T. Ben, R. Fath, J. G. Lozano, D. Byrne, E. McGlynn, TEM study of the mechanism for the growth of uniform ZnO nanorod arrays using a substrate independent three-step process. Poster presentation at the 17th International Microscopy Congress - IMC17, September 19th - September 24th 2010, Rio de Janeiro, Brazil.

D. Byrne, M.O. Henry, E. McGlynn, Controlled growth of aligned and ordered ZnO nanorod arrays. Poster presentation at the Nanoweek Conference 2011 - Nanotechnology: Research Excellence & Commercial Opportunities, January 31st - February 1st 2011, Kildare, Ireland.

D. Byrne, M.O. Henry, E. McGlynn, Controlled growth of aligned and ordered ZnO nanorod arrays. Poster presentation at the ISOLDE Dublin Workshop 2011, September 9th 2011, Dublin, Ireland.

R. Fath, D. Byrne, T. Ben, D. González, E. McGlynn, R. García, Effect of the VPT temperature conditions on the development of aligned ZnO nanorod arrays grown by a three step catalyst-free method. Oral presentation (by R. Fath) at the First Euro-Mediterranean Conference on Materials and Renewable Energies (EMCMRE – 1), November 21st – 25th 2011, Marrakech, Morocco.

Chapter 1

1.1 Introduction

Semiconductors undoubtedly play a ubiquitous role in modern life, being found in practically every electronic device commercially available. Accordingly they play an equally important aspect in many areas of scientific research and development. While silicon (Si) is probably the most well known semiconductor both by the general public and in terms of scientific investigation, there are many other semiconductors whose properties are more suited to specific applications. Of these semiconductors zinc oxide (ZnO) is currently the subject of considerable interest among many research groups. This interest is due in part to the availability of ZnO raw materials at relatively low cost and high levels of purity and in part due to a large number of potential applications for which it has been proposed that ZnO will have a considerable advantage over other semiconductors. In tandem with the increasing interest in ZnO as a semiconductor, the field of nanotechnology has also surged in popularity due to demands for increased device performance, device miniaturisation, reduced power consumption and materials with novel properties. Consequently the area of ZnO nanostructure research is extremely active with over 26000 papers on the subject being published within the last ten years alone. This output accounts for over half of all publications on ZnO during the same time frame and approximately 20% of all semiconductor publications and 37% of all nanotechnology publications.[1] Despite this huge degree of interest, many fundamental questions remain unanswered. In particular, despite

[1] (figures based on the number of search returns on ISI web of knowledge using the search terms "zno", "zinc oxide", "nano" and "nanostructures" on the 10th of November 2011)

many potential applications being suggested based on the material properties, fewer reports deal with the practicalities of incorporating ZnO into existing device architectures in a controlled manner. This is particularly important for nanostructures, where the morphology of the material is expected to influence the performance of the particular device. In this thesis some of the practical challenges associated with the growth of ZnO nanostructures and their characterisation are addressed, and the underlying motivation is to develop growth techniques which might ultimately be suitable in terms of reliability, reproducibility and scalability for the incorporation of these nanostructures into devices.

ZnO has had a long and interesting history and is by no means a new material. Some of the earliest recorded uses date back as far as 1500BC, where it was used in conjunction with copper to form brass.[1] Interestingly in these early brass foundries ZnO was used as a raw material for zinc extraction. By mixing the ZnO powder with carbon and copper and heating in a closed vessel zinc vapour was produced which lead to the production of brass. As will be discussed later in this chapter, 3500 years later high quality ZnO is still being produced by similar methods. While these early uses of ZnO were as a source material for zinc production, it is believed that ZnO also found other uses. Moving forward in time, ZnO later found commercial use as a pigment in the 1700-1800s. However accounts vary as to by whom and when the commercial potential of ZnO was realised. Barnett *et al.* on his historical review of pigments, credited Winsor and Newton of London working with Michael Faraday with the invention of "Chinese White" giving London artists their semi-opaque white water colour.[2] Period literature suggests the commercial value was realised much earlier with initial development by Courtois of Djion and subsequent commercial development by Sorel in 1834.[3] The curious reader can find a list of some of the earliest modern applications of ZnO, such as ointments, glues, pottery glazing and rubber production in Smith's book on ZnO from 1909.[3] As the number of applications grew from paints to catalysts for rubber production, so to did the number of patents describing methods of producing ZnO, with patents from as early as 1876 now available online.[4] In the 1930's with the advent of modern semiconductor theories, ZnO along with many other metal oxides were already recognised for their semiconducting properties.[5-8] By the 1940s it was recognised that ZnO both absorbed UV light and also could be stimulated using an electron beam to emit light within the UV region of the spectrum, with a corresponding visible emission band.[9-10] By the beginning of the 1950s many of the fundamental properties of ZnO had been recognised such as its catalytic behaviour,[11] UV and green emission spectrum,[9, 12] absorbance spectrum,[13] crystallographic properties,[14-15] electrical

properties[13, 16] and many of its chemical properties. During the 1950s much of the interest surrounding ZnO was in its potential for use as a phosphor, along with its now well founded use as a pigment and catalyst. Despite this wealthy abundance of early publications and applications, ZnO would go on to become a rich field of activity for the next 60 years and is currently still an extremely active area of research. For the interested reader there are many excellent review articles and books available on the various aspects of ZnO.[17-22]

This thesis is broken in to 7 chapters. Chapter 1 presents an overall introduction to ZnO, including the motivation for this work and an overview of some of the relevant material properties and an outline of some ZnO growth techniques. Chapter 2 details the experimental techniques used in this work, giving specific information on the growth process and a brief introduction to the methods used to characterise the materials deposited. Chapter 3 examines the properties of ZnO seed layers prepared by a drop coating technique and of ZnO nanorod arrays grown by chemical bath deposition (CBD) thereon. Chapter 4 present our results on the use of CBD nanorod arrays as a nucleation film for carbothermal vapour phase transport deposition (CTR-VPT). In chapter 5, we extend the work presented in chapter 4, to include a method of controlling the alignment and position of ZnO nanorods. The final experimental results presented in chapter 6 deals with optical properties and defects of ZnO nanorods and of bulk single crystal samples. Lastly, chapter 7 summarises the main findings of this work, the conclusions drawn and briefly discusses which future directions of research may be fruitful.

1.2 Applications and motivation for this work

ZnO has attracted considerable attention in the last decade as a potential material for electronic device manufacture. Its wide direct bandgap of 3.3 eV at 300 K and large exciton binding energy of ~60 meV[19] has fuelled interest in this material for electronic and optoelectronic devices, such as field emitters, UV-lasers, photovoltaic cells and photodiodes.[20, 23-25] Optical applications are of particular interest as it has been widely reported that ZnO has some distinct advantages over the current gallium nitride (GaN) technology. Specifically, the higher exciton binding energy of ZnO (~60 meV as compared to GaN's ~25 meV[26]) means that the free exciton is stable (or at least significant electron hole correlation remains) at or even above room temperature, thereby increasing the probability of photon emission during hole-electron recombination at normal operating temperatures. Therefore, it has been suggested that ZnO based LEDs may be significantly

brighter than their GaN competitors.[25] In addition, ZnO is available in large single crystal substrates, and can be processed using wet chemical methods, albeit with some difficulties given the anisotropic nature of the ZnO Wurtzite crystal. However, given that the current internal quantum efficiency (IQE) of GaN quantum well based technology is greater than 80%, it is unlikely that any gains resulting from the use of ZnO in LEDs would outstrip the current high performance GaN based technology.[27-28] In addition, there is a major bottleneck in ZnO based LED technology, as reliable and stable methods of producing p-type ZnO have not been realised. In an attempt to overcome these difficulties, many groups have investigated p-n heterojunctions, using ZnO in combination with other materials such PEDOT/PSS, an organic semiconductor polymer and other wide bandgap inorganic semiconductors such as $CuAlO_2$.[29-30] While electroluminescence has been reported using these heterostructure combinations, the observed emission intensities are extremly weak. Consequently ZnO based heterostructure LEDs, while showing some indications of progress, face serious challenges if they are to become competitive device technologies. Substantial work in this area and in particular, in understanding the electronic band structure around the interfaces is necessary if improvements in device performance are to be achieved. While research into ZnO based heterostructured LEDs may not ultimately result in commercially viable devices, research in this area may still be quite valuable as it can be transferable to other potential applications such as solid state photovoltaic devices.

ZnO is also of interest for field emission applications such as x-ray sources and flat panel displays. Filament based or “hot cathode” thermionic electron emission sources typically have a short lifetime, owing to the high operating temperatures and currents necessary to achieve reasonable emission currents. Field emission based sources or cold cathodes have much lower power requirements and operating temperatures, which results in longer device lifetimes and more stable emission. Low dimensional conductive nanostructures such as nanorods are potentially ideal field emission sources having much lower turn on voltages and power requirements as compared to hot cathode devices. For improved device performance it is necessary to use materials that are both physically robust whilst still being able to control the deposition parameters such as aspect ratio and a rod density. [31-34] ZnO is an excellent candidate material as it is physically robust, has a high melting temperature, can be further doped to improve its conductivity and currently there are many techniques available to deposit various different morphologies, including high aspect nanorod arrays.

ZnO nanorods are also of considerable interest for dye sensitised solar cell (DSSC) applications. For these applications increasing the amount of light captured by the cell is of critical importance in improving the device performance. It is also necessary to prevent electron-hole recombination as this limits the current output of the cell. ZnO nanostructures in the form of nanorod arrays with high aspect ratios increase the surface area of the cell, which in turn increases the dye loading achievable and increases the photon capture, leading to higher currents.[35] In addition, using single crystal nanorods increases the electron transport speed out of the cell as compared to polycrystalline films, thereby reducing the probability of unwanted parasitic electron-hole recombinations. It should be noted however that despite the improved device performance achieved using high surface area single crystal ZnO nanorod arrays, ZnO has a poor resistance to harsh chemical environments, consequently focus is shifting towards using ZnO/TiO_2 core/shell structures.

In addition to the applications discussed above, ZnO is also a material of interest for many other applications such as solid state gas sensors where the surface reactivity is known to affect the electronic properties of low dimensional structures,[36-37] while theoretical predictions suggest that transition metal doped ZnO may be ferromagnetic and suitable for room temperature spintronic applications.[38] Other novel ZnO applications have also been developed, such as nano-electrical generators based on the piezoelectric properties of 1D nanorod arrays.[39] Finally, ZnO has other advantages in that it is biocompatible,[40] available in high purity at low cost and is compatible with many aspects of conventional silicon processing technology.[20]

It is interesting to note that, despite the availability of high quality single crystal substrates / wafers, many of the proposed applications are for nanostructures and in particular nanostructures deposited on substrates of different varieties, such as silicon, FTO, polymers or glass. To meet the demand of this wide variety of applications, a wide variety of ZnO nanostructures and morphologies have been developed, such as thin films, walls, rods, belts, springs and hemispheres.[35, 41-45] Aligned ZnO nanorod arrays are an interesting subset of these morphologies as they are ideally suited to many of the applications just described. To fully realise the application potential, certain key difficulties need to be addressed. Firstly, for many applications and in particular optoelectronic applications, the quality of material deposited is a crucial aspect as impurities and defects can lead to non-radiative recombination centres, quenching the UV emission. Therefore,

techniques which deposit high quality ZnO, in both a reproducible manner and inexpensively, are of particular importance. Secondly, if ZnO is to be incorporated into device structures, not only must the appropriate material quality and morphology be achieved, it is also essential to be able to accurately position the nanostructures within the overall device. Finally, it is also important to understand how the ZnO nanostructure interacts with the host device and if this interaction interferes with device performance.

In this work we have attempted to address some of these factors, by developing a method to deposit high quality *c*-axis aligned ZnO nanorods using facile techniques, by which we mean techniques that do not require particularly expensive or unusual equipment setups. Following on from this work we have developed and demonstrated a method to control the position of the *c*-axis aligned nanorods, using a nanosphere self-assembly technique. Finally, we have used optical characterisation, electron microscopy, x-ray diffraction and other techniques throughout all aspects of the work to understand both the deposition processes and the interactions between substrate and nanorods.

1.3.1 Material Properties: Crystal structure

Zinc oxide is a d-block metal oxide which can be synthesised directly from zinc metal or from salts of zinc. It is normally (at standard temperature and pressure and over a wide temperature and pressure range) found in the hexagonal Wurtzite crystal form but can also exist in the cubic zincblende or cubic rocksalt form.[46-48]

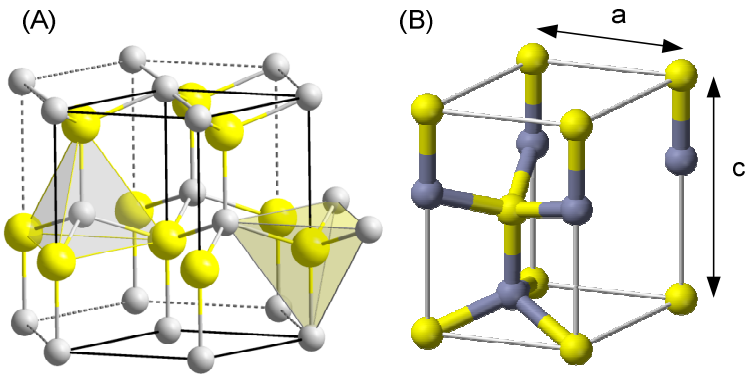

Figure 1.1: (a) The Wurtzite crystal structure of ZnO showing the tetrahedral coordination of each atom with 4 atoms of the second type (b) The unit cell of Wurtzite structured ZnO. Images reproduced from reference 49.

Figure 1.1 (a) shows the hexagonal structure of the Wurtzite crystal structure, while 1(b) shows the unit cell. The ideal Wurtzite unit cell has two lattice parameters, c and a in the ratio c/a=√(8/3) = 1.6330. For ZnO the measured lattice parameters at room temperature are a = 3.2498 Å, c = 5.2066 Å, giving c/a=1.6021.[48] The deviation from the ideal lattice parameters are most likely due to the ionic nature of the ZnO bond, leading to a distortion of the bond angle.[20] The structure consists of planes of a single type of atoms in a hexagonal close packed configuration. Each atom is coordinated with four atoms of the other type who in turn form hexagonal close packed planes above and below. The unit cell volume is approximately 23.8 $Å^3$.[48] The ZnO Wurtzite structure is classified by the C_{6v} point group and C^4_{6V} space group using Schoenflies notation. The crystal structure therefore has only one axis of symmetry which leads to sixfold rotational symmetry about the *c*-axis and other indirect symmetries but does not possess inversion symmetry.[50]

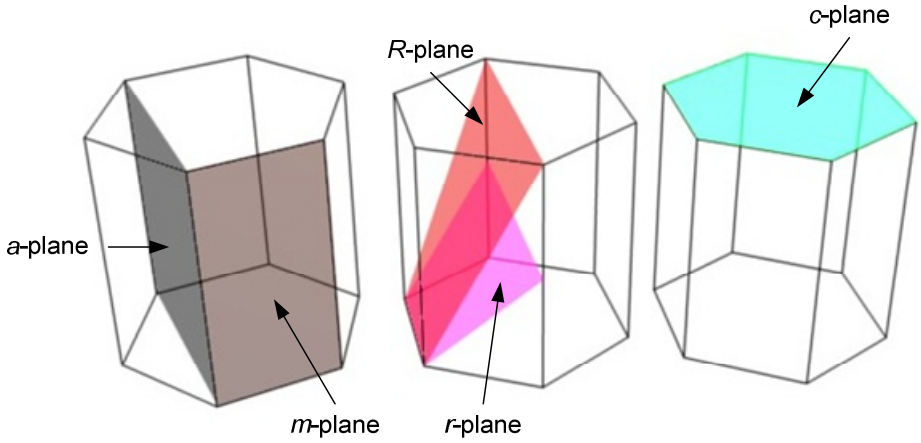

Figure 1.2: Hexagonal ZnO structure showing the various different planes.

The principal planes of the ZnO Wurtzite structure are shown in figure 1.2. The *a*-plane runs parallel to the c-axis and is denoted by (1-120) using Miller – Bravais notation. This plane is terminated by both Zn and O atoms and is non-polar. Similarly, the *m*-plane is also non-polar and is denoted by (10-10). The *c*-plane consists of alternating positively charged Zn planes (0001) and negatively charged O planes (000-1). This creates a spontaneous polarisation across the crystal structure and leads to variation in the surface energies. The dipole moment on the Zn (0001) is stabilised by the formation of triangular holes with a mono-atomic step height. Stepped terraces with both triangular pits and islands have also been observed on this surface. The presence of oxygen terminations along the steps and pits reduces the excess zinc thereby stabilising the surface. The oxygen terminated (000-1) plane is stabilised by double step terraces with a 120° step edge angle,

corresponding to the non-polar (11-20) plane.[51-52] By comparison, little information is available on the semi-polar *r*-plane (10-11) and *R*-plane (10-12). This may in part be due to difficulties in epitaxial growth of crystals on these planes.[53]

1.3.2 Material Properties: Electronic bandgap

The outer electron configuration of zinc metal is $3d^{10}\ 4s^2$ while oxygen has an outer electron configuration of $2s^2\ 2p^4$. ZnO has sp^3 hybridised bonding. As oxygen (O) has a greater electronegativity than zinc (Zn) the outer $4s^2$ electrons of the zinc are drawn into unequal bonds with the oxygen to stabilise the oxygen outer shell. Precise determination of the complete band structure of ZnO is a complicated task which has been investigated for several decades. Theoretical calculations of the band structure of ZnO have been performed in a variety of ways including local density approximations and tight binding techniques. Theoretical calculations have failed to accurately explain all aspects of experimental results. The problem has been partly explained in some theoretical interpretations by the treatment of the Zn 3d electrons. For ease of calculation the 3d electrons have been treated as core level features. However experimental evidence suggests that the 3d electrons have an influence on the position of the Zn-4s and O-2p valence band electrons.[20, 54] Despite the uncertainty in the role and position of the 3d electrons in the band structure of ZnO, the valence band position is most strongly influenced by the hybrid orbitals of the Zn 4s and O 2p electrons. Figure 1.3 shows a schematic representation of the band structure of ZnO, were the band gap is between the oxygen $O^{2-}2p$ valence band states and $Zn^{2+}4s$ conduction band states.

As mentioned earlier, ZnO has a direct bandgap of approximately 3.3 eV. The conduction band minimum and valence band maximum occur at the same location in phase space, and therefore their wave functions are indexed by the same value, i.e. they have the same *k*-vector. The conduction band is primarily composed of the empty Zn $4s^{2+}$ *s*-type orbitals, having Γ_7 symmetry. The valence band is formed from the occupied O $2p^{2-}$ *p*-type orbitals. The *p*-type orbitals are split into three bands with twofold degeneracy, by the hexagonal crystal field and spin-orbit coupling. These bands are labelled A to C from the highest energy to lowest and have Γ_7, Γ_9, and Γ_7 symmetries respectively. It should be noted that the ordering of these bands has been the subject of controversy for many years now. For a more comprehensive discussion see chapter 4 of reference 55. By convention holes

formed in the A valence band are referred to as light holes, whilst holes in the B and C bands are called heavy holes' and spin orbit split-off band holes respectively.

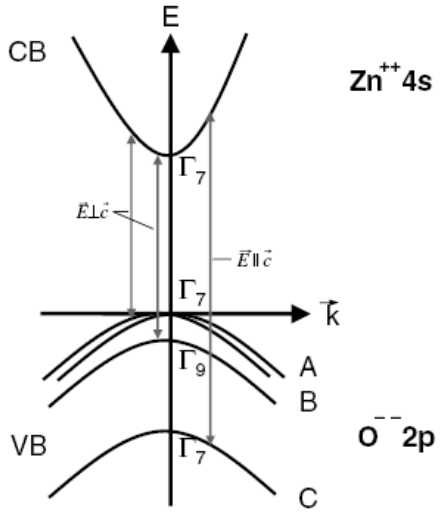

Figure 1.3: Schematic diagram of ZnO band structure at zone centre. Image reproduced from reference 56. Copyright: (2007) John Wiley and Sons.

ZnO has an intrinsic *n*-type conductivity that has been the source of much debate for many years, with varying origins being put forward in the literature. Consequently efforts to dope ZnO *p*-type in a reproducible and reliable fashion have faced serious challenges. Despite these difficulties *p*-type doping has been reported by numerous groups using a variety of different dopants and growth techniques.[57-62] However the ultimate success of these attempts will have to be judged by the reliable and stable production and then commercialisation of homoepitaxial ZnO *pn* junction based devices. To date this has not been the case following any of the reported *p*-type doping successes in the literature, to our knowledge.

Deviations in the stoichiometry lead to the formation of Zn interstitials (Zn_i) and O (V_o) vacancies. Originally it was believed that these point defects in ZnO are the dominant source of the intrinsic n-type conductivity. However differences remain as to whether it is due to Zn_i or V_o.[20, 63-64] First principle calculations later predicted that point defects were not the dominant source of the intrinsic n-type conductivity, although they may act as compensation centres during p-type doping. There is also strong evidence to suggest that hydrogen (H) plays an important role in the electrical conductivity. In most semiconductors H is amphoteric, meaning that it is found in the H^+ in p-type material or H^- state in n-type material. In ZnO it is found exclusively in the H^+ state and therefore acts as a donor.[20] In

some reports, it is suggested that intrinsic point defects play little role in the n-type conductivity and that this effect is primarily due to hydrogen incorporated during the growth process.[65, 66] Given the high diffusivity of H and its ubiquitous presence during growth this explanation has been given particular prominence in recent literature.[20, 55] ZnO can be further doped n-type with atoms of aluminium (Al) gallium (Ga) and indium (In) both intentionally and unintentionally. In this work Al was found extensively in our samples despite no efforts to deliberately introduce this dopant. Intentional and unintentional doping of ZnO is discussed further in chapter 6.

1.3.3 Growth techniques

The number of methods to grow or deposit ZnO is almost as numerous as the number of proposed applications. In this section we will give a brief outline of some of the more common methods used and some of their advantages and disadvantages. The different growth techniques can be separated into three classes, albeit with some degree of overlap. Typically ZnO is grown as either bulk single crystals / substrates, as powders which can be either mesoscale or nanoscale, or on substrates in the form of films or isolated structures. The choice of ZnO growth technique is then naturally dependent on the properties needed for a specific application.

Bulk single crystals

Currently there are three methods for producing bulk single crystal ZnO. The first is by vapour phase transport, the second by melt processes and the last by hydrothermal techniques. First we shall consider the vapour phase growth method. Like many aspects of ZnO this method is not new, in that publications on single crystal growth have been available since the 1950's with further improvement in the technique occurring more recently.[63, 67-71] Growth by VPT typically begins with high quality ZnO powders as a raw material. The ZnO is then reduced to Zn and O_2 at high temperatures in a furnace. The Zn vapour is then allowed to flow away from the hot zone of the furnace to a cooler zone where it is redeposited and oxidised. Typically growth temperatures around 950 to 1150°C are required, depending on the reducing agent used. Growth times can vary from several

hours to several weeks depending on the technique used and the size of the final single crystal. The reaction chemistry is relatively straight forward and is described by the equations:

$$ZnO(s) + R \rightarrow Zn(g) + RO \quad (1.3.1)$$

$$2Zn(g) + O_2(g) \rightarrow 2ZnO \quad (1.3.2)$$

Usually either carbon or hydrogen are employed as the reducing agent (R), however other reducing agents such as NH_3 and NH_4Cl have been reported.[72] In order to improve the stoichiometry of the final product, water vapour is sometimes added to the reaction system.[63, 71] The choice of reducing agent influences the temperature necessary to reduce the ZnO source material, with carbon reduced reactions occurring at slightly lower temperatures. The experimental configuration varies between methods, with both open ended quartz tubes in conjunction with a carrier gas and also sealed ampoule systems being used.

Melt processes are significantly more challenging, due to the high melting temperature of ZnO (1975°C). The difficulty arises in selecting a crucible capable of withstanding these temperatures and also that ZnO at high temperatures decomposes into a defective ZnO_{1-x} material. These difficulties have been addressed by the development of the pressurised melt or skull melt technique by the Cermet company.[73] In this method ZnO is melted in a custom designed induction furnace using a cold wall crucible. The wall of the crucible is coated with ZnO to prevent contact with the outer material. The induction heating is then able to melt the inner contents of the crucible without melting the outer ZnO coating on the crucible wall, thereby preventing any unwanted interactions. An over pressure of oxygen in the furnace chamber is used to reduce the defects associated with the decomposition of ZnO into ZnO_{1-x}. More recently, it has been proposed that iridium may be suitable for use as a crucible to overcome the strain in the ZnO, induced by the large temperature gradient across the crucible wall, allowing single crystals to be grown by the Bridgeman technique.[74] However initial results indicate that further development is necessary in order to overcome difficulties that include the incorporation of defects and impurities into the crystals. Single crystal ZnO has also been grown at lower temperatures

using a Bridgeman flux method from PbF_2.[75] However these crystals are a lot smaller in size as compared to the other two methods discussed in this section.

The largest single crystal substrates currently available commercially are grown by hydrothermal methods. In principle, hydrothermal growth is similar to VPT growth in that material is transported from a hot zone and redeposited in a cold zone. In the hydrothermal technique this transport is achieved by convective flows though the solvent solution. The reducing agent in the VPT growth is replaced with a mineralisation agent, which dissolves the ZnO into solution in the hotter part of the autoclave. The dissolved ZnO is then transported to a cooler region where the solubility of the ZnO is reduced. Consequently the ZnO precipitates out of solution onto seed crystals. The choice of mineraliser is an important factor in preventing secondary nucleation, with a mixture of LiOH and KOH being used.[76-77] However, the LiOH used to prevent dendrite formation is the dominant impurity found in hydrothermally grown ZnO with concentrations typically around 0.5 to 12 ppm.[77-78]

Nanostructure and film growth

At present, growth of ZnO nanostructures and thin films by chemical bath deposition (CBD) is growing in popularity. This is undoubtedly due to the relative ease and inexpensive nature of CBD techniques. Consequently there have been many reported techniques using a variety of different precursor chemicals. Usually Zn salts such as Zn formate, nitrate, acetate, sulphate and chloride are used with a base to form a partially soluble zinc hydroxide.[79-83] Depending on the specific conditions employed, in particular the pH, dissolved zinc hydroxide is decomposed to form ZnO or alternatively Zn^{2+} can be directly oxidised to form ZnO.[84] Many different bases have been used for these reactions including hexamine (HMT), ammonia, urea, sodium hydroxide, potassium hydroxide, and ethanolamine in solvent such as water, ethanol, methanol, propanol and ethylene glycol.[43, 85-93] CBD offers distinct advantages in that the chemistry can be adapted to tailor the synthesis giving unparalleled control over the morphology of the ZnO structures and films. The choice of base, zinc salt, substrate, complexing agent, the addition of surfactants and the choice of solvent have all been shown to influence the final morphology of the ZnO deposit produced. Given that the synthesis is generally carried out at relatively low temperatures (usually less than 100°C) and that the solvent used can be easily interchanged, CBD growth is possible on many substrates that would not be suitable for

high temperature growth techniques, including substrates as diverse as paper and flexible polymers.[82, 94] In this work CBD methods were used extensively and further information on the specific deposition methods used is given in chapters 2 and 3. In addition to the standard CBD techniques there are also a host of other low temperature wet chemical techniques reported in the literature, such as electrochemical deposition, successive ionic layer adsorption reaction (silar), dip-coating and spin coating.[95-98] However, some of these methods require further thermal treatments to enhance the properties of the as-deposited films.

ZnO nanostructures and films have also been deposited on substrates and as loose powders using higher temperature methods such as chemical vapour deposition (CVD), plasma assisted CVD and vapour phase transport (VPT) of various types.[33, 99-107] CVD is based on the decomposition of a precursor on the substrate surface or in the case of powder production in the atmosphere. For film and nanostructure deposition, the substrate is heated to a temperature at which the precursor will decompose. The precursor is brought to the substrate by a carrier gas flow. In order to transport the precursor to the substrate via the gas stream through the reaction chamber, it is necessary to choose a precursor that has sufficient volatility. Consequently metal-organic precursors such as dimethylzinc, dimethylzinc triethylamine and zinc acetylacetonate are used.[55, 99] Alternatively the precursor can be carried into the reaction chamber by fine aerosols prepared by ultrasonic nebulisation of a solution of the dissolved precursor, although this method could be considered a refinement of spray pyrolysis methods also used to deposit ZnO films.[108]

VPT growth of ZnO nanostructure and films is quite similar to the VPT methods used to grow bulk crystals. Usually substrates are placed down stream from an elemental Zn source in a furnace. As with the bulk growth method the Zn source can be Zn powder or ZnO mixed with a reducing agent. During growth, a carrier gas brings the Zn vapour to substrate, where it undergoes an oxidisation reaction to deposit ZnO nanostructures. Two distinct growth routes may be used, the first being vapour liquid solid (VLS). In this method, the substrates are coated with a catalyst such as gold (Au), which at the deposition temperature is molten. The Zn vapour is absorbed into the catalyst droplets forming a saturated alloy. The accumulation of the zinc in the alloy droplet ultimately leads to the precipitation of Zn from the droplet, oxidation of the precipitated Zn and crystallisation of ZnO, in the form a ZnO nanorod.[107, 109] The second route, vapour solid (VS), is where the

zinc vapour is adsorbed onto the substrate surface, where it directly oxidised. The latter method is used extensively in this work and is discussed in greater detail in chapters 2, 4 and 5.

1.4 References

(1) Biswas, A. K. *Indian journal of history of science* **1993** *28* (4) 309-330

(2) Barnett, J. R.; Miller, S.; Pearce, E. *Optics & Laser Technology 38* (4-6) 445-453

(3) Smith, J. C., *Oxide of Zinc: Its Nature , Properties & Uses*. The Decorator. **1909**, Chambers W.C.: The Trade Papers Publishing Company

(4) Hughes, S., *Improvement in Zinc-Oxide Furnaces*, United States Patent Office, **1876**, Samuel Hughes: United States.

(5) Fuoss, R. M. *Journal of Chemical Education* **1942,** *19* (4) 190

(6) Seitz, F.; Johnson, R. P. *Journal of Applied Physics* **1937,** *8* (3) 186-199

(7) Miller, P. H., Jr. *Physical Review* **1941,** *60* (12) 890-895

(8) Wagner, C. *Transactions of the Faraday Society* **1938,** *34* 851-859

(9) Nicoll, F. H. *J. Opt. Soc. Am.* **1948,** *38* (9) 817-817

(10) Shrader, R. E.; Leverenz, H. W. *J. Opt. Soc. Am.* **1947,** *37* (11) 939-940

(11) Wagner, C. *The Journal of Chemical Physics* **1950,** *18* (1) 69-71

(12) Hill, C. G. A. *British Journal of Applied Physics* **1955,** *6* (S4) S6

(13) Hahn, E. E. *Journal of Applied Physics* **1951,** *22* (7) 855-863

(14) Fuller, M. L. *Journal of Applied Physics* **1944,** *15* (2) 164-170

(15) Heller, R. B.; Mcgannon, J.; Weber, A. H. *Journal of Applied Physics* **1950,** *21* (12) 1283-1284

(16) Harrison, S. E. *Physical Review* **1954,** *93* (1) 52-62

(17) Willander, M.; Nur, O.; Zhao, Q. X.; Yang, L. L.; Lorenz, M.; Cao, B. Q.; Pérez, J. Z.; Czekalla, C.; Zimmermann, G.; Grundmann, M.; Bakin, A.; Behrends, A.; Al Suleiman, M.; El-Shaer, A.; Mofor, A. C.; Postels, B.; Waag, A.; Boukos, N.; Travlos, A.; Kwack, H. S.; Guinard, J.; Dang, D. L. S. *Nanotechnology* **2009,** *20* (33) 332001

(18) Klingshirn, C.; Fallert, J.; Zhou, H.; Sartor, J.; Thiele, C.; Maier-Flaig, F.; Schneider, D.; Kalt, H. *Phys Status Solidi B* **2010,** *247* (6) 1424-1447

(19) Reynolds, D. C.; Look, D. C.; Jogai, B.; Litton, C. W.; Collins, T. C.; Harsch, W.; Cantwell, G. *Phys Rev B* **1998,** *58* (19) 13276-13276

(20) Ozgur, U.; Alivov, Y. I.; Liu, C.; Teke, A.; Reshchikov, M. A.; Dogan, S.; Avrutin, V.; Cho, S. J.; Morkoc, H. *Journal of Applied Physics* **2005,** *98* (4) 041301

(21) Morkoç, H.; Özgür, Ü., *Zinc Oxide: Fundamentals, Materials and Device Technology*. Zinc Oxide. 2009: Wiley-VCH Verlag GmbH & Co. KGaA.

(22) *Zinc Oxide Bulk, Thin Films and Nanostructures Processing, Properties, and Applications* ed. C. Jagadish and S.J. Pearton. 2006: Elsevier Science.

(23) Hofstetter, D.; Bonetti, Y.; Giorgetta, F. R.; El Shaer, A. H.; Bakin, A.; Waag, A.; Schmidt-Grund, R.; Schubert, M.; Grundmann, M. *Applied Physics Letters* **2007,** *91* (11) 111108

(24) Lee, C. J.; Lee, T. J.; Lyu, S. C.; Zhang, Y.; Ruh, H.; Lee, H. J. *Applied Physics Letters* **2002,** *81* (19) 3648-3650

(25) Huang, M. H.; Mao, S.; Feick, H.; Yan, H. Q.; Wu, Y. Y.; Kind, H.; Weber, E.; Russo, R.; Yang, P. D. *Science* **2001,** *292* (5523) 1897-1899

(26) Xu, S. J.; Liu, W.; Li, M. F. *Applied Physics Letters* **2002,** *81* (16) 2959-2961

(27) Zhao, Y.; Sonoda, J.; Pan, C.-C.; Brinkley, S.; Koslow, I.; Fujito, K.; Ohta, H.; Denbaars, S. P.; Nakamura, S. *Applied Physics Express* **(2010)** *3* 102101

(28) Nishida, T.; Saito, H.; Kobayashi, N. *Applied Physics Letters* **2001,** *79* (6) 711-712

(29) Chang, C. Y.; Tsao, F. C.; Pan, C. J.; Chi, G. C.; Wang, H. T.; Chen, J. J.; Ren, F.; Norton, D. P.; Pearton, S. J.; Chen, K.-H.; Chen, L.-C. *Applied Physics Letters* **2006,** *88* (17) 173503

(30) Ling, B.; Sun, X. W.; Zhao, J. L.; Tan, S. T.; Dong, Z. L.; Yang, Y.; Yu, H. Y.; Qi, K. C. *Physica E: Low-dimensional Systems and Nanostructures* **2009,** *41* (4) 635-639

(31) Yue, G. Z.; Qiu, Q.; Gao, B.; Cheng, Y.; Zhang, J.; Shimoda, H.; Chang, S.; Lu, J. P.; Zhou, O. *Applied Physics Letters* **2002,** *81* (2) 355-357

(32) Jo, S. H.; Lao, J. Y.; Ren, Z. F.; Farrer, R. A.; Baldacchini, T.; Fourkas, J. T. *Applied Physics Letters* **2003,** *83* (23) 4821-4823

(33) Garry, S.; McCarthy, E.; Mosnier, J. P.; McGlynn, E. *Applied Surface Science* **2011,** *257* (12) 5159-5162

(34) Mcloughlin, C.; Hough, P.; Costello, J.; McGlynn, E.; Mosnier, J. P. *Ultramicroscopy* **2009,** *109* (5) 399-402

(35) Law, M.; Greene, L. E.; Johnson, J. C.; Saykally, R.; Yang, P. D. *Nature Materials* **2005,** *4* (6) 455-459

(36) Nanto, H.; Minami, T.; Takata, S. *Journal of Applied Physics* **1986,** *60* (2) 482-484

(37) Wang, J. X.; Sun, X. W.; Yang, Y.; Huang, H.; Lee, Y. C.; Tan, O. K.; Vayssieres, L. *Nanotechnology* **2006,** *17* (19) 4995-4998

(38) Ueda, K.; Muraoka, Y.; Tabata, H.; Kawai, T. *Applied Physics Letters* **2001,** *78* (4) 512-514

(39) Wang, Z. L.; Song, J. H. *Science* **2006,** *312* (5771) 242-246

(40) Yang, J.; Li, S.; Li, Z. W.; Mcbean, K.; Phillips, M. R. *J Phys Chem C* **2008,** *112* (27) 10095-10099

(41) Bao, D.; Gu, H.; Kuang, A. *Thin Solid Films* **1998,** *312* (1-2) 37-39

(42) Grabowska, J.; Meaney, A.; Nanda, K. K.; Mosnier, J. P.; Henry, M. O.; Duclere, J. R.; McGlynn, E. *Phys Rev B* **2005,** *71* (11) 115439

(43) Greene, L. E.; Law, M.; Tan, D. H.; Montano, M.; Goldberger, J.; Somorjai, G.; Yang, P. D. *Nano Letters* **2005,** *5* (7) 1231-1236

(44) Kong, X. Y.; Wang, Z. L. *Nano Letters* **2003,** *3* (12) 1625-1631

(45) Chen, Y. X.; Zhao, X. Q.; Sha, B.; Chen, J. H. *Materials Letters* **2008,** *62* (15) 2369-2371

(46) Bragg, W. L.; Darbyshire, J. A. *Transactions of the Faraday Society* **1932,** *28* 522-529

(47) Snedeker, L. P.; Risbud, A. S.; Masala, O.; Zhang, J. P.; Seshadri, R. *Solid State Sciences* **2005,** *7* (12) 1500-1505

(48) Desgreniers, S. *Phys Rev B* **1998,** *58* (21) 14102-14105

(49) *Wurtzite Crystal Structure - Wikipedia, the free encyclopedia*. 24/11/2011; Available from: http://en.wikipedia.org/wiki/Wurtzite_crystal_structure.

(50) Davidson, G., *Group Theory for Chemists*. Macmillan Physical Science. 1991, Hampshire: Macmillan.

(51) Dulub, O.; Boatner, L. A.; Diebold, U. *Surf Sci* **2002,** *519* (3) 201-217

(52) Diebold, U.; Koplitz, L. V.; Dulub, O. *Applied Surface Science* **2004,** *237* (1-4) 336-342

(53) Aggarwal, R.; Zhou, H.; Jin, C.; Narayan, J.; Narayan, R. J. *Journal of Applied Physics* **2010,** *107* (11) 113530-113536

(54) Girard, R. T.; Tjernberg, O.; Chiaia, G.; Soderholm, S.; Karlsson, U. O.; Wigren, C.; Nylen, H.; Lindau, I. *Surf Sci* **1997,** *373* (2-3) 409-417

(55) Klingshirn, C. F.; Meyer, B. K.; Waag, A.; Hoffmann, A.; Geurts, J., *Zinc Oxide From Fundamental Properties Towards Novel Applications*. Springer Series in materials science, ed. R.Hull, et al. 2010, Heidelberg: Springer-Verlag.

(56) Klingshirn, C. *Phys Status Solidi B* **2007,** *244* (9) 3027-3073

(57) Kim, J. B.; Byun, D.; Ie, S. Y.; Park, D. H.; Choi, W. K.; Ji Won, C.; Basavaraj, A. *Semiconductor Science and Technology* **2008,** *23* (9) 095004

(58) Park, C. H.; Zhang, S. B.; Wei, S.-H. *Phys Rev B* **2002,** *66* (7) 073202

(59) Ryu, Y. R.; Lee, T. S.; White, H. W. *Applied Physics Letters* **2003,** *83* (1) 87-89

(60) Xiu, F. X.; Yang, Z.; Mandalapu, L. J.; Zhao, D. T.; Liu, J. L.; Beyermann, W. P. *Applied Physics Letters* **2005,** *87* (15) 152101

(61) Look, D. C.; Reynolds, D. C.; Litton, C. W.; Jones, R. L.; Eason, D. B.; Cantwell, G. *Applied Physics Letters* **2002,** *81* (10) 1830-1832

(62) Mathew, J.; Hitoshi, T.; Tomoji, K. *Japanese journal of applied physics. Pt. 2, Letters* **1999,** *38* (11) L1205-L1207

(63) Look, D. C.; Reynolds, D. C.; Sizelove, J. R.; Jones, R. L.; Litton, C. W.; Cantwell, G.; Harsch, W. C. *Solid State Communications* **1998,** *105* (6) 399-401

(64) Vanheusden, K.; Seager, C. H.; Warren, W. L.; Tallant, D. R.; Voigt, J. A. *Applied Physics Letters* **1996,** *68* (3) 403-405

(65) Janotti, A.; Van De Walle, C. G. *Phys Rev B* **2007,** *76* (16) 165202

(66) Chris G, V. D. W. *Physica B: Condensed Matter* **2001,** *308-310* (0) 899-903

(67) Scharowsky, E. *Z Phys* **1953,** *135* (3) 318-330

(67) Zhang, X.; Herklotz, F.; Hieckmann, E.; Weber, J.; Schmidt, P. *Vapor phase growth of ZnO single crystals*. 2011: AVS.

(69) Mycielski, A.; Kowalczyk, L.; Szadkowski, A.; Chwalisz, B.; Wysmołek, A.; StęPniewski, R.; Baranowski, J. M.; Potemski, M.; Witowski, A.; Jakieła, R.; Barcz, A.; Witkowska, B.; Kaliszek, W.; JęDrzejczak, A.; Suchocki, A.; Łusakowska, E.; Kamińska, E. *Journal of Alloys and Compounds* **2004,** *371* (1-2) 150-152

(70) Mikami, M.; Eto, T.; Wang, J.; Masa, Y.; Isshiki, M. *Journal of Crystal Growth* **2005,** *276* (3-4) 389-392

(71) Ntep, J. M.; Barbé, M.; Cohen-Solal, G.; Bailly, F.; Lusson, A.; Triboulet, R. *Journal of Crystal Growth* **1998,** *184-185* 1026-1030

(72) Shiloh, M.; Gutman, J. *Journal of Crystal Growth* **1971,** *11* (2) 105-109

(73) Nause, J.; Nemeth, B. *Semiconductor Science and Technology* **2005,** *20* (4) S45

(74) Schulz, D.; Ganschow, S.; Klimm, D.; Neubert, M.; Roßberg, M.; Schmidbauer, M.; Fornari, R. *Journal of Crystal Growth* **2006,** *296* (1) 27-30

(75) Xu, J.; He, Q.; Shen, H.; Jin, M.; Zhang, Y.; Li, X. *Crystal Research and Technology* **2011,** *46* (11) 1107-1110

(76) Laudise, R. A.; Kolb, E. D.; Caporaso, A. J. *J Am Ceram Soc* **1964,** *47* (1) 9-12

(77) Ohshima, E.; Ogino, H.; Niikura, I.; Maeda, K.; Sato, M.; Ito, M.; Fukuda, T. *Journal of Crystal Growth* **2004,** *260* (1-2) 166-170

(78) Avrutin, V.; Cantwell, G.; Jizhi, Z.; Song, J. J.; Silversmith, D. J.; Morko, H.; *Proceedings of the IEEE* **2010,** *98* (7) 1339-1350

(79) Afzaal, M.; Malik, M. A.; O'brien, P. *New Journal of Chemistry* **2007,** *31* (12) 2029-2040

(80) Govender, K.; Boyle, D. S.; Kenway, P. B.; O'brien, P. *J Mater Chem* **2004,** *14* (16) 2575-2591

(81) Kakiuchi, K.; Hosono, E.; Kimura, T.; Imai, H.; Fujihara, S. *J Sol-Gel Sci Techn* **2006,** *39* (1) 63-72

(82) Greene, L. E.; Law, M.; Goldberger, J.; Kim, F.; Johnson, J. C.; Zhang, Y. F.; Saykally, R. J.; Yang, P. D. *Angew Chem Int Edit* **2003,** *42* (26) 3031-3034

(83) Vayssieres, L.; Keis, K.; Hagfeldt, A.; Lindquist, S. E. *Chem Mater* **2001,** *13* (12) 4395

(84) Ashfold, M. N. R.; Doherty, R. P.; Ndifor-Angwafor, N. G.; Riley, D. J.; Sun, Y. *Thin Solid Films* **2007,** *515* (24) 8679-8683

(85) Lokhande, C. D.; Gondkar, P. M.; Mane, R. S.; Shinde, V. R.; Han, S.-H. *Journal of Alloys and Compounds* **2009,** *475* (1-2) 304-311

(86) Saito, M.; Fujihara, S. *Energy & Environmental Science* **2008,** *1* (2) 280-283

(87) Chu, D.; Masuda, Y.; Ohji, T.; Kato, K. *Langmuir* **2009,** *26* (4) 2811-2815

(88) Peterson, R. B.; Fields, C. L.; Gregg, B. A. *Langmuir* **2004,** *20* (12) 5114-5118

(89) Kokotov, M.; Hodes, G. *J Mater Chem* **2009,** *19* (23) 3847-3854

(90) Kokotov, M.; Biller, A.; Hodes, G. *Chem Mater* **2008,** *20* (14) 4542-4544

(91) Wang, M.; Kim, E. J.; Hahn, S. H.; Park, C.; Koo, K.-K. *Cryst Growth Des* **2008,** *8* (2) 501-506

(92) Hosono, E.; Fujihara, S.; Kimura, T. *Electrochem Solid St* **2004,** *7* (4) C49-C51

(93) Hosono, E.; Fujihara, S.; Kimura, T.; Imai, H. *Journal of Colloid and Interface Science* **2004,** *272* (2) 391-398

(94) Manekkathodi, A.; Lu, M. Y.; Wang, C. W.; Chen, L. J. *Adv Mater* **2010,** *22* (36) 4059-4063

(95) Cui, J. B.; Gibson, U. J. *Applied Physics Letters* **2005,** *87* (13) 133108

(96) Kumar, P. S.; Yogeshwari, M.; Raj, A. D.; Mangalaraj, D.; Nataraj, D.; Pal, U. *J Nano Res* **2009,** *5* 223-230

(97) Valle, G. G.; Hammer, P.; Pulcinelli, S. H.; Santilli, C. V. *Journal of the European Ceramic Society* **2004,** *24* (6) 1009-1013

(98) Natsume, Y.; Sakata, H. *Thin Solid Films* **2000,** *372* (1-2) 30-36

(99) Baxter, J. B.; Aydil, E. S. *J Electrochem Soc* **2009,** *156* (1) H52-H58

(100) Xu, W. Z.; Ye, Z. Z.; Zeng, Y. J.; Zhu, L. P.; Zhao, B. H.; Jiang, L.; Lu, J. G.; He, H. P.; Zhang, S. B. *Applied Physics Letters* **2006,** *88* (17) 173506

(101) Singh, P.; Kumar, A.; Deepak; Kaur, D. *Optical Materials* **2008,** *30* (8) 1316-1322

(102) Liu, X.; Wu, X.; Cao, H.; Chang, R. P. H. *Journal of Applied Physics* **2004,** *95* (6) 3141-3147

(103) Gruber, T.; Kirchner, C.; Waag, A. *physica status solidi (b)* **2002,** *229* (2) 841-844

(104) Bakin, A.; Che Mofor, A.; El-Shaer, A.; Waag, A. *Superlattice Microst 42* (1-6) 33-39

(105) Biswas, M.; McGlynn, E.; Henry, M. O. *Microelectron J* **2009,** *40* (2) 259-261

(106) Li, C.; Fang, G.; Fu, Q.; Su, F.; Li, G.; Wu, X.; Zhao, X. *Journal of Crystal Growth* **2006,** *292* (1) 19-25

(107) Yang, P.; Yan, H.; Mao, S.; Russo, R.; Johnson, J.; Saykally, R.; Morris, N.; Pham, J.; He, R.; Choi, H. J. *Adv Funct Mater* **2002,** *12* (5) 323-331

(108) Waugh, M. R.; Hyett, G.; Parkin, I. P. *Chemical Vapor Deposition* **2008,** *14* (11-12) 366-372

(109) Li, Y.; Feneberg, M.; Reiser, A.; Schirra, M.; Enchelmaier, R.; Ladenburger, A.; Langlois, A.; Sauer, R.; Thonke, K.; Cai, J.; Rauscher, H. *Journal of Applied Physics* **2006,** *99* (5) 054307-054309

Chapter 2: Experimental Techniques

2.1 Introduction

This chapter will discuss details of the experimental procedures used to both grow and characterise ZnO samples, along with the necessary background information on the procedures used. A significant portion of this thesis is devoted to understanding the factors influencing the growth processes used to deposit *c*-axis aligned ZnO nanorods on non-epitaxially matched substrates and the effect of these factors on the morphology and optical properties of the nanorods. For reasons that will be discussed in further detail in later chapters, the aligned nanorods were typically grown by a three step process, consisting of: (1) seeding the substrate with an initial ZnO layer, (2) growth of nanorods by a CBD technique and (3) the deposition of high quality nanorods by carbothermal reduction vapour phase transport (CTR-VPT). A variety of different characterisation techniques including scanning electron microscopy (SEM), field emission scanning electron microscopy (FESEM), x-ray diffraction (XRD), x-ray photoelectron spectroscopy (XPS), atomic force microscopy (AFM), white light profilometry (WLP) and photoluminescence spectroscopy (PL), were used to characterise samples at various stages during their preparation. In this chapter the emphasis will be on the physical processes used to produce and characterise the samples, while later chapters will expand in more detail on the rationale and results obtained. Specifically, chapter 3 focuses on the seed layer preparation and examines the CBD process, chapter 4 concentrates on the CTR-VPT process, chapter 5 outlines a technique developed to control both the orientation and position of the nanorods while maintaining excellent crystal quality and chapter 6 will concentrate on the study of the defect luminescence band in ZnO nanorods and single crystal samples.

2.2 Substrate preparation

The majority of samples were grown on silicon, with only a small proportion of samples being prepared on other substrates, such as glass slides, fused quartz or sapphire. Normally n-type phosphorous doped silicon with (111) or (100) surface orientation was cleaved into rectangles or squares, typically 1-2 cm^2. Once the desired substrate size was achieved, the substrates were then blown with a stream of nitrogen for several seconds to remove any silicon fragments created during the cleaving process. Immediately before use, the substrates were cleaned by sonication in acetone for ten minutes, followed by rinsing in fresh acetone and sonication in absolute ethanol for a further ten minutes. Finally the substrates were rinsed in absolute ethanol and dried under a nitrogen stream. No attempt was made to remove the amorphous native oxide layer of the silicon. A similar cleaning stage was also used for other substrate types.

2.3 Buffer layer preparation

In order to achieve nanorod growth by CBD on a substrate, it is necessary to seed the substrate with a thin ZnO seed layer. This seed layer provides nucleation sites for ZnO and subsequent ZnO nanorod growth. Seed layers prepared for CBD growth were prepared by the method proposed by Greene and Law *et al*. [1-2] from a zinc acetate solution. A 5mM zinc acetate solution is prepared by dissolving zinc acetate dihydrate in absolute ethanol (EtOH). This solution is then sonicated for up to 1 hour and allowed to cool, to ensure the complete dissolution of the zinc acetate. A drop of this solution, typically 3.5 µl per cm^2, is applied to the previously cleaned substrate surface and allowed to spread across the surface. The droplet is allowed to remain on the substrate surface for up to 20 seconds before being rinsed off with copious quantities of ethanol. The size of the drop applied to the surface is an important parameter and is discussed in further detail in chapter 3. This drop-coating procedure is repeated a further three times. Once coated the substrate is annealed at 350°C for 20-30 minutes, to decompose the residual zinc salt into zinc oxide.

2.4 Chemical bath deposition

ZnO nanorods were grown by three different CBD techniques. In the first technique examined, ZnO nanorods were grown from aqueous solutions of zinc nitrate and hexamethylenetetramine (HMT). Typically equimolar solutions of zinc nitrate and HMT are

used. For the bulk of samples grown, the initial zinc nitrate and HMT concentration was 25 mM. The second technique used was the direct thermal decomposition of zinc acetate in solution. In this method solutions of zinc acetate were heated, which results in the loss of the acetate anion leading to the formation of a partially soluble zinc hydroxide which goes on to form ZnO. The third technique examined involves depositing ZnO nanorods from a metastable $Zn(OH)_4^{-2}$ solution, derived from zinc nitrate and sodium hydroxide (NaOH). This technique differs radically from the HMT and acetate methods as no other precipitates or debris is formed during the reaction.

For all three techniques a similar equipment setup can be used, a schematic of which is shown in figure 2.1. A hotplate is used as the source of heating, while reactions are performed in a closed reaction vessel fitted with a reflux condenser or a laboratory beaker. In both equipment setups, the reaction solutions are stirred with using a PTFE coated magnetic stirring bar, while the reaction solution temperature is monitored with either an alcohol filled thermometer or a digital temperature probe. The variation in equipment setup did not influence the final morphology of the ZnO nanorods. However the addition of a reflux condenser was convenient for longer reaction times as it eliminated the risk of the solution level falling below the substrate height.

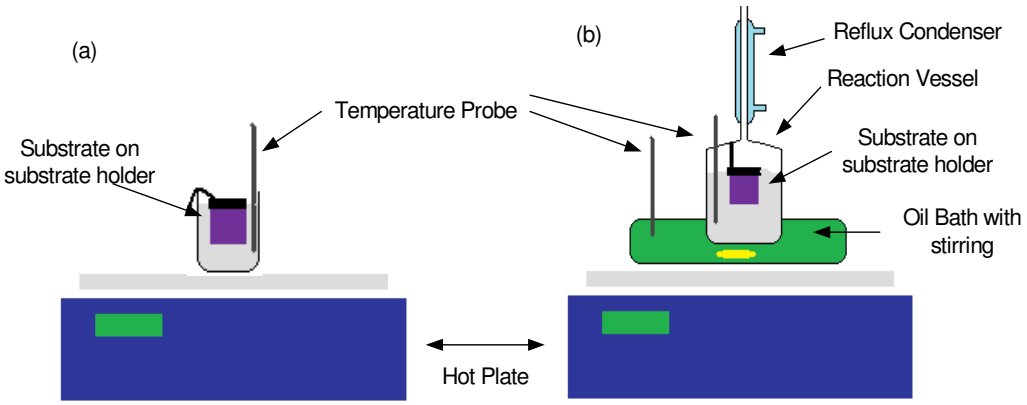

Figure 2.1: Schematic representation of (a) basic equipment setup (b) more advanced equipment set up for CBD deposition of ZnO nanorods.

2.4.1 HMT based reaction

Zinc nitrate is dissolved in deionised water (DI-H_2O) to make the desired concentration for the reaction. For a 25mM solution this equates to a mass of 7.4 mg of zinc nitrate per ml of reaction solution. The total reaction solution volume used is typically around 40 ml. A reaction volume of 40 ml was chosen as it was ideal for the size of

equipment used and the accuracy of the weighing balance. No significant variation in growth was observed when reaction solution volumes above or below 40 ml were used. The appropriate mass of HMT is then added to the zinc nitrate solution and dissolved by stirring. For an equimolar reaction of zinc nitrate and HMT, 3.5mg of HMT is required per 7.4 mg of zinc nitrate. Once prepared, the ZnO seeded substrate is submerged in the reaction solution and heated to 90°C with continuous stirring. After 30 minutes, the substrate is removed from the reaction solution and washed with copious quantities of water, before being allowed to dry at room temperature.

The addition of polyethylenimine (PEI) to the reaction solution is used to increase the aspect ratio of the deposited nanorods.[2] The PEI molecule is a water soluble polymeric amine, which has a high affinity for the negatively charged lateral facets of ZnO. This affinity leads to the adsorption of the PEI molecules onto the nanorod lateral facets. The long polymer chains of the molecule ensure that the ZnO prismatic planes are well screened from further growth leading while the c-plane remains unscreened and continues to grow. For the equimolar 25 mM HMT based reaction a PEI concentration of 5 mM was used.

2.4.2 Acetate based reaction

Zinc acetate is dissolved in DI-H_2O to form a 25 mM solution. Typically 50-100 ml of solution was used. The seeded substrates are then submerged in the reaction solution and gently heated with slow stirring until the solution reaches a temperature of 65 ± 5°C. The solution is maintained at this temperature for up to three hours with continuous stirring. Following deposition the substrate is removed and washed with copious amounts of DI-H_20.

2.4.3 NaOH based reaction

Performing the NaOH based reaction requires special care to ensure the reaction equipment is free from residual ZnO. In order to ensure the complete removal of ZnO from previous reactions, the chemical deposition equipment is first washed with a dilute solution of sulphuric acid (H_2SO_4), followed by rinsing with copious quantities of DI-H_2O. The addition of H_2SO_4 forms the water soluble zinc sulphate which is then easily removed during rinsing. Similar to the HMT process, a reaction volume of 40ml is used. NaOH is

dissolved in 20ml of DI-H_2O to make a concentration of 0.8 M. In a separate beaker, zinc nitrate is dissolved in 20ml of DI-H_2O to make a concentration of 0.02 M. Once both solutions are fully dissolved and well mixed, the zinc nitrate solution is slowly added to the NaOH solution while the solution is vigorously stirred. Vigorous stirring ensures the zinc nitrate concentration remains low during addition, preventing the precipitation of zinc hydroxide from the solution. Correctly prepared, the initial reaction solution is completely clear and free from all precipitates with a NaOH and zinc nitrate concentration of 0.4 M and 0.01 M, respectively. The solution is heated to 70°C. Nanorod growth is initiated when a ZnO seeded substrate is submerged in the solution with stirring. The reaction is maintained at a constant temperature for 30 minutes before the seeded substrate is removed and washed with copious quantities of DI-H_2O.

2.5 Carbothermal reduction vapour phase transport deposition

Nanorods were grown by carbothermal reduction vapour phase transport (CTR-VPT), mainly on Si substrates with a ZnO buffer layers but also occasionally on Si substrates with an Au catalyst. The role of a buffer layer during the growth of ZnO by CTR-VPT was investigated using the very thin ZnO layers generated by the drop-coating techniques described in 2.2 and the thicker CBD derived nanorod buffer layers described in 2.3. All CTR-VPT depositions were performed in a quartz tube (length:115cm, internal diameter: 37mm) positioned in a single temperature zone horizontal tube furnace (Lenton Thermal Designs), with a high purity argon flow through the system controlled by a mass flow controller (Analyt GFC 17), a schematic of which is shown in figure 2.2.

Typically 0.06g of high purity ZnO powder is mixed with an equal mass of graphite until a homogenous mixture is obtained. The powder mixture is then ground together using a mortar and pestle to increase the contact area between the ZnO and graphite powders. After mixing the powder is carefully loaded into an alumina boat and spread evenly over a 2cm length of the boat. The substrate is placed directly above the powder on two thin strips of silicon acting as supports for the substrate. The alumina boat with substrate is loaded into the quartz tube and positioned so that the ZnO/Graphite powder is at the centre of the hot zone of the furnace. The quartz tube end caps are replaced and a 90 sccm high purity argon flow is used to purge the tube for 5-10 minutes. Once purged, the

furnace is heated to the target reaction temperature, usually 850-925°C, maintaining the flow of argon. For consistency, the CTR-VPT reaction time was kept to 1 hour which included the furnace heat up period. After this period the furnace temperature is reduced and the system is allowed to cool for several hours before the argon flow is stopped and the alumina boat/substrate is removed.

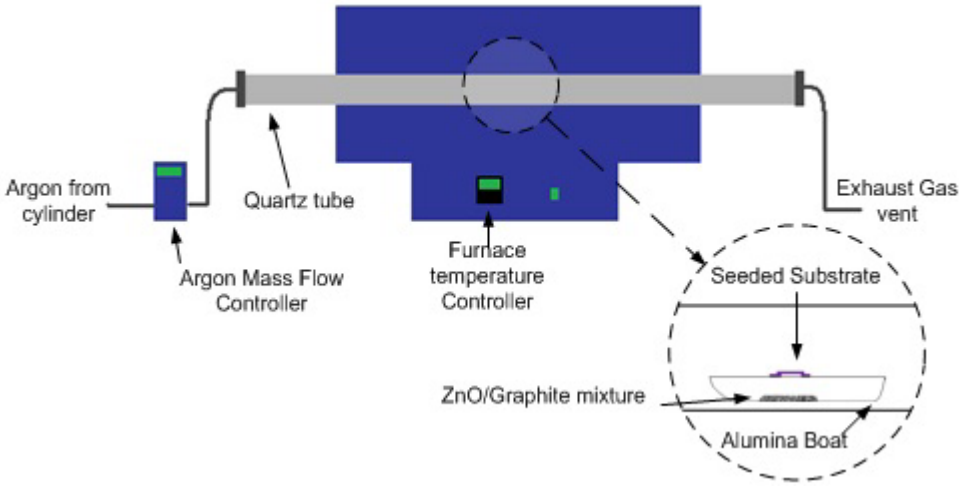

Figure 2.2: Equipment setup for CTR-VPT growth of ZnO nanorods

2.6 Nanosphere lithography

Nanosphere lithography is based on exploiting the natural tendency of certain materials to self assemble into particular formations. Hexagonal closed packed (HCP) colloidal monolayers are a promising route to develop spatially ordered nanorod arrays. In this work we have developed a method for growing *c*-axis aligned nanorod arrays using HCP monolayers of polystyrene spheres as a growth template. The first step of this process is the generation of the colloidal monolayers. Three methods of creating monolayers were examined. The first method investigated was a spin coating technique.[3] The second method, based on the work of Ng *et al.,*[4] is a facile method where by the evaporation of a suspension of nanospheres forces the self assembly of a monolayer. The third method proposed by Rybczynski *et al.*[5] allows us to generate colloidal monolayers of polystyrene nanospheres on the surface of water. This technique facilitates the transfer of the

monolayer onto any flat substrate quickly and easily. After the colloidal monolayer is transferred to the substrate the next step is to grow a nanorod array using the monolayer as a template. The deposition methods described in 2.4.1, 2.4.2 and 2.4.3 were then used to attempt the growth of ordered arrays, using the aperture created between the spheres as a template to growth, as shown in figure 2.3 (a). We also investigated methods to create inverse nanosphere templates for subsequent growth of ordered ZnO nanorod arrays, as shown in figure 2.3 (b).

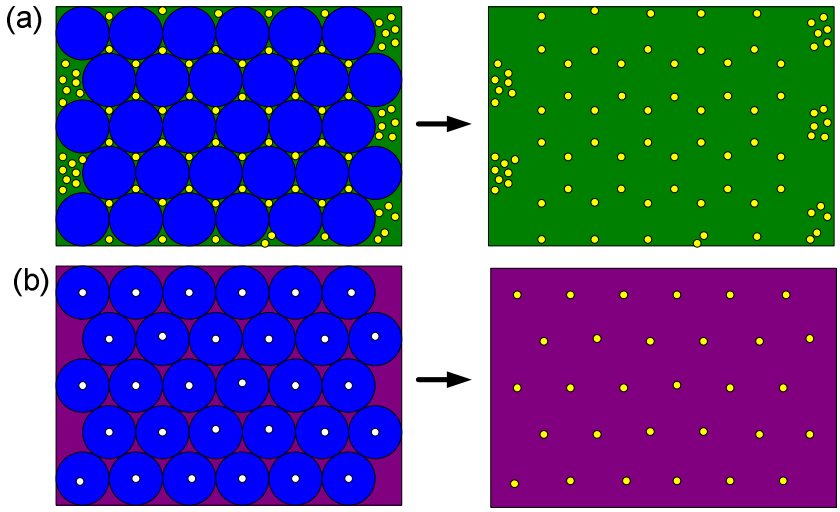

Figure 2.3: A schematic repsentation of the two approaches to positioning nanorod arrays using nanosphere lithography. (a) the nanorods shown in yellow are deposited directly on to the substrate (green) and grown through the nanosphere template. (b)The substrate is covered with a secondary material (purple) leaving the contact points between the nanospheres and substrate uncovered by the secondary material and therefore exposing the underlying ZnO (shown in white). The nanorods are then deposited at the locations where the spheres were in contact with the substrate.

2.6.1 Generating colloidal monolayers

Method 1: Spin Coating

A dilute solution (0.5% by weight, diameter 285nm) of polystyrene nanospheres in water, both with and without the presence of surfactants such as Triton-X or sodium dodecyl sulphate, is dropped onto a silicon substrate that has been pre-treated in a piranha solution. The substrate is first spun at a low speed (300-600rpm), to spread the sphere

mixture out evenly across the substrate surface and then at a higher speed (~2000rpm) to cast any excess spheres off and force the formation of a HCP monolayer.

(Note: Piranha base is a mixture of ammonium hydroxide and hydrogen peroxide, which cleans the substrate by decomposing organic matter and makes the substrate hydrophilic by hydroxylating the surface of the substrate.)

Method 2: Drop-coating

A solution containing 1 part in 400 by volume of Triton-X in methanol is mixed with an equal volume of 1% by weight nanospheres (diameter 285nm) in DI-H_2O. 20µl of this solution is then spread on a 1cm^2 silicon substrate which had been pre-treated in a piranha base solution. The substrate is then left to dry.

Method 3: Assembly on the surface of water

A low form glass crystallisation dish is filled to approximately 70% capacity with DI-H_2O. A glass microscope slide, previously cleaned by rinsing with acetone, is then inserted into the water and clamped in place at an angle. Alternately the side wall of the crystallisation dish can be used if it is cleaned well before use. 100µl of a 10% by weight solution of polystyrene nanospheres in water (500 nm or 1 µm diameter, Duke Scientific) is diluted with 100µl of ethanol and mixed well. Using a µl syringe the nanosphere/ethanol solution is slowly applied to the glass slide, just above the upper surface of the water. The tip of the syringe is used to push the applied liquid horizontally across the slide untill a streak 5-10mm is observed. This procedure is repeated until the solution flows down the glass slide and reaches the surface of the water. At this point the nanospheres can be observed dispersing across the surface of the water. A schematic representation of this process is shown in figure 2.4. It is important to note that the nanosphere solution should not be allowed dry on the glass slide during the application, as this leads to the formation of large clumps of nanospheres. Care should also be taken to ensure that the tip of the syringe does not touch the surface of the liquid during the application as this often leads to spheres being dispersed under the monolayer. Once on the surface of the water the spheres self assembled into small monolayer crystals up to 3mm^2. The small monolayer areas can be grown in size by gently lifting the dish to create waves on the surface of the water. Once monolayers of a suitable size have formed, a silicon substrate is submerged under the water in a monolayer free area and positioned under the nanospheres. By gently

lifting the substrate up through the monolayer, the colloidal crystal is transferred to the silicon surface. The substrate is allowed to dry leaving the self assembled monolayer attached to the silicon surface.

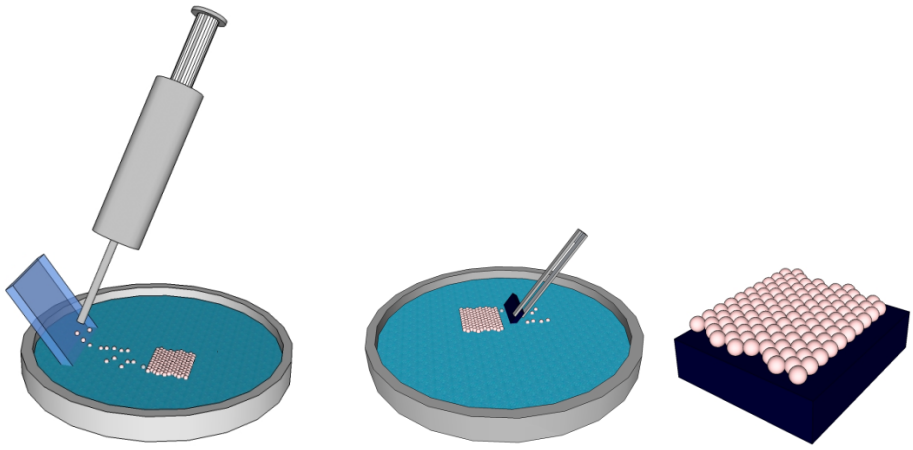

Figure 2.4: A schematic representation of the equipment and method to obtain nanosphere monolayers on silicon substrates. First the sphere solution is applied to the glass slide close to the water interface. Once assembled, the monolayer is lifted of the water surface and onto the substrate, before being allowed to dry.

2.6.2 Direct template assisted nanorod growth

In order to achieve template assisted ZnO nanorod arrays, nanosphere monolayers were coated onto silicon substrates previously seeded by the drop coat technique outlined in section 2.3, by gently lifting the pre-seeded substrates through monolayer crystals assembled on the surface of water and allowing the substrate to dry. Once dry, the substrates are annealed on a hot plate at 110°C for 30 seconds to slightly melt the nanospheres and improve their adhesion to the ZnO seed layer. This annealing step helps prevent the delamination of the nanosphere monolayer, when the substrate is resubmerged into a solution for the CBD step. Nanorod arrays were then grown through the apertures created by the monolayer coating using the methods outlined in sections 2.4.1 and 2.4.2 (shown schematically in figure 2.3).

2.6.3 Inverted template assisted nanorod growth

In contrast to the direct use of nanospheres monolayers as a template, we also attempted to use the nanosphere monolayer to make a secondary template (shown schematically in figure 2.3b). Growth is then performed on the substrate after the nanospheres have been removed. This avenue of research allows high temperature deposition techniques to be used, as the low melting temperature nanospheres are no longer present. Selection of materials is an important step in this method as they must be compatible with all stages of the growth technique. Three materials were tested for their suitability in forming secondary templates, copper oxide, carbon and silica. Copper oxide was produced using a thermal decomposition of copper salt, while the carbon templates were generated by dehydrating sucrose and the silica templates by a common sol-gel process.

Method 1: Copper Oxide Templates

A thin ZnO buffer layer is first prepared on silicon using the method outlined in section 2.3. A HCP monolayer is then applied to the surface using method 3 in section 2.6.1 and annealed for 30 seconds at 110°C. 5µl of a 1mg/ml solution of copper sulphate in methanol is applied to the surface of the substrate and allowed to infill the nanosphere array. After 20 seconds the methanol solution is displaced from the substrate with a short pulse of nitrogen. Prior to the drop-coating process the nanosphere monolayer has a characteristic opalescence as the nanosphere monolayer acts as a diffraction grating on the substrate surface. The drop-coating procedure is repeated until the characteristic opalescence from the nanosphere array starts to diminish, indicating that the copper sulphate coating is of sufficient thickness to suppress the opalescence and is therefore of the same order of magnitude as the wavelength of visible light and consequently, of comparable thickness to the nanosphere size. The substrate is then placed in a furnace at 700°C for 30 minutes before being cooled to room temperature. Copper oxide templates were also synthesised from copper nitrate using an identical technique. However as copper nitrate has a lower decomposition temperature the final step was performed in a furnace at 400°C

Method 2: Carbon from the dehydration of Sucrose

Carbon templates were synthesised using the method of Zhou.[6] A substrate with ZnO buffer layer and nanosphere monolayer is prepared in an identical fashion to method 1. A 5µl drop per cm^2 of substrate, of a solution containing sucrose, DI-H_2O, ethanol and H_2SO_4 in a ratio by mass of 1:5:35:0.18 respectively, is applied to the surface of the nanosphere monolayer/substrate and allowed to evaporate for 20 seconds. The excess solution is displaced from the substrate with a short pulse of nitrogen. Due to the viscosity of the solution, sufficient amounts of material remain on the substrate and the drop-coating procedure does not need to be repeated. The sucrose coating is partially polymerised by heating on a hotplate for 2 hours at 90°C. The nanosphere array can now be removed by the rinsing the substrate in toluene several times. The carbon template is then completed by heating the substrate at 140°C for 4 hours.

Method 3: Silica sol template

Silica templates were formed by silica sol templating on the surface of CBD deposited buffer layers made by the methods outlined in section 2.4.1 and 2.4.2. This technique was an adaption of the work described by Li *et al*. and Wang *et al*.[7-8] In all cases the silica sol was prepared from a catalysed reaction of tetraethyl orthosilicate (TEOS) with DI-H_2O in ethanol. TEOS reacts slowly with water to form silicon dioxide (SiO_2). This process is a combination of two reactions, a hydrolysis reaction followed by a condensation reaction.[9] The hydrolysis reaction is shown in equation 2.6.3.1 while the condensation reaction is shown in equation 2.6.3.2. In the first reaction (2.6.3.1) the water molecule replaces one of the alcohol ligands with a hydroxide group. The second reaction occurs when two hydrolysed TEOS molecules come into contact with each other. One hydroxide group is removed from silicon centre taking with it the hydrogen atom from the second hydroxide group to form a water molecule. The second hydroxide group then bonds to the silicon atom to form a Si-O-Si linkage. While both reactions occur naturally between TEOS and water, they are generally considered to be too slow to be of practical purposes. Consequently the reactions are generally catalysed. The first reaction is catalysed by bases while the second reaction is catalysed by acids.

$$Si(OC_2H_5)_4 + H_2O \rightarrow HO\text{-}Si(OC_2H_5)_3 + OC_2H_6$$

(2.6.3.1)

$$HO\text{-}Si(OC_2H_5)_3 + HO\text{-}Si(OC_2H_5)_3 \rightarrow (OC_2H_5)_3Si\text{-}O\text{-}Si(OC_2H_5)_3 + H_2O$$

(2.6.3.2)

The choice of catalyst has a strong influence on the final properties of the silica. When the reaction is catalysed by a base the first reaction proceeds faster than the second, leading to an increase in the rate of removal of the ethanol ligand. The silicon atom is therefore more likely to cross-link during the second reaction, forming hard dense nanoparticles. This is the basis of the Stöber process used to produce silica nanospheres.[10-11] When the reaction is catalysed by an acid, the second reaction proceeds faster, leading to long chained polymeric silica sols. The degree of cross linking affects many of the solutions properties such as viscosity, final silica density and solubility in alkaline conditions.[9]

In this work silica templates were made from base catalysed, acid catalysed and acid-base catalysed sols. Typically 1 ml of TEOS was added to 20 ml of anhydrous EtOH and mixed well. For acid catalysed sols 1 ml of 0.05 M sulphuric acid (H_2SO_4) or 1 ml of 0.1 M hydrochloric acid (HCl) was added to the TEOS solution, followed by stirring for several hours. Base catalysed sols were prepared by adding 1 ml of 0.1 molar sodium hydroxide (NaOH) solution to the TEOS/EtOH solution, followed by several hours of stirring. Acid-base catalysed sols were prepared as per the acid based sols, however immediately before use 1 ml of 0.1 M NaOH was also added to the TEOS solution. All sol solutions were further diluted with fresh EtOH before use. The silica sols were then used to produce a dense silica template of the nanosphere array by drop-coating a small volume of the sol solution on to the nanosphere coated CBD buffer layers. Typically 15 µl of sol solution was drop coated per cm^2 of substrate. Once the sol has dried, it is necessary to densify the silica to reduce the coatings porosity and reduce the stress in the coating. This was performed by annealing the coating at 450 – 500 °C. The nanosphere coating can be removed before the densification process by sonicating the substrate in toluene, however it was found that this step was not essential as the densification process also resulted in the “burning off” of the polystyrene spheres.

2.7 Characterisation techniques

As mentioned earlier, a large variety of techniques were used to characterise the nanorods deposited. The techniques can be separated into two general areas; methods to examine the morphology of the deposited material and methods to characterise the fundamental properties of the material such as the crystal structure / alignment, chemical composition or optical properties. Figure 2.5 outlines the role of each of the techniques used in the overall process of sample characterisation. In the following sections a brief introduction into the various different characterisation techniques will be given, including a description of their principles of operation and equipment setup. Due to the specialist nature of some of the characterisation techniques external help was necessary to complete some aspects of the characterisation. The details of where and by whom these experiments were performed are given at the end of each of the relevant sections.

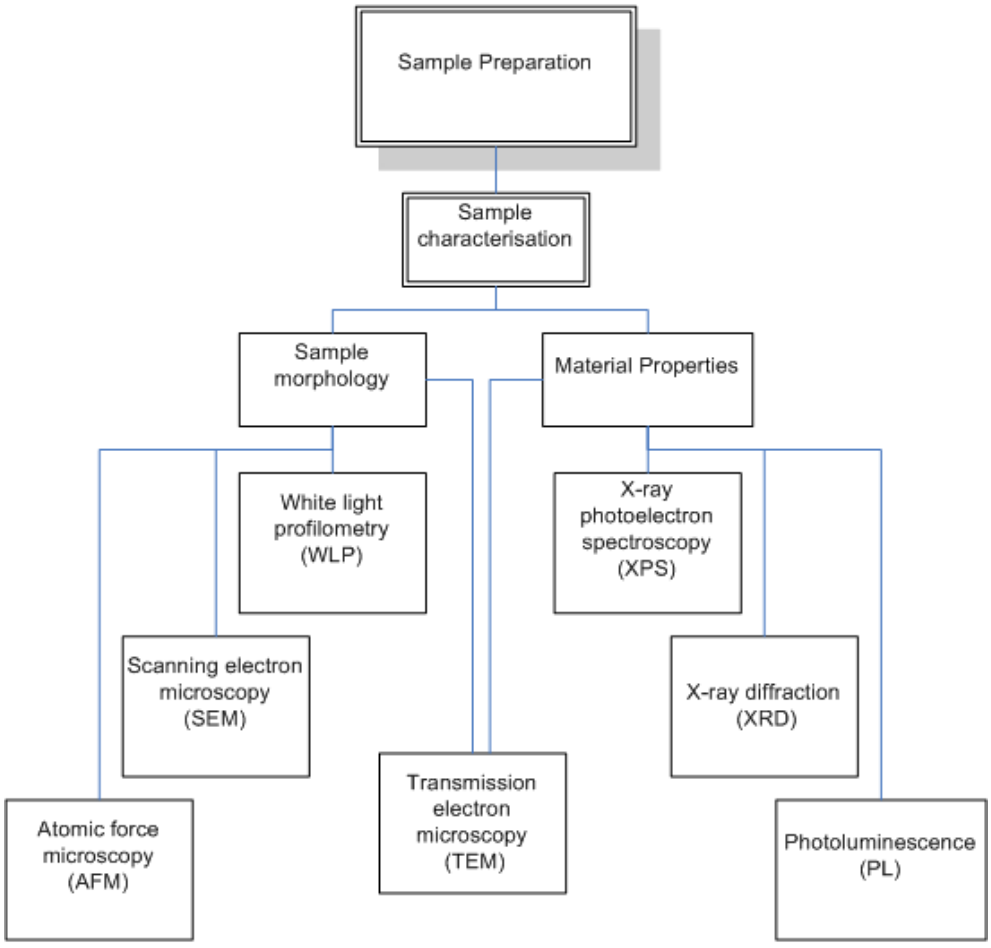

Figure 2.5: Organisational chart showing the various different characterisation techniques used to examine the deposited nanorod arrays.

2.7.1 White light profilometry

WLP, also known as coherence scanning interferometry, is a fast and convenient method for topographical measurements of samples. In a typical WLP system a coherent beam of white light is sent to a beam splitter which directs half the light along a reference optical path while the second half shines onto the sample surface. The two light paths are then recombined forming an interference pattern on a CCD array. The interference pattern formed on each pixel of the CCD camera is related to the optical path difference of the two beams. In the simplest case this configuration can be viewed as a Michelson interferometer. By changing the optical path difference between the two beams, the interference pattern collected by the CCD camera will be varied and can thus be correlated to the to path difference. The path difference at any one point on the CCD array then depends on the distance moved by the instrument during vertical scanning but also on the height of the surface of the sample. A simplified schematic diagram of WLP instrument is shown in figure 2.6.

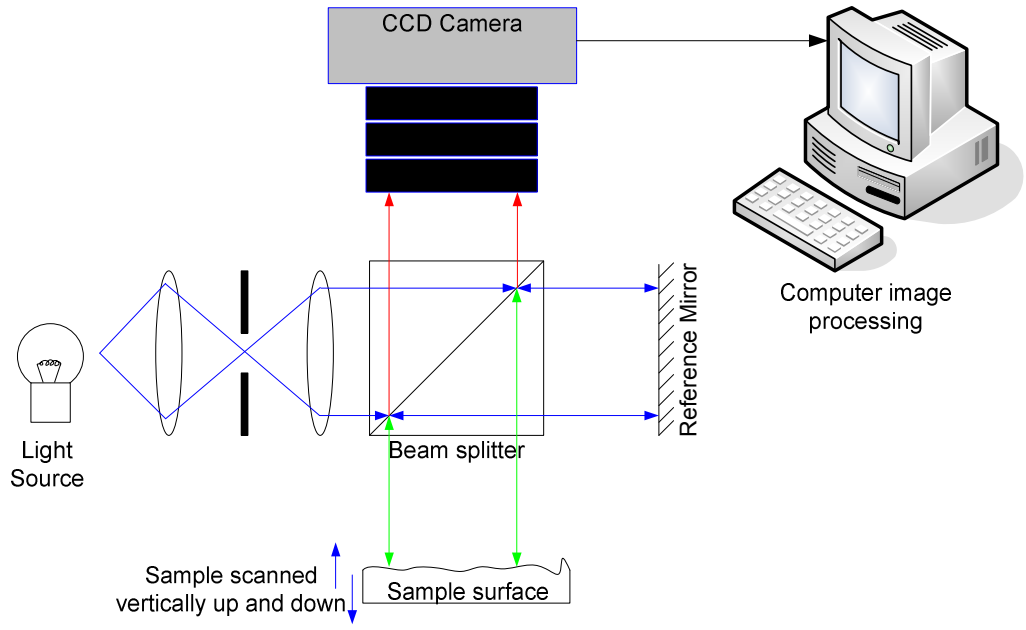

Figure 2.6: Simplified schematic of a WLP instrument where the different coloured lines represent the different optical paths of the Michelson interferometer.

In practice the instrumental setup is slightly more complex, while the underling principle remains the same. Additional optical elements are required to control the illumination and field of view of the CCD camera. The external reference mirror is usually

replaced by a Mirau type interference objective. This allows the interference pattern to be formed by scanning the interference objective rather that the sample stage. Each pixel of the CCD camera only sees an interference pattern when the surface area in question is in focus due to the short coherence length of the white light used. Consequently the surface can be determined by measuring the position of maximum fringe contrast during the vertical scan of the Mirau interference objective.

While the vertical sensitivity of modern WLP instruments are considered very good, with resolutions down to 0.1 nm the horizontal resolution is limited by the density of pixels on the CCD camera. However for larger area observations WLP, offers a distinct advantage in that the field of view of the CCD camera is much larger than the area sampled by conventional surface scanning techniques such as AFM and STM. Also, as no contact is made with the sample surface, large or sudden variations in surface feature height which may damage scanning tips used in AFM or STM do not present any difficulty to WLP instruments.

In this work WLP was used to complement AFM in the characterisation of the seed layers prepared by drop-coating. As these seed layers were extremely fragile it was found that contact profilometry was unreliable and led to seed layer damage, and while AFM allowed an accurate determination of certain aspects of the seed layer, it was unsuitable to characterise larger areas of the sample, in particular, any differences that might arise between different areas of the sample.

2.7.2 Scanning electron microscopy

SEM was used extensively during this research given the size of the features that required imaging. It is well known that optical microscopes are limited by diffraction through the aperture. For individual features to be resolved the system used to image them must be able to obey the Rayleigh criterion. For an optical microscope this means that the diffraction pattern for neighbouring features should not overlap to such a degree that the centre of one diffraction pattern coincides with the first minima of the second diffraction pattern. However, given the size of individual features present in samples prepared during the course of this research, the wavelength of light is too large and consequently optical microscopes were unable to resolve the sample's features with

sufficient clarity. This common problem with light based microscopy systems has been addressed some time ago by the development of electron optics in the 1930s. From this field came the scanning electron microscope, with one of the first reports of ZnO characterisation by SEM being published in 1942.[12]

In a typical SEM, a beam of high energy electrons are directed at the surface of the sample being analysed. The electrons then undergo different interactions when they hit the surface. Some of the electrons undergo an elastic scattering process; others undergo an inelastic scattering process with the emission of secondary electrons and electromagnetic radiation. Each of these different emissions can then be detected and used to give information about the sample being analysed. Figure 2.7 shows a schematic layout of a typical SEM. The instrument consists of a column under vacuum. At the top of the column is a source of electrons (an electron gun). This can either be a tungsten filament (hot cathode) or cold emission source (field emission). Below the electron gun is an anode with provides additional acceleration and some focusing to the emitted electrons. Similar to a light microscope, the beam of electrons is the focused by a series of lenses. For electron beams these are magnetic lenses capable of bending the path of the electron beam. In addition the focused electron beam is raster scanned across the sample surface and the resultant interactions and emitted species measured by a variety of detectors, including a secondary electron detector, a back scattered electron detector and an x-ray detector. Each of the detectors provides different information about the sample under analysis as discussed below.

Elastic scattered electrons are those electrons that were originally in the SEM beam, however after hitting the sample surface the electrons are deflected away from the sample and are known as backscattered electrons. The quantity of electrons deflected in this manner is highly dependent on the mass of the element that deflects the electrons in the first place, with larger mass elements typically deflecting more electrons. This relationship can then be used to identify regions of the sample that differ in composition, as this difference shows up as a variation in the contrast of the sample image during the SEM's raster scan. These electrons are detected by a circular detector surrounding the beam emission point as more electrons are deflected back towards the beam than at higher angles, towards the sample chamber wall.

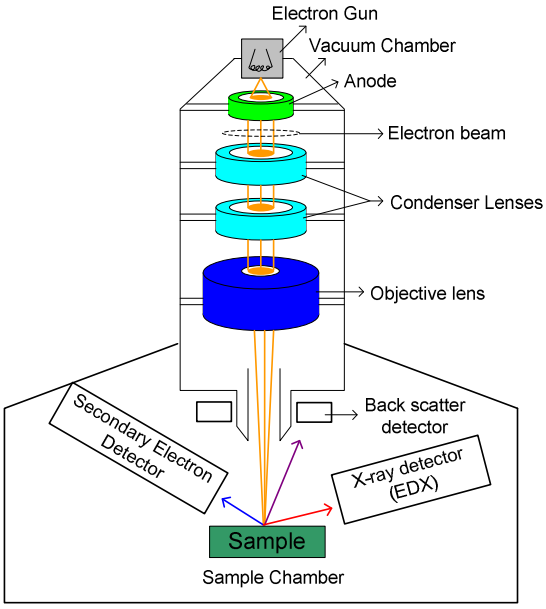

Figure 2.7: A schematic representation of a scanning electron microscope showing all the major components.

When electrons in the beam undergo an inelastic scattering process, electrons from the atoms on the sample's surface are knocked out of their orbitals. These ejected electrons are referred to as secondary electrons and are the most commonly used signal to form images of the sample surface and visualise topography. The ejected electrons are detected by accelerating them to a sufficiently high velocity that they can activate a scintillator. The light emitted by the scintillator is then amplified using a photomultiplier tube before collection and conversion to a digital image. Secondary electron detectors can be used to create images of the sample features with a very large depth of field and almost 3D like qualities. This is due to the number of secondary electrons emitted from the sample surface. As the angle between the surface normal and the incoming electron beam increases the number of secondary electrons emitted increases leading to a contrast based on the angle of the surface in the final image. This contrast, in addition to the excellent depth of field of the image leads to highly detailed, life like images.

The electrons ejected during the scanning process also lead to a second detectable signal. Some of the electrons that are ejected from the surface atoms leave behind an inner shell hole, or empty state. Electrons from outer orbitals of the atoms can then combine with the inner shell holes created in the inner orbitals. The difference in energy between higher and lower electron orbitals is dissipated in the form of x-rays. The x-ray energies emitted are characteristic of the atomic orbitals present which form a unique finger print of

the different atoms present. This process is known as energy dispersive x-ray spectroscopy (EDX) and allows the accurate determination of the different atomic species present. It can also be used to form elemental maps to determine the distribution of the different elements within a composite material.

In this work the majority of SEM characterisation was performed using a Karl-Zeiss EVO series SEM, fitted with secondary electron, back scatter and EDX detectors. Additional characterisation was performed in conjunction with Dr. Brendan Twamley of the school of Chemical Sciences in DCU, using a Hitachi S5500 FESEM.

2.7.3 Atomic force microscopy

The AFM is a member of the family of instruments known as scanning probe microscopes. It was developed by Gerd Binnig in 1986 as a method to overcome the serious limitations of the scanning tunnel microscope (STM).[13] That is, an AFM can be used to image any material's surface and unlike the STM it does not require the surface to be conductive. AFM instruments measure the force of interaction between a small tip mounted on a cantilever and the surface of the sample. Under appropriate conditions the instrumental resolution can reach the atomic scale.[14]

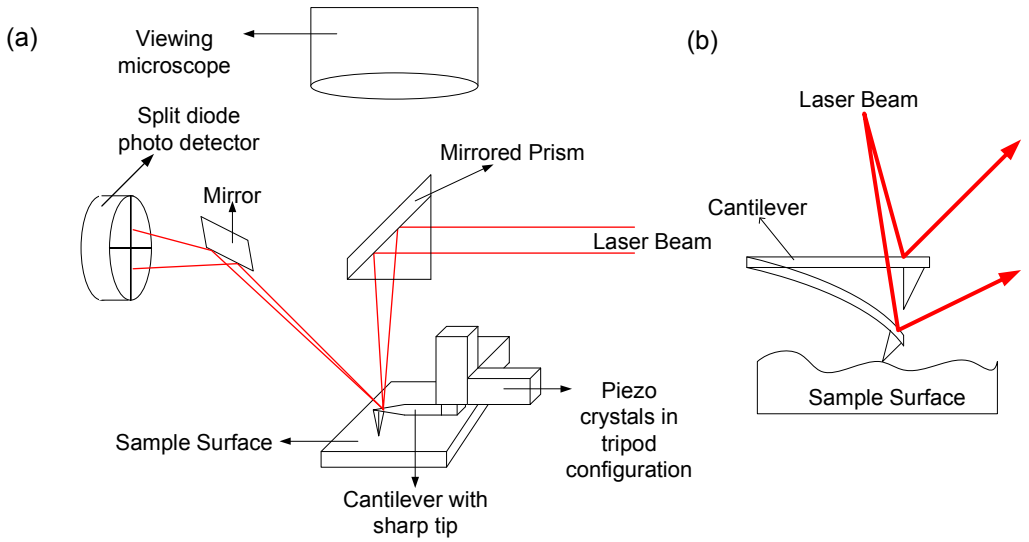

Figure 2.8: (a) Schematic representation of a typical AFM instrument (b) A schematic representation of the effect of bending the cantilever on the laser beam path during tapping mode oscillations.

A standard AFM instrument consists of a laser focused onto the upper surface of a small cantilever. The cantilever inturn is mounted on piezo crystals in a tripod configuration, that allows the cantilever to be moved in the X Y and Z directions. The laser spot focused on the cantilever is reflected towards a mirror which then directs the beam to a split photodiode detector.[15] Movement of the cantilever is then detected as a shift in the detection area of the split photodiode. Figure 2.8 (a) shows a typical AFM configuration while 2.8 (b) shows the effect of the cantilever movement on the laser beam path during measurement.

There are different modes of operation available with AFM including contact mode, dynamic mode, and tapping mode. In contact mode the tip of the AFM is brought into contact with the sample and scanned across the surface. The repulsive force experienced by the cantilever tip is measured as a deflection of the cantilever, which in turn shifts the laser beam path, leading to a variation in the intensity of the signal detected in each of the areas of the split photodiode detector. The difference in intensity detected in the different regions of the photodiode is proportional to the deflection of the cantilever tip which yields height images or deflection force images. In addition to the vertical deflection the tip can also experience horizontal torque which causes a twisting in the cantilever. On flat surface this enables one to distinguish between areas with different frictional coefficients.[15] As the tip is in contact with the surface, contact mode is often not suitable for soft or delicate surfaces which may deform during the raster scan. This problem may be overcome using dynamic mode. In this mode the cantilever is held above the sample and vibrated at its resonance frequency. The interaction forces between the sample surface and the tip alters the resonance frequency, phase and amplitude of the oscillating tip. Another mode that can be used for delicate surfaces is tapping mode. The cantilever is oscillated close to its resonance frequency and is brought close enough to the sample surface that it comes into intermittent contact with the surface. This mode was originally intended for ambient – condition experiments so as to allow the tip to overcome the “contamination overlayer”.[15]

In this work, AFM was used to characterise the surface of drop coated seed layer and in particular to characterise the individual crystallites formed during coating and determine the film thickness and regional variations. A Veeco Nanoscope Dimension 3100 instrument operating in tapping mode using aluminium-coated silicon AFM probes, with a resonant frequency of 300 kHz, was used for all AFM imaging.

2.7.4 X-Ray diffraction

XRD is used to probe the crystal structure of materials. When a beam of x-rays is incident on a crystal structure, two things can occur. The x-rays can be absorbed, which is the basis of x-ray photoelectron spectroscopy as discussed in section 2.7.5 or the x-rays can be scattered either elastically or inelastically. Inelastic scattering, also known as Compton scattering transfers some of the incident x-ray's energy to the electrons of the material being examined. This leads to an increase in the wavelength of the x-ray. There is no phase relationship between the incident and scattered waves and the scattered waves from different electrons do not interfere with each other. Therefore no crystallographic information can be obtained from Compton scattered x-rays. However when a monochromatic beam of x-rays is scattered elastically by the material, the emerging x-rays are partially coherent and can interfere with each other under certain conditions. By measuring these interference patterns, a good deal of information can be gained about the crystal structure under examination.

The conditions necessary for constructive interference to occur in XRD are described by the Bragg equation shown in equation 2.7.4.1.[16]

$$2d \cdot sin\theta = n\lambda \tag{2.7.4.1}$$

Where d is the interatomic distance, θ is the incident angle and λ is the wavelength of the x-rays and *n* is an integer. In this case the crystal structure is viewed as a series of atomic planes, with nodes equally spaced along each atomic plane as shown in figure 2.9. The incident x-rays strike the planes of the crystal and are elastically scattered by the nodes of the planes at an angle θ. Each of the planes of the crystal structure are separated by a distance *d*. Consequently the path length of the x-rays striking the different crystals planes vary. When path length of the x-rays scattered form each of the different planes differ by a whole number multiple of the incident x-ray wavelength then constructive interference can occur. When the additional path length of x-rays is not a whole number multiple of the wavelength then destructive interference occurs. The left hand side of the Bragg equation shown in 2.7.4.1 simply describes the additional path length travel by the x-rays when being deflected by the increasing number of planes.

By scanning a collimated beam of monochromatic x-rays through the angle θ while simultaneously scanning the x-ray detector through the same angle to measure the scattered x-rays, an interference pattern is collected. The peaks present in this pattern are located at the angle θ which satisfy the Bragg equation, allowing the spacing of the different crystal planes to be determined. In practice there are many different methods to perform XRD measurements depending on the equipment geometry and sample type. In this work a Bruker AXS D8 Advance Texture Diffractometer was used for all XRD measurements. This system is a proportional counter diffractometer. The geometry of the instrument is shown in figure 2.9(b). Essentially the sample is rotated through the angle θ, while the detector is rotated at twice this rate to give an angle 2θ. The direction of the x-ray beam is kept constant. When the Bragg condition is satisfied the x-ray detector is in the correct position to collect the scattered rays from planes locally parallel to the sample surface. This technique is used to identify planes or determine the interplanar spacing of planes that are perpendicular to the axis of the x-ray source and detector. In a second mode of operation the detector is held at the 2θ angle where scattering from a plane has been detected. The sample is then rotated about the θ angle. This mode is called a rocking curve and it allows the degree of alignment or texture of crystallites in a deposit to be compared between samples.

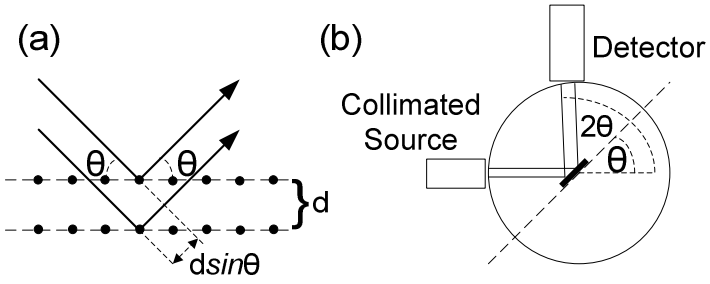

Figure 2.9: A schematic representation of the Bragg diffraction condition used in XRD (b) the geometric layout of the Bruker AXS D8 diffractometer for a θ/2θ measurement.

XRD is an important technique for material characterisation as it allows the determination of many important parameters. Firstly it can be used to measure interplanar distances, or diffraction angles. By comparing these measurements to databases, it can then be used to indentify the material present and its crystallographic structure. In addition it allows the material orientation with respect to a substrate to be identified, a very important factor when trying to deposit nanostructures with a particular alignment or orientation. In addition if there are impurity phases present, these may also be detected,

helping to determine the quality of the material. In this work XRD was used primarily to determine the orientation or nanorods with respect to the substrates that they were deposited on and as a comparison tool for ordered arrays grown by various different techniques.

2.7.5 X-Ray photoelectron spectroscopy

XPS is a characterisation technique that is extremely sensitive to surface chemistry, allowing chemical state information to be examined.[17] XPS utilises the photoelectric effect to eject electrons from below the valence band of the atoms at the surface of the sample being analysed. As the name suggests, this is achieved by illuminating the sample surface with x-rays, which have sufficient energy to eject electrons from these sub-valence band orbitals. In the simplest case an electron bound to a nucleus of an atom in the surface of the sample being analysed absorbs a photon of energy (hν). When this energy ($h\nu > E_b$) exceeds the binding energy of the electron E_b, then the electron is ejected from the atom with a kinetic energy equal to the difference between the electron binding energy and the incoming photon energy, that is $E_{ke}=(h\nu - E_b)$.[18] It follows that the greater the binding energy of the electron, the less kinetic energy the ejected electron will have after absorbing the photon energy. This variation in electron kinetic energy provides a convenient method to identify the origin of the electron from the electronic structure of the atom. A typical XPS spectrum is a plot of the electron binding energy as determined from the kinetic energy of the emitted electron versus the number of electrons detected at this energy. While this simplistic picture allows the process to be easily visualised, many more effects are present during XPS analysis, of which relaxation shift and chemical shift are particularly interesting. In relaxation shift, the sudden departure of the electron causes a shift in the energy as compared to the idealised model discussed above. As the photoelectron leaves the atom, the remaining electrons should relax to a lower energy screening the departing electron from the hole, thereby increasing the kinetic energy available to the departing electron. However as the photo excitation process is so rapid, the final state of the atom may have an electron in a bound excited state or eject an electron into an unbound state, both situations which would lead to a reduction in the kinetic energy of the ejected electron. If the atom is on a metallic surface where metal's valence electrons are very mobile then screening can still occur and the reduction in kinetic energy is the sum of the

two effects. The chemical shift in the kinetic energy is of particular value as it allows some information regarding the bonding of the atom to be determined. Here the shift is due to the change in the electron's original binding energy due to variations in the atom's electronic environment which is caused by the atom's interactions with neighbouring atoms. Given the complexity of the various factors influencing both peak positions and peak shapes, a significant degree of care is required in analysing XPS spectra. It is therefore useful to have all possible information about the likely composition of the surface available during analysis.

XPS must be carried out in ultra high vacuum (UHV) in order to efficiently detect the photoelectrons. Therefore a sample is normally inserted into a UHV chamber fitted with an x-ray source and electron energy analyser such as a concentric hemispherical analyser. Given the ubiquitous presence of carbon, XPS systems are often calibrated to the "adventitious" carbon contamination layer found on all samples.[19] In this work XPS was used to identify the chemical pathway and help understand the role of atmospheric humidity during the formation of drop-coated seed layers. In this study the material surface composition was examined using a Vacuum Generators X-ray photoelectron spectrometer (XPS) at base pressures in the preparation and analysis chambers of $2x10^{-6}$ and $1x10^{-9}$ mbar, respectively, using an Al Kα (hγ =1486.6 eV) x-ray source. The pass energy of the analyser was set at 20 eV yielding a resolution of approximately 1.0 eV. The XPS peaks were fitted with mixed ratio of Gaussian and Lorentzian line shapes and a Shirley background function. All XPS spectra were collected and peak fitted by K. Kumar in the School of Physical Sciences, National Centre for Sensor Research, Dublin City University (DCU).

2.7.6 Photoluminescence

PL is a powerful tool for nondestructive analysis of the electronic properties of a material and in particular semiconductors. In brief, it involves using the absorption of light to excite an electron from the valence band of a material into a higher excited state, typically the conduction band. The electron in the excited state then decays back to the ground state of the material and re-emits light with a wavelength corresponding to the difference in energy between the two energy levels. From this, the difference in energy between the different electronic bands can be determined. While this in itself is very

useful, the real power of PL lies in the fact that the electrons can also be excited to electronic energy states within the forbidden bandgap, due to defects in the crystal structure, such as impurity atoms, defects in the crystal planes, atoms of the crystal structure in an incorrect location (antisite), or atoms missing from the crystal structure. Many of these defects will have characteristic effects on the electronic band structure and consequently on the electronic properties of the material. By careful analysis of the PL spectrum and often by comparison to deliberately introduced defects it is often possible to use PL to identify both the electronic structure and defect induced electronic structure of the material under examination.

The excitation and emission process involved in PL can be easily visualised in the electron energy versus crystal momentum diagram in figure 2.10. Firstly the sample is excited using a light source of higher energy than the bandgap of the material. The absorption of the photon energy by the electron gives the electron sufficient energy to promote the electron from the valence band of the material to the conduction band or other higher energy bands, leaving a hole in the valence band. Since the energy provided by the photon in exciting the electron is larger than the band gap of the material the excited electron and hole have an excess energy than the band gap in the form of kinetic energy and are called hot carriers. The hot carriers undergo a thermalisation process, where excess kinetic energy is lost to the crystal structure in the form of a phonon or phonons, thereby bringing the carriers back to metastable states at the band edges.

This thermalisation process is typically very fast, occurring on a picosecond time scale. In the case of direct semiconductors as illustrated in figure 2.10(a) the position of the peak energy of the valence band and the bottom energy of the conduction band correspond to the same wave vector or crystal momentum. The electron can then return to the ground state annihilating the hole to emit a photon whilst conserving total crystal momentum. This recombination process occurs on a significantly longer time scale than the thermalisation process, thus creating a population of metastable electron-hole pairs in the conduction and valence band respectively. The quantum mechanical probability of this transition is high compared to competing processes, as it involves only two bodies, i.e. the photon and electron. In the second case, as seen in figure 2.10(b) the semiconductor has an indirect bandgap, meaning that the wave vector for the top of the valence band is not the same as the wave vector for the bottom of the conduction band. Consequently the return of the electron to the ground state and annihilation of the hole is more complex. The

electron must undergo further interactions in order to recombine with the hole. Typically this involves the absorption or emission of a phonon or phonons which also changes the energy of the electron. Given that additional interactions with the crystal are necessary, the probability of a transition emitting a photon is significantly reduced. Therefore semiconductors with direct transitions absorb and emit light much more efficiently that those with indirect bandgaps.

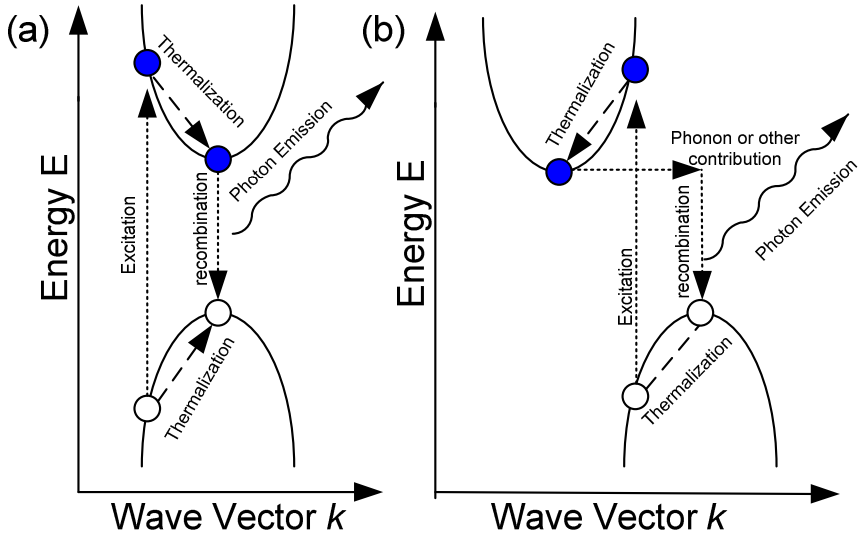

Figure 2.10 (a) A schematic representation of the electron-hole recombination in a (a) direct (b) indirect band-gap semiconductor. Blue circles represent electrons. Open circles represent holes

As mentioned earlier the energy of the emitted light (ħω) is approximately equal to the bandgap energy (E_g). The excitation process creates an electron in an excited state and a hole in the valence band. Naturally the electron has a charge but the hole also has an effective charge and the electron-hole pair can experience an attractive Coulombic force, which keep their positions correlated to each other. This electron-hole pair is typically referred to as an exciton and is a quasi particle with a formation energy slightly lower than that bandgap.[20-21] Excitons can fall into two different categories, Frenkel type or Wannier type.[21] In highly ionic materials where the dielectric constant of the material is low, the Coulombic interaction between the electron-hole pair is strong. Consequently the electron-hole pair are more localised in space and are typically found within a single unit cell of the crystal. In covalently bonded crystals or weakly ionic crystals the dielectric constant of the material is higher, resulting in increased screening of the attractive Coulombic forces,

allowing the electron hole pair to be more delocalised, with the electron roaming many unit cells around the hole. The distance that the electron can travel away from the hole is called the Bohr radius. A schematic representation of the different types of excitons can be seen in figure 2.11. In both cases the exciton can move from unit cell and propagate through the crystal. The principle difference between the two different types of excitons is in their theoretical treatment. Wannier type excitons are more easily treated as the effective mass approximation applies and therefore the hole-electron pair can be modelled as a hydrogen-like system with a Coulombic potential. The hole in this case is viewed as analogous to the proton. The effective mass approximation is a method of reducing the complexity of the calculations, whereby the electron is considered as a free electron, with the effect of moving in a periodic potential due to the ion cores treated by a renormalisation of the electron mass to an "effective" mass. The effect of other electrons is taken to provide a contribution to the periodic potential in the form of a mean field which will also effect the effective mass.[20] This approximation is particularly relevant to the maxima of the valence band and the minima of the conduction band, where the effective mass is approximately constant. Conveniently, the thermalisation process prior to recombination moves the hole and electron to these locations. The effective mass approximation is not a valid assumption for Frenkel excitons and these are therefore more difficult to model. The excitons formed in ZnO are of the Wannier type and therefore Frenkel excitons are not relevant to this work.

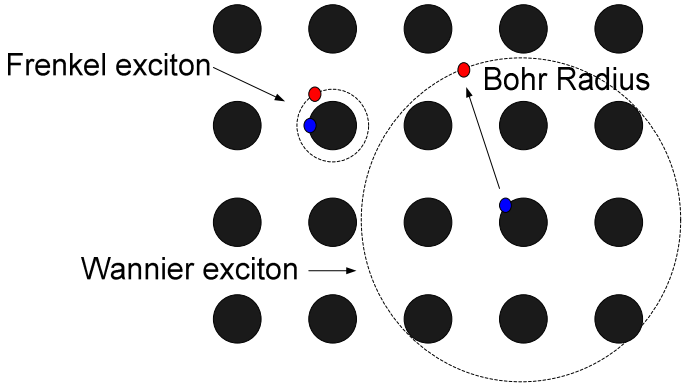

Figure 2.11: Schematic representation of the two different varieties of excitons, where the red circles represent electrons, blue circles represent holes and the black circles represent atomic nuclei.

In a relatively pure material the excitons are free to travel through out the crystal structure and are therefore called free excitons (FX). When impurity atoms such as donors

or acceptors are present the excitons can become trapped at these impurities and are consequently referred to as bound excitons (BX). Bound excitons are normally labelled in spectra according to the centre to which they are bound as given by table 2.1.

The bound excitons trapped at a defect have a localisation energy which depends on the nature of the defect that they are trapped at. At low temperatures, due to the thermalisation process most of the free excitons are trapped at defect sites, giving rise to strong emissions at characteristic wavelengths during PL measurements.

Label	Emission centre
FX	Free exciton
A^0X	Exciton bound to neutral acceptor
D^0X	Exciton bound to neutral Donor
D^+X	Exciton bound to Ionised Donor
eA	Conduction band electron to acceptor
-LO	Longitudinal optical phonon replica
TES	Two electron satellite
DAP	Donor-acceptor pair

Table 2.1: Nomenclature for low temperature PL spectra.

When the temperature is raised the free excitons can gain sufficient energy to escape from the defect site reducing the intensity of bound exciton emissions. In addition at low temperatures the exciton is less likely to be thermally dissociated. Consequently PL spectra acquired at low temperatures contain significantly more information on the defect states in a semiconductor than those acquired at or near room temperature. Usually the localisation energy of an exciton at an impurity site follows a similar pattern. Typically the localisation energy is largest for neutral acceptor (A^0X) complexes, followed by neutral donor (D^0X) then ionised donor (D^+X).[20] In addition to the AX and DX processes, if a material contains both donors and acceptors then it is possible for donor-acceptor transitions (DAP) to emit photons.[21] An electron trapped at a donor site can recombine with a hole trapped at an acceptor site, which are detected at lower energies than the AX or DX emissions. Two electron satellites also can occur when an exciton bound to a neutral donor, following recombination, leaves the donor in an excited 2s or 2p state. Finally, excitons can recombine and some of the energy goes into the emission of phonons such as longitudinal optical (LO) phonons leading to emitted photons of lower energies which are called phonon

replica peaks which are shifted by a fixed energy equal to the energy of the phonon for the particular crystal structure.

Deep centres and internal transitions also play an important role in the photoluminescence spectra of wide band-gap semiconductors. Essentially they are impurities in the semiconductor material who have energy levels located around the centre of the band gap of the material (i.e. far from the bandedge). They can often interact with both the valence band holes and the conduction band electrons, making them particularly active recombination centres. If the transitions involving these centre are non-radiative then they can seriously impact the emission yield during photoluminescence or in light emitting devices, whilst in direct semiconductors they can yield optically bright wide band emissions at photon energies well below the bandgap energy.

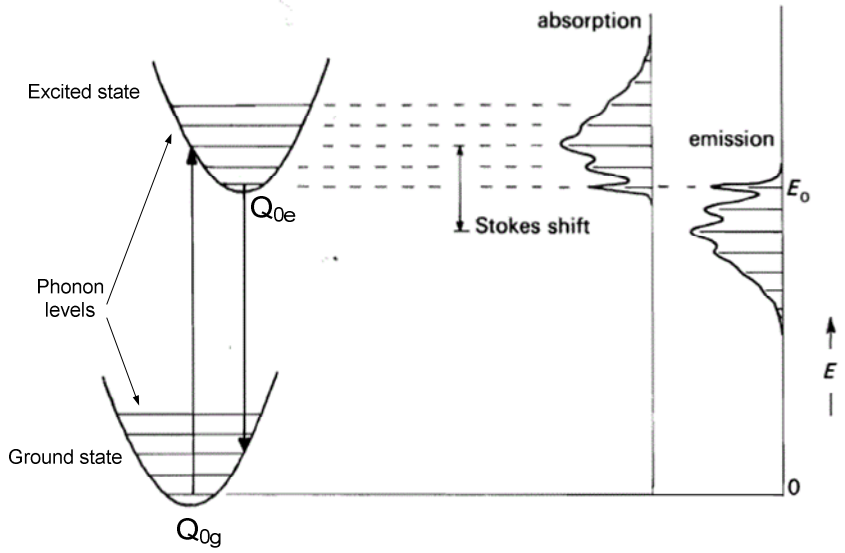

Figure 2.12: Configurational coordinate diagram from showing the ground and excited state of a dopant atom and corresponding absorption and emission spectrum. Reproduced with some modifications from reference 22. Copyright: (1989) Oxford University Press.

The various emission processes described above can interact with the crystal structure via coupling with the lattice vibrations or phonons, as commented upon previously. This often yields replica peaks with an energy difference characteristic of the lattice vibration to which the exciton was coupling to. This coupling is most easily understood using configurational coordinate diagrams.[22] In the simplest version of this model only one mode of vibration is considered, the breathing mode, where the lattice distorts by expanding and contracting about the dopant lattice site, although other modes

can be included by extending the treatment to higher dimensional coordinate spaces. By treating this vibrational mode as a harmonic oscillator, only one parameter is necessary to describe the system, the configurational coordinate Q, which is the distance of the dopant atom to its nearest neighbour. The average value of Q may vary depending on the state that the dopant is in as can be seen in figure 2.12.

At low temperatures the most likely transition is from the zero phonon position at Q_{0g} into the various phonon energy levels of the excited state. When the electron is in the excited state it relaxes to the Q_{0e} level via thermalisation before recombining back to the various phonon levels of the ground state. The phonon related absorption spectrum then appears at higher energy than the luminescence spectrum. In the case where the oscillation frequency of the ground and excited state are equal, the absorption and emission spectra mirror each other around the zero phonon line, as before with the absorption occurring at higher energies while the emission occurs at lower energies. The degree of coupling between the lattice and the dopant is generally discussed in terms of the systems Huang-Rhys parameter S, which in turn is related to the difference between configurational coordinate in the ground and excited states and the harmonic oscillation frequency. Larger values of S increase the coupling strength between the lattice vibrations and the dopant energy bands, leading to phonon replica peaks or, where S is large enough to cause the peaks to be broadened significantly, a large single "structured" dopant related band.

In this work PL was used to characterise the defect related emissions in ZnO nanowires and single crystals. ZnO has a rich spectrum with a wide variety of different spectral features. The spectrum can be separated into two distinct regions, the near band edge emission and the deep level luminescent centres. The near band edge emission is characterised by a number of sharp and bright lines centred around 3.36 eV known as the I-lines.[23] At present 18 individual emission peaks have been identified in this region. The chemical identity or origin of some of these lines has been identified and a summary of this cluster of lines can be found in reference 23. More recently another set of lines known as the DD lines or Y lines, which are centred around 3.34 eV have been identified. The origin of these lines is still uncertain and is the subject of ongoing investigation by various groups.[24-25] The two electron satellite lines associated with the I-lines and DD or Y-lines are located around 3.33 to 3.26 eV. Figure 2.13 shows a convenient summary of the positions of the various near band edge lines found in ZnO.

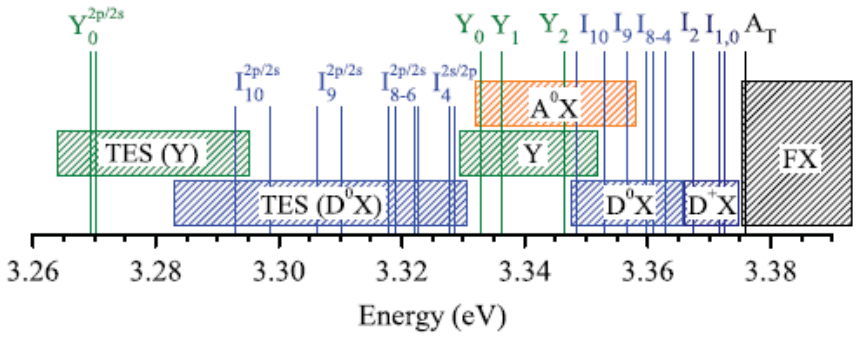

Figure 2.13: A schematic diagram of the various near band edge emission lines found at low temperature in ZnO. Reproduced from reference 24. Copyright (2011) the American Physical Society

In addition to the near band edge emission lines there are also a number of deep level luminescent centers found in ZnO including a broad unstructured green band,[26] a broad structured green band[27] a yellow-orange band[28] and a red band.[29] Of these deep level centres the green bands are of most significance as they are found in practically all samples of ZnO irrespective of the method used to grow the sample. As will be demonstrated in chapter 6, even if the green band is not present in a sample it can be very easily introduced. The origin of the structured green band is the primary focus of the optical studies in this work and controversy surrounding its origin is explored in greater detail in chapter 6.

In this work all PL spectra were collected at low temperatures using a Bomem DA8 Fourier transform (FT) spectrometer fitted with a model IPH8200L photomultiplier tube. The samples were excited using the 325 nm line of continuous wave HeCd laser, whilst the samples were kept at temperatures between 19 and 21 K using a Janis research Co. closed cycle helium cryostat. The sample emissions were coupled to the spectrometer using a lens to parallelise the emission before condensing the beam into the spectrometer with a parabolic mirror. A schematic representation of the experimental setup can be seen in figure 2.14. The spectrometer is a key component in any PL system. Most spectrometers are dispersion spectrometers where the light is separated into in to its component wavelengths using a diffraction grating. The spectrum is then obtained by scanning the separated wavelengths across a detector and measuring the intensity of the emission at each wavelength. However this process is limited by a number of different factors, such as the dispersion of the grating, the path length of the spectrometer and the width of the

aperture slits all of which can act to reduce the maximum achievable resolution. In FT spectroscopy many of these factors are negated as the mode of operation is fundamentally different.

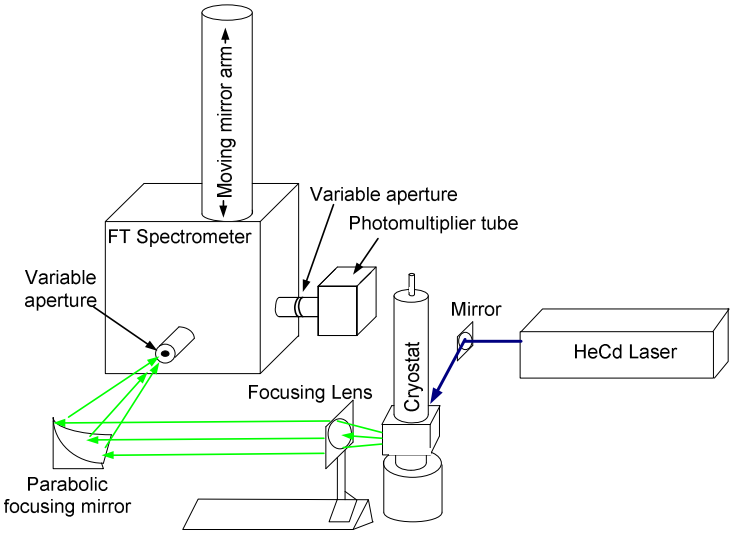

Figure 2.14: Schematic representation of the photoluminescence experimental configuration, showing the laser path in blue the photoluminescence path in green and all the major components of the system.

At the heart of a FT spectrometer is a Michelson interferometer, similar to that used in the WLP equipment shown in figure in 2.6. The emission beam enters the spectrometer where is hits a beam splitter and is separated in to two beams. Each beam is then sent down a different arm of the spectrometer before being reflected back and recombined into a single beam which is then sent to a detector. One of the arms or beam paths is kept fixed whilst the length of the second arm is varied. Assuming a single frequency, monochromatic, light source in the first instance, then when the path length of the two arms is equal or differs by a whole number multiple of the wavelength of the light, then constructive interference occurs. When the path length of the two arms is not a whole number multiple of the wavelength then different conditions of interference occur. When the mirror is moving, changing the path length of one of the arms, the detector will see a series of bright and dark fringes at a distance related to the wavelength of the light. The intensity of light detected by PMT is simply the sum of the combined beams factoring in the phase difference caused by the variation in path difference. For a single frequency light source the detector will see a cosinusoidal variation in intensity as the two beams move in and out of phase. To understand how this process relates to the spectral signal it is

necessary examine this process in more detail. The two beams recombining can be described by two electric fields with a phase difference between them as given by:

$$E_1 = E\cos(\omega t) \text{ and } E = E\cos(\omega t + \varphi)$$

(2.7.6.1)

where ϕ is the phase difference between the two electric fields. The amplitude of the electric field at point of recombination E_T is then given by the vector sum of the two phasors, that is:

$$E_T^2 = E^2 + E^2 - 2E^2\cos(\pi - \varphi)$$

(2.7.6.2)

Rearranging this gives:

$$E_T = 2E\left|\cos\frac{\varphi}{2}\right|$$

(2.7.6.3)

Given that the detector measures the intensity rather than the electric field it is more convenient to write the combined beams in terms of the intensity as given by the relationship:

$$I = \frac{1}{2}\epsilon_0 c E_T^2$$

(2.7.6.4)

Giving:

$$I = \epsilon_0 c E^2\cos^2\frac{\varphi}{2}$$

(2.7.6.5)

It follows on that given the signal intensity is at its maximum when the phase difference is 0 then equation 2.7.6.5 can be rewritten in terms of the maximum intensity I_0 :

$$I = I_0 \cos^2 \frac{\varphi}{2}$$

(2.7.6.6)

Or

$$I_x = \frac{1}{2} I_0 + \frac{1}{2} I_0 \cos \varphi$$

(2.7.6.7)

We now have an expression that relates the intensity to the phase difference ϕ between the two beams. The phase difference is described by the difference in path lengths of the two beams in terms of the number of wavelengths in radians:

$$\varphi = 2\pi \frac{1}{\lambda} x$$

(2.7.6.8)

Where λ is the wavelength of the light and *x* is the difference in path lengths. At this point it more convenient to use wave numbers defined as $= \frac{1}{\lambda}$. Combining equations 2.7.6.7 and 2.7.6.8 yields:

$$I_x = \frac{1}{2} I_0 + \frac{1}{2} I_0 \cos 2\pi \nu x$$

(2.7.6.9)

Where multiple monochromatic lines are present then the intensity is the sum of their contributions giving the intensity from the *i*th line as:

$$I_x = \frac{1}{2} \sum_i I_i + \frac{1}{2} \sum_i I_i \cos 2\pi \nu x$$

(2.7.6.10)

In reality monochromatic lines do not exist so even the sharpest emission will have a spectral distribution. Consequently the intensity I_i is replaced by the term *L(v)dv*, which corresponds to the intensity between *v* and *v+dv.* The total intensity detected is then given as:

$$I_x = \frac{1}{2} \int_0^\infty L(\nu) d\nu + \frac{1}{2} \int_0^\infty L(\nu) \cos 2\pi \nu x d\nu$$

(2.7.6.11)

Equation 2.7.6.11 corresponds to the Fourier transform of the emission spectrum and is called the interferogram. During operation the intensity of the light is recorded as a function of the mirror displacement. Taking the inverse Fourier transform of this data yields the original spectrum. In practice the mirror cannot extend to infinity so the actual achievable resolution is limited to $1/X_{max}$ where X_{max} is the maximum mirror displacement. While the above discussion is useful in understanding the operation of an FT spectrometer, the actual process is significantly more complex as many factors such as the aperture size, apodisation, mirror alignment, detector noise (both white and pink), imperfections in the optics and analogue to digital signal conversion and signal amplification must be addressed.[30] A detailed analysis of these and other issues can be found in reference 30.

For this work FT spectroscopy offered a number of distinct advantages over regular dispersion spectroscopy. In particularly the degree of resolution necessary to resolve the fine spectral features of the ZnO green band sharp line emission was simply unachievable using the conventional dispersion spectrometers available at DCU. In addition given that the signal was quite weak the circular aperture used by the instrument has a much higher throughput than the narrow slits used by dispersion spectrometers. Given that the signals of interest were very weak some issues regarding the dynamic range of the instrument were encountered. As the FT spectrometer detects the entire spectrum simultaneously weak emission peaks only account for a small proportion of the detected signal intensity. The weak spectral information can become lost in the background as compared to more intense signals. To overcome this issue it was necessary to filter the PL emission so as to only allow specific frequency ranges into the spectrometer. Despite this it was found that the signal to noise ratio was still poor as the dark count of the PMT was very high (i.e. of the same order of magnitude as the signal). As cooling the PMT was not a practical option, it was necessary to average out the noise by co-adding a large number of interferograms. While this process increased the length of time it took to obtain each spectra, it allowed otherwise unobtainable spectral information to be collected.

2.7.7 Transmission electron microscopy

In this work transmission election microscopy (TEM) was used to characterise individual nanostructures grown by both CBD and CTR-VPT methods. While TEM instruments bear many similarities to SEM instruments, in that focused electron beams are used to image samples, the nature of the data obtained is significantly different. Whilst SEM instruments use secondary or other scattered electrons coming back from the sample surface to image the surface of samples, as the name suggests transmission electron microscopes pass a focused beam of electrons through the sample. However this is only possible when the electrons are accelerated to much higher velocities and the samples are very thin. SEM instruments typically operate with an electron accelerating voltage between 5-25kV while TEM instruments typically operate between 100 and 300 kV representing a large increase in the electron energy. As with an SEM, electrons are produced in an electron gun in and evacuated chamber by either thermionic emission or field emission. The electron current is then directed into a suitable spot size for the analysis of the sample. Once the beam has passed through the sample more lenses are used to focus and magnify the image and the image is recorded on a phosphor screen or specially adapted CCD screen. There are many different modes of operation for a TEM, including scanning transmission microscopy (STEM), dark field (DF-TEM), bright field (BF-TEM), selected area electron diffraction (SAED), High Resolution (HR-TEM) and electron energy loss spectroscopy (EELs). A brief description of each will now be given.

Bright field TEM

BF-TEM is the most straight forward and common mode of operation. In this mode the beam of electrons is passed through and around the sample. The electrons are then either scattered by the sample or where no sample is present pass straight through. The objective aperture after the sample and objective lens acts as a stop preventing electrons with larger scatter angles from passing. An image of the sample is then formed by the contrast created by the electron density passing through the aperture. Areas of the sample that are thin, scatter less electrons beyond the critical cut off angle and appear bright whilst thicker areas scatter more electrons thus appearing darker.

Dark field TEM

As with BF-TEM a focused beam of electron is passed through the sample, where they can be either scattered or pass straight through. By shifting the optical axis of the beam with respect to the aperture then electrons which have not been scattered by the sample are excluded from the image. This can be achieved in a number ways including shifting the objective lens aperture, tilting the electron beam with respect to the optical axis of the objective lens and aperture or using a beam stop at the centre of the objective aperture.[31] An example of dark field mode as compared to bright field mode is shown figure 2.15 (a) and (b). In this configuration the contrast is reversed as compared to BF-TEM. That is, unscattered electrons are stopped by the aperture, so thin areas or areas where no sample is present appear dark. Only in areas of the sample where the electrons have undergone scattering are visible in dark field mode.

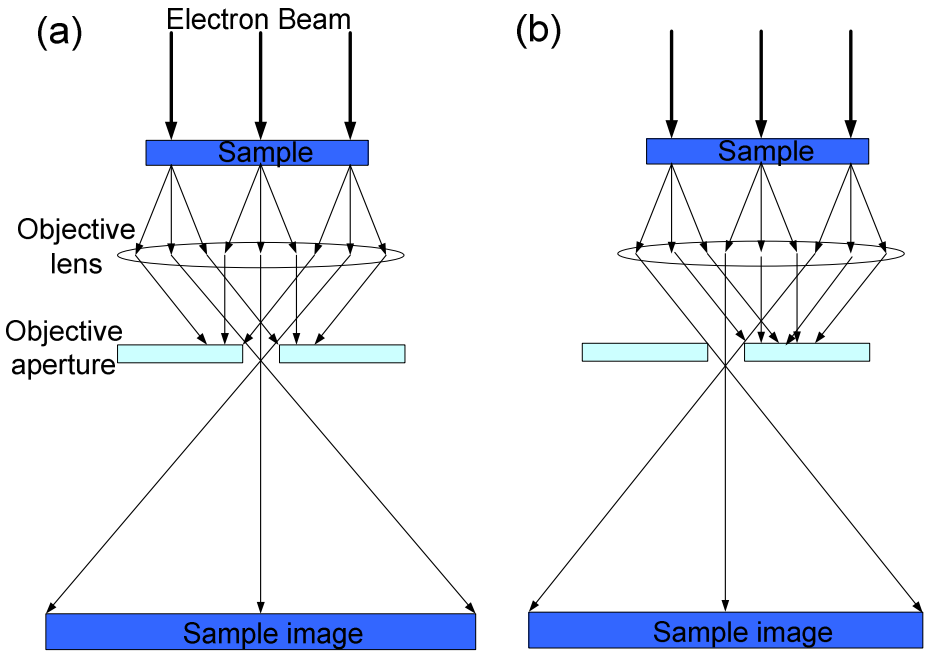

Figure 2.15: Optical layout of a TEM operating in (a) bright field mode and (b) dark field mode using a shifter aperture.

Scanning transmission microscopy

Unlike conventional TEM, where the entire sample area under examination is continuously illuminated by the (parallel) electron beam, in STEM, a focused beam is raster scanned across the surface. Similar to conventional TEM, STEM can operate in both bright and dark field mode. It provides advantages over conventional TEM in that raster scanning

produces other electron effects such as secondary electrons or an energy dispersive x-ray signal, which can be collected simultaneously along side the primary TEM image. In addition STEM provides better signal to noise ratios as the process requires larger illumination and detector apertures, as compared to conventional TEM.

High resolution TEM

HR-TEM or phase contrast TEM allows individual planes of a crystal structure to be imaged. It combines the regular contrast obtained by the electron beam passing through a sample with the interference created from elastically scattered electrons. This is achieved by removing the objective aperture. The phase shift caused by the scattering process along different atomic planes leads to a diffraction pattern representative of the crystal structure. While atomic resolution is possible using HRTEM, the images formed despite their appearance are not real images of the atomic structure, rather they represent a multiple beam diffraction pattern of the crystal structure.

Selected area electron diffraction

SAED in principle is similar to XRD. The highly accelerated electrons passing through a crystalline sample can be treated as a wave. In this case, the regular structure of a crystal acts as a diffraction grating to the electron wave passing through, scattering electrons at particular angles. By adjusting the TEM focus in dark field mode the scattered electron image can be focused as a diffraction pattern from which crystallographic information can be obtained. In this manner it is similar to XRD. However, given that electron beam is very tightly focused only a small area of the sample is examined. This allows the crystallographic properties of individual features to be examined.

Electron energy loss spectroscopy

Electron energy loss spectroscopy is a useful tool in TEM studies as it allows chemical composition information about the sample to be determined. The beam of electrons in the TEM will have a particular kinetic energy. Some of the electrons passing through the sample will undergo inelastic collisions with the sample. The electron will lose some of its kinetic energy during these interactions, due to a variety of possible interactions, such as inner shell ionisation. This loss is often characteristic of the material present and, as with XPS, can yield chemical state information about the sample.

In this work TEM, STEM, HRTEM, SAED and energy loss spectroscopy were used to investigate the crystal structure of nanorods grown by CBD and CTR-VPT methods as these techniques allowed the crystal structure of individual nanorods to be investigated. These techniques were also used to investigate the effects of high temperature growth on crystal structures and buffer layers. As TEM and related techniques were unavailable in DCU, this work was performed by collaborators in Dpto. Ciencia de los Materiales e Ingenieria Metalurgica y Q.I., Facultad de Ciencias, Cadiz , Spain, and is included in this thesis for completeness of the discussion and findings.

2.8 References

(1) Greene, L. E.; Law, M.; Tan, D. H.; Montano, M.; Goldberger, J.; Somorjai, G.; Yang, P. D. *Nano Letters* **2005,** *5* (7) 1231-1236

(2) Law, M.; Greene, L. E.; Johnson, J. C.; Saykally, R.; Yang, P. D. *Nature Materials* **2005,** *4* (6) 455-459

(3) Yu, C. W.; Lai, S. H.; Wang, T. Y.; Lan, M. D.; Ho, M. S. *J Nanosci Nanotechno* **2008,** *8* (9) 4377-4381

(4) Ng, V.; Lee, Y. V.; Chen, B. T.; Adeyeye, A. O. *Nanotechnology* **2002,** *13* (5) 554-558

(5) Rybczynski, J.; Banerjee, D.; Kosiorek, A.; Giersig, M.; Ren, Z. F. *Nano Letters* **2004,** *4* (10) 2037-2040

(6) Zhou, Z.; Zhao, X. S.; Zeng, X. T. *Surface and Coatings Technology* **2005,** *198* (1-3) 178-183

(7) Li, C.; Hong, G. S.; Wang, P. W.; Yu, D. P.; Qi, L. M. *Chem Mater* **2009,** *21* (5) 891-897

(8) Wang, L. K.; Yan, Q. F.; Zhao, X. S. *Langmuir* **2006,** *22* (8) 3481-3484

(9) Brinker, C. J.; Scherer, G. W., *Sol-gel science: the physics and chemistry of sol-gel processing* 1990, San Diego: Academic Press Limited.

(10) Nozawa, K.; Gailhanou, H.; Raison, L.; Panizza, P.; Ushiki, H.; Sellier, E.; Delville, J. P.; Delville, M. H. *Langmuir* **2004,** *21* (4) 1516-1523

(11) Stöber, W.; Fink, A.; Bohn, E. *Journal of Colloid and Interface Science* **1968,** *26* (1) 62-69

(12) Hillier, J.; Baker, R. F.; Zworykin, V. K. *Journal of Applied Physics* **1942,** *13* 571-577

(13) Giessibl, F. J. *Reviews of Modern Physics* **2003,** *75* (3) 949

(14) Chung, Y.-W., *Practical Guide to Surface Science & Spectroscopy*. 2001, San Diego: Academic Press.

(15) Magonov, S. N.; Whangbo, M.-H., *Surface Analysis with STM and AFM: experimental and theoretical aspects of image analysis*. 1996, Weinheim: Cambridge.

(16) Rousseau, J. J., *Basic crystallography*. 1998, Sussex: John Wiley & Sons Ltd.

(17) Venables, J. A., *Introduction to surface and thin film processes*. 2000, Cambridge: Cambridge University Press.

(18) Woodruff, D. P.; Delchar, T. A., *Modern techniques of surface science*. 1986, Cambridge: Cambridge University Press.

(19) Moulder, J. F.; Stickle, W. F.; Sobol, P. E.; Bomben, K. D., eds. *Handbook of X-Ray Photoelectron Spectroscopy* 1st ed., ed. J. Chastain. 1992, Perkin-Elmer Corporation: Eden Prairie, Mn.

(20) Klingshirn, C., *Semiconductor Optics*. 2nd ed. 2005, Berlin Heidelberg: Springer.

(21) Basu, P. K., *Theory of Optical Processes in Semiconductors: Bulk and Microstructures* 1997, Oxford: Oxford University Press.

(22) Henderson, B.; Imbusch, G. F., *Optical Spectroscopy of Inorganic Solids*. 1989, Oxford: Oxford University Press.

(23) Meyer, B. K.; Alves, H.; Hofmann, D. M.; Kriegseis, W.; Forster, D.; Bertram, F.; Christen, J.; Hoffmann, A.; Strassburg, M.; Dworzak, M.; Haboeck, U.; Rodina, A. V. *Physica Status Solidi B-Basic Research* **2004,** *241* (2) 231-260

(24) Wagner, M. R.; Callsen, G.; Reparaz, J. S.; Schulze, J. H.; Kirste, R.; Cobet, M.; Ostapenko, I. A.; Rodt, S.; Nenstiel, C.; Kaiser, M.; Hoffmann, A.; Rodina, A. V.; Phillips, M. R.; Lautenschlager, S.; Eisermann, S.; Meyer, B. K. *Phys Rev B* **2011,** *84* (3) 035313

(25) Johnston, K.; Cullen, J.; Henry, M. O.; McGlynn, E.; Stachura, M. *Phys Rev B* **2011,** *83* (12) 125205

(26) Leiter, F.; Alves, H.; Pfisterer, D.; Romanov, N. G.; Hofmann, D. M.; Meyer, B. K. *Physica B: Condensed Matter* **2003,** *340-342* (0) 201-204

(27) Dingle, R. *Physical Review Letters* **1969,** *23* (11) 579

(28) Schirmer, O. F.; Zwingel, D. *Solid State Communications* **1970,** *8* (19) 1559-1563

(29) Marotti, R. E.; Badán, J. A.; Quagliata, E.; Dalchiele, E. A. *Physica B: Condensed Matter* **2007,** *398* (2) 337-340

(30) Chamberlain, J., *The principles of interferometric spectroscopy*, ed. G.W. Chantry and N.W.B. Stone. 1979, Chichester: Wiley-Interscience

(31) Reimer, L., *Transmission Electron Microscopy*. 2 ed. Springer Series in Optical Sciences, ed. P.W. Hawkes. 1989, Berlin: Springer-Verlag.

Chapter 3: Chemical Bath Growth

3.1 Introduction

In this chapter seed layers prepared by drop-coating solutions of zinc acetate in ethanol (as described in the experimental chapter, section 2.3) are examined. While this step of the growth process may seem facile, the details of the deposition process are extremely important to the subsequent growth of *c*-axis aligned ZnO nanorods by both CBD and CTR-VPT. In the second half of this chapter we examine the results of the various CBD growth processes described in chapter 2, section 2.4 and identify factors that are important for subsequent CTR-VPT deposition, which is then discussed in chapter 4. For completeness of the investigation it was necessary to use techniques not available in our group and therefore this chapter and chapter 4 contain data acquired both by us and other groups. Specifically, the XPS results and fittings presented here were obtain by Kumar Kumarappan of the School of Physical Sciences in DCU and TEM data was obtained by Rabie Fath Allah, Teresa Ben and David Gonzalez of the University of Cadiz, hereafter called UCA Cadiz collaborators.

3.2 Seed layer characterisation

Without the initial seed layers, nucleation and growth of ZnO nanorods on many substrates by both CBD and CTR-VPT would simply not occur. In solution based systems, where the concentration of a dissolved species is in a meta-stable state with respect to the solubility curve of the solute, the seed layer provides an energetically favourable nucleation

site to enable heterogeneous nucleation and crystal growth and thus reduce the solution concentration. In the absence of a seed layer, many amorphous substrates such as glass or silicon, where the native oxide has not been removed, do not initiate nucleation as there are no energetically favourable sites. In such cases homogenous nucleation within the solution is dominant and the target material forms in the bulk of the solution rather than on the substrate. This is true of both simple crystallisation of a dissolved species and of more complex systems such as the growth of ZnO nanorods in solutions where a chemical reaction is also occurring. In this case, excluding the special conditions achieved by the CBD growth described in section 2.4.3, both homogeneous and heterogeneous nucleation can occur together leading to nanorod growth on the substrate surface in conjunction with precipitation of homogeneously nucleated ZnO particulates.[1] It has been shown that the presence of crystalline substrates under some reaction conditions leads to heterogeneous nucleation on the substrate surface, seemingly irrespective of the substrate composition. [2] However further work in this area has shown that *c*-axis alignment on crystalline and non-crystalline substrates is substantially improved by depositing seed layers prior to growth. [3-5]

Many methods exist to deposit such seed layers including sol-gel,[6] magnetron sputtering[7] and pulsed layer deposition.[8] While useful for research purposes, many of these techniques would provide serious challenges in terms of scalability in an industrial production scenario. In contrast, the method reported by Greene and Law, based on the drop-coating of zinc acetate solutions is sufficiently simple to be easily scaled and implemented in a manufacturing environment. Originally it was believed that a residual zinc acetate film remained on the surface of the substrate which was subsequently decomposed to ZnO at 350°C. Later work by Lee *et al.* found a direct link between atmospheric humidity and the deposition of the seed layer by drop-coating.[9] They proposed that the seed layer formation was not caused by residual zinc acetate but rather zinc hydroxide, suggesting that water from the atmosphere diffused into the alcoholic solution and reacted with the zinc acetate to form an insoluble zinc hydroxide precipitate. By controlling the atmospheric conditions during the drop-coating procedure, they were able to control the number of drop-coats required to completely cover a substrate. They also identified features linking the growth of the ZnO rod to the seed layer. It was found that if the density of seeds was too low, multiple rods would nucleate from a single seed, leading to a loss of *c*-axis alignment. Conversely if the seed layer was too dense, parallel neighbouring rods fused, to form thicker structures. Despite the convincing evidence of the

role atmospheric humidity on the deposition of the seed layer, no chemical analysis was performed to confirm their proposed mechanism. Irrespective of these uncertainties, the relative simplicity of the drop-coating method makes it an attractive option for the preparation of *c*-axis aligned seed layers and subsequent CBD growth of ZnO nanowires.

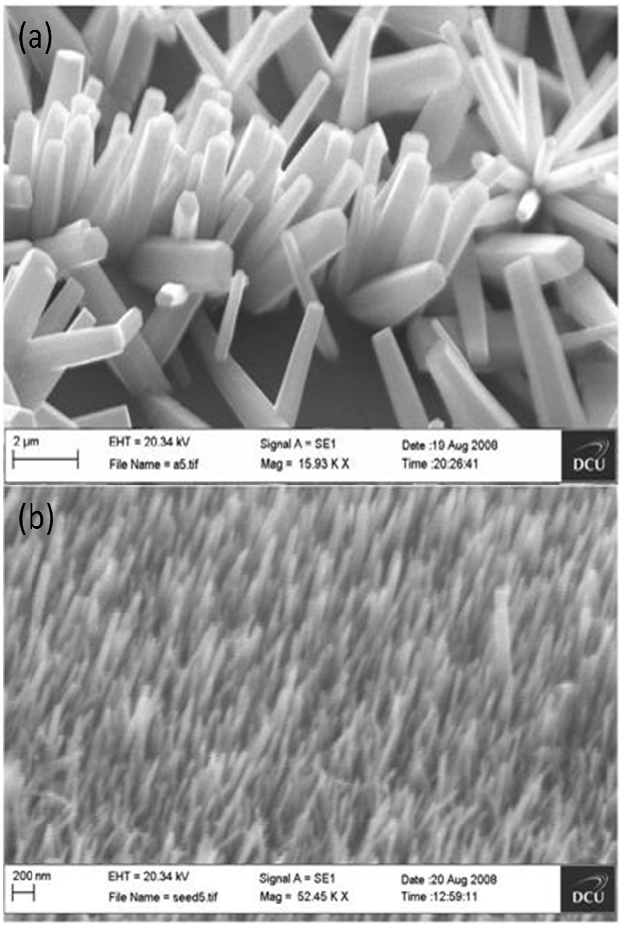

Figure 3.1: CBD ZnO nanorods grown on a textured ZnO seed layer prepared by (a) drop-coating an alcoholic zinc acetate solution and (b) by evaporation of a ZnO sol.

The first work that we performed in this area was to try to replicate the growth of CBD nanorods on a textured ZnO seed layer, as reported by Greene and Law using the zinc acetate drop-coating technique that they had pioneered. Initial attempts were unsuccessful as samples produced were inconsistent in many ways. Typically, growth was observed on most samples, however complete coverage of the substrate area was rarely achieved. Samples were often covered in debris, such as homogenously nucleated ZnO particles and amorphous zinc hydroxide gels. While nanorod growth was often observed, rod density varied across the sample from completely bare to densely packed. Alignment with respect to the substrate was generally poor and it often appeared as if many rods were nucleating

from single points on the substrate, an example of which can be seen in figure 3.1 (a). At this stage it was unclear if the poor results obtained were the result of the CBD growth chemistry or the seeding process. Many of the problematic features bear a striking resemblance to the issues identified by Lee *et al*.[4], such as the multi-rod nucleation which can be clearly seen in figure 3.1 (a). To identify the origin of the poor density / alignment control and confirm that the CBD reaction solution chemistry was not the issue, a seed layer was prepared by an alternative technique. A concentrated ZnO sol was first prepared by the method of Hasse,[10] which was then drop-coated onto a substrate and allowed to completely evaporate. Repeating the HMT-CBD growth on substrates prepared in this manner produced a dense array of nanorods, completely covering the substrate. In contrast to figure 3.1 (a), nanorods grown on a ZnO sol derived seed layer, as seen in figure 3.1 (b) show a significant improvement in the density of growth and some improvement in nanorod alignment. Substrates coated with sol derived seed layers had nanorod coverage close to 100%, with no evidence of multi-rod nucleations from single points, thereby indicating that the poor results were due to a failure in the initial seeding step and not the CBD solution chemistry. Therefore, it was necessary to understand why the drop-coating process was failing to produce results similar to those reported elsewhere.[5] In order to do this, a clear understanding of the chemical origin of the seed layer was considered critical. The clarification of the chemical origin of the seed layer was performed by a detailed XPS analysis of samples at various stages of the process.

3.3 Chemical origins of the ZnO seed layer

As previously mentioned, the chemical reaction pathway to creation of the seed layer was the subject of conflicting reports in different publications.[4-5] The original authors suggested the formation of the seed layer was due to residual zinc acetate, while others believed that the seed layer formed by an intermediate zinc hydroxide layer. To clarify the chemical pathway, XPS analysis was performed on substrates after the drop-coating step, both prior to and after annealing. Coated substrates were annealed in air at 350°C and under vacuum in the XPS chamber at 300°C and 450°C respectively. However, in parallel with the examination of the XPS data it is useful to examine the chemical structures of the species that may be present or involved. Both the schematic chemical structures and XPS spectra of the various samples are shown in figures 3.2, 3.3. and 3.4.

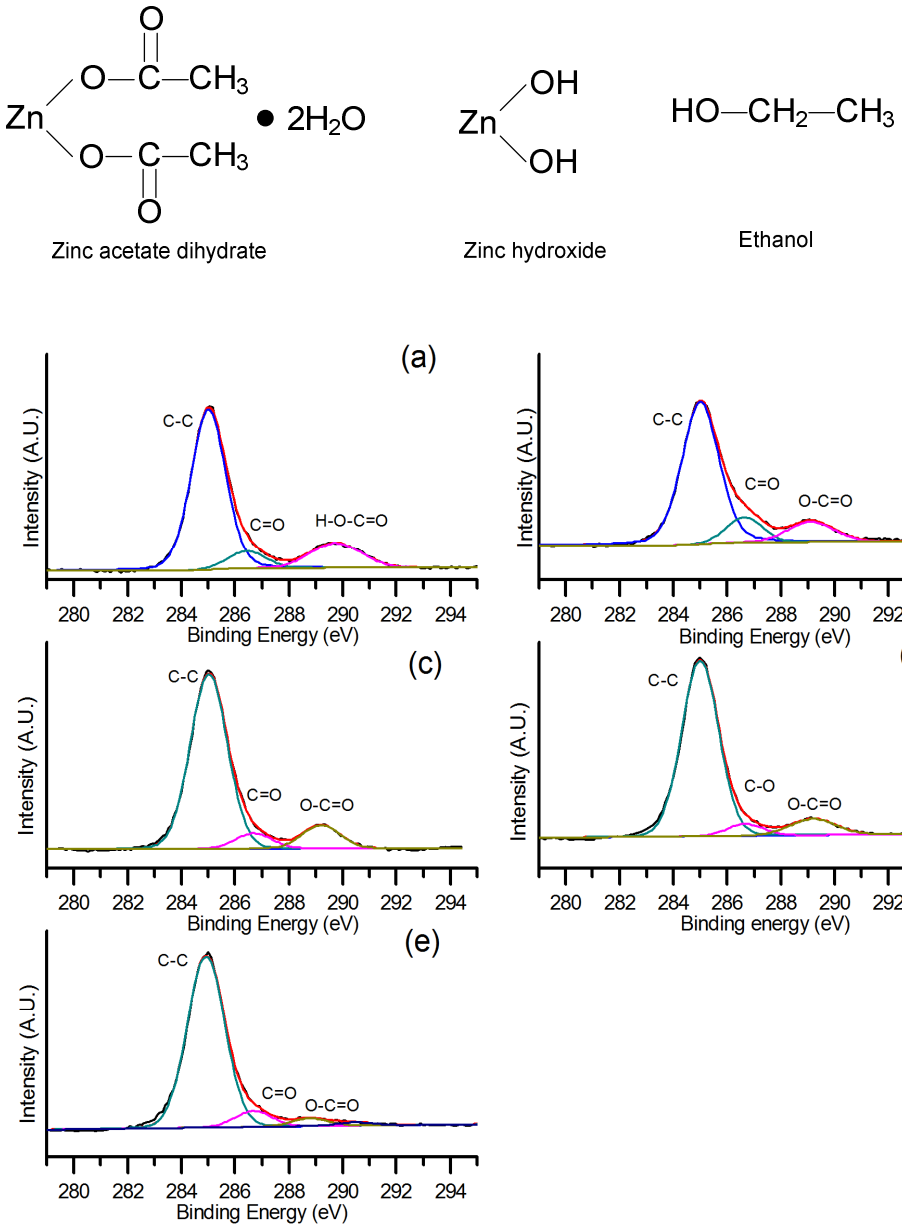

Figure 3.2: (top) structure of the various chemical species which may be present (bottom) Peak fitted XPS spectra of the C-1S region of the spectrum showing drop-coated seed layer (a) before annealing in air at 350°C (b) after annealing in air at 350°C (c) before annealing in vacuum at 350°C (d) after annealing in vacuum at 300°C (e) after annealing in vacuum at 450°C.

As shown in figure 3.2, the zinc acetate molecule contains 2 acetate anions bound to a single zinc ion. The acetate ion is comprised of a carboxcycilic acid group with a methyl termination. In contrast the zinc hydroxide molecule is simpler, consisting of two hydroxide anions bound to a single zinc cation. The C 1s region of the spectrum for different samples

is shown in figure 3.2 and shows similar features for samples before and after annealing, including C-C (285 eV) and C=O (286.5 eV) contributions. A slight variation is observed between the first unannealed substrate (figure 3.2 (a)) which has a HO-C=O (289.7 eV) peak, while the remainder of the samples have an O-C=O (289.1 eV) contribution. The HO-C=O component at 289.7 eV is not detected in the second unannealed sample (figure 3.2 (c)). After annealing all the samples have a similar distribution of chemical environments. Little variation is observed in the C-C peak intensity before and after annealing, suggesting that this peak is primarily due to adventitious carbon and not due to the C-C bond from the acetate group. While residual acetate and its decomposition products may contribute to the carboxyl signals at 286.5 eV 289.7 eV and 289.1 eV, it is more likely that parts of these signals are due to surface adsorbed carbonates and hydrogen carbonates. It should be noted that the 289.7 eV HO-C=O could also correspond to an acetic acid molecule. The formation of zinc hydroxide would produce hydrogen cations which would naturally balance the charge on the acetate anion, forming acetic acid. The acetic acid, which has a much higher boiling point than ethanol, may remain on the sample surface even after all of the ethanol washings have been dried off. It is well established that both CO and CO_2 are readily adsorbed onto the surface of ZnO.[11-15] Previous XPS analysis on thin film samples prepared directly from ZnO by sputtering, without the use of acetate salts, show similar peaks in this region, which were attributed to surface carbonates or hydrocarbonates.[16] While the higher binding energy peak position sheds little information as to the origin of the carbonates, some further insight can be gained from the relative peak intensity. In figure 3.2 it can be seen that the higher binding energy contribution prior to annealing is small in comparison to dominant adventitious carbon peak, similar to the results obtained for acetate-free ZnO by Saw *et al*.[16] In direct decomposition studies of acetate salts (zinc and nickel), very strong higher binding energy contributions are seen which diminish rapidly with annealing below 300°C.[17-19] In our case, no significant reduction in the higher binding energy signal at 289.1eV is observed until the annealing temperature is raised to 450°C, 100°C higher than the temperature generally employed to decompose the substrate coating and ~200°C over the melting temperature of zinc acetate.[5, 20] The resistance of the higher binding energy peak to annealing at 350°C is inconsistent with the behaviour of acetates, as a significant decrease in such signals is expected when acetate salts are annealed at temperatures as low as 240°C. This behaviour has also been confirmed by thermogravimetic analysis and in situ Raman studies of the thermal decomposition zinc

acetate.[21] These data therefore suggest that the origin of the signal in the higher binding energy region is primarily due to strongly chemisorbed atmospheric carbonates.

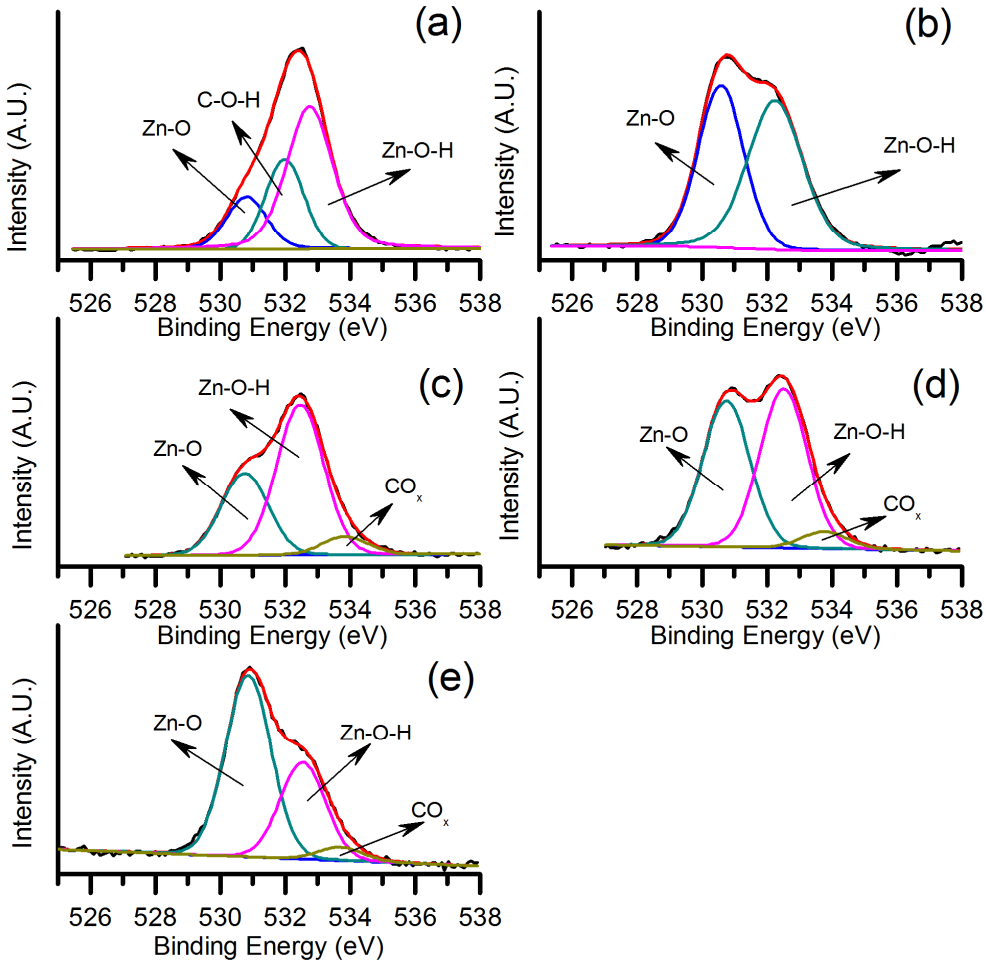

Figure 3.3: Peak fitted XPS spectra of the O-1S region of the spectrum showing drop-coated seed layer (a) before annealing in air at 350°C (b) after annealing in air at 350°C (c) before annealing in vacuum at 350°C (d) after annealing in vacuum at 300°C (e) after annealing in vacuum at 450°C.

In the oxygen O-1s region of the spectrum, shown in figure 3.3, the dominant spectral component in both samples prior to annealing is Zn-OH around 532.5 eV with a smaller ZnO contribution at 530.5 eV. [22-23] While the precise origin of the ZnO component prior to annealing is unknown, it may be due to a partial photo-induced decomposition of zinc hydroxide.[24] The strong emission peak at ~536.6 eV associated with zinc acetate observed by other groups was not detected in any samples either before or after annealing, and would be easily resolved in our experiment if it was present.[19] The complete absence

of this peak in any of the samples, strongly suggests that the thin film formed at the substrate surface is not due to a residual acetate film and that the chemical pathway proceeds via the zinc hydroxide intermediate. The sample held in air prior to annealing had an additional carbonate component at 532 eV, which was not detected in the sample held in vacuum. However this carbon-derived signal is substantially weaker than the zinc hydroxide component. A small carbon-derived signal at ~533.8 eV is detected in the samples held in vacuum both before and after annealing. After annealing both in air and in vacuum the ZnO peak at 530.5 eV increases substantially while the zinc hydroxide component is attenuated, as shown in figures 3.3 (a)-(e).

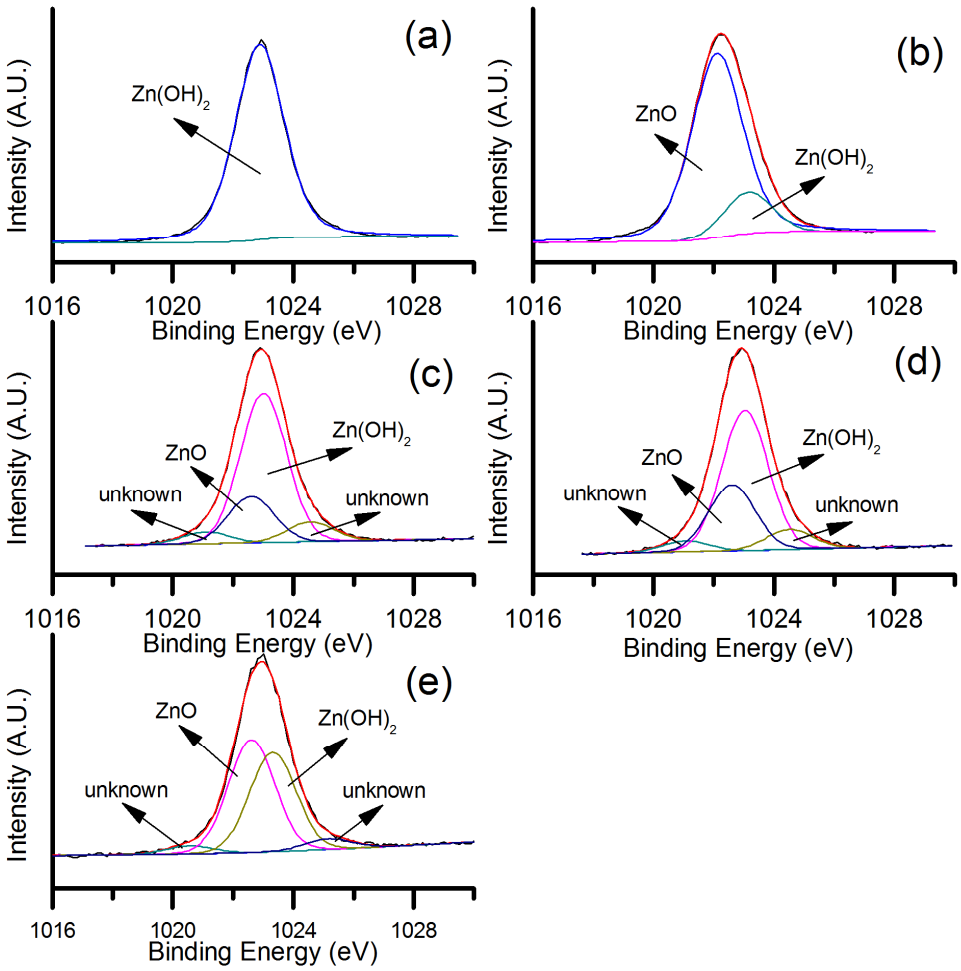

Figure 3.4: Peak fitted XPS spectra of the Zn 2P3/2 region of the spectrum showing drop-coated seed layer (a) before annealing in air at 350°C (b) after annealing in air at 350°C (c) before annealing in vacuum at 350°C (d) after annealing in vacuum at 300°C (e) after annealing in vacuum at 450°C.

The XPS spectra for the Zn 2p3/2 region of the spectrum is less clear. Before annealing in air (figure 3.4 (a)) The dominant component is zinc hydroxide, whilst after annealing in air the peak shift indicates ZnO is now the dominant contributor. The second sample both before and after annealing (figure 3.4 (c), (d) and (e)) showed additional contributions at both lower energy (1020.5 eV) and at higher energy (1024.7 eV), whose origin is uncertain. The higher energy contribution appears to correlate with a zinc chloride species, of unknown origin. It may result from residual impurities in the zinc acetate or ethanol. However the peak positions in the Zn 2P3/2 region are more difficult to interpret, given that some zinc bonds have very similar peak positions in this region. In particular zinc silicate overlaps the ZnO and ZnOH peak positions.[25] Therefore less emphasis should be placed on the analysis of this region of the XPS spectrum.

Overall the photoemission results strongly suggest that prior to annealing the dominant component of the substrate coating is zinc hydroxide, which transforms to ZnO after annealing. As XPS is a surface characterisation technique with a shallow sampling depth, the presence of both oxide and hydroxide species in the XPS spectra is symptomatic of the surface reactivity of ZnO and therefore very difficult to avoid. The smaller quantities of carboxyl/acetate-based compounds do not appear to play a significant role in the formation of the ZnO seed layer. The complete absence of the higher binding energy contribution in the O1S region associated with zinc acetate[19], suggests that it is either completely absent or present in such small quantities as to be beyond the limit of detection of our XPS system. From these results, we conclude that the original mechanism put forward by Greene and Law et *al.* was incorrect. Our findings are in agreement with those of Lee.[4] The complete reaction mechanism is given in figure 3.5.

By identifying the chemical pathway in the formation of the ZnO seed layer some important parameters become apparent. Specifically, the role of atmospheric humidity and the drop-coating volume are now discussed. The formation of zinc hydroxide is driven by an excess of water in ethanolic solution. This excess tips the equilibrium toward the hydrolysis of the zinc acetate leading to the formation of an insoluble zinc hydroxide, which subsequently precipitates onto the substrate surface. Anhydrous ethanol is hydroscopic, rapidly absorbing water from the surrounding atmosphere. It is this diffusion of water into the solution that drives the reaction forward. The rate of diffusion of water across the air-liquid interface is driven by the relative humidity of the air surrounding the solution on the

substrate surfaces. This effect has been observed many times during the course of this research.

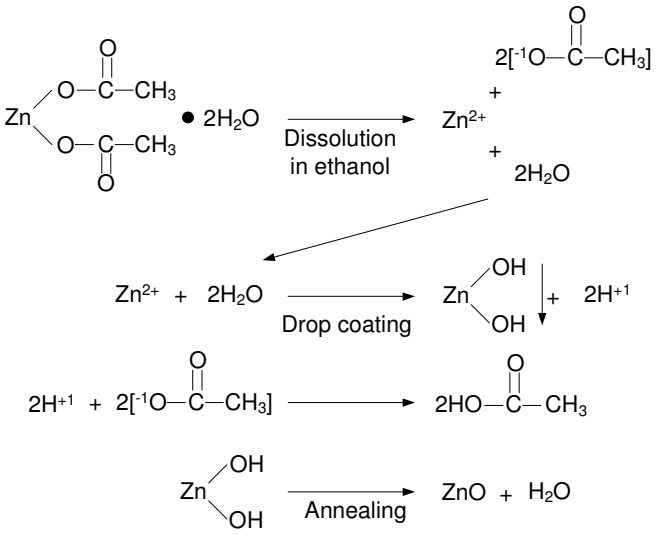

Figure 3.5: Proposed chemical route to the formation of ZnO seed layers by drop-coating alcoholic solutions of zinc acetate.

When the relative humidity of the lab was low, typically below 20%, the drop-coating process was less efficient and an increased number of drop-coats were required to compensate for the reduced reaction rate. When the relative humidity was high (>50%), fewer drop-coats were required. The best and most uniform seed layers, as determined from the subsequent CBD growths, were achieved when the relative humidity was in the 35 - 45% range. In this range the samples grown by the HMT-CBD method were uniform and well orientated with respect to the substrate. The second factor that can affect the deposition process is the ethanol film thickness. When the drop-coating solution is on the substrate surface, the water diffusion leads to the formation of the hydroxide precipitate which must reach the substrate surface before the ethanol evaporates or is rinsed off. Given that the concentration of the water will be greatest at the air / ethanol interface, it is reasonable to conclude that the precipitate forms first at or close to this interface and must therefore travel through the bulk of solution before reaching the substrate. It was this limit on the diffusion speed that was causing the poor results described at the beginning of the chapter. There is a narrow balance between applying too much solution and the precipitate not reaching the substrate or applying too little solution and the ethanol evaporating depositing a much thicker residue of zinc acetate. It was found that a volume of 3-5 µl of solution per cm^2 of substrate applied to the surface for 20 seconds was ideal for silicon

substrates with a surface area of 1-3 cm^2. For larger substrates it was found that increasing the volume above the pro-rata increase slightly improved the seed layer. This increase (typically ~10-20%) helped improve the spreading of the ethanol droplet across the larger surface area, thus reducing the possibility of areas of the sample not being wet by the ethanol solution. Furthermore, for substrates that did not wet well with ethanol, it was necessary to increase the volume further. An interesting point to note is that when uniform growth takes place during the CBD growth the amount of debris (in the form of trapped ZnO particles and $Zn(OH)_2$ gel) on the nanorod array surface decreases significantly. There is no evidence to suggest that the reaction solution is producing less precipitate. One possible explanation of this phenomenon is that the highly uniform and dense growth prevents precipitated particles from becoming trapped in inter-rod spaces, although this theory has not been investigated in detail.

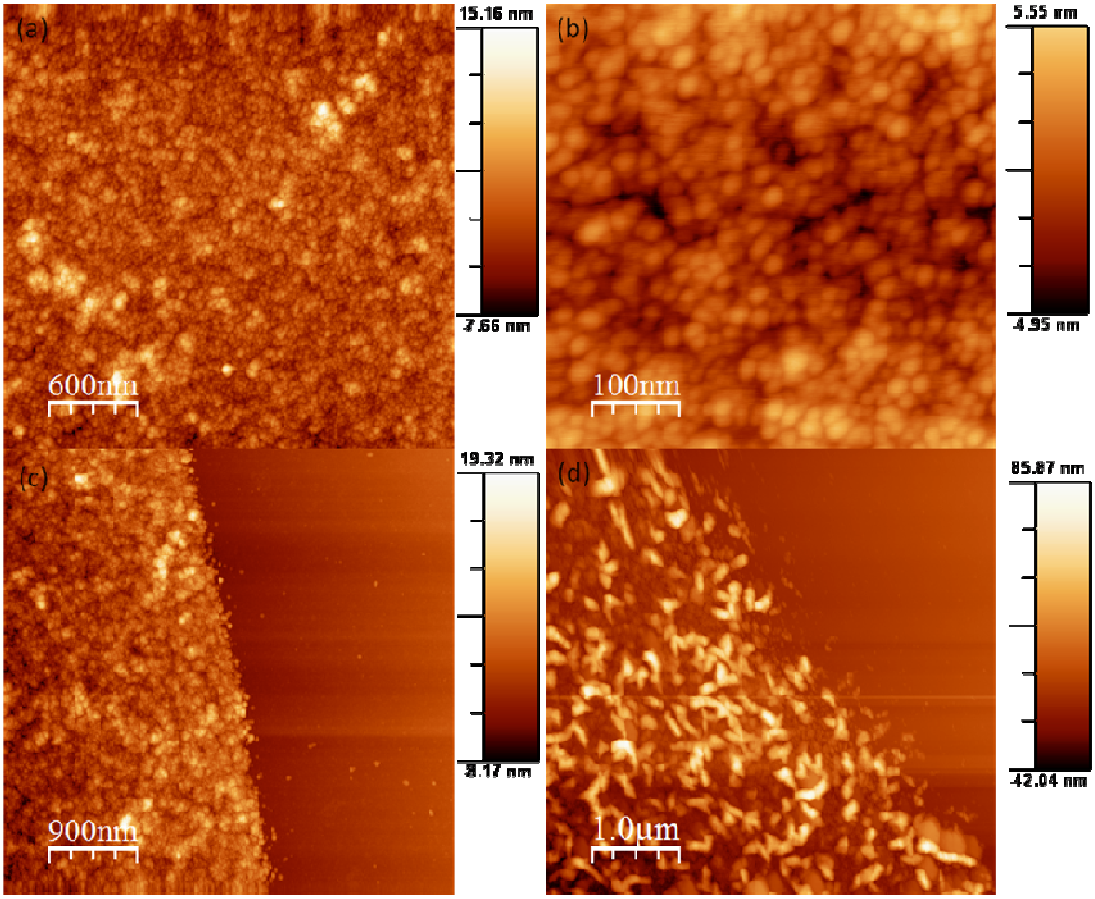

Figure 3.6: AFM images of a drop-coated seed layer (a) at the substrate centre (b) in the same region as shown in (a) but at higher magnification (c) in a region like that shown in (a) but which has been partially etched to reveal the underlying substrate at the substrate centre (d) at the substrate edge.

3.4 Seed layer morphology

Given the importance of the seed layer to subsequent deposition processes it was important to understand in greater detail the nature of the ZnO seed layer. Further insight was gained by AFM and FESEM analysis. After drop-coating 5 times and annealing at 350°C for 30 minutes, AFM analysis as shown in figure 3.6, reveal that the seed layer consisted of billions of individual plate-like crystallites randomly deposited across the substrate, stacking on top of each other to form a thin film. Cross-sectional analysis of the seed layers, an example of which is shown in figure 3.7, confirm that the crystallites have diameters of approximately 10-20 nm and a thickness ranging from 1-4 nm. To determine the total film thickness the seeds were etched from one half of the substrate using a dilute (1 mg/ml) H_2SO_4 solution, as shown in figure 3.6 (c) and (d). A clear variation is seen between the centre of the substrate (figure 3.6 (c)) and the substrate edge (figure 3.6 (d)). At the sample centre, the seed layer is significantly thinner, being composed of individual seeds or a couple of seeds stacked in an ad hoc manner. At the substrate edge (figure 3.6 (d)) the ZnO film is composed of larger thicker crystals forming a bulky continuous mass. The thickness in this region of the sample is in the order of 20 to 145 nm as compared to 5 to 25 nm for the bulk of the substrate. However, from the AFM images it is unclear whether this is an isolated deviation or if the behaviour of the seeding process is different at the substrate edges. As will be seen in later chapters, this is an important issue for high temperature CTR-VPT growths.

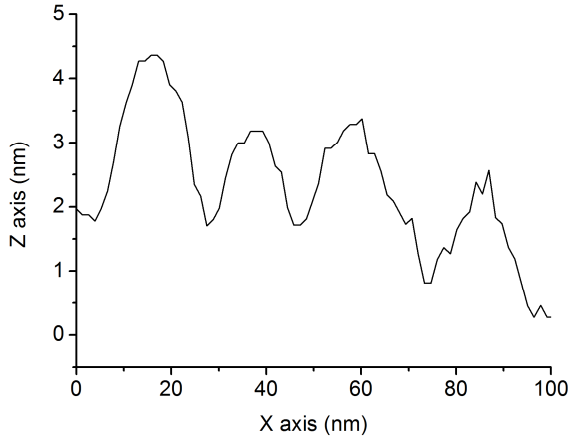

Figure 3.7: AFM cross sectional profile of ZnO seeds deposited by drop-coating a zinc acetate solution.

WLP was used to sample a larger area of the substrate surface than is easily available to AFM analysis. It can be seen in figure 3.8(a) for a sample drop-coated 15 times that there is a clear variation in the seed layer height across the sample. The bulk of the substrate surface is relatively uniform, with one or two large raised defects most likely due to dust and debris from the preparation environment. The seed layer also has a clear raised band going continuously around the outer edges following the rough contour of the sample edge. The height of the raised edge is approximately 300 nm. Given that the number of drop-coats used to prepare this sample was three times that of the samples used for the AFM analysis shown in figure 3.5, the height of this band correlates well with AFM determined thickness for the thinner sample. It can be seen from the FESEM image in figure 3.8 (b) that these large ridged structures are in fact an agglomeration of a large number of smaller individual crystallites.

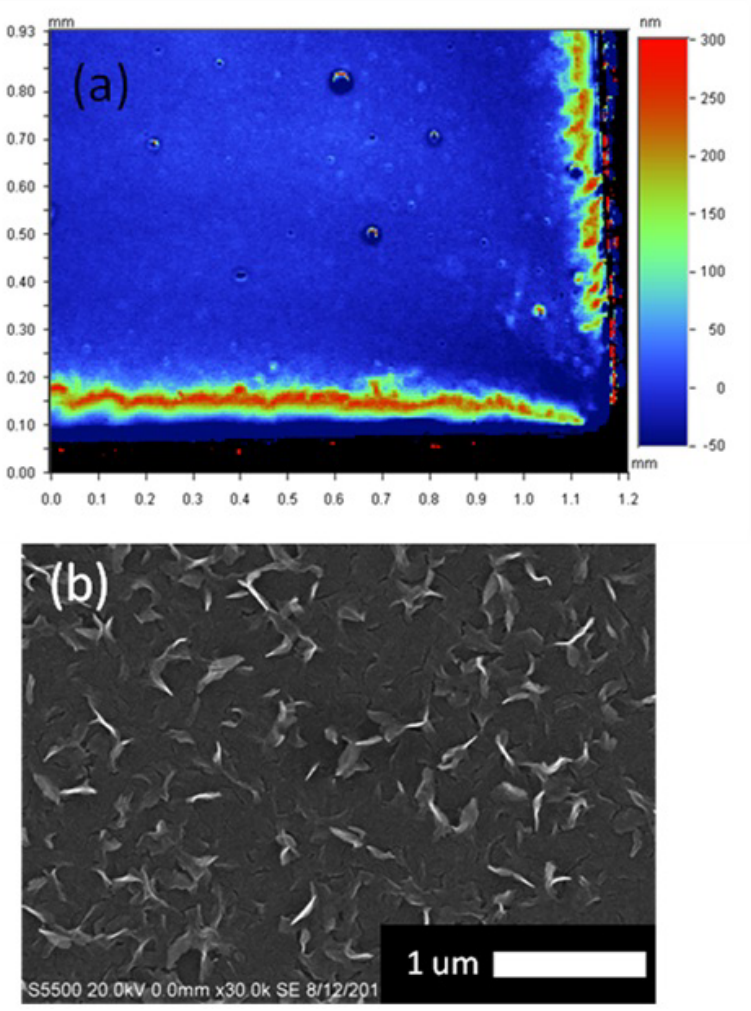

Figure 3.8: (a) WLP image of a substrate surface drop-coated 15 times (b) FESEM close to the edge of a substrate drop-coated 5 times.

When the film morphology at the sample edge (figure 3.8 (a)) is compared to the morphology from the bulk of the substrate (figure 3.8 (b)), it is clear that the rate of material deposition or aggregation is substantially higher at the substrate edges than at the centre of the sample. It can also be seen from the WLP in figure 3.8 (a) that this peak deposition / aggregation region occurs slightly away from the substrate edge. The question then arises if this edge effect can be understood in terms of the chemical pathway identified with the XPS analysis or if this is an indication of a second deposition process occurring which is unique to the edge region.

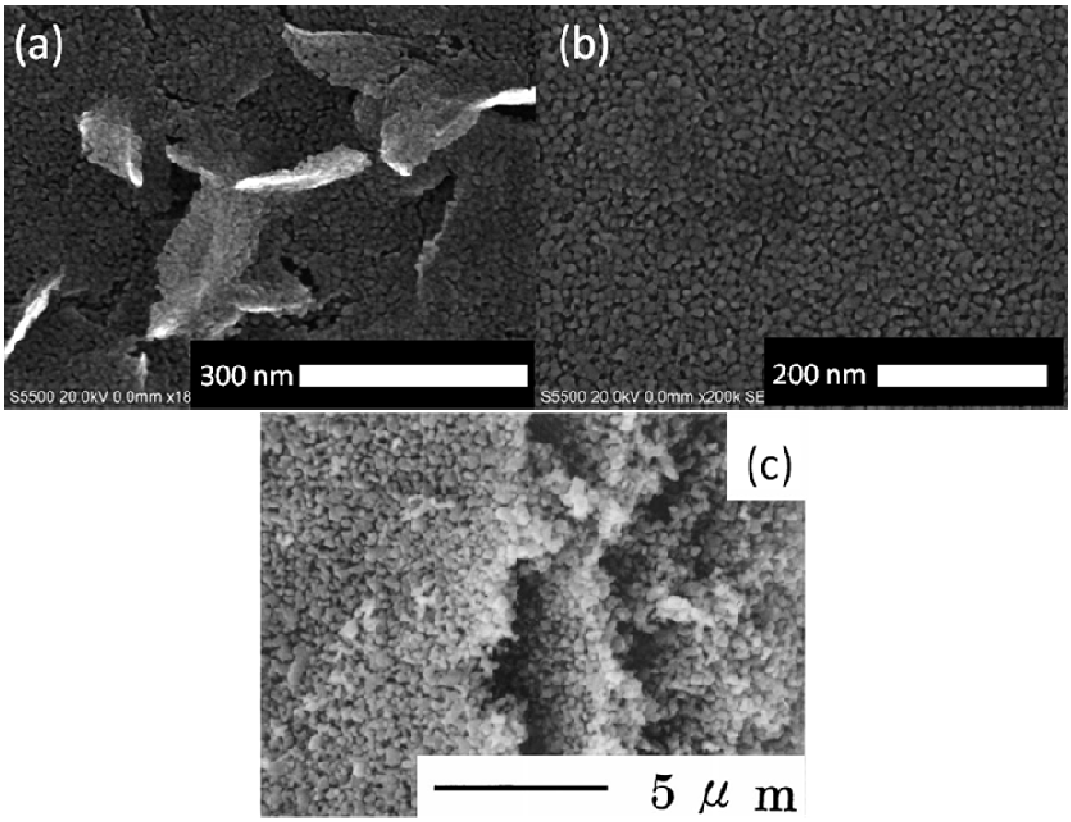

Figure 3.9: FESEM image of a substrate drop-coated 5 times at (a) the thick edge region (b) the substrate centre. (c) A ZnO film derived from thermal decomposition of layered basic zinc acetate. Reproduced from reference 26. Copyright: (1999) Springer Science & Business Media

The first point to consider is the similarities of the films found at the substrate edge and the substrate centre. While the centre consists of one to two layers of seed crystallites as previously described, the edge mounds appear to consist of the same or very similar crystals only stacked and fused into much larger irregular structures. This would suggest that the chemical origin is the same, and that residual zinc acetate is not a dominant factor,

albeit zinc acetate having some contribution cannot be definitively excluded. In particular, the formation of a layered basic zinc acetate (LBZA) type compound may have some contribution. While the thick edge layer shown in figure 3.9 (a) appears to be composed of small crystallites similar to those detected by AFM for the sample centre, the edge also bears some visual similarities to LBZA derived ZnO films (figure 3.9 (c)) produced by Morioka *et al.*[26] This similarity may be coincidental, or, despite not being detected in C1s region of the XPS spectra,[19] an indication that a small amount of LBZA is being produced at the substrate edges while the ethanol is evaporating.[27]

The next point to consider is the physical process of deposition. The native oxide on silicon is hydrophilic, and will therefore have a small contact angle, as is clearly the case given that 3 - 4 µl is sufficient to wet 1 cm^2 of substrate. Once the drop of ethanol has been applied to the surface it rapidly covers the entire area, forming a dome shape as shown in the schematic diagram in figure 3.10.

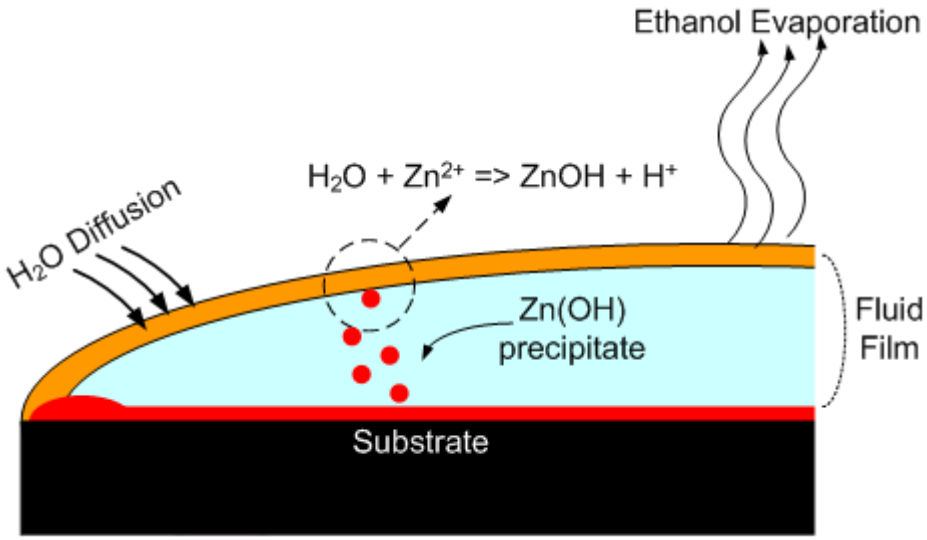

Figure 3.10: Schematic representation of the drop-coating process where the zinc acetate solution is shown in blue and the water rich region of the zinc acetate solution is shown in orange.

As the zinc hydroxide forms it begin to precipitate towards the substrate. One would then expect that the reduced distance from the air / liquid interface to the substrate would result in a more rapid build up of deposits at the substrate edges, which may in part explain the additional material build up at the substrate edge. However the assumption in this model is that the surface tension is constant and does not vary over the period that the

drop is allowed to remain on the surface. Furthermore, this description would suggest that the film is stagnant during the drop-coating process and that the crystallites reach the substrate surface by diffusion. However, it is well known that a fluid film under many conditions is not stagnant but may have turbulence or convective flows introduced by anisotropic conditions within the film itself or its surrounding environment, which is typically ascribed to a Marangoni type effect. This effect has been of interest for some time,[28] as it introduces complications in many processing applications such as electronics processing,[29] dip-coating,[30] spin coating,[31] and has even recently been used as a self assembly method for nanostructures.[32-33] Originally, this effect was observed in wine where a thin film of fluid was seen to defy gravity and run up the side of a glass. It has been recognised that the origin of these convective flows originates in the variation of the surface tension of a fluid system.[34] This variation in surface tension may be within the film or surrounding environment and has been studied for many different systems from coffee-cup stains to inkjet printers.[35-36] The question then arises as to whether this effect may be present during the drop-coating process used in this work and if it could be contributing to the seed layer film non-uniformity. While the drop-coating process may seem facile, from a fluid dynamic perspective it is extremely complex as many factors are occurring simultaneously. Consequently the process will only be discussed qualitatively with parallels drawn to similar systems.

While the ethanol film is on the substrate, the fluid interface is pinned to the substrate edges and the ethanol is evaporating. The volume of ethanol removed from the fluid film is greater near substrate edges as this region has a greater surface area. The evaporation of ethanol reduces the film volume.[35] However given that the ethanol is pinned at the substrate edges the contraction takes place in the film height. This difference in contraction, induced by the varying rate of evaporation between the centre and edges creates a geometric constraint, which is relieved by supplying additional fluid to the edge region from the bulk of the fluid film, leading to an outward flow of fluid from the drop centre to the edge region. This outward flow is strong enough to carry suspended particles outward in the convective fluid flow.[34] Secondly while the solvent is evaporating the concentration of dissolved zinc acetate will increase in the air / liquid region. Increased salt concentrations increases the surface tension,[37] thus there will be a second gradient between the thick bulk area of the fluid film and the edge region. Similar to the tears of

wine problem,[34] the surface tension gradient leads to a flow from the film centre outward to where the concentration of dissolved salts is higher.

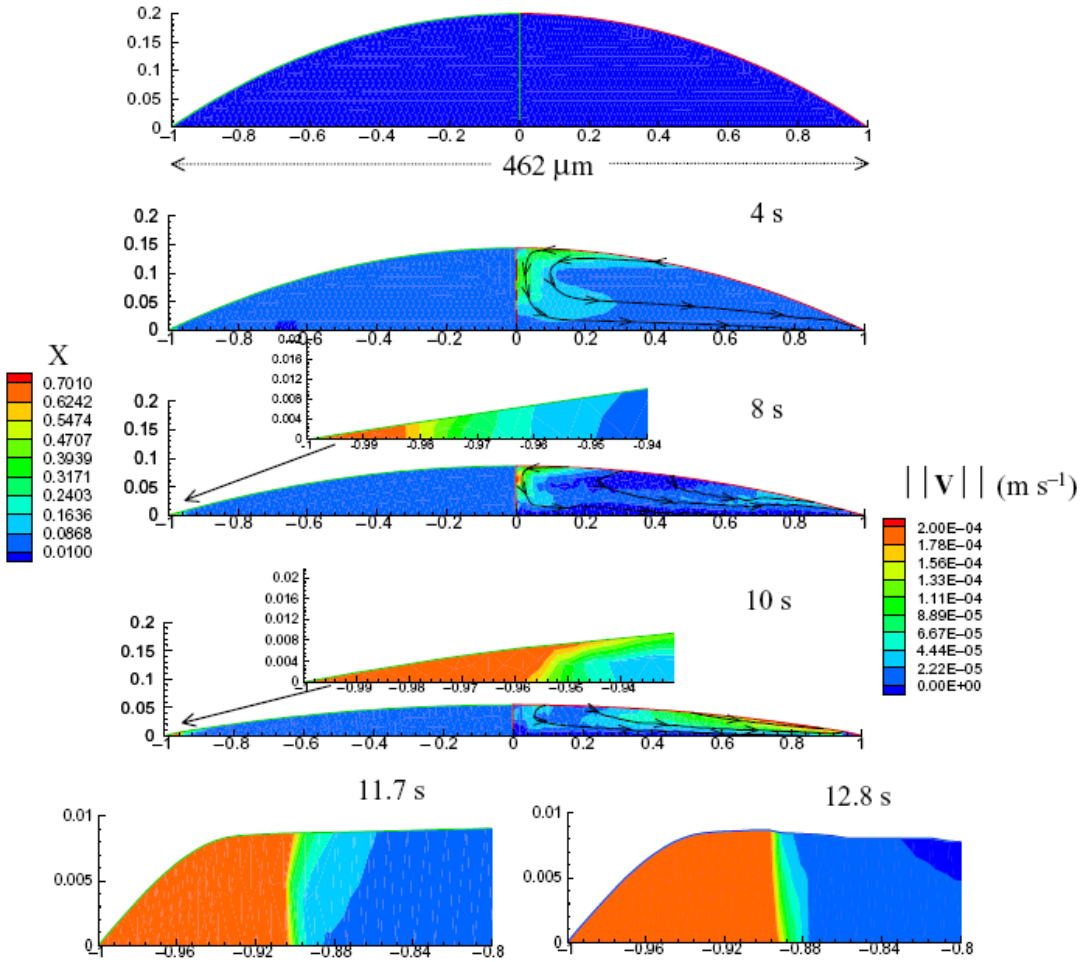

Figure 3.11: Results of a computer simulated model of an evaporating sol droplet on a surface, showing the particle density as a colour gradient and the evaporation induced Marangoni flow as the black lines. Reproduced from reference 32. Copyright: (2009) Institute of Physics & IOP Publishing

During the drop-coating process, water from the surrounding air is also being absorbed into the solution. As the same geometric conditions related to the surface area between the substrate centre and edge apply, the absorbed water also results in a surface tension gradient which would be expected to cause a Marangoni flow. However, the situation is more complex as the water reacts with the zinc ions yielding a zinc hydroxide precipitate and acetic acid. The diffusion of the reactive water front propagating through the liquid film can be deformed by the Marangoni flows present or induced by the products of the

reaction.[38] The consumption of reactants, in this case zinc acetate can also induce flows from the concentration gradient and the products of the reaction can also influence the surface tension. Consequently accurately describing the effect of a chemical front propagating through a solution is complex task. In the models proposed by Rongy *et. al*, in reactive systems, both steady state flows and convective roles can be induced in the fluid, but also more complex behaviour such as vortexes may occur.[38]

Despite the complexity of the system, what is clear is that there are several factors that can lead to the formation of convective flow within the ethanol film, and that these flows lead to an uneven distribution of particles suspended in the solution. The effect on the distribution of the zinc hydroxide crystallites is similar to the model reported by Bhardwaj, where convective flows carries the particles to the substrate edge prior to deposition.[32] An extract of this model can be seen in figure 3.11, which shows the build up of the colloidal particles at the film edge, which was subsequently confirmed by their experimental work. During the drop-coating process the newly formed crystallites coat the entire substrate, however convective flows, the origins of which are due to some or all of the aspects discussed above, results in an additional build up of particles along the substrate edge.

3.5 Chemical Bath deposition

In this work three different growth techniques were examined, as described in chapter 2 section 2.4. Aqueous routes to ZnO deposition have distinct advantages compared to high temperature techniques. Generally the need for specialised equipment and techniques are negated, while it has been demonstrated that a wide morphological variety of nanostructured ZnO deposits can be achieved.[3] The first and most commonly used technique in this work was the HMT based reaction. It has been known for some time that HMT can be used in conjunction with zinc salts to precipitate needle-like ZnO.[39] In 2001 Vayssieres *et al.* reported on the precipitation of ZnO from an aqueous solution of zinc nitrate and hexamine demonstrating that aligned nanorods could be grown on various substrates using the nitrate/HMT system.[2, 40] The reaction chemistry was based on the thermal decomposition of hexamine which then reacts with the Zn^{2+} ion to form ZnO. The precise role of hexamine has been difficult to determine. Hexamine is a highly water soluble cyclic tertiary amine which can form complexes with zinc ions. At elevated

temperatures hexamine decomposes to form ammonia and formaldehyde. Ammonia in solution can form complexes with Zn^{2+} while a portion of the ammonia also deprotonates water to form hydroxide ion species. Hydroxide ions readily react with Zn^{2+} to form zinc hydroxide. This complex behaviour has been investigated by Ashfold *et al.* who identified the major chemical reactions taking place and illustrated the complexity of the system by producing a speciation diagram, shown here in figure 3.12.[41]

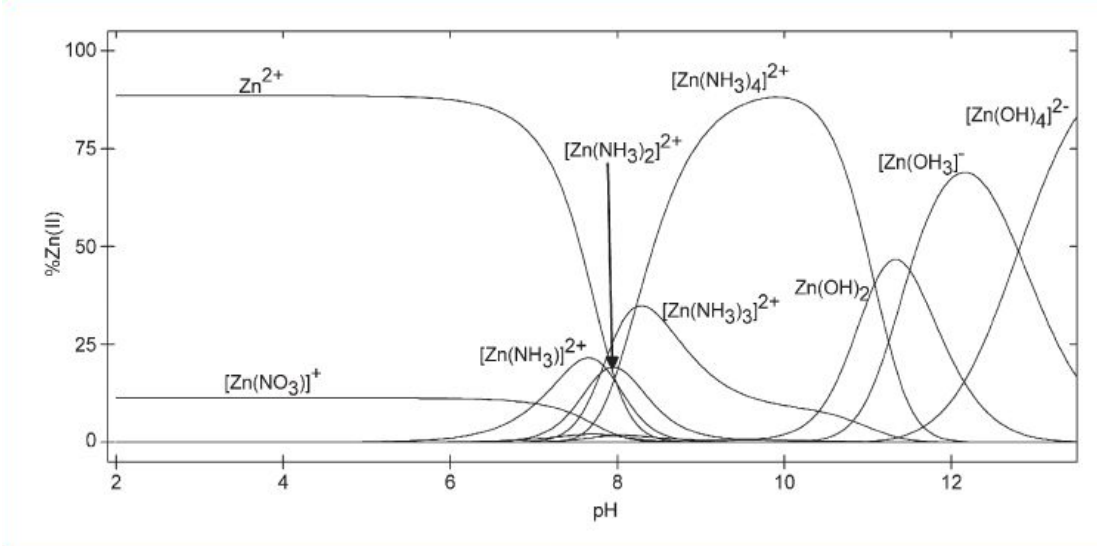

Figure 3.12: Speciation diagram showing Zn^{2+} present in a hexamine solution and the dependence on the solution pH. Reproduced from reference 41. Copyright: (2007) Elsevier.

The general reaction chemistry during chemical bath deposition is described by the following steps. At high temperature hexamine decomposes to form ammonia and formaldehyde, given by:

$$C_6H_{12}N_4 + 10\ H2O \rightarrow 6CH_2O + 4NH_4+ + 4OH^- \quad (3.5.1)$$

Then a hydroxide ion reacts with the Zn^{2+} ion to form zinc hydroxide which then further reacts to form ZnO and water:

$$Zn^{2+} + 2OH^- \leftrightarrow Zn(OH)_2 \leftrightarrow ZnO + H_2O \quad (3.5.2)$$

The hydroxide ion can also react with the Zn^{2+} ion to precipitate ZnO as described by reaction 3:

$$Zn^{2+} + 2OH^- \leftrightarrow ZnO + H_2O \qquad (3.5.3)$$

Ashfold *et al.* proposed that the reaction takes place by both mechanisms. In contact with the substrate the less stable phase will precipitate first. In the initial stage of the reaction the pH and concentration of Zn^{2+} ions favour the precipitation of ZnO via the hydroxide intermediate.[41] As the reaction continues, the pH increases due to the continued decomposition of hexamine and release of OH^- ions. This increase in pH redissolves the $Zn(OH)_2$ and the deposition of ZnO proceeds via the direct formation of ZnO described equation 3.5.3.

While the decomposition of HMT is widely regarded to be the driving force of the ZnO growth in chemical baths, other research groups that have attempted to monitor *in-situ* the decomposition process have reported contradictory evidence and have suggested the role of hexamine is that of a chelating agent, binding to the surface of ZnO crystals to promote wire-like growth.[42] Sugunan *et al.* found that when monitoring solutions of hexamine using attenuated reflectance mode Fourier transform infrared spectroscopy, no significant decrease was observed in the hexamine C-N vibrational signal at ~1012cm^{-1}. Despite this work, no convincing alternate mechanisms have been proposed.

The second chemical bath technique investigated was based on the work of Peterson *et al.* [43] In this technique sodium hydroxide is used as the source of OH^- ions. By careful control of the solution pH, a metastable zinc hydroxide solution is generated. When hydroxide ions are added to an excess of a dissolved metal salt, the corresponding hydroxide salt is formed. In the case of Zn^{2+}, the corresponding hydroxide salt is poorly soluble in water and a $Zn(OH)_2$ precipitate is quickly observed. Increasing the pH of the solution further by the addition of excess NaOH redissolves the precipitate, forming $Zn(OH)_4^{-2}$ ions. Submerging a seeded substrate into a solution of $Zn(OH)_4^{-2}$ the seeds act as nucleation sites for the dehydration of $Zn(OH)_4^{-2}$ into ZnO. While the growth procedure is more simplistic, the mechanism behind the growth is complex. Li *et al.* have investigated this issue and have identified factors which explain the preferential *c*-axis growth in this system.[44] Central to their argument is the idea of growth units. The growth units are ionic

species which can be incorporated into the crystal lattice before the final dehydration reaction. In the system proposed by Peterson similar mechanisms are suggested with the growth unit as follows:

$$[Zn(OH)_n]^{2-n} + [Zn(OH)_n]^{2-n} \leftrightarrow [Zn_2O(OH)_{2n-2}]^{4-2n} + H2O \quad (3.5.4)$$

By binding the growth unit to the ZnO seed layer surface, the activation energy for the conversion of the growth unit to ZnO is reduced. A desirable feature of this reaction process is the lack of any other precipitates as the structural fit of the growth unit is only incorporated at the seeded surface. The growth of zinc oxide takes place only at the surface of the seeded substrate. This presents a distinct advantage over the HMT based system, where the solution contains a significant proportion of precipitates which must be subsequently removed from the nanorod array.

In the third technique, the direct decomposition of zinc acetate by forced hydrolysis was used to deposit columnar thin films.[3, 45] In this technique a source of hydroxide ions is not used and the reaction proceeds in a similar chemistry to the drop-coating chemistry described in section 3.2. An aqueous solution of zinc acetate is heated at 60 – 70°C, which results in the hydrolysis of the acetate salt to yield zinc hydroxide, which subsequently decomposes into ZnO as given by the equations:

$$Zn(OCCH_3)_2.2H_2O \rightarrow Zn^{2+} + 2(O_2CCH_3^{-1}) + 2H_2O \quad (3.5.5)$$

$$2(O_2CCH_3)^{-1} + 2H_2O \leftrightarrow 2HOOCCH_3 + 2OH^{-1} \quad (3.5.6)$$

$$2OH^{-1} + Zn^{2+} \rightarrow Zn(OH)_2 \quad (3.5.7)$$

$$Zn^{2+} + 2OH^{-} \leftrightarrow Zn(OH)_2 \leftrightarrow ZnO + H_2O \quad (3.5.8)$$

This technique has the distinct advantage in that the reaction solution and conditions required are particularly mild, allowing substrates that are sensitive to bases to be used.

For applications such as field emission and solar cells control of ZnO nanorod aspect ratio is an important parameter.[46] Control of aspect ratio can be achieved through the use of cationic surfactants. Recently groups have demonstrated that the addition of polyethyleneimine during CBD deposition can be used to control the aspect ratio of nanorods grown.[47-48] Polyethyleneimine (PEI) is a water soluble, non polar polymer containing a large amount of amino groups. Branched PEI contains a mixture of primary, secondary and tertiary amino groups which can be protonizated over a wide range of pH values.[48] The positively charged PEI molecules are adsorbed on to lateral facets of the ZnO nanorods by electrostatic attraction as the lateral facets become negatively charged at elevated pH.[48] The long polymer chain of the PEI molecule adsorbed onto the nanorods, effectively screen the lateral facets from further growth. This technique has been used to boost the aspect ratio of ZnO nanorods to over 100.[47] In this work, the use of PEI as a potential route to high aspect nanorod arrays was assessed.

3.5.1 Growth of HMT CBD Nanorod arrays

The first method examined was the reaction based on the decomposition of HMT in the presence of zinc nitrate. As mentioned earlier, before analysing the seed layer deposition technique, the growth of ZnO nanorods using this technique was very unreliable. When the factors identified in sections 3.2, 3.3 and 3.4 are taken into account, it was found that ZnO nanorods readily grew on non-epitiaxially matched substrates and on non-crystalline substrates. Depending on the growth conditions used, the morphology of the rods varied from fused columnar films to dense aligned nanorods. By carefully controlling the reaction conditions a uniform film of ZnO nanorods could be readily produced, with a consistent morphology. An example of such a nanorod array is shown in figure 3.13. After 30 minutes of growth the nanorods were typically 300 – 400 nm in length with a diameter of ~50 nm with a rounded tip giving the rods a bullet shape. It was found that several factors influenced the morphology of the nanorods including the solution temperature, the concentration of reactants and the point at which the seeded substrate were placed into the solution. At higher HMT concentrations the diameter of the nanorods

decreased. A reduction in nanorod diameter also occurred when the samples were inserted into the reaction solution once it had reached the target reaction temperature range of 80 to 90°C. When the samples were inserted into the reaction solution before heating, it was found that the average rod diameter increased. A lower reaction temperature also leads to an increase in the average nanorod diameter. In all of these cases it appears that the diameter of the rods depends heavily on the concentration of the reactants, particularly the hydroxide ions. However others have reported that the hexamine also has an important role as it is preferentially adsorbed onto the lateral facets of the growing rods, screening them from further growth.[42]

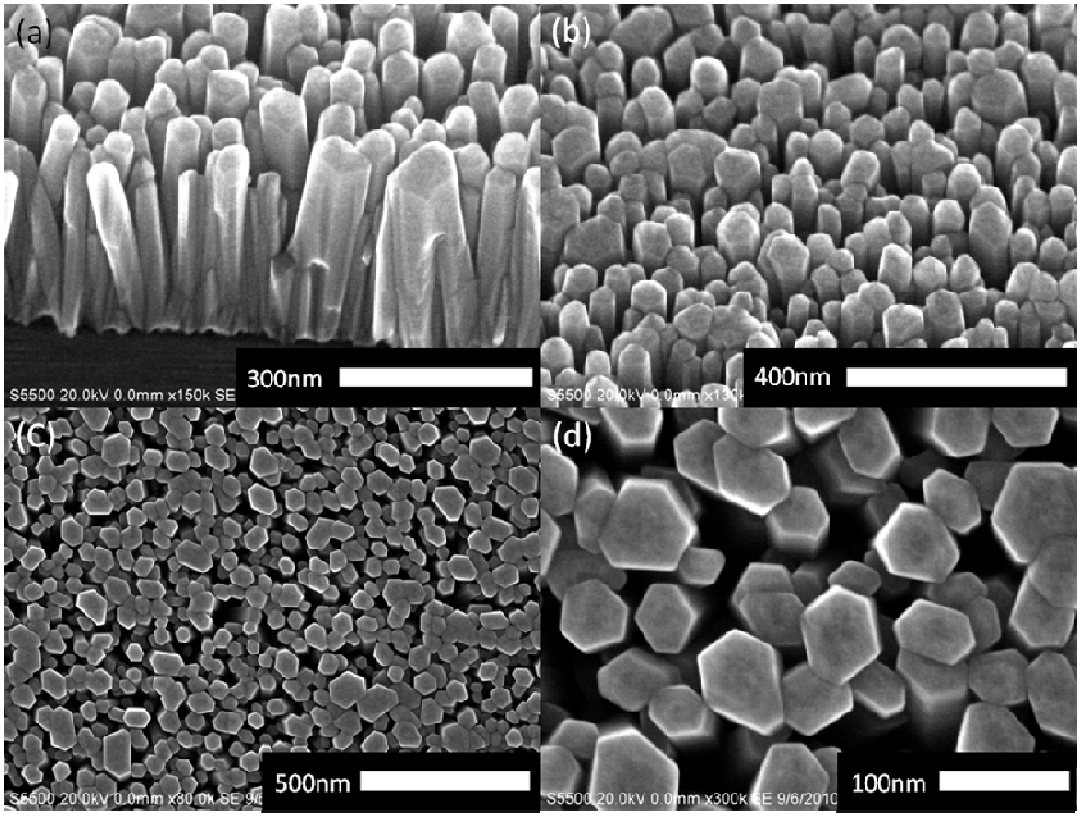

Figure 3.13: FE-SEM images of a HMT CBD nanorod array (a) along a freshly cleaved edge (angled at 30°) (b) at the centre of the sample (angled at 30°) (c) plan view of the nanorod array (d) higher magnification plan view clearly showing the hexagonal shape of the nanorods

Previously it has been recognised that both the temperature and degree of solution supersaturation influence the morphology of ZnO crystals grown by CBD. Vergés *et al.* observed distinct differences in the morphology of ZnO nanorods grown at different temperatures in the zinc nitrate-HMT system.[39] At lower temperature (~78°C) the ZnO

growth had larger diameters and lower aspect ratios. Using higher temperatures and maintaining all other factors equal, the rods had sharper needle-like morphology, with narrower diameters and higher aspect ratios. By examining the precipitates at various stages during the growth process (while maintaining the temperature constant) it was apparent that an orientated attachment process was taking place, with spherical homogeneous nucleated particles aligning along their *c*-axis and joining to form single crystal ZnO rods. Similar behaviour has also been demonstrated by Pacholski *et al.* where ZnO quantum dots when aged under reflux underwent a orientated attachment process to form single crystal ZnO rods.[49] Further examination by Govender *et al*. identified different growth mechanisms depending on the solution supersaturation. At low solution saturations, heterogeneous nucleation is dominant and crystal faces develop via an outward spiral mechanism from screw dislocations. As the supersaturation increases homogeneous nucleation becomes more important. At an intermediate supersaturation, clusters begin to nucleate on ZnO crystal faces, leading to a 2 dimensional growth. As the saturation level increases further, the growth process becomes dominated by homogeneous nucleation and orientated attachment, leading an increase in the roughness of the lateral facets and continuous linear growth predominantly along the *c*-axis. In our experiments, the seeded substrate is inserted into the reaction solution before any heating take place. Therefore both the initial temperature and supersaturation is low. The solution is brought to the desired reaction temperature, which results in an increase in the supersaturation from its initial low starting point. During this heating step, the solution passes through the different saturation levels responsible for the different growth mechanisms. Initially the saturation and temperature is low which leads to lateral growth via either the homogeneous spiral dislocation growth or heterogeneous cluster nucleation process. However, given that no evidence of extended defects were observed in the base of the nanorods, such as screw dislocations, it is more likely that outward growth takes place via cluster nucleation along the ZnO facets. As the reaction proceeds and both the temperature and supersaturation increase, the growth mode shifts towards linear one dimensional growth along the c-axis.

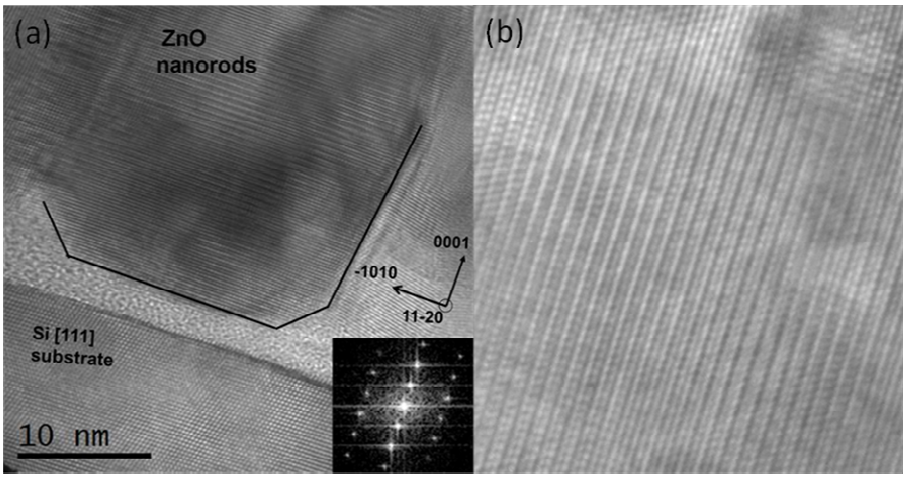

Figure 3.14: (a) HRTEM image of HMT CBD grown nanorod showing the amorphous SiO2 interface and inside its corresponding Fast Fourier transform (FFT) confirming growth direction and Wurtzite structure. (b) Increased magnification HRTEM image of the HMT CBD nanorod shown in (a) (Images acquired by UCA Cadiz collaborators)

As can be seen from the HRTEM image in figure 3.14 (a), at the base of the nanorod there is an initial increase in rod diameter. The CBD nanorod growth begins with a narrow diameter, typically around 15 nm, probably corresponding to the diameter of a single underlying seed particle. In the early stages of growth the rod diameter increases. This transition occurs within the first 10 nm of growth, after which the rod diameter appears to remains constant. Given that the transition to constant diameter occurs after only 10 nm, it suggests that the growth rate during this heating up phase is significant slower.

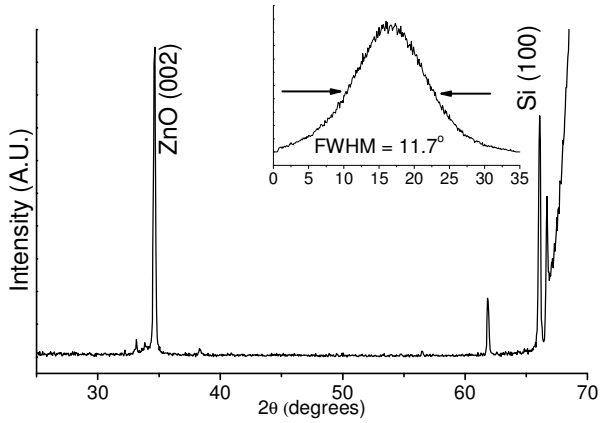

Figure: 3.15: XRD 2 θ / ω scan of HMT CBD grown nanorod array on Si (100). (insert) XRD rocking curve of the peak located at 34.4° corresponding to the ZnO (002) plane.

As seen from the HRTEM image in figure 3.14 (a) and (b), the rods deposited are of good quality with no indications of extended defects such as dislocations or twin planes. No significant variation in crystal quality has been observed between the base and the tips of the rods. The FFT of the HRTEM image confirm the rods are of the Wurtzite phase and that their long axis is aligned along the *c*-axis. The hexagonal Wurtzite structure is also clearly visible in the FE-SEM images shown in figure 3.13 (d). The structure and alignment is also confirmed by the XRD data shown in figure 3.15, where only one peak assignable to ZnO, located at 34.4°, is detected. This corresponds to the (002) plane of the ZnO Wurtzite phase (JCPDS card number: 36-1451), indicating that the nanorods are predominantly growing with their *c*-axis normal to the substrate. The rocking curve data of the peak located around 34.4° (figure 3.15 insert) has a full width half max (FWHM) of 11.7° degrees, suggesting that the nanorods are quite highly textured with respect to the substrate normal. While there are many reports of high quality aligned ZnO films/nanostructures grown by CBD or hydrothermal methods, few report the rocking curve FWHM for polycrystalline films on non-epitaxially matched substrates, making a direct comparison difficult. However a FWHM of ~11.7° is in broad agreement with results published by Wang *et al.* and Yang *et al.*[1, 50]

3.5.2 The effects of surfactants on HMT CBD growth

For applications such as field emission and solar cells the aspect ratio of the nanorods is an important parameter.[46-47] The deposition technique using zinc nitrate and HMT is limited in this regard. While the *c*-axis is the fastest growing axis, the lateral faces of the nanorods are also growing, albeit at a slower rate. This fact is demonstrated in figure 3.16. This sample was grown in two successive 45 minute, 25mM zinc nitrate / HMT baths. After the sample was transferred to the second bath, air bubbles trapped at the substrate surface screened some areas from further growth.

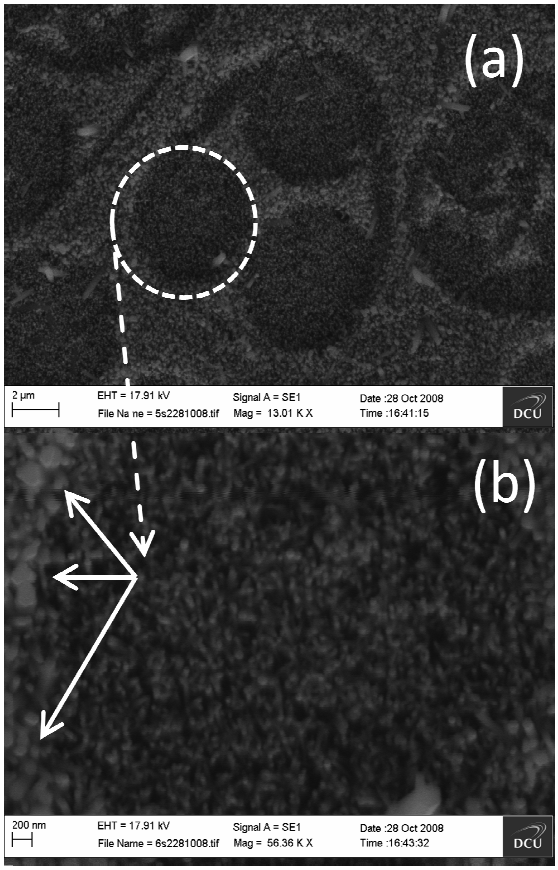

Figure 3.16: (a)Plan view of ZnO nanorods patterned during growth by trapped bubbles (b) higher magnification view of patterned area circled in (a). The patterned edge is indicated by blue arrows.

In figure 3.16 (a) the unusual patterns created by the bubbles can clearly be seen. Figure 3.16 (b) is a higher magnification of the region circled in 3.16 (a). The arrows in 3.16 (b) indicate the border between the bubble masked and unmasked regions. In the masked regions of the sample the nanorod growth appears shorter and also have much smaller diameters than areas where the second chemical bath deposition took place. There is evidence of nanorods merging to form thicker structures as the distribution of rod diameters in the unmasked regions is greater than in the masked regions. This can be more clearly seen in the unmasked region shown in figure 3.17 (a), where both individually hexagonally faceted nanorods and coalescing nanorods can be seen. In the masked region shown in figure 3.17 (b) the nanorod diameters are significantly smaller and show less signs of coalescence.

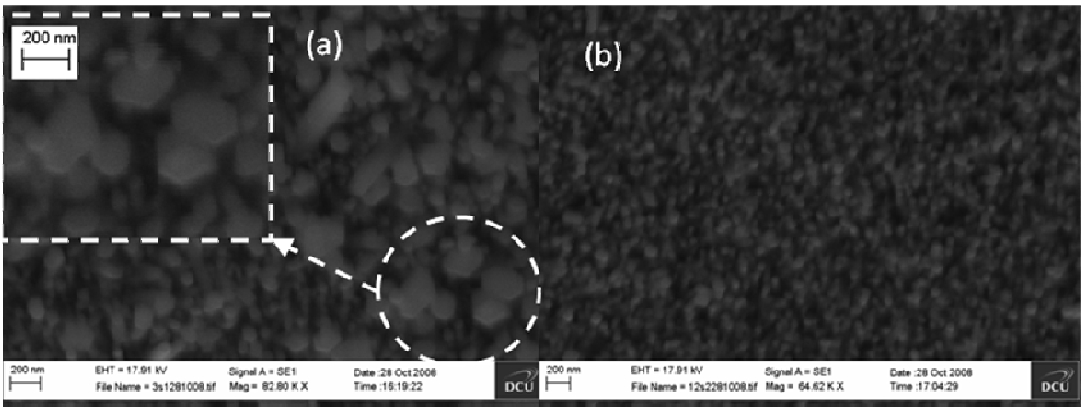

Figure 3.17: (a) Plan view of Zno nanorods grown in two successive 45 minute, 25mM zinc nitrate / HMT baths (b) Different area of the same sample where growth in the second bath was prevented by trapped bubbles.

This is direct evidence that as the deposition time is increased, the nanorod diameters slowly increase, merging into neighbouring nanorods until a dense columnar ZnO film is formed. Similar observations have been reported by Govender *et al.*, who observed an increase in aspect ratio as growth times were increased from 2 minutes to 2 hours. After this time, the aspect ratio of the nanorod arrays decreased as the array became more film-like.[3] The use of surfactants, specifically PEI, to counteract film formation during extended growth times with multiple bath changes was examined. Samples were deposited with or without the addition of PEI to the reaction solution maintaining identical conditions for all other reaction parameters. A summary of the deposition results is presented in table 3.1, and SEM images of the deposited rods with varying aspect ratios can be seen in figure 3.18.

Sample	Growth time (Hours)	PEI concentration (mM)	Average length (nm)	Average diameter (nm)	Aspect ratio
A	6.5	0	3000	400	6.5
B	2.5	0	500	140	3.5
C	6.5	5	800	50	17
D	2.5	5	450	50	9

Table 3.1: Summary of the dimensions and aspect ratios for nanorods grown with or without the addition of PEI, keeping all other deposition parameters identical.

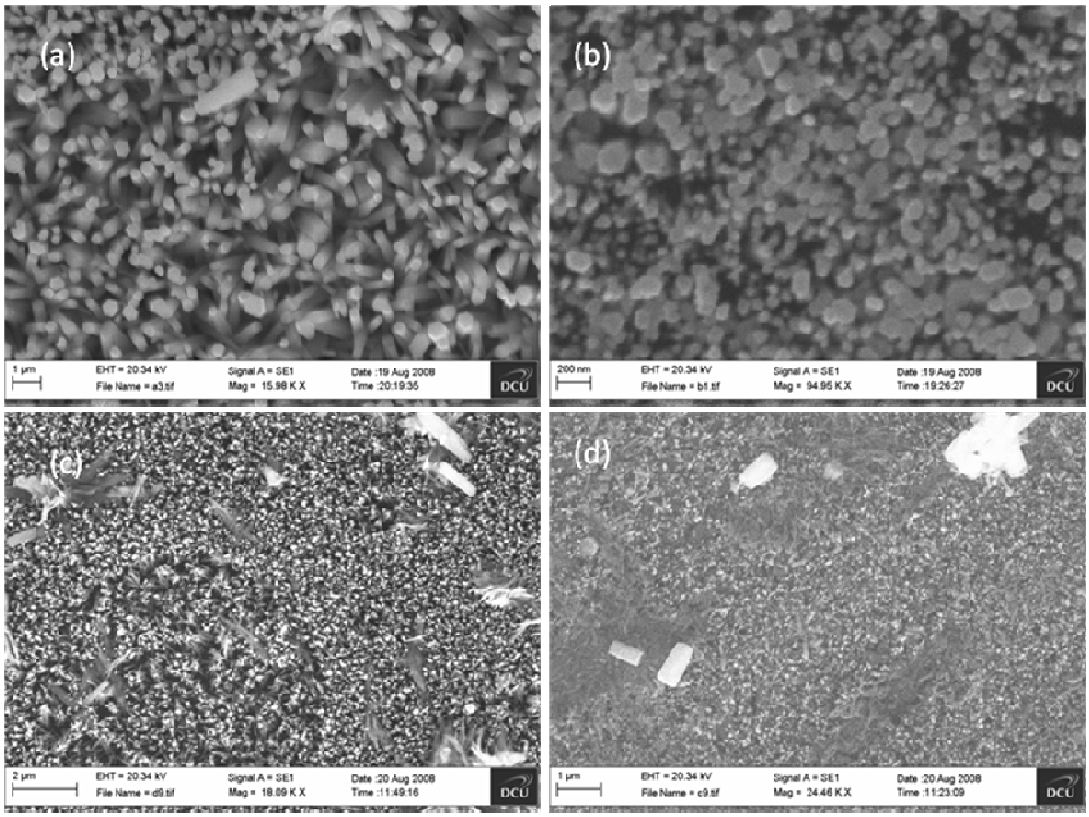

Figure 3.18: Plan view of nanorods deposited for (a) for 6.5 hours with out any PEI (b) 2.5 hours without any PEI (c) 6.4 hours with 5mM PEI (d) 2.5 hours with 5mM PEI

The addition of PEI reduces the growth of the lateral facets of the nanorods for both short growth periods and for extended periods. Both samples to which PEI was added had higher aspect ratios than those samples that were deposited without PEI. The diameters of the nanorods grown for 6.5 hours were strikingly different, with a variation in diameter of over 300 nm. Without the addition of PEI, rod diameters grew with deposition time until they were several hundred nanometers, while the increase in nanowire diameter in samples deposited with PEI was negligible. The addition of PEI also reduced the rate of *c*-axis growth. After 6.5 hours the nanorods grown with PEI are less than half the length of those samples grown without PEI. Zhou *et al*. proposed that this reduction in rod length is the result of Zn^{2+} coordination complexes forming with the PEI molecule, reducing the Zn^{2+} concentration.[48] The reduction in *c*-axis length can be compensated for by prolonging the growth time further with regular bath changes to replenish the reactant concentrations. Nanorods with aspect ratios over 100 have been achieved in this manner.[47]

3.5.3 Origin of *c*-axis alignment

The origin of the *c*-axis alignment is a crucial factor in the CBD deposition process because, as will be seen in chapter 4, the initial nanorod alignment is continued through to rods grown by CTR-VPT. It is therefore important to understand the origin of the alignment. Originally it was reported that the seed layer was the principle factor leading to *c*-axis alignment.[5] TEM and XRD analysis of the seed layer produced by drop-coating identified that the seeds are flat platelets with their *c*-axis perpendicular to the large platelet face and that the platelets generally lie flat (i.e. large basal plane parallel) to the substrate surface, regardless of the substrate details, assuming it is reasonably flat itself.[5] In contrast seed layers prepared from ZnO sols showed multiple ZnO XRD peaks, indicating that they when deposited on substrates they typically had a random orientation. This analysis is consistent with our results, in that nanorods grown on sol derived seed layers showed poorer *c*-axis alignment with respect to the substrate as compared to those prepared from drop-coating the acetate solution. This can be seen clearly by comparing figure 3.1 (b) (sol derived seed layer) with 3.13 (a) (acetate derived seed layer). Surface profile analysis of the AFM images, shown in figure 3.6, also confirm the reported dimensions of the crystallites to be flat platelets.

There are however, strong indications that this natural orientation of the crystallites is only partially responsible for the *c*-axis orientation. As mentioned previously, when the density of crystallites is low, multiple rods can nucleate on a single crystal, leading to a complete loss of alignment of the rods, as shown in figure 3.1 (a) and reported in reference 4. When the seed layer density is high the rods are better aligned, but may have some tilt with respect to the substrate, as can be seen by the relatively high FWHM of the rocking curve, as compared to single crystals or epitaxially grown nanostructures.[51-52] This tilt can also be clearly seen in figure 3.13. Both of these facts suggest that although the orientation of the seed crystal is important, spatial confinement is also an important factor in the *c*-axis alignment.

When the seed layer has a low density of nucleation sites, alignment is lost through the multi-rod nucleation process. At higher seed layer densities the rods appear better aligned with respect to the substrate but still have some degree of tilt. The drop-coating is a stochastic process, with zinc hydroxide crystallites forming randomly in the zinc acetate solution and precipitating onto the substrate surface. Subsequently, during annealing the

hydroxide precipitate decomposes to form hexagonal ZnO flat platelet-type seeds in a textured layer on the substrate with *c*-axis predominantly normal to the substrate. However, there remains some variation in both the thickness and degree of *c*-axis alignment of the seed layer crystals because of the overlapping of seeds, especially in areas of increased seed density. The effect can be likened to dropping a deck of playing cards on a flat surface. The majority of cards will lie flat, but some overlapping and tilting will be seen where many cards land in the same region.

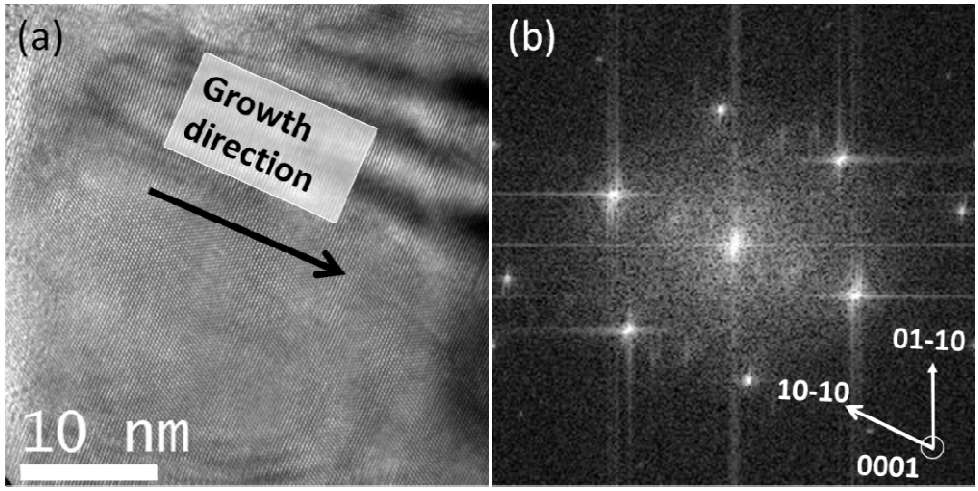

Figure 3.19: (a) HRTEM image and (b) corresponding FFT or a ZnO CBD deposited nanorod growing with its' (10-10) axis perpendicular to the substrate normal. (Images acquired by UCA Cadiz collaborators)

During the CBD growth the nanorords follow the initial alignment of the seed crystal. However as the growth progresses, (with the fastest growth direction generally along the *c*-axis) the rods become larger and they begin to push against each other forcing the *c*-axis closer to the substrate normal to reduce strain effects. The spatial confinement effect also leads to rod coalescence, as can be seen in figure 3.13 (d). When the rods are tilting away from their neighbours into a void in the nanorod array, the rods typically have a perfect hexagon shape with each side having an equal length. When the rods are pushing against each other the side length is greater along the free side as compared to the confined side. Clear evidence of this spatially confined orientation was found during the TEM analysis of the CBD deposited nanorods. While most rods grew along their *c*-axis, some rods were found to be growing along other axes, an example of which is shown in figure 3.19. The rod shown is growing with its (10-10) axis perpendicular to the substrate normal, a clear indication that the *c*-axis was so mis-orientated with respect to the

substrate that the spatial confinement effects were overcome and the rod growth predominantly took place along the [10-10] axis.

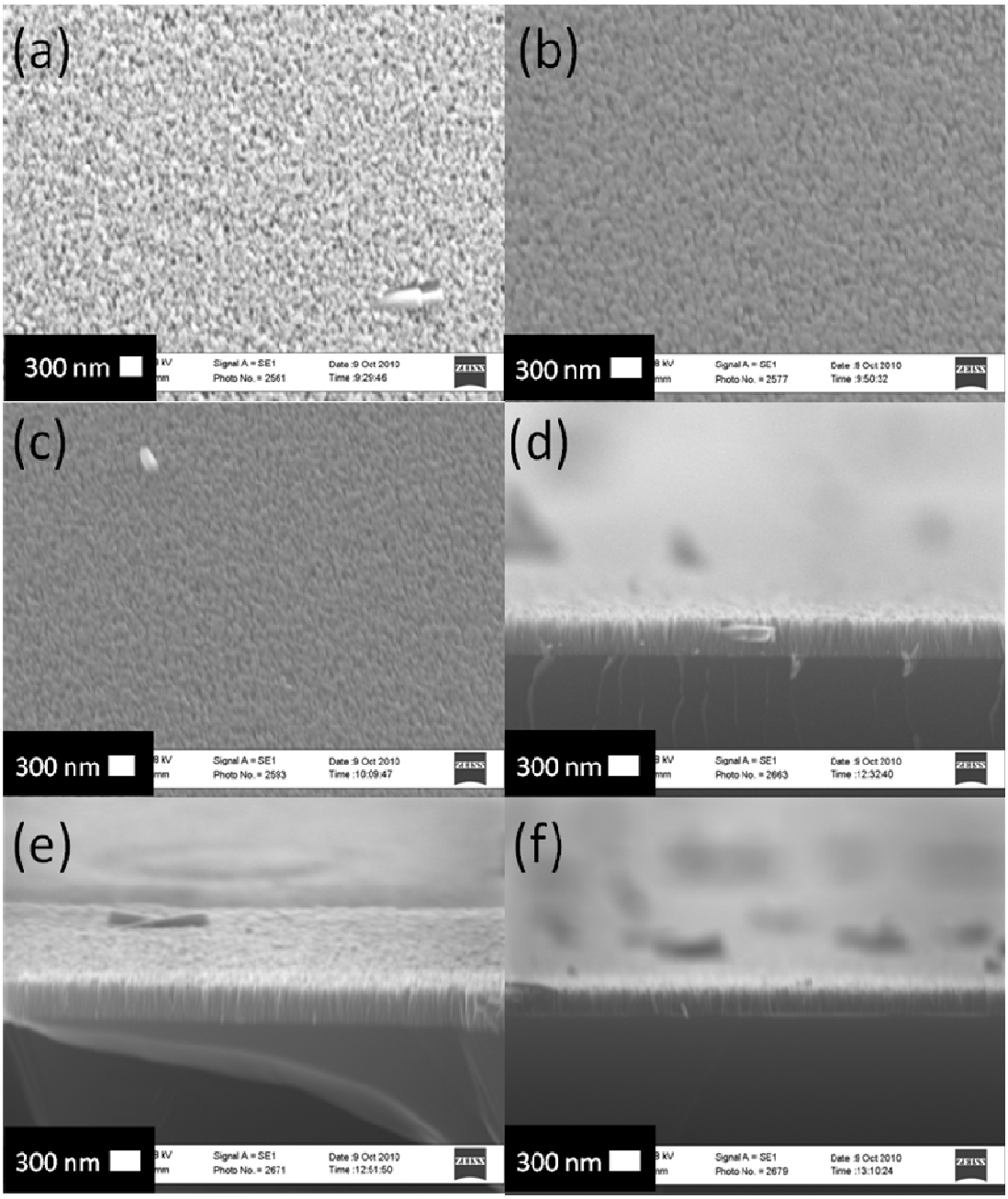

Figure 3.20: (a) Plan view of CBD sample grown on 3 drop-coat seed layer (b) Plan view of CBD sample grown on 5 drop-coat seed layer (c) Plan view of CBD sample grown on 7 drop-coat seed layer (d) 90° view of CBD sample grown on 3 drop-coat seed layer (e) 90° view of CBD sample grown on 5 drop-coat seed layer (f) 90° view of CBD sample grown on 7 drop-coat seed layer

To further understand the effect of density and confinement of the nanorod growth, samples were prepared with varying number of drop-coats from 3 to 5 to 7, as shown in figure 3.20. From examining the plan views of the samples shown in 3.20 (a), (b) and (c) it is clear that all three samples show complete coverage of nanorods. On closer inspection, while all the samples are all uniformly covered, sample (a), corresponding to the least number of drop-coats (3), appears to have a larger number of voids and gaps between nanorods. Fewer or less inter-rod gaps are visible in the sample drop-coated 5 times. However due to resolution limits of our SEM, it is difficult to see if the inter-rod gaps are reduced in sample (c) as compared to sample (b). 90° views of all three samples show that all three samples are composed of similar morphology, however it appears as if the rods of the sample drop-coated 3 times, shown in image (d) are less well aligned and better separated that those in image (e) and (f), again confirming the importance of the spatial confinement on the *c*-axis aligned CBD growth.

3.5.4 NaOH and Acetate based CBD nanorod arrays

As will be discussed in more detail in chapter 5, the use of HMT based nanorod arrays presented specific difficulties for depositing positional controlled *c*-axis aligned ordered arrays. In brief, the roughness of the CBD surface and the large mass of precipitates inhibited the deposition of ordered arrays. Consequently other CBD deposition techniques were investigated in an attempt to overcome these difficulties. The use of HMT during ZnO rod growth leads to a large mass of precipitate. As the pH rises zinc hydroxide quickly become supersaturated and precipitates as an amorphous gel from the reaction solution. This material can become trapped on the surface of the nanorod array, as seen in figure 3.21. If the nanorod array is sufficiently dense, with a small inter-rod distance, the precipitate sits mainly on top of the surface of the nanorods and is easily removed by washing post deposition. When the nanorod density is reduced, the reaction precipitate becomes embedded in the nanorod array and becomes difficult to remove without damaging the underlying array. When low density nanorod arrays such as those described in chapter 5 are required, the presence of these precipitates is a nuisance. To overcome this problem the use of a precipitate-free reaction was investigated.

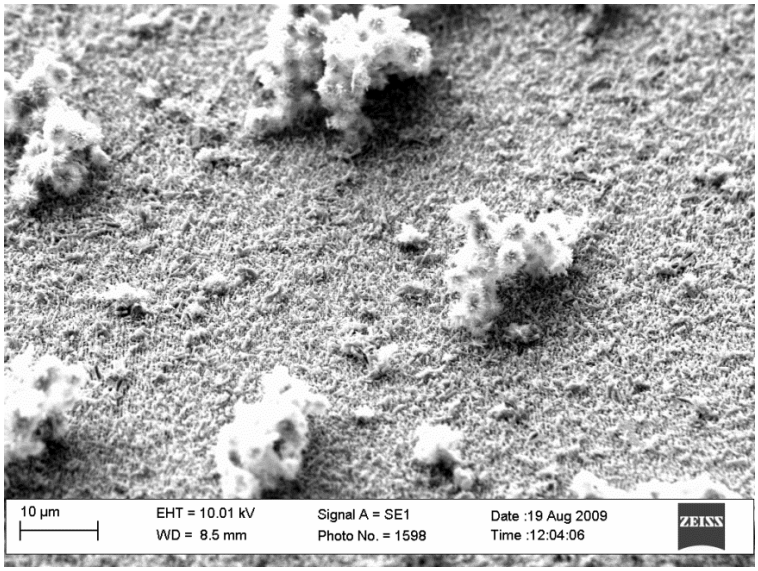

Figure 3.21: 45° view of a low density nanorod array, with a large mass of debris trapped on the surface of the substrate.

Figure 3.22 shows a typical growth using the NaOH method described in chapter 2.4.3. The substrate has a near 100% coverage of nanorods with no visible signs of extraneous matter or trapped precipitate. The nanorods are extremely uniform. After 30 minutes growth the average diameter is 65nm while the average length is 500nm, giving an aspect ratio of ~7. Each nanorod appears pointed at the tip and sharper than the HMT deposited nanorods, which Peterson and Li *et al.* have ascribed to the faster growing *c*-axis plane.[43-44] As the deposition reaction proceeds, the concentration of Zn^{2+} ions in solution decrease with respect to the hydroxide ion concentration. Once the concentration of Zn^{2+} shifts beyond the meta-stable concentration the hydroxide ions begin to etch the deposited ZnO nanorods. The fastest growing axis of ZnO is also the most rapidly etched axis. If the growth time is prolonged past the meta-stable equilibrium the hydroxide ions start to etch the rods which causes the pointed tips to become rounded.[43] Given that the rods are still pointed with no signs of rounding, this suggests that after 30 minutes the reaction solution in our experiments had not gone past its equilibrium and growth times could have be extended to yield longer nanorods. Keeping the reaction time below the time necessary for the solution to exceed its equilibrium is a convenient method for ensuring a sharp nanorod tip for applications such as field emission.

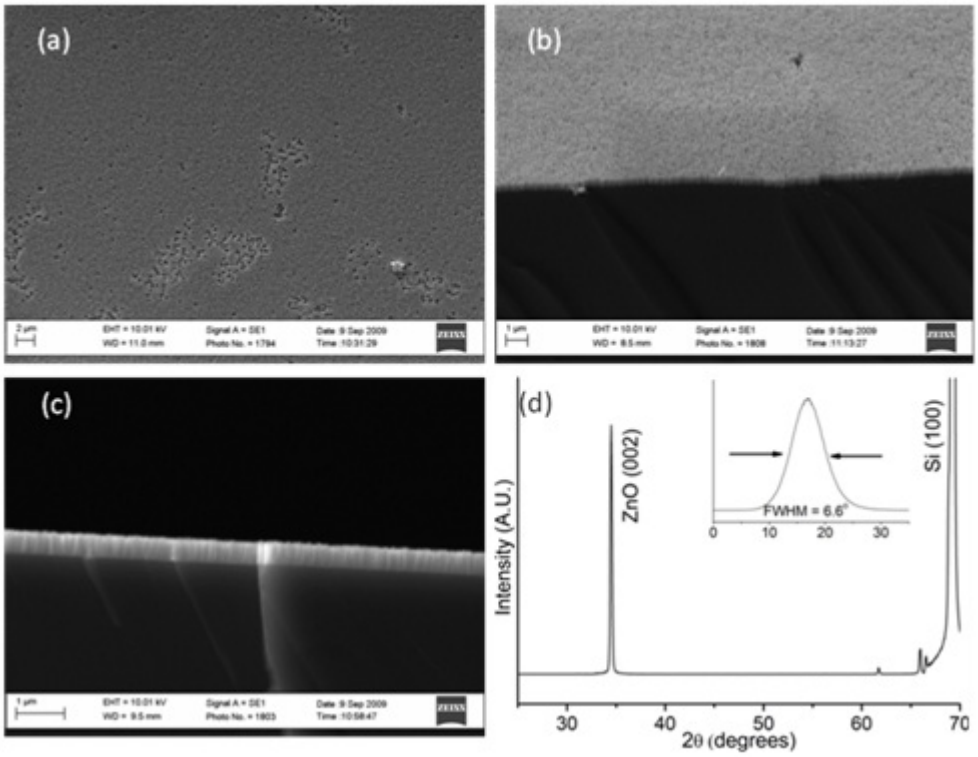

Figure 3.22: ZnO nanorod array grown by NaOH method (a) Plan view (b) 45° view (c) 90° view (d) XRD 2 θ / ω scan of NaOH CBD grown nanorod array on Si (100). (insert) XRD rocking curve of the peak located at 34.4° corresponding to the ZnO (002) plane.

As with the HMT based reaction, XRD analysis of the sample yielded only a single ZnO peak, again corresponding to the (002) plane as shown in figure 3.22 (d). The rocking curve of this peak, had a FWHM of only 6.6°, showing some improvement over the HMT based reaction, in terms of the nanorod alignment. Overall it was found that the NaOH based reaction was preferable to the HMT based reaction because (i) the growth rate was faster, (ii) the rods appeared better aligned, (iii) there was no loss in material quality and (iv) there were no difficult to remove precipitates. Despite these considerable advantages, the NaOH based growth was more difficult to implement. Any variation in the reaction concentration was likely to lead to a rapid dense precipitate similar to the HMT based reaction. Extreme care had to taken to ensure that the reaction vessel, substrate holder and thermometer were completely free of any residue of ZnO. The reaction solution was also very sensitive to any variations in concentration. Given that both the zinc nitrate and NaOH used are both hydroscopic, significantly more care had to be taken in preparing the reaction solution. Variation in the zinc nitrate concentration, which was unavoidable due to

variations in the water of crystallisation of the material itself, often resulted in variations in the ZnO growth rate.

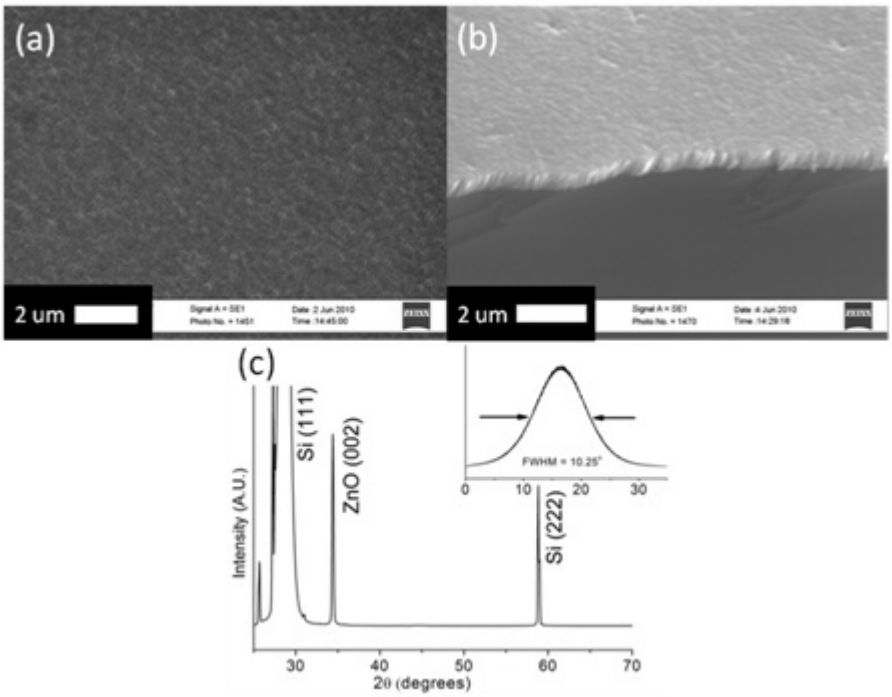

Figure 3.23: ZnO nanorod array grown by zinc acetate method (a) Plan view (b) 45° view (c) XRD 2 θ / ω scan of zinc acetate CBD grown nanorod array on Si (111). (insert) XRD rocking curve of the peak located at 34.4° corresponding to the ZnO (002) plane.

The most straight forward growth process examined was the direct decomposition of zinc acetate in solution. Zinc acetate is dissolved in water, and gently heated to decompose the acetate into the hydroxide. A small quantity of the hydroxide then dissolves and subsequently decomposes into ZnO on the seeded substrate. The reaction is driven forward by the evaporation of acetic acid from the reaction solution which would otherwise prevent the growth of ZnO on the substrate.[44] Similar to the HMT based reaction, a large mass of zinc hydroxide is precipitated during the reaction, however, little or none of this precipitate gets trapped on the substrate surface. This is due to the effect of the counter ion on the nanorod morphology. Like other carboxylic acids, the acetate counter ion is preferentially absorbed on to the Zn^{2+} (001) face, screening it from growth.[53] This blocking action of the counter ion, forces the nanorods to merge into a film, preventing Zn(OH) and ZnO precipitates from becoming trapped in gaps left in the nanorod array. The counter ion also affects the morphology of the nanorods, causing them to have a flat top, which in turn leads to a smoother film surface. As can be seen in figure 3.23 (a)

and (b), there are little or no gaps between the nanorods, and the surface is completely fused. The XRD data shown in figure 3.23 (c) shows that despite the capping effect of the counter ion on the growth, the columnar film is highly textured along the *c*-axis, with no indications of other crystal orientations. The FWHM of the rocking curve of the peak associated with the (002) plane is 10.25°, indicating that the alignment is similar to that of the HMT derived nanorod array. The slight reduction in the FWHM can be explained by the increase in spatial confinement induced by the lateral growth of the rods' thus forcing the rod alignment perpendicular to the substrate.

3.6 Conclusions

In this chapter, we have examined the growth of *c*-axis aligned ZnO nanorod arrays by a two step chemical deposition process on non-epitaxially matched substrates. The first step of the process involved creating a thin ZnO seed layer by drop-coating an alcoholic zinc acetate solution onto the substrate. The chemical origin of this seed layer has been confirmed by XPS analysis. Atmospheric water diffuses into the ethanol leading to the formation of an insoluble zinc hydroxide precipitate, which remains on the substrate surface after the drop-coating solution has been washed off. This precipitate is then thermally decomposed into a thin ZnO seed layer. This process has therefore two important parameters, the relative humidity during sample preparation and the ethanol film thickness. AFM and FESEM analysis of the deposited film has shown that it comprised of small platelet-like crystallites typically 10 - 20 nm in diameter and 2 – 4 nm thick, stacked on the substrate surface, mainly with the large platelet face flat to the surface, but with some degree of randomness, especially in areas of high seed crystallite density. Variations in the thickness of the seed layer around the substrate edges have been identified, the origin of which has been explained in terms of a Marangoni induced convective flow which can be affected by several features of the drop-coating process. In addition the presence of a second material, LBZA, which was not detected by XPS, may also contribute to the material build up along the substrate edges.

By taking into account the features identified in preparing the seed layer, we have demonstrated that well aligned uniform nanorod arrays can be grown on non-epitaxially matched substrates, using a variety of chemical bath methods. The uniformity and morphology of the nanorod growth is affected by the density of the seed layer, the reaction conditions, the temperature at which the substrate is introduced into the reaction solution,

the chemistry of the reaction and the presence of surfactants including counter ions from the zinc salt used. XRD and SEM analysis of all three chemistries used have shown that the nanorods grow primarily with their *c*-axis normal to the substrate and this alignment is due to a combination of the natural alignment of the underlying seed layer and spatial confinement effects from neighbouring nanorods.

3.7 References

(1) Yang, Z.; Shi, Y. Y.; Sun, X. L.; Cao, H. T.; Lu, H.-M.; Liu, X. D. *Materials Research Bulletin* **2010,** *45* (4) 474-480

(2) Vayssieres, L.; Keis, K.; Lindquist, S. E.; Hagfeldt, A. *Journal of Physical Chemistry B* **2001,** *105* (17) 3350-3352

(3) Govender, K.; Boyle, D. S.; Kenway, P. B.; O'brien, P. *J Mater Chem* **2004,** *14* (16) 2575-2591

(4) Lee, Y. J.; Sounart, T. L.; Scrymgeour, D. A.; Voigt, J. A.; Hsu, J. W. P. *Journal of Crystal Growth* **2007,** *304* (1) 80-85

(5) Greene, L. E.; Law, M.; Tan, D. H.; Montano, M.; Goldberger, J.; Somorjai, G.; Yang, P. D. *Nano Letters* **2005,** *5* (7) 1231-1236

(6) Wang, M.; Ye, C. H.; Zhang, Y.; Wang, H. X.; Zeng, X. Y.; Zhang, L. D. *J Mater Sci-Mater El* **2008,** *19* (3) 211-216

(7) Wu, W. Y.; Yeh, C. C.; Ting, J. M. *J Am Ceram Soc* **2009,** *92* (11) 2718-2723

(8) Chu, M. H.; Kim, S. Y.; Sung, S. Y.; Lee, J. H.; Kim, J. J.; Norton, D. P.; Pearton, S. J.; Heo, Y. W. *J Nanoelectron Optoe* **2010,** *5* (2) 186-190

(9) Lee, Y. J.; Sounart, T. L.; Liu, J.; Spoerke, E. D.; Mckenzie, B. B.; Hsu, J. W. P.; Voigt, J. A. *Cryst Growth Des* **2008,** *8* (6) 2036-2040

(10) Haase, M.; Weller, H.; Henglein, A. *The Journal of Physical Chemistry* **1988,** *92* (2) 482-487

(11) Wang, J.; Hokkanen, B.; Burghaus, U. *Surf Sci* **2005,** *577* (2-3) 158-166

(12) Gutierrez-Sosa, A.; Evans, T. M.; Parker, S. C.; Campbell, C. T.; Thornton, G. *Surf Sci* **2002,** *497* (1-3) 239-246

(13) Moller, P. J.; Komolov, S. A.; Lazneva, E. F.; Pedersen, E. H. *Surf Sci* **1995,** *323* (1-2) 102-108

(14) Xia, X.; Strunk, J.; Busser, W.; Naumann D'alnoncourt, R.; Muhler, M. *The Journal of Physical Chemistry C* **2008,** *112* (29) 10938-10942

(15) Lopes Martins, J. B.; Longo, E.; RodríGuez Salmon, O. D.; Espinoza, V. A. A.; Taft, C. A. *Chemical Physics Letters* **2004,** *400* (4-6) 481-486

(16) Saw, K. G.; Ibrahim, K.; Lim, Y. T.; Chai, M. K. *Thin Solid Films* **2007,** *515* (5) 2879-2884

(17) Mar, G. L.; Timbrell, P. Y.; Lamb, R. N. *Chem Mater* **1995,** *7* (10) 1890-1896

(18) Jesus, J. C. D.; Gonzalez, I.; Quevedo, A.; Puerta, T. *Journal of Molecular Catalysis A: Chemical* **2005,** *228* (1-2) 283-291

(19) Mar, L. G.; Timbrell, P. Y.; Lamb, R. N. *Thin Solid Films* **1993,** *223* (2) 341-347

(20) Zhao, X. Y.; Zheng, B. C.; Li, C. Z.; Gu, H. C. *Powder Technol* **1998,** *100* (1) 20-23

(21) Vithal Ghule, A.; Lo, B.; Tzing, S.-H.; Ghule, K.; Chang, H.; Chien Ling, Y. *Chemical Physics Letters* **2003,** *381* (3-4) 262-270

(22) Hsieh, P. T.; Chen, Y. C.; Kao, K. S.; Wang, C. M. *Appl Phys a-Mater* **2008,** *90* (2) 317-321

(23) Ramgir, N. S.; Late, D. J.; Bhise, A. B.; More, M. A.; Mulla, I. S.; Joag, D. S.; Vijayamohanan, K. *Journal of Physical Chemistry B* **2006,** *110* (37) 18236-18242

(24) Hu, X. L.; Masuda, Y.; Ohji, T.; Kato, K. *Langmuir* **2008,** *24* (14) 7614-7617

(25) Armelao, L.; Fabrizio, M.; Gialanella, S.; Zordan, F. *Thin Solid Films* **2001,** *394* (1-2) 89-95

(26) Morioka, H.; Tagaya, H.; Kadokawa, J. I.; Chiba, K. *J Mater Sci Lett* **1999,** *18* (12) 995-998

(27) Hosono, E.; Fujihara, S.; Kimura, T.; Imai, H. *Journal of Colloid and Interface Science* **2004,** *272* (2) 391-398

(28) Scriven, L. E.; Sternling, C. V. *Nature* **1960,** *187* (4733) 186-188

(29) Leenaars, A. F. M.; Huethorst, J. A. M.; Van Oekel, J. J. *Langmuir* **1990,** *6* (11) 1701-1703

(30) Qu, D.; Rame, E.; Garoff, S. *PHYSICS OF FLUIDS* **2002,** *14* (3) 1154-1165

(31) Mellbring, O.; Kihlman Øiseth, S.; Krozer, A.; Lausmaa, J.; Hjertberg, T. *Macromolecules* **2001,** *34* (21) 7496-7503

(32) Rajneesh, B.; Et Al. *New Journal of Physics* **2009,** *11* (7) 075020

(33) Kang, Y. *Chemistry Letters* **2008,** *37* (8) 874-875

(34) Vuilleumier, R.; Ego, V.; Neltner, L.; Cazabat, A. M. *Langmuir* **1995,** *11* (10) 4117-4121

(35) Deegan, R. D.; Bakajin, O.; Dupont, T. F.; Huber, G.; Nagel, S. R.; Witten, T. A. *Nature* **1997,** *389* (6653) 827-829

(36) De Jong, J.; Reinten, H.; Wijshoff, H.; Van Den Berg, M.; Delescen, K.; Van Dongen, R.; Mugele, F.; Versluis, M.; Lohse, D. *Applied Physics Letters* **2007,** *91* (20) 204102

(37) Stairs, R. A.; Rispin, W. T.; Makhija, R. C. *Canadian Journal of Chemistry* **1970,** *48* (17) 2755-2762

(38) Rongy, L.; Wit, A. D.; Homsy, G. M. *Physics of Fluids* **2008,** *20* 072103

(39) Verges, M. A.; Mifsud, A.; Serna, C. J. *J Chem Soc Faraday T* **1990,** *86* (6) 959-963

(40) Vayssieres, L. *Adv Mater* **2003,** *15* (5) 464-466

(41) Ashfold, M. N. R.; Doherty, R. P.; Ndifor-Angwafor, N. G.; Riley, D. J.; Sun, Y. *Thin Solid Films* **2007,** *515* (24) 8679-8683

(42) Sugunan, A.; Warad, H. C.; Boman, M.; Dutta, J. *J Sol-Gel Sci Techn* **2006,** *39* (1) 49-56

(43) Peterson, R. B.; Fields, C. L.; Gregg, B. A. *Langmuir* **2004,** *20* (12) 5114-5118

(44) Li, W. J.; Shi, E.-W.; Zhong, W.-Z.; Yin, Z.-W. *Journal of Crystal Growth* **1999,** *203* (1-2) 186-196

(45) Matijevic, E. *Chem Mater* **1993,** *5* (4) 412-426

(46) Garry, S.; Mccarthy, E.; Mosnier, J. P.; McGlynn, E. *Applied Surface Science* **2011,** *257* (12) 5159-5162

(47) Law, M.; Greene, L. E.; Johnson, J. C.; Saykally, R.; Yang, P. D. *Nature Materials* **2005,** *4* (6) 455-459

(48) Zhou, Y.; Wu, W. B.; Hu, G. D.; Wu, H. T.; Cui, S. G. *Materials Research Bulletin* **2008,** *43* (8-9) 2113-2118

(49) Pacholski, C.; Kornowski, A.; Weller, H. *Angew Chem Int Edit* **2002,** *41* (7) 1188

(50) Wang, M.; Hahn, S. H.; Kim, J. S.; Hong, S. H.; Koo, K.-K.; Kim, E. J. *Materials Letters* **2008,** *62* (30) 4532-4534

(51) Chen, Y.; Bagnall, D. M.; Zhu, Z.; Sekiuchi, T.; Park, K.-T.; Hiraga, K.; Yao, T.; Koyama, S.; Shen, M. Y.; Goto, T. *Journal of Crystal Growth* **1997,** *181* (1-2) 165-169

(52) TEW Tokyo Denpa, High Quality ZnO Substrates for wide band gap applications, **2011**

(53) Cho, S.; Jang, J. W.; Jung, S.-H.; Lee, B. R.; Oh, E.; Lee, K. H. *Langmuir* **2009,** *25* (6) 3825-3831

Chapter 4: Carbothermal Vapour Phase Transport Growth

4.1 Introduction

In this chapter, growth of ZnO nanorods by CTR-VPT and the some of the various factors affecting growth will be discussed. This work concentrates specifically on VPT deposition on non-epitaxially matched substrates using a previously deposited buffer layer to act as both a nucleation site and to provide initial *c*-axis alignment. As with chapter 3, the TEM data presented here was acquired by our UCA Cadiz collaborators. A carbothermal reduction vapour phase transport technique (CTR-VPT) was used in this work, which is a fast and economical route to high quality ZnO nanorods. This technique is based on the ability of carbon to act as a reducing agent. At high temperatures metal oxide powders in contact with carbon are reduced to metal vapour and carbon monoxide by the given equation:[1-4]

$$MO + C \rightarrow M + CO \quad (4.1.1)$$

$$MO + CO \rightarrow M + CO_2 \quad (4.1.2)$$

A second reduction involving the metal oxide and carbon monoxide (CO) as given by equation 4.1.2 also occurs. This reaction however is dominant in a different temperature

range. The metallic vapour is quickly reoxidised by residual oxygen following condensation on the regions of the growth substrate where energetically suitable nucleation sites exist, leading to the growth of metal oxide nanostructures on substrates placed in the vicinity of the source material. ZnO nanorods grown on non-epitaxially matched substrates tend not to be aligned.[2] In order to achieve *c*-axis growth perpendicular to a substrate using higher temperature growth methods such as CTR-VPT it is generally necessary either to use substrates that are epitaxially matched to ZnO with catalysts such as Au or Cu or to use substrates with pre-deposited ZnO buffer layers.[5-7] Li *et al.* has studied the effects of different ZnO buffer layers on the growth of nanorods using a CTR-VPT growth technique.[7] This work did not extend to thin ZnO buffers layer prepared from zinc salts, concentrating instead on buffer layers deposited by reactive sputtering, RF sputtering, thermal oxidation of Zn films and pulsed laser deposition. Greene *et al.* has suggested that it is possible to grow ZnO nanorods by CTR-VPT on thin zinc acetate derived buffer layers, with or without the use of Au catalysts.[5] In these and other techniques reported, the experimental setup is complicated by the fact that the substrate is placed down stream from the graphite/ZnO source powder. Moving the buffered substrate can have a significant effect on the overall morphology and so positioning of the substrate becomes a critical growth parameter.[8] The use of this complicated configuration, makes reproducible results difficult to achieve as both the concentration of Zn vapour and the substrate temperature vary with distance from the source powder.[8] Other groups have reported successful reproducible nanorod growth by positioning the substrate directly above the source powder using Au as a catalyst and epitaxially matched substrates.[2, 9] To date there have been few reports of the effect of growing ZnO nanorods using buffered substrates directly over the source powder, nor have there been many reports of successful nanorod growth on CBD derived buffer layers.[10] The goal of our work is to develop a reliable technique for growing uniform large area, well aligned ZnO nanorod arrays, using a facile CTR-VPT technique in combination with CBD derived buffer layers. In addition, we sought to clarify the role of the buffer layer on the CTR-VPT process and identify the factors which influence the growth and morphology of the nanorods. For the purposes of clarity, for the remainder of this work, thin ZnO films prepared by drop-coating zinc acetate solutions will be referred to as seed layers and thicker CBD deposited nanorod arrays will be referred to as buffer layers.

4.2 Carbothermal deposition on acetate derived seed layers

In the original report by Greene *et al.* the zinc acetate derived seed layers were primarily used to grow ZnO nanorods by CBD. However they also demonstrated that the acetate derived seed layers could also be used to grow nanorods by CTR-VPT under specific conditions outlined in reference 4.[4-5] In this technique, the ZnO seeded substrate is placed downstream from ZnO / graphite source powder in a quartz tube furnace. Under a gentle flow of Argon the furnace was heated to temperatures of 800-1000°C for up to 1 hour. Their best results were obtained when Au was used in conjunction with the thin seed layer. Without the Au catalyst, only short nanorods with significantly higher diameters than aqueous grown nanorods were observed. As the positioning of the substrate/substrate temperature can have a strong bearing on the type of growth observed,[8] we attempted to simplify the CTR-VPT deposition technique by positioning the seeded substrates directly over the source powder thereby maintaining the substrate and source powder at the same temperature. A large variation in growth over cm-sized substrates was observed in samples grown in this manner. For the thinnest acetate derived seed layers (5 drop-coats) growth was only ever observed at the edges of the substrate. To confirm whether this was a feature of the seed layer or other experimental parameters such as the direction of argon flow across the sample, substrates were cleaved into two pieces and orientated so that one piece of the seeded substrate had the cleaved edge perpendicular to the argon flow and one piece parallel to the argon flow. In each case the cleaved edge had little or no growth while the non-cleaved edge had some nanorod growth. The bulk of the substrate area had very sparse growth. This is a strong indication that the direction of gas flow had little impact on the growth observed and that the variations in the underlining buffer layer was influencing the CTR-VPT growth process. The rod growth observed at the edges was unaligned and appeared in areas to grow from rounded ridges on the substrate. The growth also showed two distinct morphologies within individual nanorods.

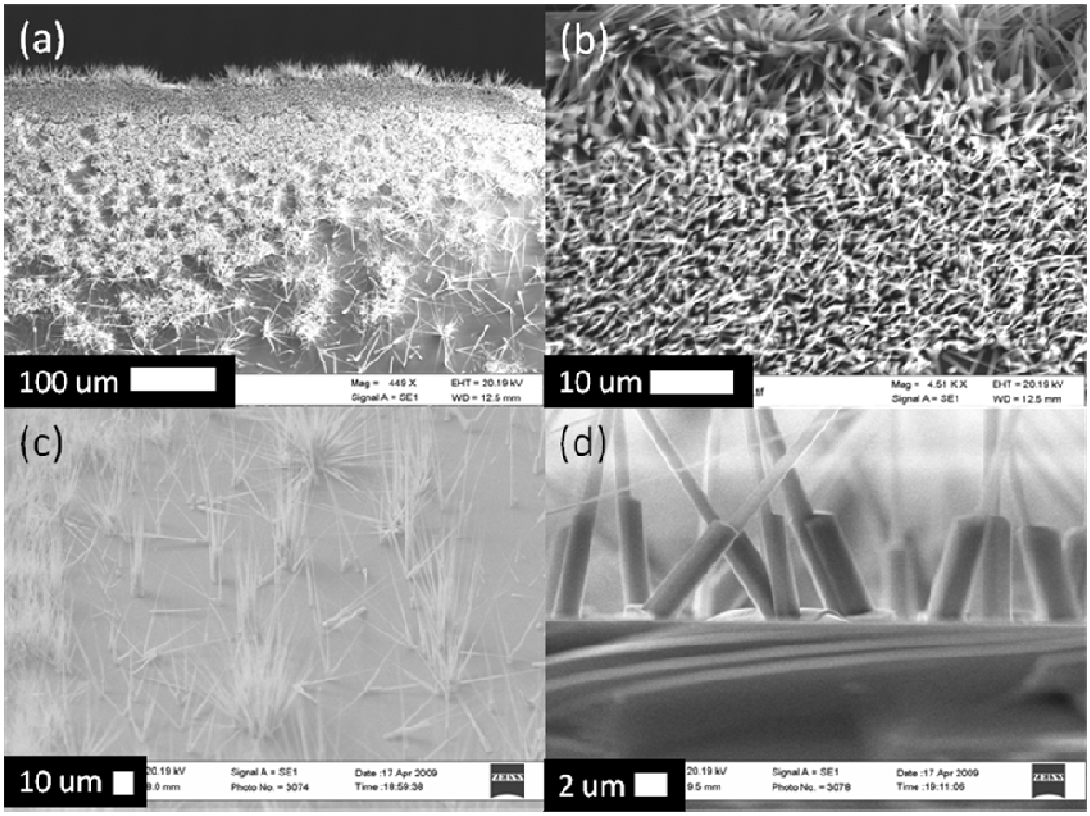

Figure 4.1: Carbothermal Reduction growth on a thin (5 drop-coat) acetate derived seed layer at 925°C with a 90 sccm argon flow for 1hour (a) Wide plan view of the substrate edge (b) Higher magnification plan view close to the substrate edge (c) 45° view approximately 200 µm from the substrate edge (d) 90° view approximately 200 µm from the substrate edge.

In figure 4.1 (a) & (b) dense poorly aligned nanorod growth extends out from the edge of the substrate. Approximately 300 µm from the substrate edge, the density of nanorods rapidly decreases and small clusters / single nanorods appear to nucleate from small separated islands. These nucleation points at the base of the nanorods can be clearly seen in figure 4.1 (d). In the lower density regions the nanorods are straight with the poor alignment with respect to the substrate being caused by the nucleation site. In the higher density regions the misalignment is a combination of nanorod bending and nucleation based misalignment. The nanorods in both high and low density regions have an interesting morphology. The bases of the rods have a wide diameter of approximately 2 µm. After several µm the diameters of the rods reduces significantly at a specific point creating a sharp step along the length of the rod.

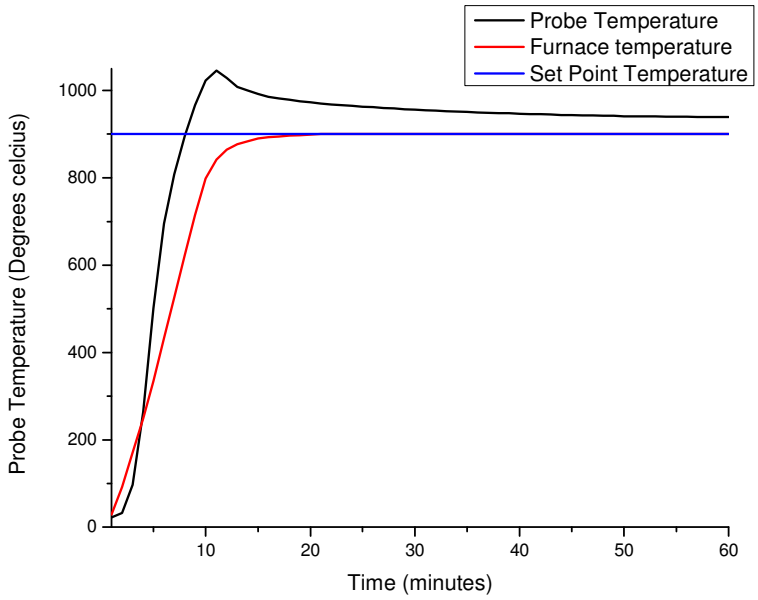

Figure 4.2: Temperature ramp profile of CTR furnace set to 900°C. Black line: Actual temperature of furnace as measured by a temperature probe. Red Line: Displayed furnace temperature. Blue Line: Set Point temperature.

While the exact reason for this rapid change in diameter is unknown, one possible factor is the temperature of the furnace. Biswas *et al.*, using an identical sample configuration, suggested that at very high temperatures an increased evolution of Zn vapour can displace oxygen from the region around substrate thus inhibiting growth.[2] At the start of growth the furnace is set to a nominal temperature of 925°C. The furnace rapidly heats to the target temperature but overshoots the set-point temperature by over 140°C. The actual furnace temperature profile for a set point of 900°C is shown in figure 4.2. Once the furnace reaches the minimum temperature required for the CTR reaction to proceed, growth of large diameter nanorods is initiated. The large diameter nanrods continue to grow until the increasing Zn vapour evolution displaces all the oxygen from the area around the substrate, inhibiting further 2D growth. As the furnace reaches its equilibrium temperature, closer to the set-point temperature, the concentration of Zn vapour decreases with respect to the oxygen concentration and nanorod growth recommences at a different rate or by a different mechanism leading 1D growth as seen by the reduction in nanorod diameter.

Increasing the number of drop-coats prior to carbothermal deposition, the density of nanorod growth across the substrate increases. In figure 4.3 the substrate was drop-

coated 30 times prior to carbothermal deposition. The entire substrate surface was covered with a dense array or poorly aligned nanorods, similar to the deposition observed at the edges of thin seed layer substrates (≤5 drop-coats).

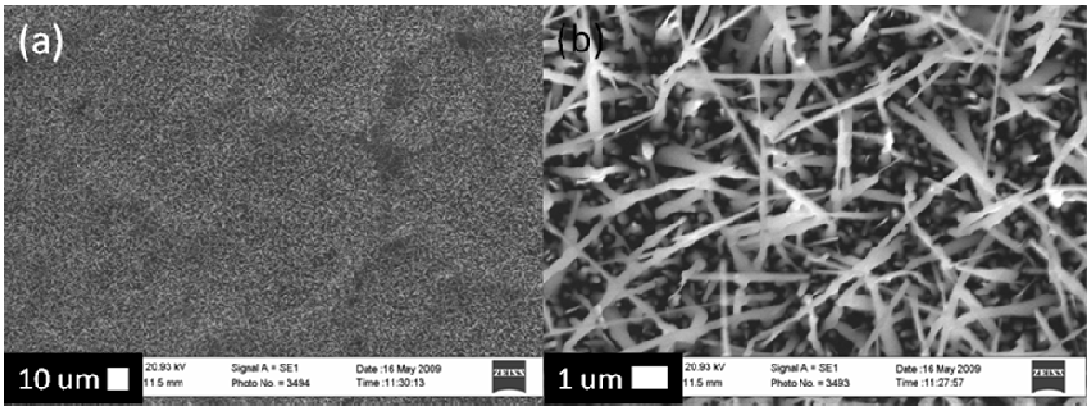

Figure 4.3: Carbothermal Reduction growth on a thick(30 drop-coat) acetate derived seed layer at 925°C with a 90sccm argon flow for 1hour (a) Wide plan view (b) Higher magnification plan view close to the centre of the sample

The unusual step in rod diameter in not as evident as compared to the samples grown on thin acetate derived seed layers, but some rods do have smaller thinner rods emerging from their tips. As with the thinner seed layers the misalignment appears to stem from a combination of nucleation based alignment and rod bending. There is also some indication of rods coalescing into unified structures at random points along their various growth axes. It is clear that despite the increase in substrate coverage with increasing number of drop-coats, at high deposition temperatures the acetate derived seed layers lose their alignment and are therefore not suitable for the growth of *c*-axis aligned nanorod arrays using the simplified configuration. The loss of rod alignment was demonstrated further by carbothermal deposition on acetate derived seed layers which were coated with 5nm of Au (not shown). The nanorods deposited in this manner showed no improvement in alignment or morphology.

The variations in the seed layer discussed in section 3.3, clearly has an important impact on the CTR-VPT deposited nanorods, with growth being confined principally to the edge regions where the thicker seed layer was detected. However, as has been demonstrated by the CBD growths, the thin seed layer found across the substrate should serve as suitable nucleation sites. To further understand what was causing the reduction in nucleation sites during the CTR-VPT process, seed layers were treated to an identical

thermal cycle as the CTR-VPT process, without any source powder present. During the heat treatment cycle all reaction parameters, such as argon flow (90 sccm), substrate positioning, and anneal temperature (925°C) and duration were kept the same as during an actual CTR-VPT deposition run.

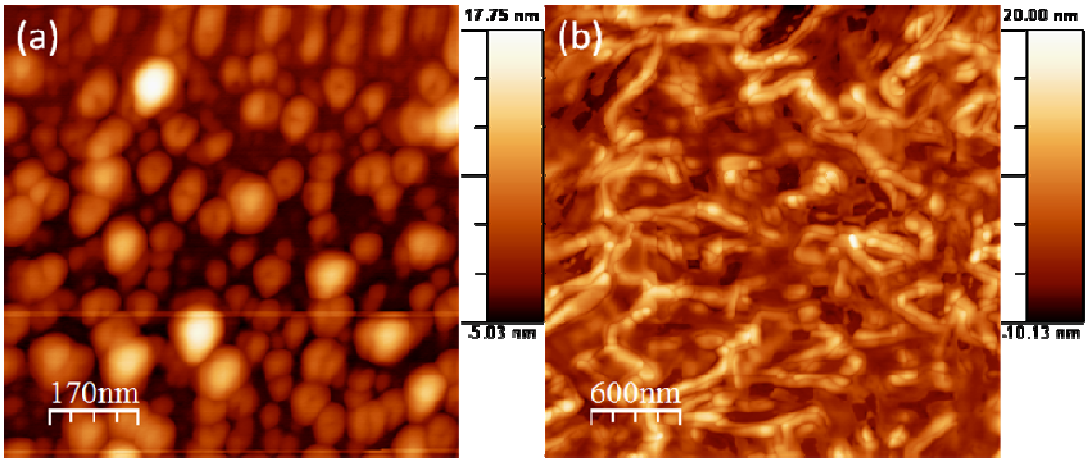

Figure 4.4: AFM images of (a) acetate derived seed layer close to the centre of the substrate which has been annealed at 925°C using identical parameters as the CTR-VPT growth (b) acetate derived seed layer close to the edge of the substrate which has been annealed at 925°C using identical parameters as the CTR-VPT growth

Annealing at a nominal furnace temperature of 925°C has a dramatic effect on the thin acetate derived seed layers, as shown in figure 4.4. The small individual crystallites (as seen in figure 3.6 a) are no longer detected and have been replaced by larger structures (figure 4.4 a), reducing the density of seeds dramatically. Similar growth in crystal grain size has been previously reported. It has been observed that annealing ZnO at high temperature causes neighbouring crystals to merge.[11-12] Zhi *et al*. has suggested that this phenomenon is due to defect sites at crystal grain interfaces being favourable sites for crystal coalescence. At the surface of each crystal there are many defects such as dangling bonds, which increase chemical potential, leading to a higher reactivity at the surface.[11] In addition to the large reduction in the seed density, some of the remaining features have an unusual bowl shape. At the substrate edges (figure 4.4 b), the larger crystals also undergo grain growth as compared to similar regions prior to annealing (figure 3.6 d), leading to random ridged structures. While studying residual stress relaxation in ZnO thin films Ozen *et al.* have observed strong structural changes in thin ZnO films annealed at high temperature, including stress induced diffusive crystal growth.[13] The thermal energy provided by the

annealing promotes pore growth and mass transport though ZnO films accompanying stress relief. In addition, other effects such as plastic deformations, film cracking and delamination were observed.[13] The thin seed layers, composed of random crystallites are likely to have a substantial number of pores in the film, which may then lead to diffusive crystal and pore growth. While delamination of some of the film or crystallites may be possible, further investigation has shown that this is not a dominant effect.

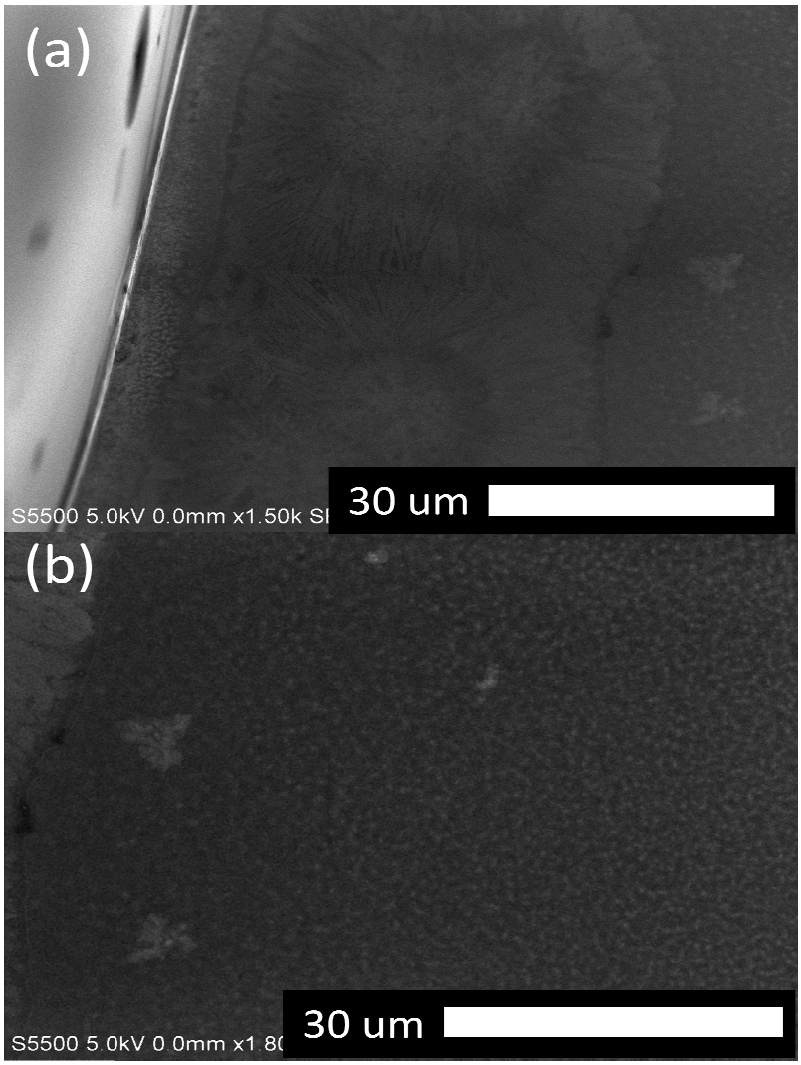

Figure 4.5: 30° FESEM images of (a) acetate derived seed layer close to the edge of the substrate which has been annealed at 925°C using identical parameters as the CTR-VPT growth (b) acetate derived seed layer away from the substrate edge which has been annealed at 925°C using identical parameters as the CTR-VPT growth.

FESEM analysis of the seed layer post thermal treatment as shown in figure 4.5 (a) and (b) indicate that in addition to the diffusive crystal growth, additional process are

occurring. A clear distinction can be seen between the edge region and the bulk area of the sample. At the sample edges the ridged structure is clearly visible, corresponding to the fused mounds where CTR-VPT growth takes place. Away from the substrate edge, a clear speckled contrast can be seen on the substrate surface. However no individual features could be resolved despite their size being well within the imaging magnification range of the FESEM instrument. The lack of resolvability suggests that the contrast is from subsurface features, which are buried suitably close to the substrate surface that the high accelerating voltage of the FESEM is able to penetrate through to them, thereby acting in a quasi transmission mode. This was later confirmed by HAADF-STEM analysis of the annealed seed layers which indicated that the crystallites become imbedded in the amorphous silicon oxide layer.

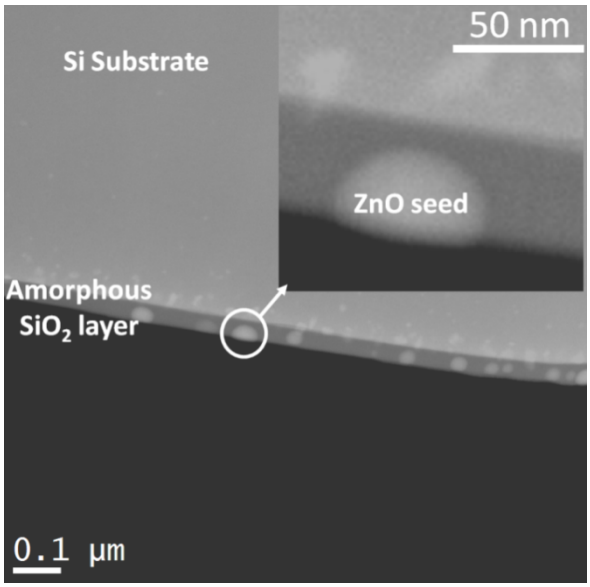

Figure 4.6: HAADF-STEM image of a drop-coated seed layer annealed (insert) higher magnification HAADF-STEM showing an original crystallite imbedded in the surface SiO_2. (Image acquired by UCA Cadiz collaborators)

During the high temperature treatment there is an over-growth of the seeds by the SiO_2 layer. It is well known that at high temperatures silicon wafers can be oxidised, forming much thicker oxide layers than the native oxide present. This growth in thermal oxide is sufficient to encapsulate the small seed crystals rendering them inactive for subsequent nanorod nucleation. This suggests that the buffer layer must have a minimum particle size / thickness ratio during CTR-VPT deposition, to prevent the SiO_2 overgrowth inhibiting the ZnO nucleation process. Furthermore the size of the particles embedded in

the substrate in figure 4.6 suggests crystal coalescence may also be taking place since the sizes of the particles are significantly larger than those previously observed in our work or reported elsewhere, consistent with the AFM data in figure 4.4 above.[5] EDX analysis of these seeds shows the composition as a ZnO/SiO_2 mix. While the silicon signal is unavoidable due to the small particle size of the embedded seeds, it cannot be ruled out that the seeds also undergo a chemical reaction forming a $Zn_xSi_{1-x}O_y$ type compound at high temperatures as similar reactions have been observed before.[14]

4.3 CTR-VPT deposition on CBD derived buffer layers

To date, there have been few reports of CBD derived ZnO nanorod arrays being used as a template for carbothermal depositions.[10] In this work we have developed a reliable technique to grow highly aligned ZnO nanorod arrays, by combining the distinct advantages of CBD with CTR-VPT. As discussed in chapter 3, when prepared correctly the acetate derived seed layer can be used to create *c*-axis aligned ZnO nanorod arrays by chemical bath deposition. However when these seed layers alone are combined with a carbothermal reduction technique at high temperatures, the seed layers rapidly loses orientation and coverage can vary substantially with the number of drop-coats. While it has been demonstrated that high aspect ratio nanorods can be realised using CBD in combination surfactants,[15-16] the optical quality of CBD deposited nanorods, as determined by bound exciton linewidths in low temperature PL and similar criteria is inferior to CTR-VPT deposited nanorods.[17-18] Both of these issues have been addressed by developing a hybrid technique taking advantage of the reliability of CBD techniques to initiate *c*-axis aligned growth and the CTR-VPT technique for rapid growth of high quality ZnO nanorods.

Figure 4.7 shows a nanorod array deposited by combining CBD buffer layers with CTR-VPT. An initial seed layer was deposited by drop-coating a zinc acetate solution, followed by annealing at 350° for 30 minutes. The CBD buffer layer was grown using the HMT-CBD method for 20 minutes to produce a dense array of highly aligned short nanorods. Typically, a 20 minute reaction time produces nanorod lengths of ~250 nm. Once dried, the nanorod array was grown by CTR-VPT at 925°C for 1 hour. The sample was examined at six different points on the substrate and no variation across the substrate area was observed, as shown in figure 4.7. As can be seen, the growth was very uniform across

the entire substrate with an average nanorod length of 1 µm and diameter centred around 130nm. All the nanorods are well aligned with respect to the substrate. In each of the 90° views the CBD buffer layer can still be clearly seen with each nanorod extending from an underlying CBD deposited nanorod. The CBD array is suitably robust to maintain its orientation during the high temperature deposition.

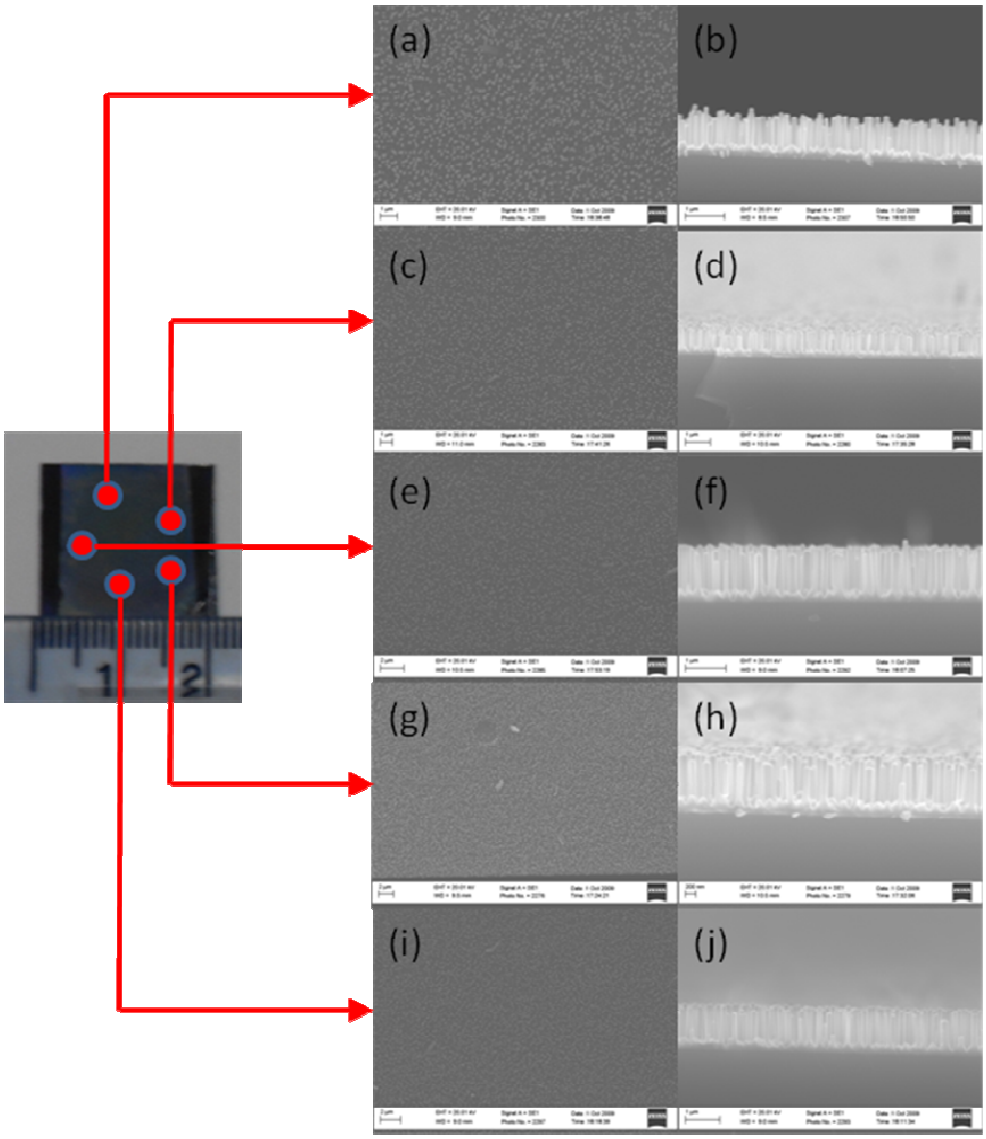

Figure 4.7: SEM images of growth using hybrid CBD/CTR-VPT technique. (a,c,e,g,h) Plan view (b,d,f,h,j) 90° view of regions highlighted on the photograph of sample after deposition.

The aspect ratio of the nanorods in figure 4.7 is approximately 7.7. Similar aspect ratios can be achieved by prolonging the CBD growth to several hours. However in the absence of surfactants increasing the CBD growth time leads to a coalescence of the

nanorods, owing to the high density of the nanorods and growth in their diameters. In the hybrid technique not every nanorod deposited by CBD results in a CTR-VPT deposited nanorod. Ultimately this leads to a significant reduction in the density of CTR-VPT nanorods as compared to the CBD buffer layer. Therefore, it may be possible to perform multiple CTR-VPT depositions on a CBD buffer layer without the neighbouring CTR-VPT nanorods coalescing to form a continuous thin film. It may then be possible to increase substantially the aspect ratio of the CTR-VPT nanorods by performing multiple CTR-VPT depositions.

4.3.1 Effect of varying substrate height over source powder

Our results indicate that control of the aspect ratios of the nanorods deposited may also be possible using a hybrid technique. By varying the substrate's distance above the source powder during the CTR-VPT step, arrays with rods with different aspect ratios have been deposited. Placing the substrate closer to the source powder leads to a decrease in the diameter of the nanorods and an increase in their length. Figure 4.8 shows a nanorod array deposited using very similar conditions to the sample in figure 4.7.

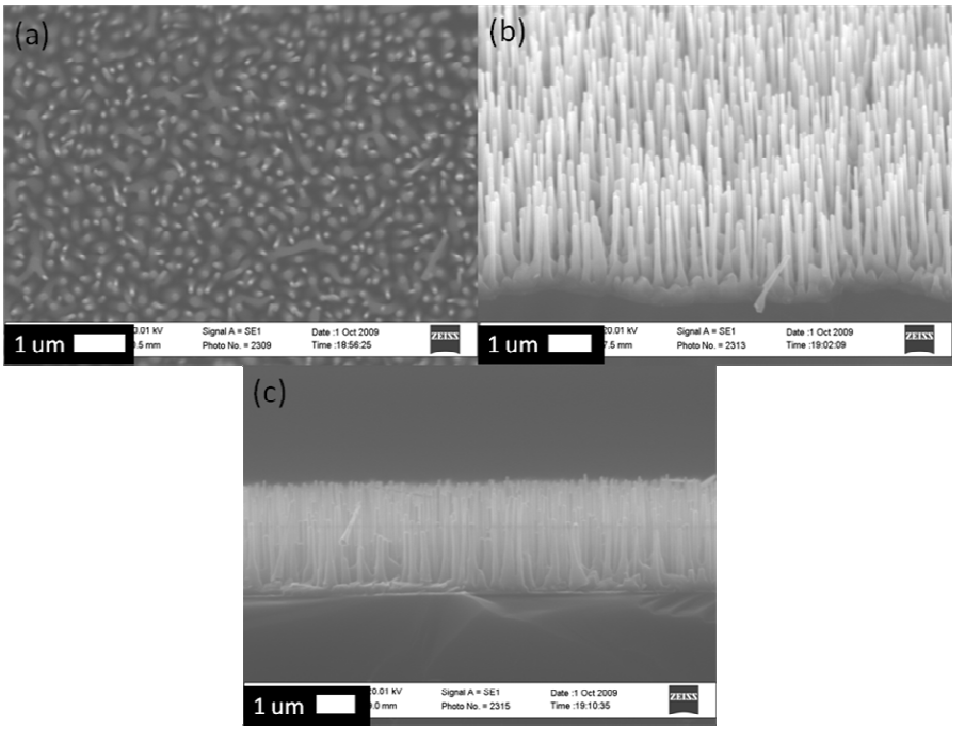

Figure 4.8: SEM images of growth using hybrid CBD/CTR technique using a smaller alumina boat during CTR step. (a) Plan view (b) 45° view (c)90° view or nanorod array deposited.

The only difference between the two samples is the size of the alumna boat used during the CTR-VPT deposition. In figure 4.8 the substrate was grown using a smaller boat and was therefore closer to the source powder. The reduction in boat size reduces the horizontal surface area where the source powder can be spread, increasing the depth of the powder. The open space between the powder and substrate, through which the argon can flow is also reduced. This minor alteration in processing conditions reduced the nanorod diameter to ~80nm and increased the length of the rods to ~2.5µm, equating to an aspect ratio of over 31. The dramatic variation in aspect ratio resulting from the variation in boat size suggests that the deposition is highly sensitive to the concentration of Zn vapour escaping from the ZnO/graphite mix. The CTR-VPT deposition has been performed at various temperatures from 825-925°C. It was found that as the nominal set-point temperature is decreased (~850°C) the diameter of the nanorods increased. From these results one could conclude that there are two factors that affect the final aspect ratios of the nanorods, the distance between the substrate and the source powder and the temperature at which the growth takes place. Given that both result in a variation in the nanorod aspect ratio it may be the case that these seemingly independent factors have a common action during the growth process. First let us consider the variation in distance between the source powder and substrate. By increasing the vertical distance between the substrate and source powder, the flux of Zn reaching the substrate would be reduced as both the volume of space which the Zn vapour can occupy has increased and the cross-sectional area through which the Ar can flow has increased. Therefore one could reasonably expect that the growth rate of ZnO rods would be reduced, leading to shorter nanorods. However, it has been established that higher Zn vapour density leads to 2D nucleation and growth whilst lower Zn vapour density leads to 1D growth.[19] Consequently the lower Zn density achieved by increasing the distance between the source powder and substrate should result in reduced nanorod diameters. These results appear inconsistent with the known growth mechanism of ZnO nanorods. Next we consider the effect of reducing the temperature. At lower temperatures, one would also expect that the rate of Zn vapour production would be reduced given the slower reaction kinetics at lower temperatures. Therefore one could also presumably expect that the growth would be primarily 1D, leading to a reduction in nanorod diameters. Again, the growth results appear at odds with expectations as to the growth behaviour.

Further growths were performed using the smaller boat using identical conditions to those used for the sample grown in figure 4.8. This time the ZnO/graphite powder was gently compressed into boat to reduce the porosity of the source powder, thereby reduce the mass of Zn vapour escaping. Post deposition, the source powder had a firm white crust where the ZnO redeposited on the surface of the source powder, indicating that the compression of the source powder was successful in reducing the mass of Zn vapour reaching the substrate. The nanorod array deposited using compressed powders, shown in figure 4.9, has a large reduction in rod length and increase in diameter compared to non-compressed growth shown in figure 4.8. The diameter of the rods increased from ~80nm to ~220nm while the length of the rods decreased form 2.5µm to 1.4µm. This corresponds to an aspect ratio of 6.4, a reduction of 24.6 or 79% compared to the non-compressed source powder deposition.

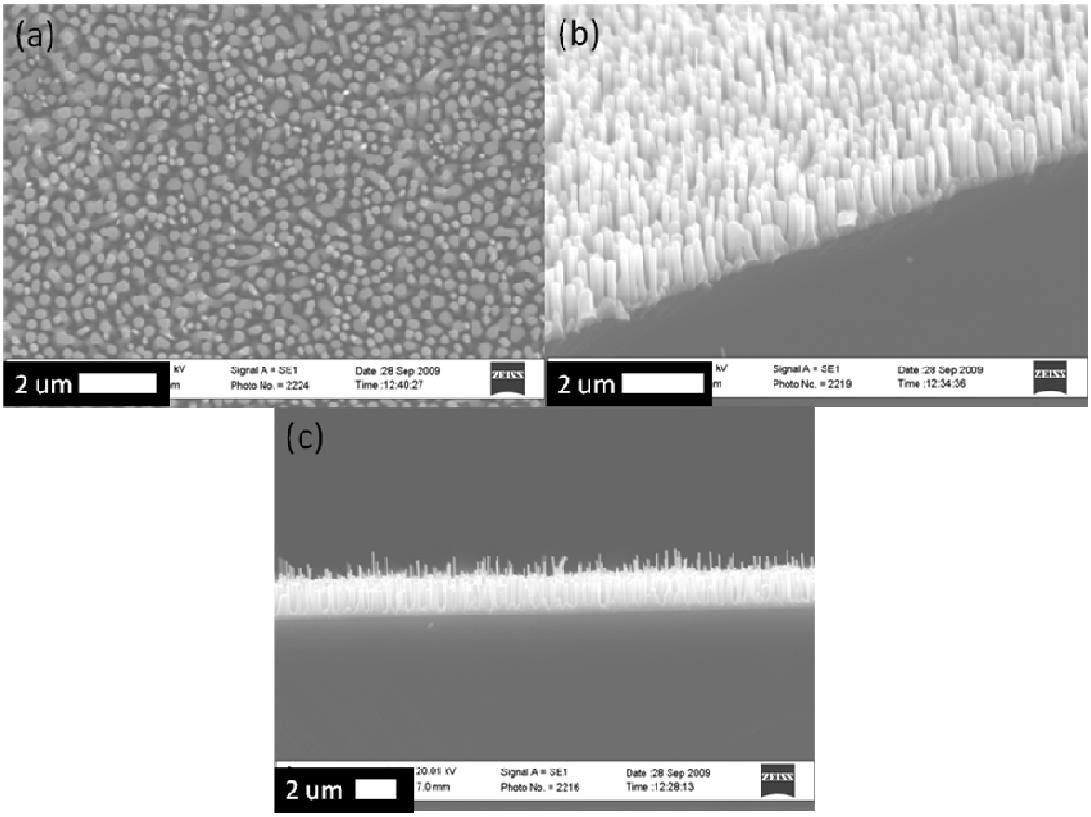

Figure 4.9: SEM images of growth using hybrid CBD/CTR-VPT technique using a smaller alumina boat and compressed source powder during CTR step. (a) Plan view (b) 45° view (c)90° view or nanorod array deposited.

These results, combined with the observed effect of temperature on deposition, imply the Zn vapour concentration at the substrate has a strong effect on the morphology

of the nanorods deposited. However the inconsistencies between these results and those previously reported results suggest that the simple assumptions made about the CTR-VPT system only partially reflect the growth process and that other factors are clearly influencing the final nanorod morphology some of which are discussed in sections 4.3.2 - 4.3.4.

4.3.2 Effect of varying the CBD buffer layer

The choice of CBD deposition technique does not seem to have a significant impact on the orientation or quality of the nanorods deposited during the CTR step. In figure 4.10, a buffer layer was deposited using the NaOH based CBD technique described in section 2.3.3. The resultant nanorod array is very similar to the array grown on the HMT deposited nanorods shown in figure 4.8. The average length of the nanorods is 1.7 µm with a diameter of 65 nm, equating to an aspect ratio of 26.

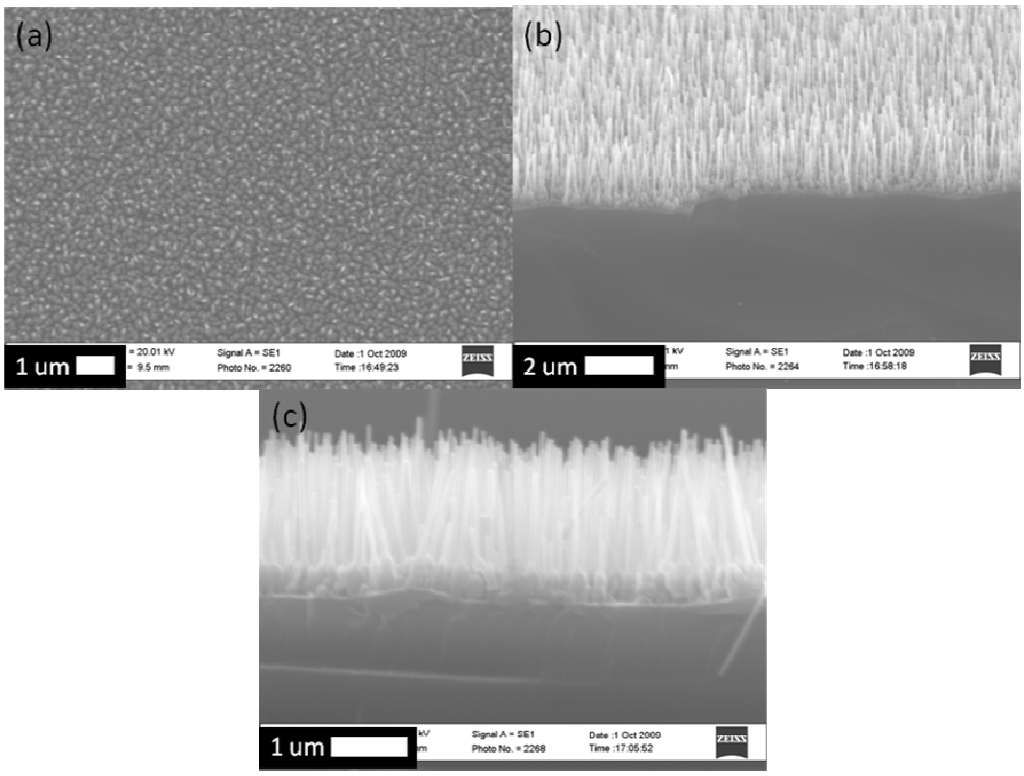

Figure 4.10: SEM images of growth using hybrid CBD/CTR-VPT technique using a smaller alumina boat during CTR step. CBD layer deposited using NaOH method (a) Plan view (b) 45° view (c)90° view of nanorod array deposited.

The cause of the difference in aspect ratio between HMT and NaOH based CTR depositions is unknown but may be due to minor variations in the processing conditions such as the spread or compression of the source powder. Although the choice of CBD buffer layer preparation did not seem to significantly impact the CTR-VPT nanorod growth process, it was found that structural transformations in the CBD buffer layer which occur during the high temperature deposition did influence the final morphology of the nanorods. These variations are discussed in more detail in section 4.4. However one can note that the underlying ZnO buffer layer shown in figure 4.10 (c) appears more intact than that of the HMT based buffer layers shown in figure 4.8.

4.3.3 Structural characterisation of the Nanorods

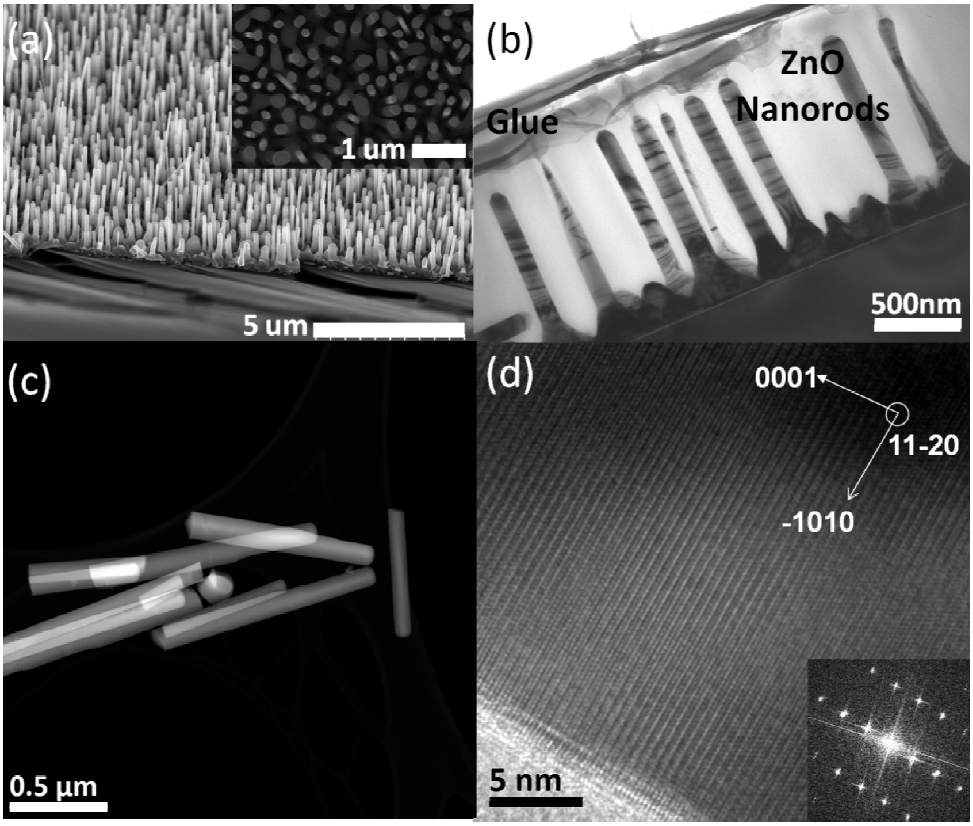

Figure 4.11: (a) FE-SEM image of a CTR-VPT grown nanorod array via FRTP on a CBD buffer layer (b) CTEM image of a sample grown in an identical fashion (c) HAADF-STEM of CTR-VPT grown nanorods scraped from the substrate surface. (d) HRTEM and its corresponding FFT of a single CTR-VPT grown nanorod confirming c-axis and Wurtzite structure. (Images (b)(c)(d) acquired by UCA Cadiz collaborators)

FESEM analysis of nanorods deposited on CBD buffer layers, as shown in figure 4.11 (a), demonstrate that the nanorods grow perpendicular to the substrate, following the alignment of the underlying CBD buffer layer. Similarly HRTEM image and corresponding FFT (figure 4.11 (d)) confirm the high quality of the material, the Wurtzite structure and *c*-axis orientation of the nanorods. HAADF-STEM analysis of material scraped from the substrate surface (figure 4.11 (c)) reveals that the nanorod compositions are uniform along their lengths. The length and diameter of the nanorods varies from sample to sample but are typically 1-3 µm in length with diameters distributed around 100 nm. An important feature to note is the reduction of the number of nanorods that emerges from the CBD buffer layer. Most samples show a visible reduction in the number of nanorods after the CTR-VPT deposition, as compared to the density of rods in the underlying CBD buffer layer.

4.4 Growth and nucleation of nanorods: the influence of temperature and buffer layer

During the initial stages of the CTR-VPT deposition, the furnace temperature overshoots the set point temperature by up to 140°C, before slowly approaching the target temperature. This is due to the furnace's PID controller settings in conjunction with the offset position of the furnaces' temperature probe. It was therefore important to asses whether this temperature overshoot had any impact on the nanorod growth. A manual temperature ramp program, which would allow the furnace to reach the target temperature with no overshoot was first determined and then subsequently used for CTR-VPT growth in order to identify any variations that the overshoot may causing. Figure 4.12 shows a comparison between the furnaces' measured natural temperature profile and the measured manually adjusted temperature profile. For clarity the natural temperature profile will be called the fast ramp temperature profile (FRTP) whilst the manually controlled temperature profile is called the slow ramp temperature profile (SRTP).

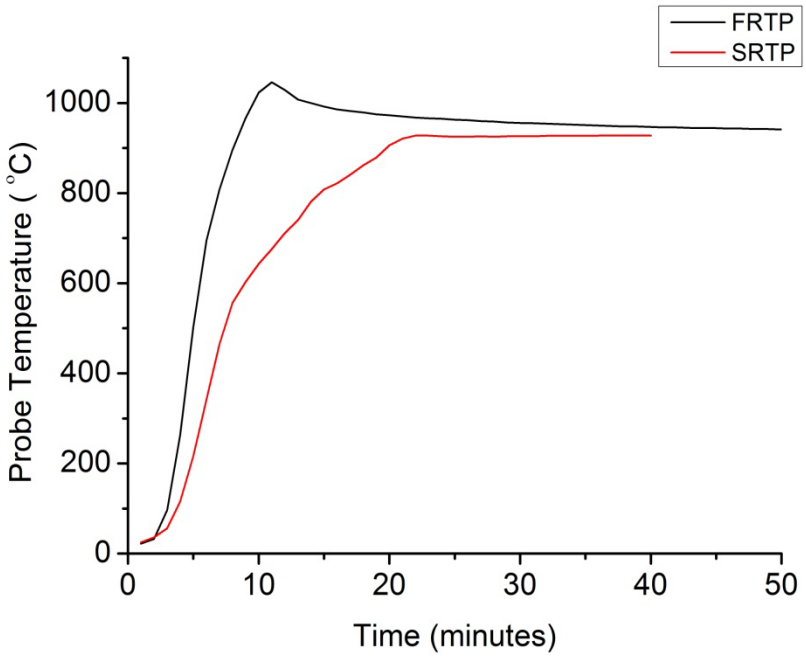

Figure 4.12: Furnace temperature profiles FRTP and SRTP used for the various CTR-VPT depositions on CBD buffer layers. Nominal set temperature 900°C.

Varying the furnace temperature profile appeared to have an influence on the morphology of the CTR-VPT deposition nanorods. The rods deposited using the SRTP, as shown in figure 4.13 appear shorter and more uniform along their entire lengths as compared to the samples grown using the FRTP. The nanorods deposited by the FRTP, using both the small and large boats appear to grow from an underlying conical base, which are formed by the fusion of several CBD nanorods. In addition to the fusion of the nanorods, Zn vapour arriving at the substrate from the CTR reaction is also being incorporated in to the conical base formation. This can be seen in the CTEM image in figure 4.11 (b). However when the temperature overshoot is eliminated, the rods appear more uniform with the growth of conical bases being suppressed. Consequently nanorods grown by the SRTP have much thinner and taller bases. The suppression of the conical base formation, suggests that the 1D growth is dominant from the start of the process, resulting from the reduced Zn vapour flux arriving at the substrate. This suggests that the temperature profile influences the change in growth conditions from 2D to 1D, which is consistent with other reports on the effect of temperature ramp on CTR-VPT growth.[19] However given that the underlying CBD buffer layer appears to undergo fewer changes compared to samples grown using the FRTP, the differences in nanorod morphology must also be due to structural changes in the CBD buffer layer induced by the two different temperature profiles. It should also be noted

that eliminating the temperature overshoot had a different effect than reducing the nominal set-point temperature. As mentioned earlier, when the set-point temperature was reduced the diameter of the rods increased. When the overshoot was eliminated no significant increase in rod diameter was observed, implying that at higher temperatures the structural changes in the buffer layer influence the final morphology. This was confirmed by performing a CTR-VPT deposition on a HCP CBD nanorod array, a more detailed description of which is given in the next chapter. The essential point to note is that prior to CTR-VPT deposition the CBD rods are not densely packed, but are spaced hundreds on nanometres apart.

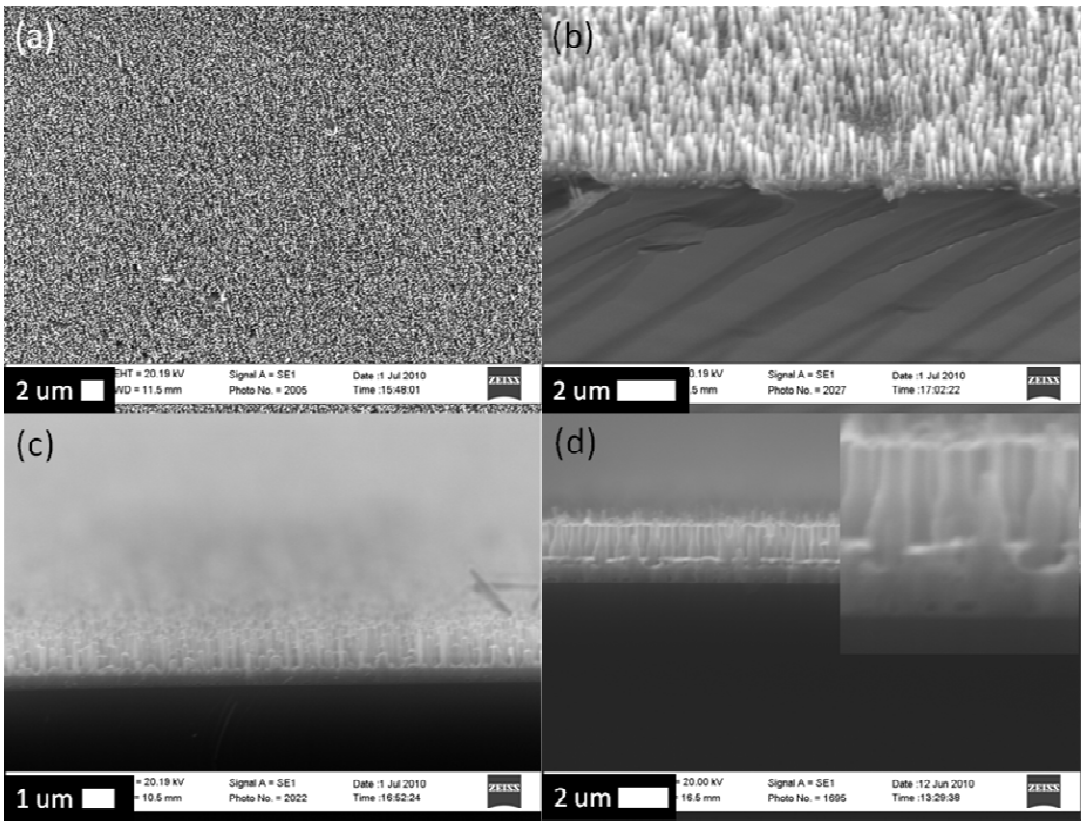

Figure 4.13: SEM images of growth using hybrid CBD/CTR technique using the SRTP. (a) Plan view (b) 45° view (c)90° view of nanorod array deposited (d) 90° view image of a HCP spaced nanorod array grown by CTR-VPT on a HCP deposited CBD nanorod array.(insert: higher magnification image showing “wine bottle” nanorod morphology)

After CTR-VPT deposition (figure 4.13 (d)), the nanorods have a wine bottle shape, where the Zn vapour coated over the CBD rods before 1D growth took place. Given that the initial spacing of the CBD rods and the clear spacing post CTR-VPT deposition, the shouldered conical base must be from the arriving Zn vapour and any structural changes

that the initial rod may have undergone. However the size of the conical base is significantly smaller that those seen where dense CBD nanorod buffer layers are used, i.e. figure 4.11 (a) compared to figure 4.13 (d). This confirms that the formation of the base of the rods is sensitive to both the arrival of Zn vapour, which is influenced by the temperature profile and the position of the substrate, and changes in the underlying buffer layer, which is also sensitive to the temperature profile. This may in part explain some of the observed morphological changes discussed in section 4.3.1.

Growth Conditions	Height (nm)	Width (nm)
FRTP (figure 4.14 a)	260 ± 40	340 ± 60
FRTP with the substrate place close to the source powder (figure 4.14 b)	510 ± 90	400 ± 70
SRTP (figure 4.14 c)	500 ± 45	125 ± 50

Table 4.1: The variation in conical base width and height for samples grown with varying conditions.

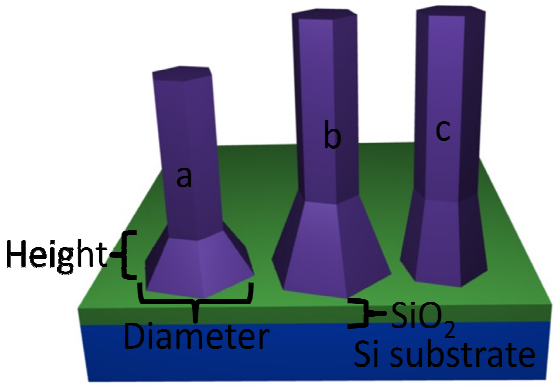

Figure 4.14: Schematic representations of the various different conical base shapes corresponding to the data shown in table 4.1

Table 4.1 and figure 4.14 summarises the morphological variations in the conical base observed for the different temperature profiles and positions. While the growth parameters have an influence on the base of the structures, no significant variations in the aspect ratio, other that those discussed in section 4.3.1 were observed. Li *et al*. reported

that both the buffer layer surface roughness and the crystallinity affects the nucleation of nanorods during CTR-VPT growth on PLD deposited buffer layers.[7] When the surface roughness was small, an intermediate continuous network was formed. With higher surface roughness, the diffusion of Zn vapour across the surface is reduced and no obvious continuous network formation was observed. While some evidence of intermediate network formation can be seen in our samples, rods also appear to grow directly from the CBD nanorods with conical bases. A comparison of the intermediate network formation observed by Li *et al.* and possible continuous networks form by our CTR-VPT deposition technique is shown in figure 4.15.

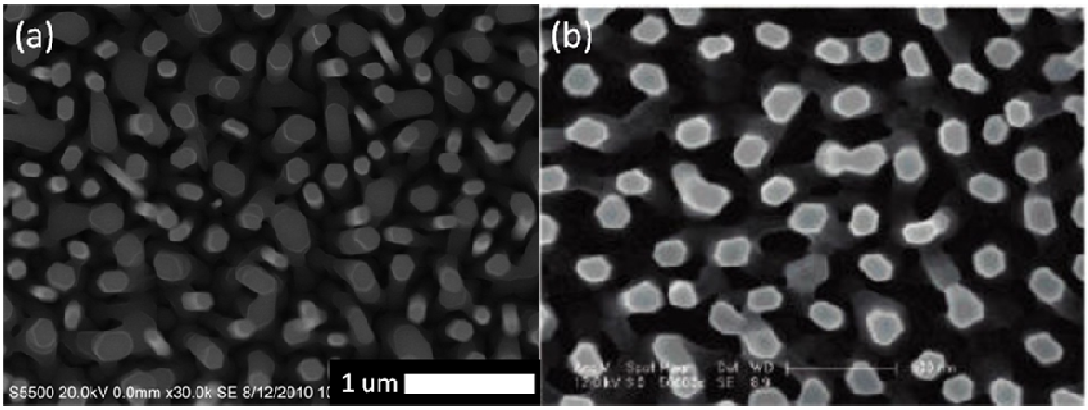

Figure 4.15: Plan view FESEM image of (a) ZnO nanorod array deposited by CTR-VPT on a CBD buffer layer in our lab (b) ZnO nanorods deposited by CTR-VPT on a PLD seed layer. Image reproduced from reference 7. Copyright: (2008) American Chemical Society

The origin of the variation in intermediate network formation versus conical base formation is not explicitly clear. However, from comparing the nanorods bases shown in figure 4.15 (a) and (b) it seems that the two are processes are related. While the network formation may result from overlapping conical bases, it may also be due to favourable nucleation ridges in the CBD buffer layer, leading to wall like structures during the high vapour saturation levels achieved in the initial stages of CTR-VPT growth. Furthermore, varying the number of drop-coats, which in turn varies the CBD buffer layer density, does not appear to significantly enhance or reduce the intermediate network formation. As mentioned in chapter 3.5.3, reducing the number of drop-coats increased the roughness of the surface, with an increase in the number of voids and gaps between the rods. However, the nucleation process is further complicated by the fact that the CBD buffer layer undergoes substantial morphological changes during CTR-VPT growth.

To further understand what happens to the CBD buffer layer during CTR-VPT growth buffer layers were annealed in identical conditions (but without Zn source material) to those used for the CTR-VPT deposition using both FRTP and SRTP. FESEM images before and after annealing can be seen in figure 4.16.

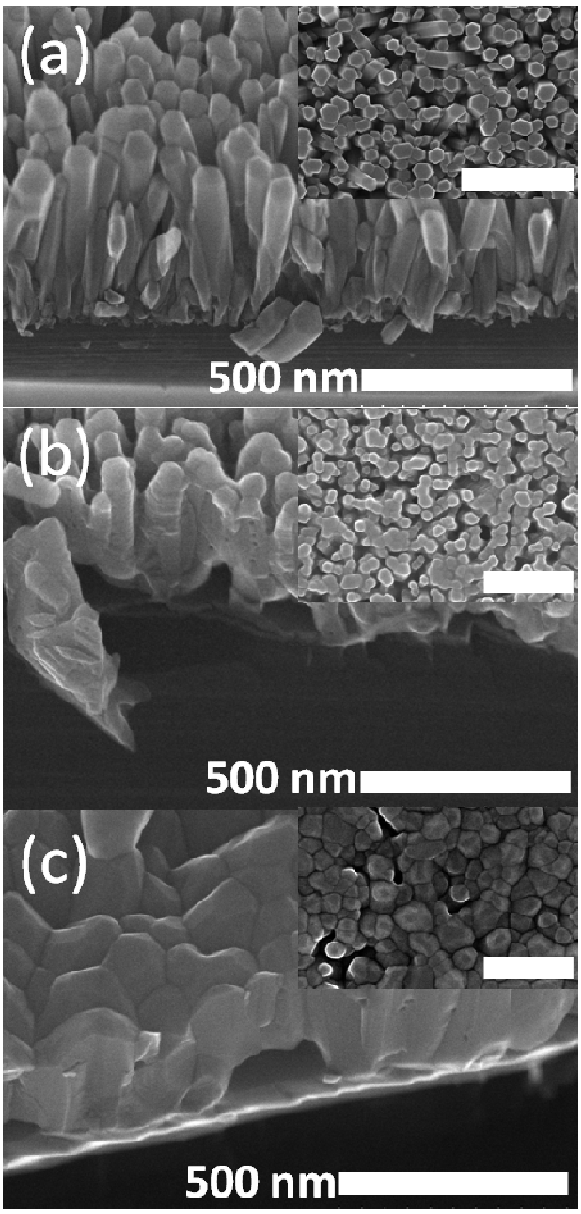

Figure 4.16: FESEM images of a CBD buffer layer (a) 30° view (insert: plan view) prior to annealing (b) post annealing using SRTP (c) post annealing using FRTP. Scale bar in all images is 500 nm

Prior to annealing, the CBD buffer layer consists of distinct hexagonal shaped nanorods, approximately 350 nm long. Post annealing using SRTP conditions, many of the rods have fused with neighbouring rods forming thicker irregular shaped structures. The

lateral facets of the rods appear rougher when compared to their unannealed counterparts. In addition, clearly faceted voids appear in the base of the CBD film. It can be seen in figure 4.16 (b) and insert that the fusing of the neighbouring rods can form fused ridges from clusters of nanorods in the buffer layer. These fused ridges may partly explain the similarity observed between the overlapping conical bases and the wetting network observed by Li *et al*. Given that these fused ridges appear in the absence of any Zn source vapour, their primary origin is due to the structural changes in the buffer layer. At the faster temperature ramp rate FRTP, the films undergo an even more dramatic transformation. The hexagonal faceting of individual rods are no longer visible, with only a granular fused film remaining. The lateral facets can no longer be observed accurately as all of the rods have substantially deformed. Thermal stress cracks formed during sample cooling are also observed, indicating the complete fusion of the CBD film.

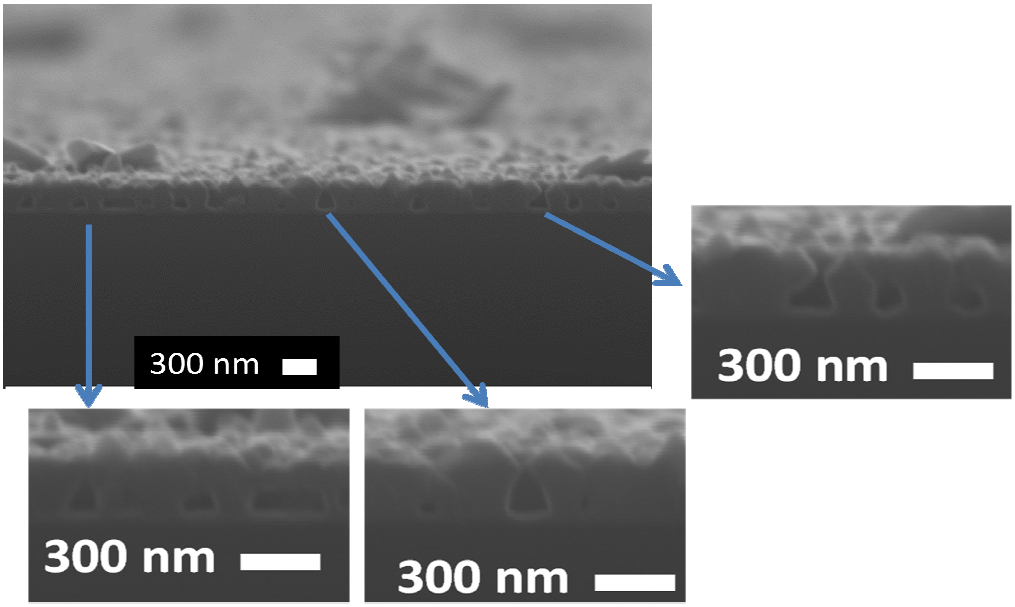

Figure 4.17: SEM images of a 90° view (cross-section) of a cleaved edge of CBD grown sample after high temperature annealing, showing the formation of faceted voids and diamond shaped structures.

Faceted voids in the buffer layer are also clearly visible and are regularly found both in CTR-VPT grown samples and SRTP annealed buffer layers. At high temperatures, the annealed layer of CBD deposited rods undergo a transformation from hexagonal shaped rods to a diamond like shape, with occasional facetted voids between structures, examples

of which are shown in figure 4.17. This transformation is most likely due to partial sublimation of the ZnO buffer and its transport along the wire length. It has been known for quite some time that the chemical etching and sublimation rate of ZnO varies between the different faces of the ZnO crystal due to the anisotropic nature of the Wurtzite crystal.[20-21] In addition, the presence of surface adsorbed impurities such as water can vary the surface free energy, further altering the initial sublimation rate of the different crystal faces.[20] While Leonard *et al.*[20] ascribed attenuated initial sublimation rates of ZnO at high temperatures to surface adsorbed impurities such as water. Ntep *et al.*[22] found that the presence of water in the gaseous mixture actually assisted the sublimation process. Given that the buffer layers are grown in solution, water and other surface impurities are undoubtedly present, leading to a reduction in the temperature necessary to achieve sublimation. In either case it is clear that the various facets of ZnO can undergo sublimation at different rates and that the reported temperatures necessary for sublimation to occur are achieved in our experiments. However, care is required in interpreting the results observed during the annealing experiments. During the CTR-VPT process, the higher vapour pressure coming from the source may limit the sublimation yield, thereby reducing the degree of structural transformation in the buffer layer as compared to the annealed buffer layers.

To compound the complexity of the structural transformations observed, it has been reported that ZnO nanostructures can have melting temperatures well below that of the bulk material.[23-25] At present this phenomenon is poorly understood. Using the theoretical model put forward by Guisbiers *et al.*[26] as described by the equation:

$$\frac{T_m}{T_{m\infty}} = 1 + \frac{(\gamma_l - \gamma_s)}{\Delta H_{m\infty}} \frac{A}{V} \tag{4.4.1}$$

where T_m is the predicted melting temperature, $T_{m\infty}$ is the bulk melting temperature, $(\gamma_l - \gamma_s)$ is the difference in surface tension between the liquid and solid phase (using the maximum and minimum of the published values), $\Delta H_{m\infty}$ is the melting enthalpy and A/V is the ratio of surface area to volume. This yields a predicted melting temperature range of 1764 - 1883°C for hexagonal nanorods with a 20 nm side length and height of 300 nm. This predicted temperature is well above the temperatures reached during our experiments, even including any error associated with the temperature overshoot. However partial

melting cannot be completely ruled out as the cause of the structural transformations and faceted void formation, as other reports have indicated that nanoparticles can (partially) melt at temperatures significantly lower than those predicted by Guisbiers's model.[23] Regardless of the precise microscopic mechanism, the key point is that the material moves from the upper basal facet and prismatic facets of the nanorod and deposits on the pyramidal facets during CTR-VPT growth / annealing, creating diamond shaped structures, leading to the partial fusing of several wires. As the redistribution of ZnO also happens during annealing where no additional Zn source vapour is being provided, it must be the case that an important aspect affecting the increase in rod diameter during CTR-VPT growth must be from material already present. The fused CBD rods provide a wider base on which the subsequent CTR-VPT deposition and coverage occurs to create the conical bases. These conical bases may not be perfectly symmetrical as they depend on the specific distribution of nanorods in the buffer layer and how they are affected by the fusing process. Consequently, bases can fuse to form structures similar to the wetting layer observed by Li *et al*.[7] Depending on the supersaturation levels in CTR-VPT step, the growth mode reverts back to 1-D more or less quickly, thus affecting the shape of the cone at the base of the nanorods. In addition the lower peak temperature reached during the SRTP, reduces the structural transformation of the underlying buffer layer, reducing the amount of wire fusion, resulting in smaller conical bases from which the nanorods emerge. Despite the conflicting reports on the influence of melting on ZnO nanostructures at temperatures less than bulk values, we believe that this transformation is primarily due to the partial sublimation, transport and redeposition of the ZnO in the nanorods because a similar effect is observed at the base of the CBD rods.

Sharp faceted edges have been observed at the interface between the SiO_2 and the nanorod bases, which is not seen prior to high temperature treatments (compare figure 4.18 (a) and 4.18 (b)), which would suggest that the interface is formed by the transport/diffusion of Zn vapour rather than the transport of material by amorphous liquid droplets. During annealing ZnO is also removed from planes of the rod base and subsequently diffuses into the silica interface layer, as shown by the schematic in figure 4.18 (c). The thermal induced structural transformation is clearly also responsible for the void formation. During CTR-VPT growth or annealing, the newly forming diamond like rods can come into contact with neighbouring rods and fuse along their sides, creating faceted caverns in the buffer layer. The various stages of this process can be seen in the figure 4.17.

As a consequence, the formation of voids in the buffer layer during CTR-VPT growth is dependent on the density of the CBD deposited buffer layer prior to growth which in turn is dependent on the number of drop-coats used to prepare the seed layer and the growth conditions during the CBD deposition step.[27-28]

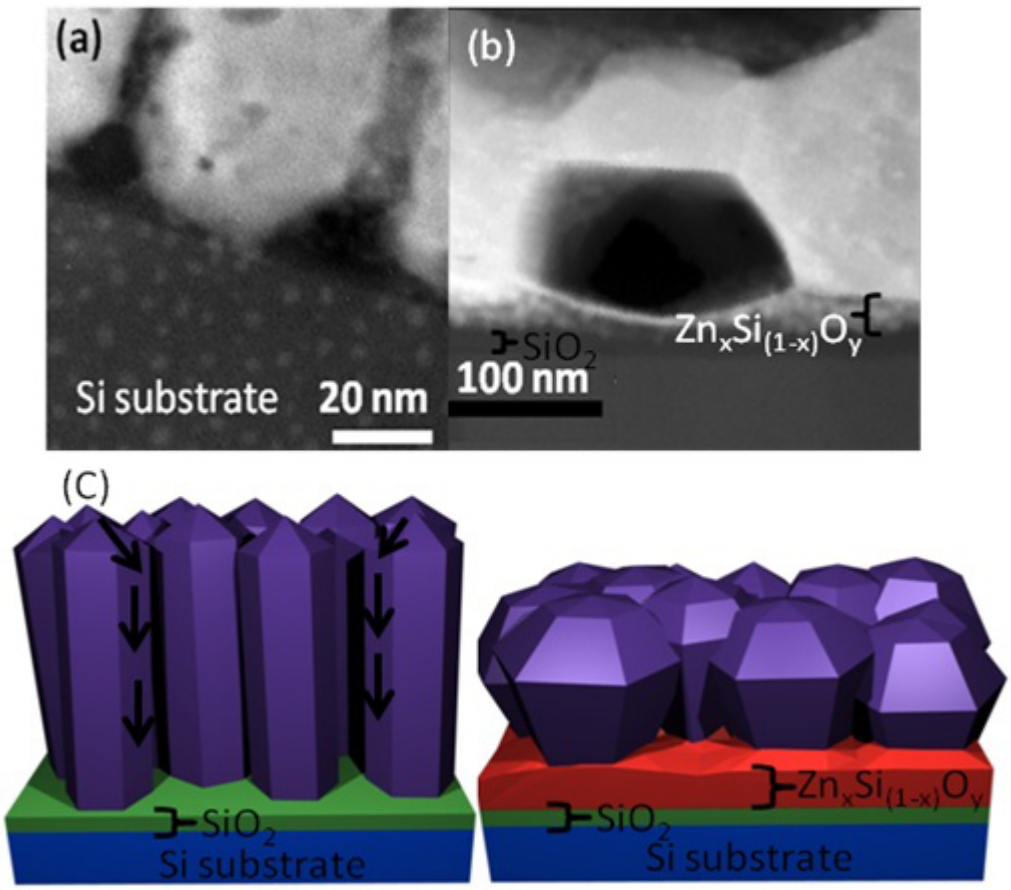

Figure 4.18: HAADF-STEM images of (a) the base of a CBD nanorod prior to CTR-VPT deposition (b) of a faceted void formed in an annealed CBD buffer layer (c) schematic representation of the diffusion of material along the CBD buffer layer during CTR-VPT growth / annealing. (Images (a)(b) acquired by UCA Cadiz collaborators)

4.5 Effect of CTR-VPT on the substrate / nanorod interface

In this work no attempt was made to remove the native oxide of the silicon substrate. As discussed in chapter 3, a thin SiO_2 layer is present between the silicon substrate and the CBD grown buffer layer and that this intermediate layer is relatively undisturbed by the CBD process, as shown in figure 3.13. Consequently, the bases of the CBD nanorods are generally flat with respect to the native oxide and are of good crystalline quality. After CTR-VPT growth or any annealing process the nature of this intermediate layer changes becoming thicker and is composed of two different regions with three distinct interfaces. These individual interfaces can be identified by the varying contrasts in HAADF-STEM image across the interface shown in figure 4.20 (b). Figure 4.19 shows a HRTEM micrograph of the interface between the nanorods grown via the SRTP clearly showing the onset of the ZnO nanorod. The corresponding FFT indicate that the base of the rod has a good crystalline structure. Just below the onset of the nanorod, dark shadows appear in the amorphous silica intermediate layer, which is an equivalent position to location 2 in figure 4.20 (b). These shadows yield weak diffraction spots implying the formation of a mixture of crystalline phases in this amorphous region of the silica.

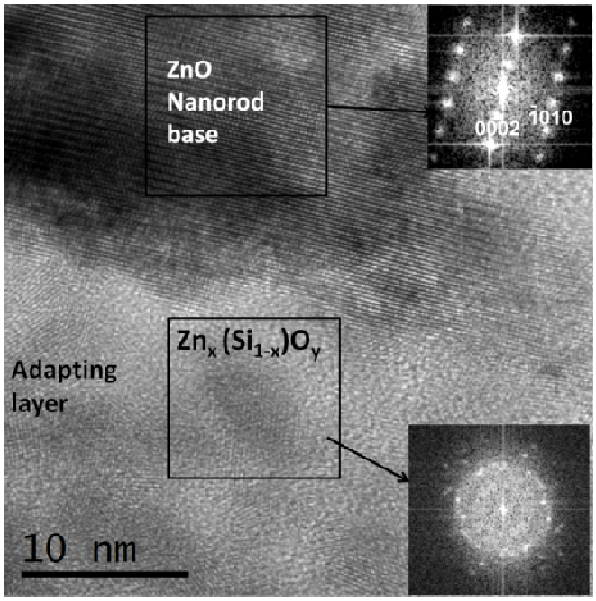

Figure 4.19: HRTEM of a CTR-VPT grown sample at the SiO_2-ZnO interface and corresponding FFT of the SiO_2 and ZnO regions. (Images acquired by UCA Cadiz collaborators)

The two distinct layers that make up the amorphous silica intermediate layer were examined by EELS and EDX. EDX analysis of a profile across the intermediate layer from the substrate shows that dominant component is not Zn but amorphous SiO_2. The individual spatially resolved EEL spectra across the interface (figure 4.20(a)) display the characteristic signal of the Zn-L and O-K edges. They indicate that a sharp interface between the silicon and SiO_2 exists, which is also clearly visible in the HAADF-STEM image in figure 4.20 (b). From the SiO_2 layer, the oxygen signal gradually decreases until it has reached a steady value corresponding to the onset of the ZnO nanorod (region 1). The Zn-L signal begins before the O-K signal has reached this steady state (region 2) suggesting that either the base of the nanorod is oxygen rich compared to the bulk of the rod or that the area also contains a significant amount of other oxygen containing species. Thus, when scanning the sample from the substrate to the ZnO base, the Zn-L edge signal doesn't vary significantly but the O-K signal of the recorded spectra does experience a progressive red-shift in the intermediate layer, more clearly highlighted by the arrows marking the peak position in the insert in figure 4.20 (a).

In addition, the Si-L signal taken at the same area also undergoes a strong signal modification between the Si substrate and the intermediate layer (figure 4.20 (c) region 4 as compared with the other regions) and moreover, a slight peak change with decreasing energy when comparing the two sub-layers defined inside the intermediate layer (region 2 with respect to region 3). This suggests that the area observed is something more than ZnO polycrystalline particles immersed in an amorphous SiO_2 matrix and that new zinc silicate species are formed where the oxidation state of Si and Zn atoms remain constant. Up to three different compounds combining Zn-Si-O have been reported.[29] Nevertheless, the accepted phase diagram of ZnO-SiO_2 only considers the thermodynamically stable intermediate compound Zn_2SiO_4 (Willemite), which melts congruently at 1512 °C and forms two eutectics with SiO_2 and with ZnO.[30] Hence, the most probable compound is Zn_2SiO_4, which can be formed at 770 °C. Furthermore, FFT reconstruction of HRTEM images for several SiO_2-ZnO interfaces reveal the existence of intense spots with interplanar spacing in agreement with the values for Zn_2SiO_4 crystals. Based on these results, we propose that a mixed crystal of ZnO, SiO_2 and Zn_2SiO_4 occurs in this region. Similar results of the mixed formation of Zn_2SiO_4 crystal and amorphous SiO_2 during annealing treatments have been reported in annealed ZnO/Si systems.[31] Taking into account all the EELS and HRTEM data,

we conclude that the intermediate layer follows this stacking sequence: Si / SiO_2 / Zn_2SiO_4 – ZnO immersed in SiO_2/ ZnO.

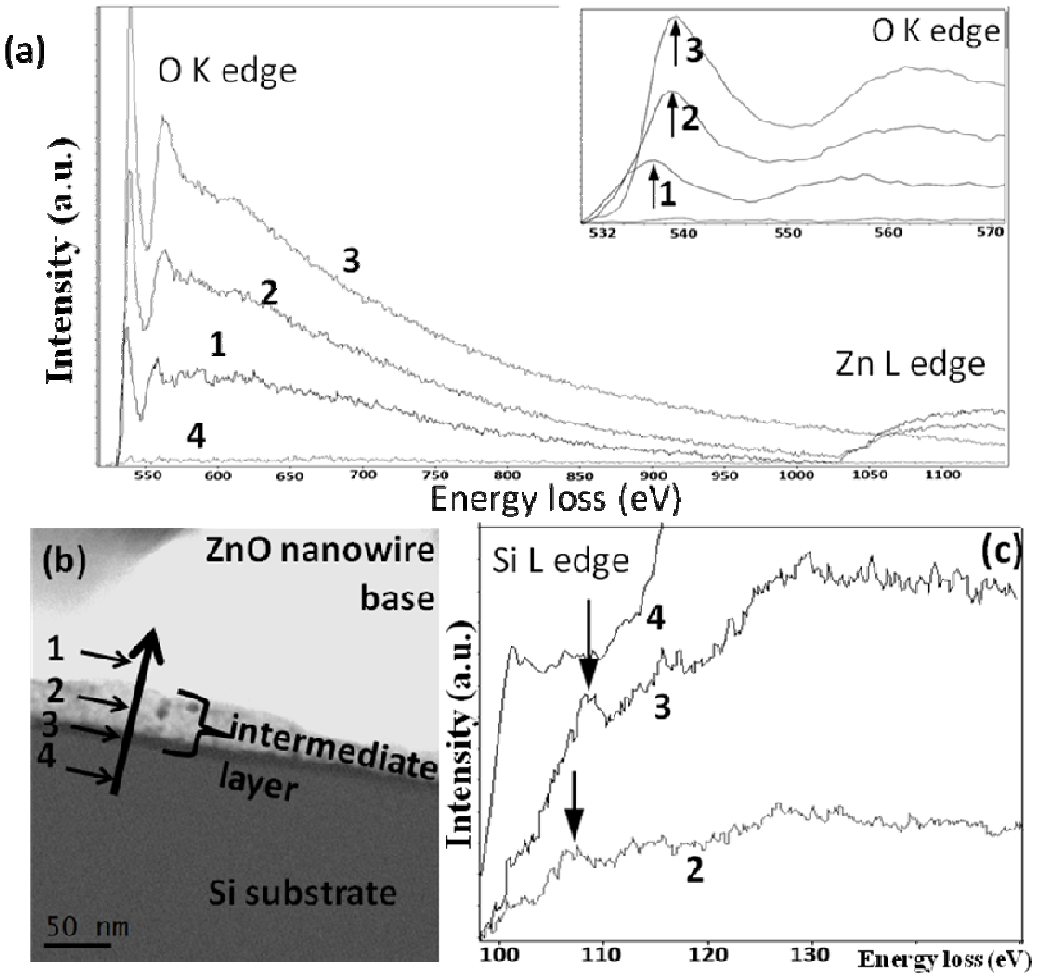

Figure 4.20: a) Individual core loss EEL spectra from several points at the Si substrate/wires interface, which are labeled in b), HAADF-STEM image of this region. The regions 1-4 correspond to ZnO wire base, $Zn_xSi_{1-x}O_y$, SiO_2 layers and Si substrate, respectively. c) Low loss spectra of this same region, exhibiting different Si-L signals. (Images acquired by UCA Cadiz collaborators)

The amorphous intermediate layer has also been observed for samples annealed without CTR-VPT growth, indicating that the presence of Zn in the intermediate layer is not solely due to Zn vapour from the carbothermal reduction reaction. In fact, the close similarity between samples either annealed or following CTR-VPT growth indicates that the main source of Zn in the intermediate layer is probably due to a partial consumption of the CBD deposited rods into the interface. With this in mind it is interesting to note that there are some differences observed in the intermediate layers between samples grown by CTR-

VPT at both temperature ramp rates and those by CBD followed by annealing as shown in figure 4.21. The interface layer of samples annealed using the FRTP is significantly rougher that those grown by CTR-VPT using the FRTP. The most uniform interface layer is achieved with the lower temperature ramp rate, thus optimising the interface between the substrate and the rod. The thickest interface layer occurs in samples grown by CTR-VPT with the FTRP. This is attributed to the higher temperatures achieved from the beginning of the step, which in turn leads to a more rapid growth of the ZnO/SiO_2 intermediate layer. The most uneven intermediate layers are observed in the samples annealed without the source powder suggesting that the Zn vapour has a moderating effect on the oxygen partial pressure leading to a more uniform growth of the SiO_2 interface. The most uniform intermediate layers were obtained using the STRP.

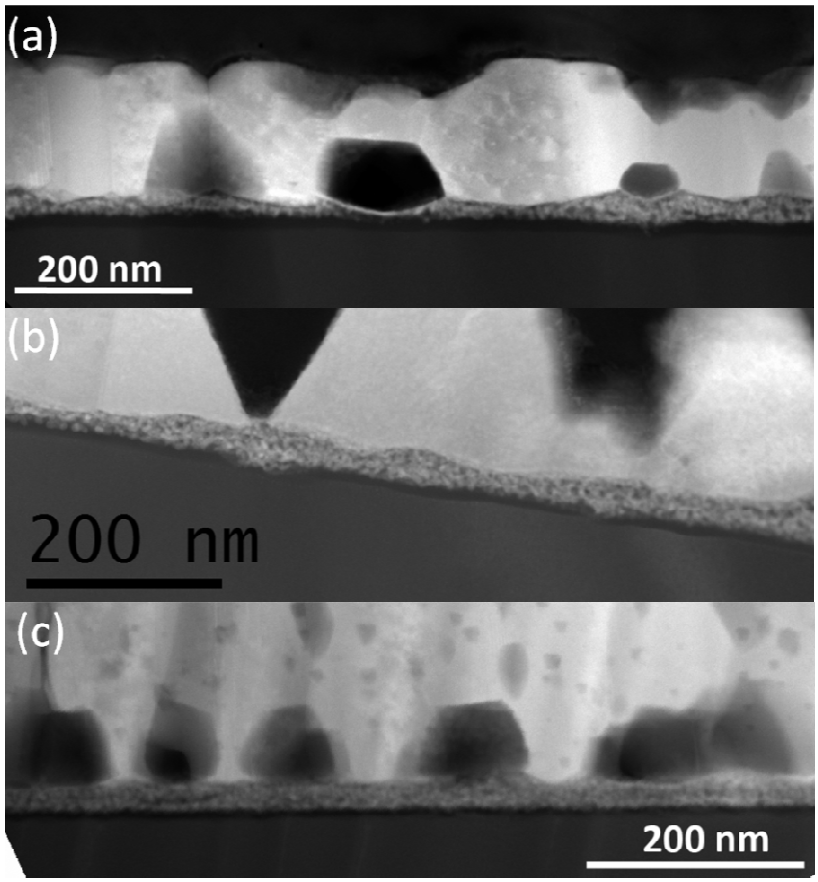

Figure 4.21: HAADF-STEM Images of (a) FRTP annealed CBD buffer layer showing rough and non uniform interface (b) FRTP VPT deposited nanorods on CBD buffer layer showing conical base and more uniform interface layer (c) SRTP deposited nanorods on CBD buffer layer showing very uniform interface layer.

4.6 Conclusions

In this chapter we have demonstrated a facile method of depositing *c*-axis aligned ZnO nanorords on non-epitaxially matched substrates without the use of catalysts, using a combination of CBD deposition with a CTR-VPT technique. While the deposition process itself may be straight forward it was found that many factors which influence the final morphology are occurring simultaneously, resulting in a process which is substantially more complex than it initially appears.

It was found that thin seed layers deposited by drop-coating solutions of zinc acetate, whilst suitable for nucleating growth in low temperature CBD process, were unsuitable for high temperature CTR-VPT. At high temperatures the silicon native oxide grows up, enveloping the thin and porous seed layer, rendering the seeds inactive for subsequent nucleation of nanorods. At the substrate edges, where the seed layer is thinker, the seeds coalesce to form rounded ridges. While nanorods can nucleate and grow on these ridges, the *c*-axis alignment is lost. Increasing the number of drop-coats prior to the CTR-VPT deposition, results in complete coverage of unaligned nanorods. By using thicker buffer layers deposited by CBD by a variety of techniques, to initiate nucleation, high quality *c*-axis aligned nanorod arrays can be deposited quickly and inexpensively.

The CTR-VPT deposition process can be performed on CBD buffer layers prepared by a number of different techniques, including the HMT, NaOH and acetate methods described in chapter 3. The final morphology of the CTR-VPT deposited nanorods is influenced by a complex interplay of varying factors, such as the Zn vapour concentration, the temperature, the buffer layer density, the position of the sample and boat size used. The Zn vapour concentration determines whether 2D or 1D growth takes place. This in turn is affected by the furnace temperature, the position of the sample and the porosity of the source powder, not to mention a host of other parameters not examined in this work, such as argon flow rate, the masses of source powder used and the oxygen concentration. The high furnace temperature during deposition can also cause individual nanorods to undergo structural changes due do to partial anisotropic sublimation of the nanorods. The structural changes of the rods can cause them to fuse with neighbouring rods creating large nucleation areas resulting in conical bases or ridged structures at the base of the nanowires. When dense CBD nanorod buffer layers are used in the CTR-VPT process fusing of neighbouring rods also leads to the formation of faceted voids in the buffer layer. During

the CTR-VPT deposition process the silicon native oxide layer grows, which can then react with the ZnO buffer layer at high temperatures leading to the formation of a second phase within the interface between the nanorods and the substrate. Specifically, these reactions lead to the formation of complex interface described by the stacking sequence: Si / SiO_2 / Zn_2SiO_4 – ZnO immersed in SiO_2/ ZnO.

4.7 References

(1) Geng, C. Y.; Jiang, Y.; Yao, Y.; Meng, X. M.; Zapien, J. A.; Lee, C. S.; Lifshitz, Y.; Lee, S. T. *Adv Funct Mater* **2004,** *14* (6) 589-594

(2) Biswas, M.; McGlynn, E.; Henry, M. O. *Microelectron J* **2009,** *40* (2) 259-261

(3) Biswas, M.; McGlynn, E.; Henry, M. O.; McCann, M.; Rafferty, A. *Journal of Applied Physics* **2009,** *105* (9) 094306

(4) Yang, P. D.; Yan, H. Q.; Mao, S.; Russo, R.; Johnson, J.; Saykally, R.; Morris, N.; Pham, J.; He, R. R.; Choi, H. J. *Adv Funct Mater* **2002,** *12* (5) 323-331

(5) Greene, L. E.; Law, M.; Tan, D. H.; Montano, M.; Goldberger, J.; Somorjai, G.; Yang, P. D. *Nano Letters* **2005,** *5* (7) 1231-1236

(6) Park, D. J.; Kim, D. C.; Lee, J. Y.; Cho, H. K. *Nanotechnology* **2006,** *17* (20) 5238-5243

(7) Li, C.; Fang, G. J.; Li, J.; Ai, L.; Dong, B. Z.; Zhao, X. Z. *J Phys Chem C* **2008,** *112* (4) 990-995

(8) Li, C.; Fang, G.; Fu, Q.; Su, F.; Li, G.; Wu, X.; Zhao, X. *Journal of Crystal Growth* **2006,** *292* (1) 19-25

(9) Grabowska, J.; Meaney, A.; Nanda, K. K.; Mosnier, J. P.; Henry, M. O.; Duclere, J. R.; McGlynn, E. *Phys Rev B* **2005,** *71* (11) 115439

(10) Kang, D.-S.; Han, S. K.; Kim, J.-H.; Yang, S. M.; Kim, J. G.; Hong, S.-K.; Kim, D.; Kim, H.; Song, J.-H. *Journal of Vacuum Science and Technology B* **2009,** *27* (3) 1667-1672

(11) Zhi, Z. Z.; Liu, Y. C.; Li, B. S.; Zhang, X. T.; Lu, Y. M.; Shen, D. Z.; Fan, X. W. *J Phys D Appl Phys* **2003,** *36* (6) 719-722

(12) Hong, R. J.; Huang, J. B.; He, H. B.; Fan, Z. X.; Shao, J. D. *Applied Surface Science* **2005,** *242* (3-4) 346-352

(13) Ozena, I.; Gulgunb, M. A. *Advances in Science and Technology* **2006,** *45* 1316-1321

(14) Lim, Y. S.; Park, J. W.; Kim, M. S.; Kim, J. *Applied Surface Science* **2006,** *253* (3) 1601-1605

(15) Law, M.; Greene, L. E.; Johnson, J. C.; Saykally, R.; Yang, P. D. *Nature Materials* **2005,** *4* (6) 455-459

(16) Zhou, Y.; Wu, W. B.; Hu, G. D.; Wu, H. T.; Cui, S. G. *Materials Research Bulletin* **2008,** *43* (8-9) 2113-2118

(17) Zhao, Q. X.; Yang, L. L.; Willander, M.; Sernelius, B. E.; Holtz, P. O. *Journal of Applied Physics* **2008,** *104* (7) 073526

(18) Kumar, R. T. R.; McGlynn, E.; Biswas, M.; Saunders, R.; Trolliard, G.; Soulestin, B.; Duclere, J. R.; Mosnier, J. P.; Henry, M. O. *Journal of Applied Physics* **2008,** *104* (8) 084309-084311

(19) Kumar, R. T. R.; McGlynn, E.; Mcloughlin, C.; Chakrabarti, S.; Smith, R. C.; Carey, J. D.; Mosnier, J. P.; Henry, M. O. *Nanotechnology* **2007,** *18* (21) 215704

(20) Leonard, R. B.; Searcy, A. W. *Journal of Applied Physics* **1971,** *42* (10) 4047-4054

(21) Iwanaga, H.; Yoshiie, T.; Yamaguchi, T.; Shibata, N. *Journal of Crystal Growth 47* (5-6) 703-711

(22) Ntep, J. M.; Barbé, M.; Cohen-Solal, G.; Bailly, F.; Lusson, A.; Triboulet, R. *Journal of Crystal Growth* **1998,** *184-185* 1026-1030

(23) Su, X.; Zhang, Z. J.; Zhu, M. M. *Applied Physics Letters* **2006,** *88* (6) 061913

(24) Yan, Z.; Ma, Y.; Wang, D.; Wang, J.; Gao, Z.; Wang, L.; Yu, P.; Song, T. *Applied Physics Letters* **2008,** *92* (8) 081911

(25) Yan, Z.; Zhu, K.; Chen, W. P. *Applied Physics Letters* **2008,** *92* (24) 241912

(26) Guisbiers, G.; Pereira, S. *Nanotechnology* **2007,** *18* (43) 435710

(27) Govender, K.; Boyle, D. S.; Kenway, P. B.; O'brien, P. *J Mater Chem* **2004,** *14* (16) 2575-2591

(28) Lee, Y. J.; Sounart, T. L.; Liu, J.; Spoerke, E. D.; Mckenzie, B. B.; Hsu, J. W. P.; Voigt, J. A. *Cryst Growth Des* **2008,** *8* (6) 2036-2040

(29) Xu, X.; Guo, C.; Qi, Z.; Liu, H.; Xu, J.; Shi, C.; Chong, C.; Huang, W.; Zhou, Y.; Xu, C. *Chemical Physics Letters* **2002,** *364* (1-2) 57-63

(30) Jak, E.; Degterov, S.; Wu, P.; Hayes, P. C.; Pelton, A. D. *Metall Mater Trans B* **1997,** *28* (6) 1011-1018

(31) Xu, X. L.; Wang, P.; Qi, Z. M.; Ming, H.; Xu, J.; Liu, H. T.; Shi, C. S.; Lu, G.; Ge, W. K. *J Phys-Condens Mat* **2003,** *15* (40) L607-L613

Chapter 5: Nanosphere Lithography

5.1 Introduction

In this chapter we present a method for depositing ZnO nanorods, controlling both the alignment with respect to the substrate and the position of the nanorods, using a self-assembled nanosphere template in conjunction with CBD and CBD / CTR-VPT deposition techniques. For certain applications such as field emission and optoelectronic applications, not only is it important to have nanorods of high quality and a high degree of alignment, it is also necessary to control the nanorod density and/or position.[1-3] Control of this nature has previously been demonstrated for ZnO and other materials using approaches such as nanosphere lithography (NSL), laser interference lithography and carbonised photoresist lithography.[2, 4-10] Significant progress has been made in depositing ordered arrays by low temperature techniques such as CBD in combination with photoresists,[9-10] while higher temperature techniques such as CTR-VPT represent a greater challenge due the harsh processing temperatures necessary for the deposition of high crystalline quality and optically bright ordered arrays. Consequently many of the reports dealing with ordered and aligned high temperature deposited arrays use selective positioning of catalysts such as Au to control the nanorod positioning,[5-7, 11-12] while relying on epitaxial matching between the substrate and the deposited material to achieve nanorod alignment. This limits the choice of substrates to those that have sufficiently close epitaxial matching to achieve alignment, while the presence of a catalyst can lead to both nanowire contamination as well as changes in morphology which can be detrimental for applications such as field emission where sharp facet edges may be crucial to performance.[3, 13]

Nanosphere lithography is a promising technique for the formation of periodic arrayed masks. These masks can be used in-situ, as templates for the synthesis of periodic structures of various materials. There have been many reports of successful applications of nanosphere-lithography to control the position of nanorod growth.[5, 7, 11, 14-15] Most of these reports rely on using the assembled nanosphere arrays as a mask to during the deposition of catalysts such as Au and Ni for subsequent growth using CTR-VPT techniques. In our work we have examined the possibility of growing ZnO nanorod arrays directly through the pores created by the nanosphere mask and creating secondary inverse masks, so that growth only takes place at the previously masked contact point between the spheres and substrate. This is an important advancement, as it allows us to grow nanorod arrays free from metal catalysts, where the position of individual nanorods or overall density can be independently controlled, using an inexpensive self-assembly technique.

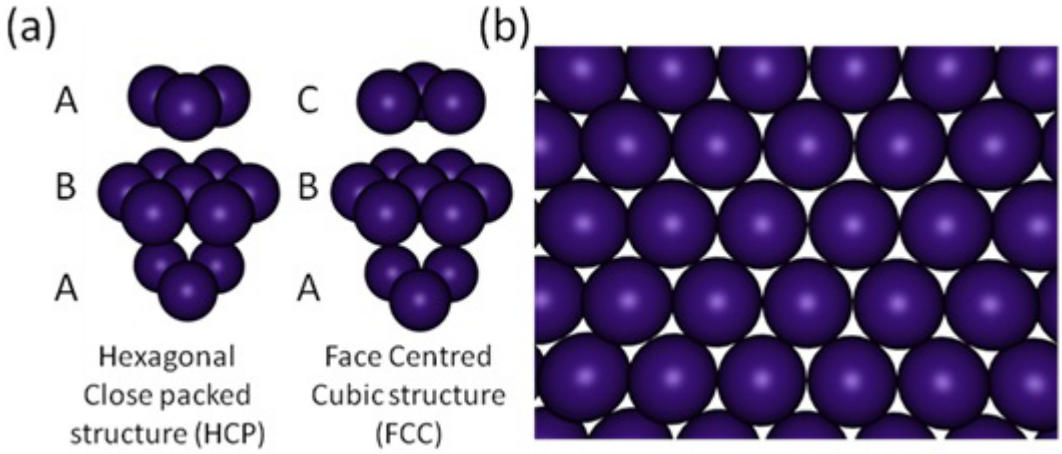

Figure 5.1: Schematic representations of (a) HCP packing and FCC packing structures (b) Top down view of the apertures created by spheres in a HCP monolayer.

Nanosphere lithography is based on exploiting the natural tendency of some materials to self-assemble into particular formations. It is normally based on creating a monolayer of spheres, although there are some reports of bi- and tri- layers of spheres being used.[14] When a monolayer of uniform spheres are forced together the highest density or packing fraction spheres that can be achieved is 0.74. This configuration is achieved by the Hexagonal Close Packed (HCP) and Face-Centred Cubic configurations (FCC). Both the HCP and FCC have identical configurations in a single layer and differ only in how the monolayers are stacked. Figure 5.1 shows the maximum packing fraction of spheres.

The HCP configuration is used as a mask for material deposition as it forms gaps or apertures between the spheres whose size and position is related to the diameter of the spheres used. Hence nanosphere-lithographic methods are often used when it is desirable to control the position of a structure relative to other similar structures grown, during a deposition step. There have been a wide variety of methods published to generate self-assembled nanosphere monolayers, including controlled evaporation of colloidal solutions,[16] dip-coating,[17] controlled spreading,[18] spin coating[19] and self-assembly on the surface of water[14, 20] to name but just a few of the techniques published. While each of these methods appears distinctly different, each have a common property in that a force acts upon the spheres to drive them into their maximum density configuration and it is the nature of this force that it is varied by the different techniques. During the controlled evaporation methods such as dip-coating, controlled spreading and controlled evaporation, convective flows similar to those discussed in chapter 3 drive the spheres together at the solvent drying front. In the spin coating methods the centrifugal force of the spinning motion drives the spheres closer together to generate the HCP structure. In this work it was found that the simplest method was that developed by by Rybczynski *et al.*[14]This technique utilises the repulsive forces between a solvent and spheres; such as the hydrophobicity interaction between polystyrene and water. In this technique, nanospheres gently applied to the surface of water self-organise and pack into the lowest possible area, creating the HCP patterned colloidal monolayer. This monolayer can then be coated from the surface of the water solution onto substrates.

5.2 Self-assembly of nanospheres

In this work three different methods of assembling colloidal nanosphere solutions into HCP monolayers were examined. Of the three methods described in section 2.5.1 for creating HCP monolayers on substrates, method 3 (self-assembly on the surface of water) was by far the most successful. Method 1 (spin coating) had many unknown factors such as the ideal concentration of spheres, optimum spin speed during coating and the optimum volume of nanosphere solution to use. Some monolayer regions were observed on the substrates but they were generally small, with large proportions of the substrates having bi and tri layers. Method 1 also requires the substrates to be pre-treated with a piranha solution, which is incompatible with the ZnO buffer layers required to initiate ZnO nanorod

growth in subsequent depositions and so this method was deemed unsuitable for our purposes. Method 2, based on drop-coating methanol/surfactant/nanosphere solutions, was considerably more successful than the spin coating technique. The lack of variable parameters made this technique easy to replicate and reasonable results were quickly obtained. Figure 5.2 (a) & (b) show SEM images of HCP monolayers obtained by method 2. Monolayer coverage extends over tens of μm^2, with small regions of bi-layer coverage scattered through out the monolayer. At higher magnification (figure 5.2 (b)) it can be seen that the domain sizes of the HCP regions are generally quite small, with many faults such as domain boundaries, gaps and missing spheres. The drop-coating method only covers a fraction of the substrate, with a large proportion remaining bare. This limiting factor reduces the usefulness of this technique if complete substrate coverage is required.

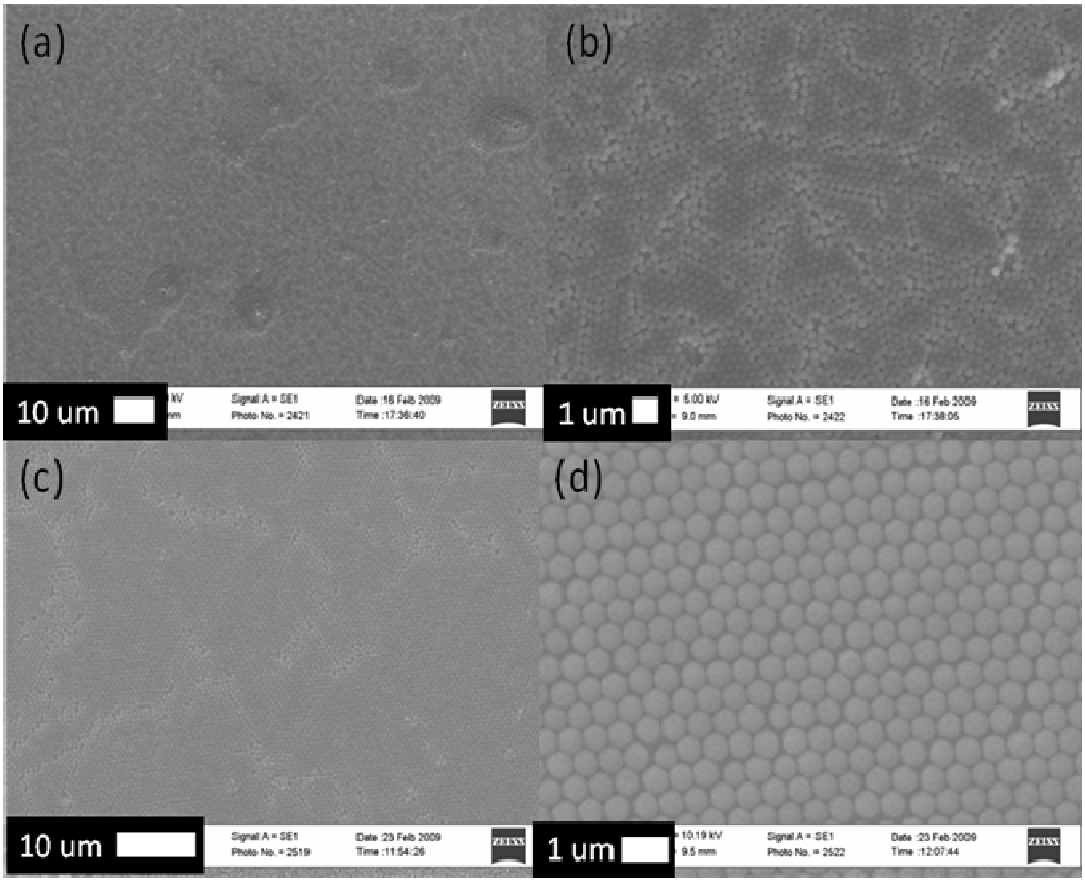

Figure 5.2: SEM images of (a) Plan view (b) higher magnification plan view of nanospheres deposited using method 2 (drop-coating) (c) Plan view (d) higher magnification plan view of nanospheres deposited using method 3 (assembly on the surface of water)

In method 3 by gently applying an ethanol/water/nanosphere solution to the surface of water, the nanospheres become trapped on the surface water due to their

hydrophobic character. On the surface of the water they naturally self-assemble into large colloidal monolayers, which can then be transferred on to substrates by gently lifting the substrates through the colloidal monolayers. A schematic representation of this process is shown in chapter 2 figure 2.4. Using this technique colloidal crystals have been prepared up to several cm^2 in size, suitable for complete coverage of substrates of a similar area. The domain sizes of the individual HCP regions in the colloidal crystals can vary from μm^2 to mm^2, larger than either of the two previously discussed methods. Substrates coated in this manner (as shown in figure 5.2 (c) & (d)) are free from bi and tri layers, with fewer domain boundaries and defects.

5.3 Spheres as templates for growth

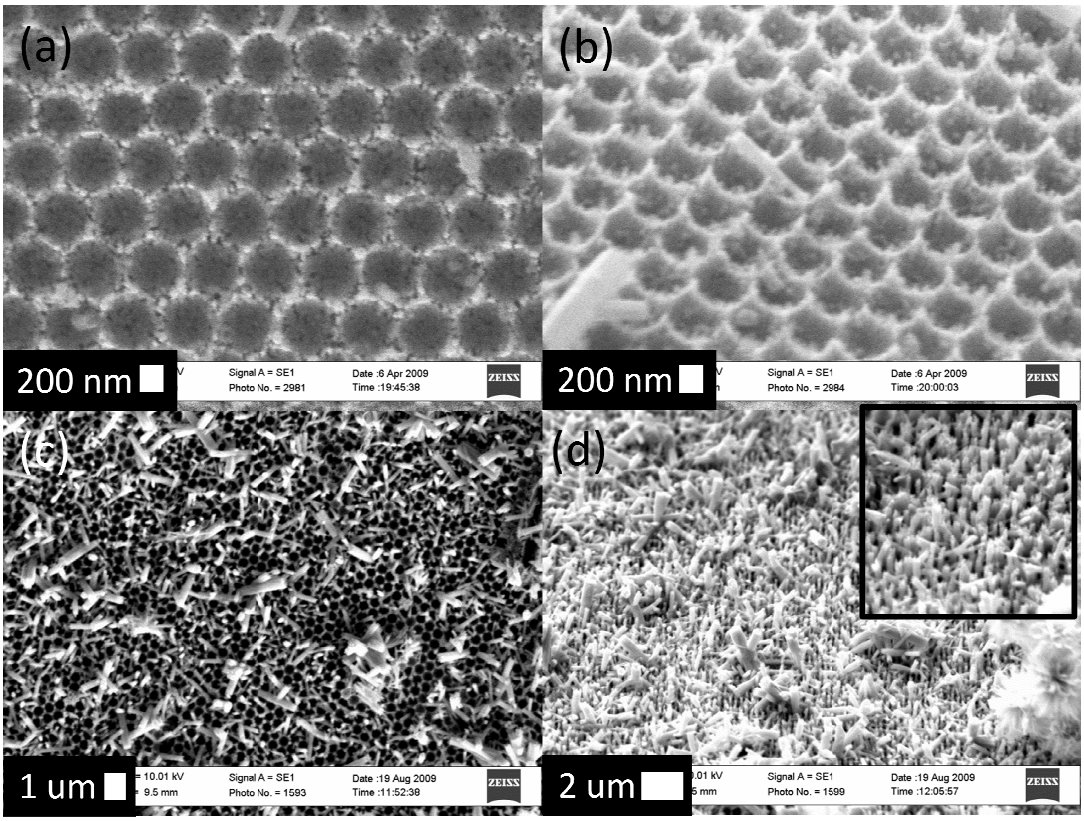

Figure 5.3: (a)Plan view (b) 45° view of ZnO HCP structure grown by CBD through nanosphere array (c)Plan view (d) 45° view of ZnO HCP structure grown by CBD through nanosphere array using extended growth times and bath changes (insert: higher magnification view of nanorods grown in a spatially ordered array)

HCP nanosphere monolayers deposited on ZnO seeded substrates were assessed for their suitability as lithographic masks during chemical bath depositions using the HMT and

NaOH and acetate CBD methods. When nanorods arrays were grown via the HMT method, it was found that the reaction conditions were suitably mild for the nanosphere mask to stay adhered to the substrate. In the early stages of the deposition, ZnO growth took place around the nanospheres, forming a porous mesh, mirroring the HCP structure. As growth of the nanorods continued, the rods under the contact points between the spheres ceased to grow while rods located at the aperture points between the spheres continued. By extending the growth time and refreshing the deposition bath solution, it was possible to grow individual nanorods out through the apertures created by the nanospheres creating a spatially organised well aligned nanorod array. However due to the large inter-rod spacing, a large mass of undesired debris becomes trapped in the nanorod array which is difficult to remove, an example of which can be seen in figure 5.3 (d). Whilst sonicating the substrate did in part remove the trapped precipitate, it typically removed part or all or the ordered array in the process. This would suggest that the sonication power was sufficiently strong to remove the well separated nanorods.

The NaOH based CBD method was incompatible with the polystyrene nanosphere monolayer. In all attempts, the monolayer delaminated within the first few minutes of submerging the substrate in the reaction solution. In many cases the monolayer was annealed at 110°C for 40 seconds, to gently melt the spheres onto the substrate to improve the adhesion of the spheres. Whilst this annealing step did lead to a noticeable increase in the length of time before the spheres delaminated, no HCP ordered arrays were successfully deposited. While no definitive reason for the delamination of the spheres was identified, it was clear that the delamination was due to the different chemical environment. Given that the concentration of zinc nitrate was significantly higher during the HMT-CBD deposition, we speculate that either the increased stirring speed or the dissolved NaOH leads to the delamination. When the stirring speed was reduced to below that of the HMT-CBD deposition, no improvement in the adhesion of the nanosphere monolayer was observed, further suggesting that the poor results were due to the chemistry of the reaction solution, rather than any other physical effects which may be occurring. Consequently, no further attempts were made to deposit HCP ordered arrays using the NaOH-CBD method.

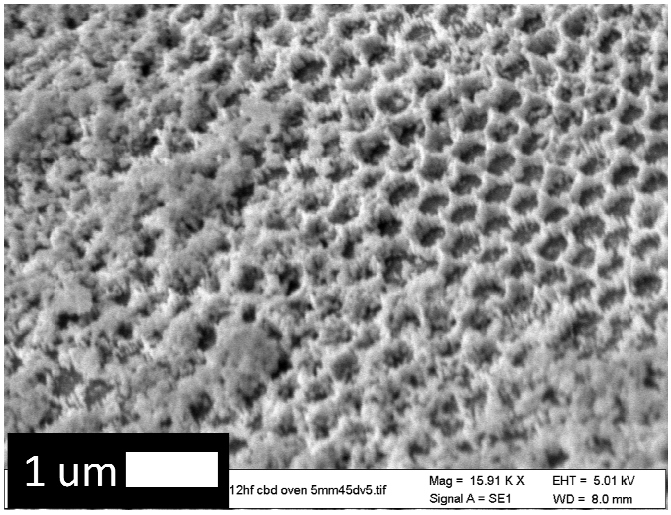

Figure 5.4: 45° SEM image of ZnO HCP structure grown by acetate CBD through a nanosphere monolayer.

The acetate based CBD deposition was also found to be unsuitable for HCP ordered nanorod growth. Given the slower deposition rate of the acetate based reaction it was necessary to increase the reaction time compared to the HMT and NaOH based reactions. It was found that the deposited material either overgrew the spheres and started to form a film, or ZnO nucleated on the polystyrene spheres and started to grow as a film. Whilst it is unlikely that the amorphous polystyrene spheres nucleated ZnO, the sphere over coating is most likely due to the homogeneous nucleation of ZnO via the decomposition of zinc hydroxide species trapped on the nanosphere surface. Figure 5.4 shows an example of the acetate-CBD through a nanosphere monolayer, where ZnO HCP regions and overgrown films can be seen.

Despite the overgrowth of the nanospheres during acetate-CBD, the presence of ordered nanohole honeycomb type structures, as seen in figure 5.4 were of interest as they may offer potential applications in photonics,[21] solar cell applications[22] and bio-diagnostics.[23] In order to produce high quality nanohole arrays, it was necessary to reduce the undesirable precipitate from becoming embedded in the array. This was achieved by isolating the two stages of the reaction. In the first step, zinc hydroxide was precipitated from a zinc salt solution using ammonia, and dehydrated with ethanol and separated by filtration. The as prepared zinc hydroxide was resuspended in water and added to a modified reaction vessel, a schematic of which can be seen in figure 5.5 (c). The reaction vessel consisted of a large beaker, with a separate tube, capped at lower end with a millipore membrane filter located inside the beaker. The beaker was then filled with DI-H_2O

so that the water level was above the height of the membrane filter. A seed substrate coated with a nanosphere monolayer was placed at the bottom of the beaker and the solution gently heated to 65°C. The zinc hydroxide suspension was then placed into the inner tube and the water level in this section was adjusted until it was approximately 1 cm above the main solution level. Both the inner tube and outer tube was gently stirred during the course of the reaction.

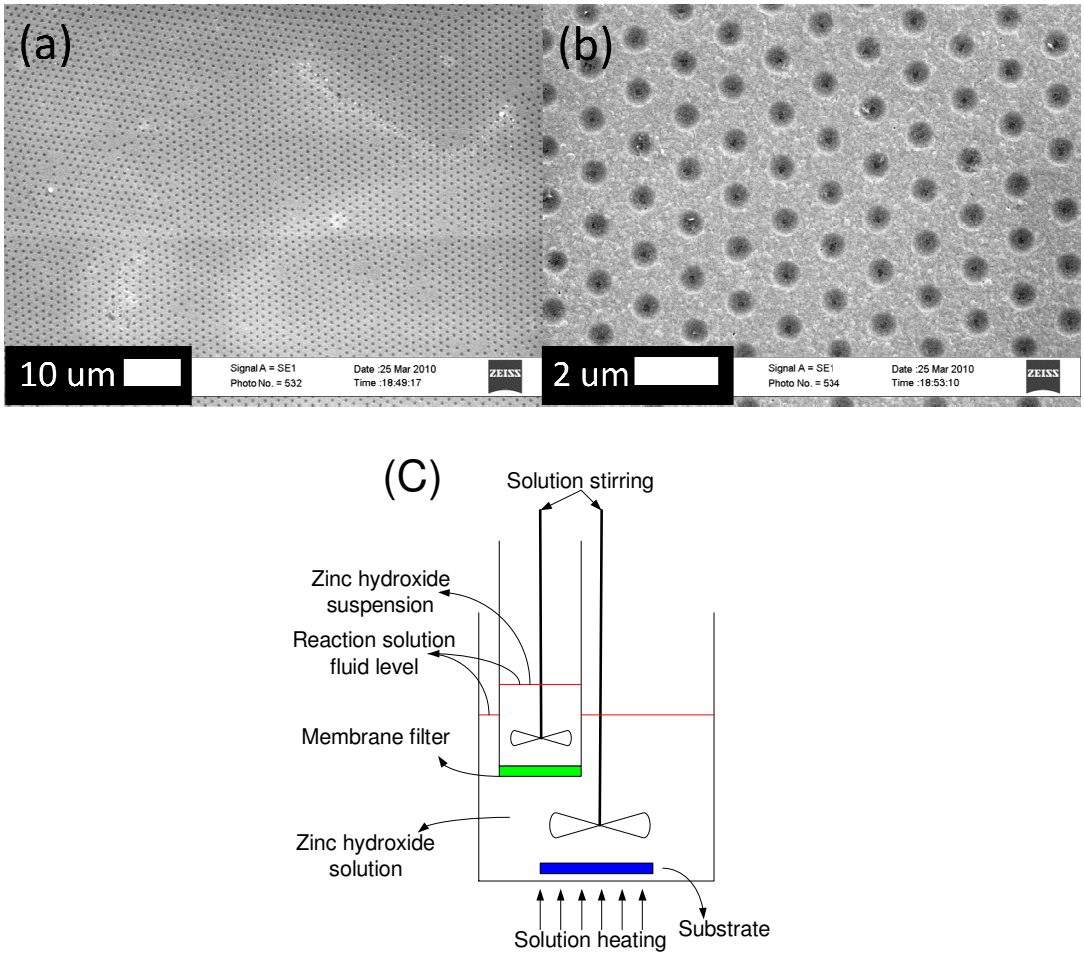

Figure 5.5: (a) low magnification and (b) higher magnification SEM image of a nanohole array. (c) Schematic representation of the reaction vessel used for the deposition of the honeycomb nanohole arrays shown in figure 5.5 (a) & (b).

During the deposition process, some of the zinc hydroxide suspension was dissolved into the water in the inner tube. The elevation of the water level in the inner tube resulted in a slow flow through the membrane filter, carrying some of the dissolved zinc hydroxide into the main beaker, whilst preventing the bulk of the precipitate from entering the main beaker. The water elevation in the inner tube was maintained during the course

of the deposition by transferring water from the main beaker back into the tube. After six hours, the substrate was removed from and the nanosphere monolayer removed. As can be seen in figure 5.5 (a) and (b) the presence of unwanted precipitates was completely eliminated by this refined deposition technique, resulting in a very clean HCP nanohole array. The deposition method leads to a ZnO film that closely follows the contours of the nanosphere, with a relatively smooth surface in between the holes. After six hours the film was approximately 70 nm thick indicating the reaction rate was significantly slower, as compared to the HMT or NaOH CBD reactions. This was ascribed to the substantially lower zinc hydroxide concentration and the limited solute diffusion across the membrane filter.

5.4.1 Inverse nanosphere lithography: CuO and Carbon templates

The polystyrene nanospheres used in this work have a glass transition temperature around 95°C and are completely melted by 180°C. Consequently they were completely unsuitable for high temperature CTR-VPT growth. Furthermore, despite the successful deposition of honeycomb structures, well defined *c*-axis aligned HCP spaced nanorod arrays were not achieved using the spheres as the deposition mask. It was therefore necessary to examine the use of a secondary material as the mask during both CBD and CTR-VPT growth.

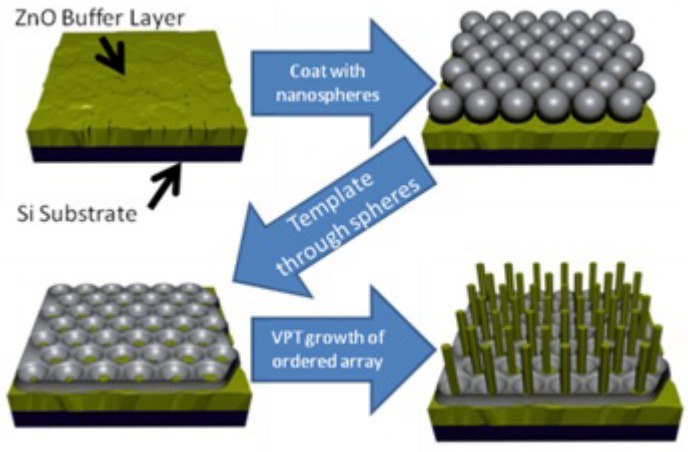

Figure 5.6: Schematic representation of the various steps required for inverse nanosphere lithography

In this method, a second material is deposited around the nanosphere forming a honeycomb mask similar to the honeycomb structure shown in figure 5.5. The nanospheres are then removed and growth takes place at the contact point between the sphere and underlying substrate or buffer layer. This process is typically called inverse nanosphere lithography[15] and offers distinct advantages in that the choice of material can be tailored to suit the nanorod deposition conditions. A schematic representation of this process is shown in figure 5.6. In this work three different materials were tested for their suitability in forming honeycomb masks and for subsequent growth of ordered ZnO arrays by either CBD or CTR-VPT techniques.

The first material examined for the formation of a secondary mask was copper (II) oxide. This material was chosen as it has a high melting temperature, making it suitable for high temperature CTR-VPT growth. In addition, copper (II) oxide is a basic oxide and therefore not soluble in weak basic solutions which would be encountered during the HMT-CBD growth process and it was both readily available and easily produced by the thermal decomposition of copper salts. Two copper salts were examined, copper sulphate and copper nitrate. Both formed secondary masks post thermal decomposition, similar to the mask shown in figure 5.7 (a). Initially it was believed that the high temperature required to decompose copper sulphate, ~750°C, leads to a failure in the ZnO seed layer during chemical bath deposition. However copper oxide templates created from the thermal decomposition of copper nitrate at lower temperatures, ~400°C, also damage the seed layer preventing CBD deposition. Subsequently if was discovered that copper salts in solution undergo a displacement reaction with ZnO, thereby etching the thin drop-coated seed layer.[24] This fact was later put to good use in identifying deep level recombination centres in ZnO and is described in more detail in chapter 6. Copper oxide templates were prepared on CBD buffer layers so as to prevent the complete etching of the underlying ZnO layer. It was found that the templates were not sufficiently robust and rapidly degrade during CBD deposition. Copper oxide is a basic metal oxide and so should not dissolve in the weakly caustic conditions during the HMT-CBD deposition. It was later discovered that copper oxide is readily soluble in ammonia, forming soluble complexes. During the HMT-CBD deposition the HMT decomposes into ammonia and formaldehyde, which lead to the dissolution of the template. Given the discontinuous nature and poor morphology of the copper oxide templates no attempt was made use them for CTR-VPT deposition.

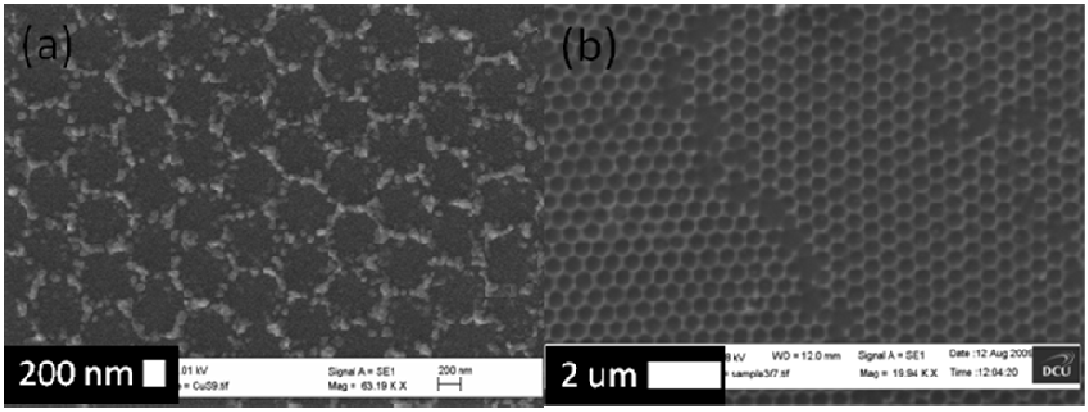

Figure 5.7: Plan view SEM images of (a) a honeycomb template deposited by the thermal decomposition of copper nitrate (b) a honeycomb template deposited from the dehydration of sucrose by H_2SO_4.

The second material chosen for the inverse mask was carbon. This material was chosen as it is unreactive in both acidic and basic conditions. In addition, if ordered arrays could be successfully deposited by CBD, then the mask could be removed easily by burning off the carbon prior to CTR-VPT deposition. Initial attempts to synthesis a carbon secondary mask (as shown in figure 5.7 (b)) showed that this technique was quite promising as high quality carbon masks were obtainable. Attempts to extend this method to create carbon masks on ZnO seed layers have not been realised, due to an unexpected interaction between the seed layer and the carbon deposition process. ZnO is amphoteric, being sensitive to both acids and bases. The carbon deposition process requires the presence of a strong acid to catalyse the reaction as given by:

$$C_{12}H_{22}O_{11} + H_2SO_4 \rightarrow 12C + 12H_20 + H_2SO_4 \quad (5.4.1)$$

The sulphuric acid acting a catalyst dehydrates the sucrose leaving behind pure amorphous elemental carbon. Due to the reactivity of ZnO a second competing reaction takes place destroying the seed layer:

$$ZnO + H_2SO_4 \rightarrow ZnSO_4 + H_2O \quad (5.4.2)$$

The zinc sulphate formed by the competing reaction given by equation 5.4.2 is highly water soluble and rapidly dissolves during a chemical bath deposition. The sulphate's

decomposition temperature is above the temperature required to remove the carbon template, which prevents reoxidisation of the zinc post carbon deposition. These factors suggest that once destroyed the ZnO seed layer is unrecoverable without destroying the carbon template. As with the copper oxide templates, in order to prevent the complete etching of the ZnO, carbon templates were prepared on thick CBD buffer layers. These carbon templates had very little adhesion to the underlying ZnO buffer layer during the CBD process. In all cases the carbon template delaminated from the buffer layer within the first few minutes. Therefore, carbon was deemed an unsuitable material for the formation of secondary masks.

5.4.2 Inverse nanosphere lithography: Silica templates

The final material examined for the formation of the inverse mask was silica. Previous reports, using zinc foil as the substrate suggested that silica deposited from a TEOS sol was sufficiently robust to withstand CBD leading to the deposition of well ordered arrays.[15] However, this approach had never been extended to thin seed layers or buffer layers prepared by wet chemical methods. The first aspect to be considered was the choice of catalyst in the preparation of the silica sol. As discussed in chapter 2.5.3, the choice of catalyst has a strong influence on the final properties of films derived from silica sols. Three different methods were considered, acid catalysed, base catalysed and acid-base catalysed. In all three cases a honeycomb template was achieved, examples of which are shown in figure 5.8. As expected, the processing conditions of the sol influenced how the final silica film performed in later deposition steps.

It was found that base catalysed sols performed the poorest. They did not coat the ZnO buffer layer exceptionally well, usually resulting in a patchy and broken template. During the densification step, base catalysed sols were found to be much more sensitive to the temperature ramp rate, as compared to the acid and acid-base catalysed sols. Increasing the temperature too quickly resulted in the formation of small cracks in the film which rapidly propagated across the entire substrate causing a complete delamination of both the silica and the underlying ZnO buffer layer. Despite extreme care being taken during the densification step, the majority of base catalysed samples failed during the densification step. Acid and acid-base catalysed sols were found to coat the ZnO buffer

layer equally well resulting in uniform honeycomb templates. Despite the sensitivity of ZnO to acids, sols prepared using acid catalysts did not appear to cause significant etching of the buffer layer. No variation was observed between films prepared from HCl catalysed sol as compared to those prepared using a H_2SO_4 catalyst of equal normality. While care was needed during the densification of these templates, typically only a small proportion of them failed, with the majority being usable for further deposition tests. The volume of sol used to coat the substrate was of critical importance to forming a uniform template. If a sufficient volume was not added, the template would become excessively thin in the centre of the sample. If too much sol was applied to the surface, upon drying large silica drying spots would appear, usually at the substrate edges, which would subsequently crack and delaminate during densification and VPT growth. In addition the volume of sol needed depended on the sphere size, with larger sphere sizes requiring more than smaller spheres.

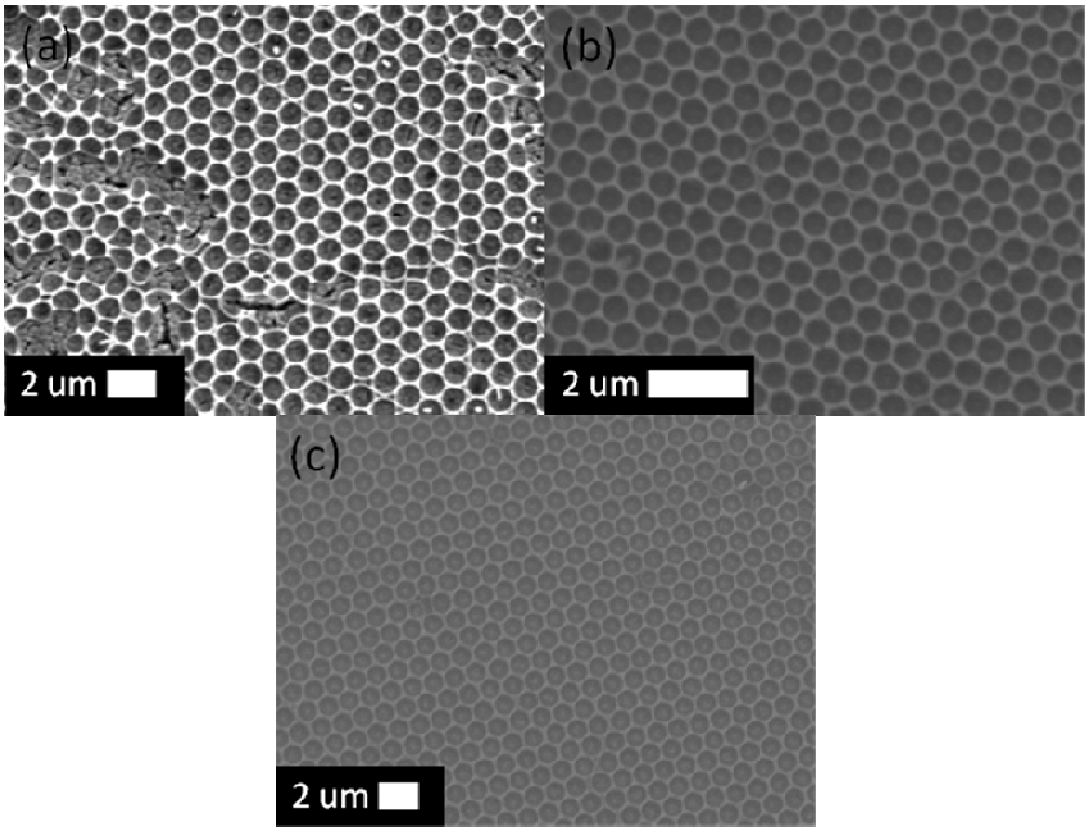

Figure 5.8: SEM images of (a) 1 µm honeycomb silica template on CBD derived from a base catalysed sol (b) 500 nm honeycomb silica template on CBD derived from an acid-base catalysed sol (c) 1 µm honeycomb silica template on CBD derived from an acid catalysed sol

As a precursor to the CTR-VPT deposition through the silica templates, it was first important to determine if the contact points between the spheres and underlying buffer layer were free from silica and would nucleate nanorod growth. This critical factor was examined by performing CBD depositions through the silica templates deposited by the acid and acid-base catalysed sols. Given the difficulties in removing unwanted precipitates from the surface of the ordered array, the NaOH method was used to test the suitability of the honeycomb templates for CBD growth. The poor resistance of silica to basic solutions resulted in rapid etching of the silica templates. However, some variations in chemical resistance were observed between samples prepared using the acid and acid-base catalysed sols. The silica templates from acid catalysed sols etched more rapidly than those prepared form the acid-base catalysed sols, consequently deposition times were kept as short as possible. As can be seen in figure 5.9 (a), small rods emerging from the template holes were detected and in general the sample appeared to be patterned. However, good SEM imaging contrast could not be obtained, suggesting that the amorphous silica had already begun to dissolve and coat the rods. The acid-base catalysed silica templates were slightly more robust in the harsh chemical environment. This increase in chemical resistance is due to the cross-linking in the polymeric silica chains enhanced by the base catalyst. In figure 5.9 (b) a small cluster of nanorods can be seen nucleating at each contact point between the spheres and underlying buffer layer, confirming that the underlying ZnO was exposed at the contact points between the spheres and buffer layer.

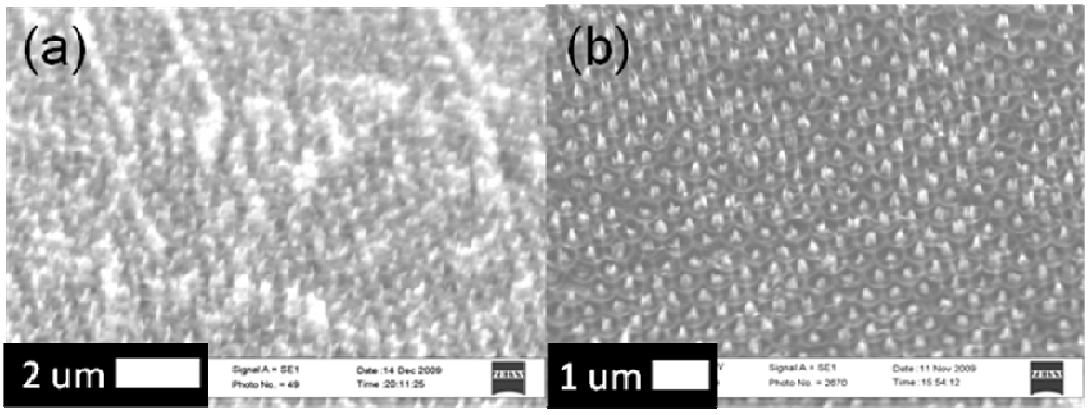

Figure 5.9: 45° SEM images of (a) nanorod array deposited through a acid catalysed silica honeycomb template using the NaOH-CBD method (b) nanorod array deposited through a acid-base catalysed silica honeycomb template using the NaOH-CBD method

5.5.1 Inverse nanosphere lithography: CTR-VPT

During our initial efforts to deposit ordered arrays by CTR-VPT through silica honeycomb templates it quickly become apparent that the contact between the spheres and the underlying substrate was an important factor. While ordered arrays did nucleate and grow through the template, the uniformity was often poor with large random areas showing no signs of nanorods growth. For clean flat substrates such as Si wafers, the monolayers appear to make good contact with the substrate. For catalytic approaches, where gold is to be deposited through the apertures created by the spheres, it is in any case debatable if the degree of contact between the spheres and the substrate is a significant factor. For silica templating however it is essential that the spheres are in good contact with the underlying ZnO, to prevent the silica sol seeping under the spheres and completely masking the CBD buffer layer. This problem was compounded by variations in the buffer layer thickness deposited by CBD. This lead to patchy growth observed during our initial investigations. A schematic representation of the mechanisms which result in the poor growth and an example of one of first attempts is shown in figure 5.10 (a). It was found that difficulties with the contact between buffer layer and spheres can be partially offset by using centripetal force to drive the spheres close to the ZnO buffer layer without significantly disturbing the HCP pattern. This was achieved by spinning the sample at ~2000 rpm with the nanosphere coated surface facing the axis of rotation. After this centrifugation step the samples were gently annealed to improve the adhesion of the polystyrene monolayer to the underlying ZnO buffer layer.

The surface roughness of the underlying buffer layer was also found to play a key role during templating. As seen in figure 5.10 (b), another problem can arise if the surface of the buffer layer is excessively rough, whereby the nanospheres may not contact the buffer layer at just one location along the central axis of the sphere perpendicular to the substrate. Post silica deposition, this roughness may lead to multiple VPT nucleation sites being formed per sphere, distorting the HCP pattern. It is therefore important that the buffer layer is as smooth as possible, prior to silica deposition. As discussed in chapter 3, the various different CBD growth techniques resulted in different nanorod morphologies, with both the HMT and NaOH CBD methods resulting in pointed bullet shaped nanorods. In contrast, due to the capping effect of the carboxylic acid group and the slower more

uniform deposition rate, buffer layers deposited by the acetate method were visibly smoother and more uniform.

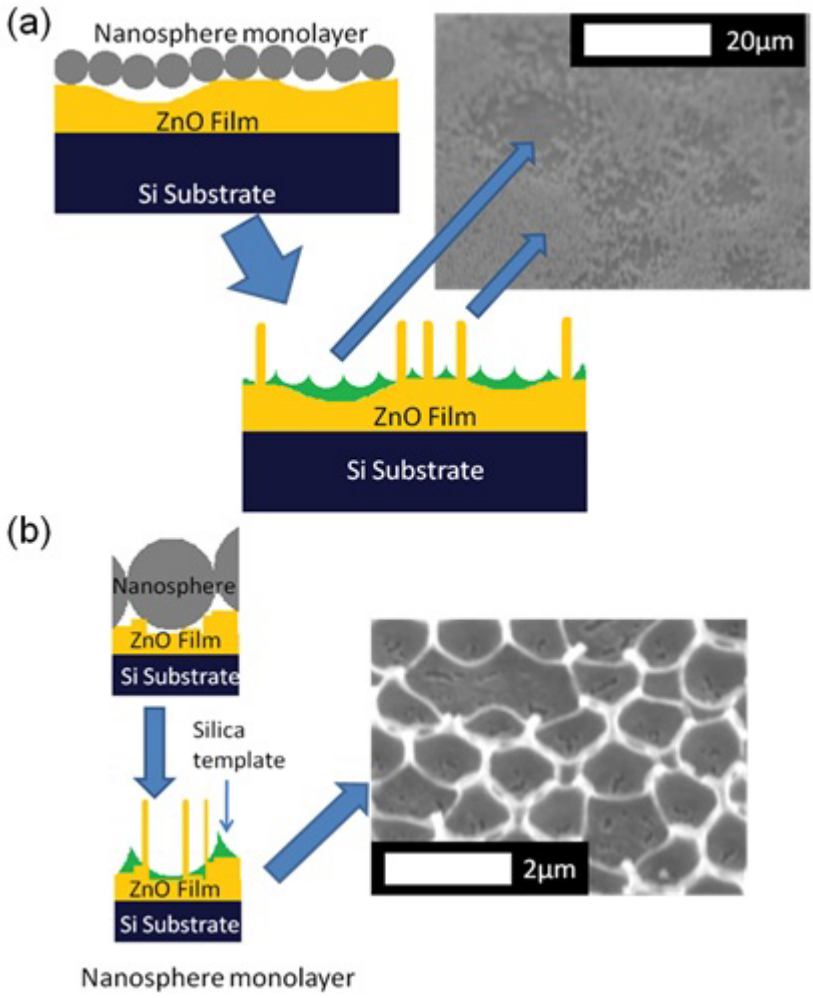

Figure 5.10: (a) Schematic representation of the effects of poor surface contact between the nanosphere monolayer and the CBD ZnO buffer layer on the VPT deposition of ordered nanorod arrays (left and bottom) and an SEM image (right) showing the resulting VPT nanorod array with poor uniformity of nanorod coverage. (b) Schematic representation and SEM image of the effects of surface roughness on contact between the underlying CBD layer and the nanospheres and its effect on the silica template.

A comparison of the acetate deposited and HMT deposited buffer layers can be seen in figure 5.11. Consequently, the acetate-CBD method was the preferred route to deposit buffer layers for CTR-VPT deposition through silica masks. By reducing the surface roughness, we have found that the nanospheres make better contact with the ZnO buffer layer leading to a reduction in the number of faults in the silica template.

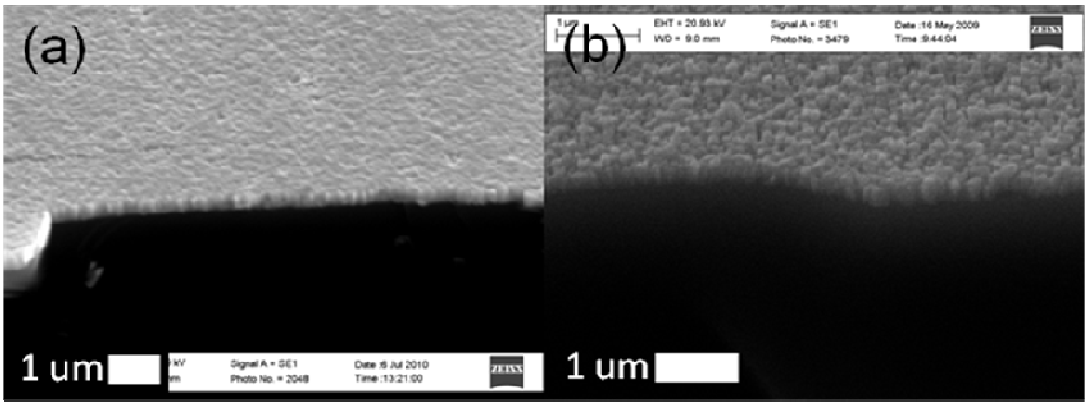

Figure 5.11: 45° SEM image of a CBD buffer layer deposited by (a) acetate method and (b) HMT method.

Two strategies for the final deposition of the ordered nanorod array were examined. First, nanorods were grown by the CTR-VPT method discussed in chapter 4 directly through the silica template. For the second strategy, a short acetate-CBD was performed after the densification of the template, to initiate the ordered nanorod growth, which was then followed by a CTR-VPT deposition. For both methods two nanosphere sizes, 1 µm and 500 nm, were tested and in both cases the nanorods deposited were predominantly confined to the locations where the nanospheres were in contact with the underlying CBD buffer layer.

Using the first strategy, i.e. direct CTR-VPT deposition through the honeycomb template, as seen in figure 5.12, resulted in a well aligned and well ordered HCP nanorod array for both sphere sizes. Some differences were observed in the nanorod morphology depending on the nanosphere size used to create the template. When 500 nm spheres were used, the majority of nanorods were 2.5 - 3 µm in length with a diameter of 140-170 nm. However when 1 µm spheres were used the average length reduced to 1.5 – 2 µm with diameters 200-260 nm. Interestingly, this represented a reduction in aspect ratio approximately inversely equal to the reduction in sphere size, which suggests that the pore size in the silica template not only influences the nanorod position but also its morphology. For both sphere sizes, the nanorods initially form conical bases, which can be seen in the insert images in figure 5.12 (a) to (d). However unlike the rods discussed in chapter 4, the base formation is constrained to specific points on top of a continuous film. Therefore the base formation must be resulting from the variation in growth conditions during the CTR-VPT step. When the growth is constrained by the silica template the bases of the rods are

significantly smaller, in agreement with the argument put forward in chapter 4, that the structural changes in the underlying buffer layer influence the base of the nanorods.

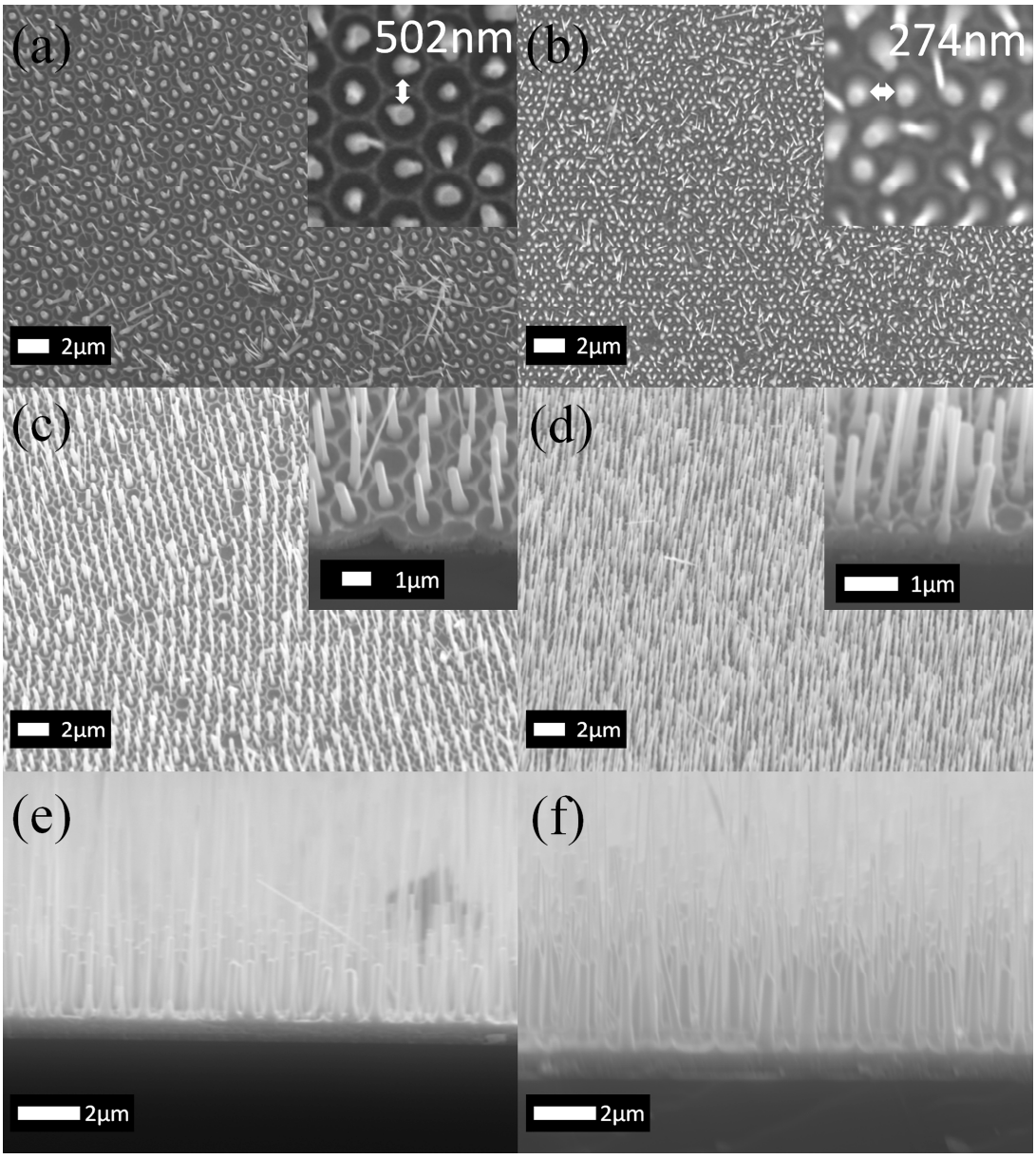

Figure 5.12: SEM images of a 1 µm spaced VPT grown ordered array in plan view (a), 45° view (c) and 90° view (e). Parts (b), (d) and (f) show the corresponding views for a 500 nm spaced array.

In samples grown by both strategies, two additional nanorod morphologies were observed, examples of which are shown in figure 5.13. The first additional morphology consisted of nanorods with substantially higher aspect ratios. These rods typically had lengths ranging from 3 µm to 15 µm with diameters centred around 100 nm. They have

been observed to nucleate from the tips of shorter nanorods, from the holes in the silica template in conjunction with a “regular” sized nanorods and from small cracks that have developed in the silica template during the growth process. The second morphology consists of two nanorods nucleating from the same location and apparently sharing the same base. Often these twinned crystals have an angle of approximately 60° between them. In both cases it is difficult to ascertain the precise origin or cause of these variations. For non-templated substrates nanorod nucleation takes place on the buffer layer at sites that are favourable by virtue of their orientation, morphology, energetics or crystalline quality. For templated substrates, the choice of nucleation site is severely constrained by the presence of the silica mask, forcing nucleation to take place at specific points irrespective of the underlying morphology of the buffer layer. As seen in figure 5.11, despite care being taken in the preparation of the buffer layer, grain boundaries, cracks and surface roughness will still be present. These natural features of CBD growth on a poly-crystalline seed layer are unavoidable. We believe that these underlying defects contribute significantly to the origin of the additional morphologies observed. If a particularly well defined grain boundary / crack in the underlying buffer runs through the spot exposed by the silica mask, then this spot may serve to provide multiple nucleation sites. Depending on the precise location of the nucleation sites with respect to the mask, then two approximately equal sized twined rods can be deposited or a dominant rod with a thinner longer rod.

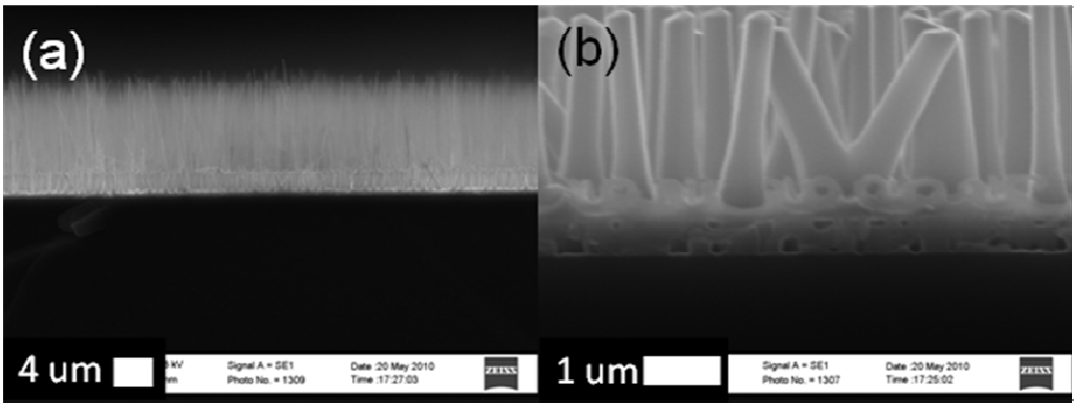

Figure 5.13: SEM images showing 90° views of a ZnO ordered array where (a) additional long and thin, high aspect ratio nanorods were observed (b) dual nanorod nucleation/crystal twinning was observed.

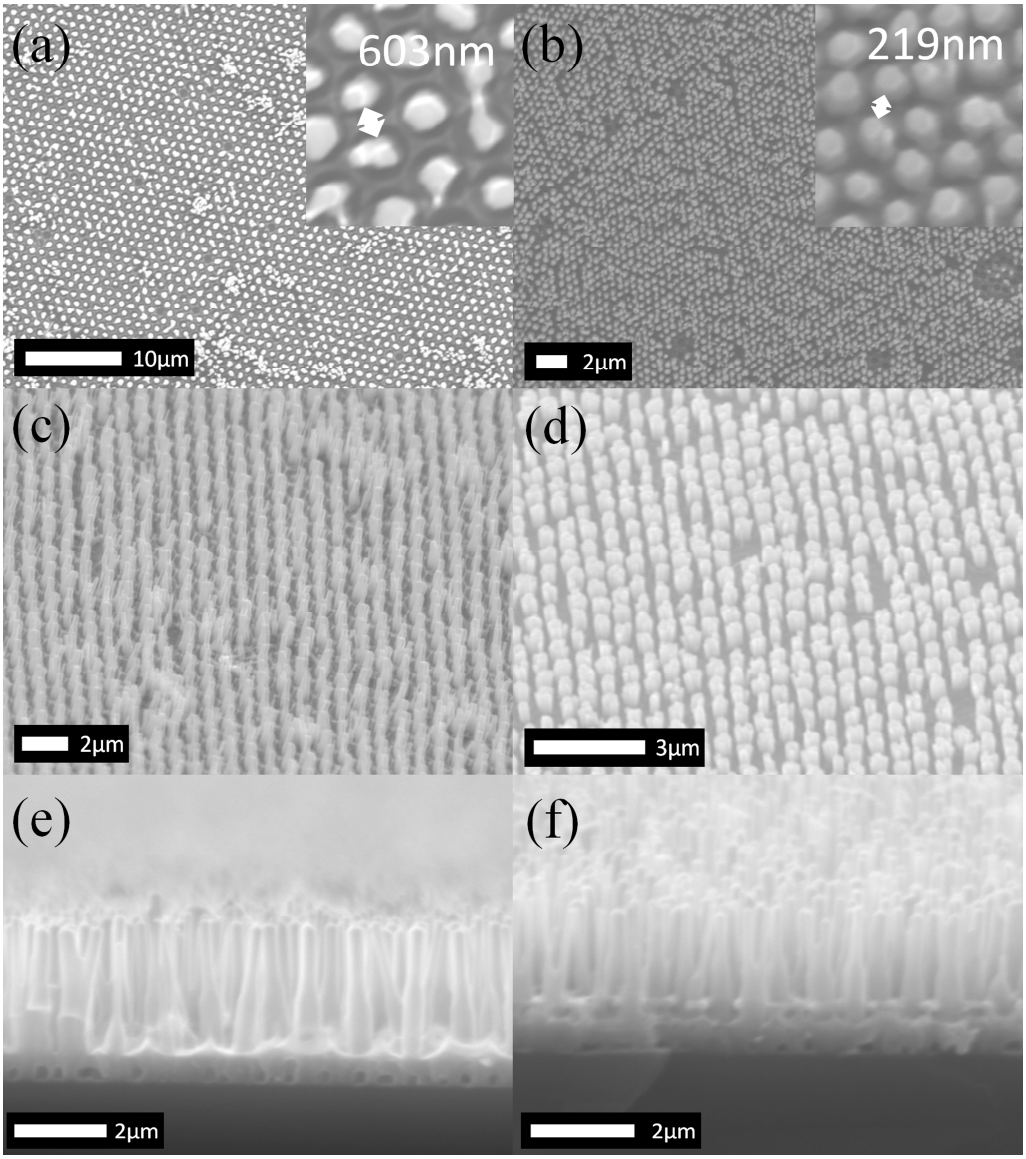

Figure 5.14: SEM images of a 1 µm spaced VPT grown ordered array grown on a substrate where a second CBD step was performed to initiate the nanorod growth, in plan view (a), 45° view (c) and 90° view (e). Parts (b), (d)and (f) show the corresponding views for a 500 nm spaced array.

In order to try and eliminate the additional observed morphologies an additional CBD step was added (strategy 2). A second short chemical bath deposition was performed, after the silica template was densified using the acetate-CBD method. This method was chosen as the adsorption of cation on the *c*-plane, which leads to lateral growth of the nanorods. This lateral growth helps reduce / eliminate the presence and effect of any grain boundaries or cracks running across the template spots. In addition the acetate-CBD deposition solution has a slightly acidic pH, thereby eliminating the prospect of etching the

template, as compared to the other CBD techniques used in this work. The second CBD deposition could only be conducted for a short time to ensure that rods did not grow sufficiently long to trap any unwanted precipitates, which would then act as nucleation sites during the CTR-VPT step.

As can be seen in figure 5.14, by performing a second CBD, in combination with a decrease in the VPT temperature ramp rate (to discourage secondary nucleation of thin rods on shorter rods), the long high aspect ratio nanorods, seen in the sample deposited directly through the silica template, were completely eliminated. In addition, there was less evidence of multiple rods per nucleation site and crystal twinning. While some twinning did occur, these rods merged at the approximate location where the tip of the nanorods deposited during the second CBD was located. This again strongly suggests that the additional morphologies observed were due to the surface of the acetate deposited ZnO rather than the CTR-VPT deposition process itself. Substrates templated with 1 μm nanospheres had average rod lengths of ~2.8 μm with a diameter of 300 nm to 500 nm. For samples templated with 500 nm nanospheres the average rod length reduced to 1.8 μm with a diameter in the range of 250 – 400 nm. The inverse relationship observed between the rod spacing and aspect ratio was not observed for the second strategy. This may be due to the second CBD step altering the CTR-VPT nucleation process, creating a more homogenously sized nucleation site between spheres of different sizes, i.e. slight lateral overgrowth of the template hole due to the capping effect of the cation. The wine bottle shape at the base of the rods, as discussed in chapter 4, is due to the overgrowth of the second CBD nanorod due to incoming Zn and any morphological changes induced in the second CBD rod by the temperature profile.

XRD analysis of the ordered nanorod arrays, as shown above is shown in figures 5.15(a) ((i) & (ii)), and the data are similar to those of the underlying buffer layers (figure 5.15 (a)(iii)) with only the ZnO (002) and (004) peaks being detected, indicating a high degree of nanorod alignment normal to the substrate surface. The FWHM of the rocking curves for the ZnO (002) peak (figures 5.15 (b) (iv) & (v)) are rather broad at ~7.5 °, showing only minor improvements over the CBD buffer layer. This would indicate that the material deposited during the VPT steps does not display a significantly higher degree of texture than that of the buffer layer, as expected, given that the underlying buffer layer is responsible for the *c*-axis alignment in the first place. This remains the case whether one or two CBD growth steps are used in producing the buffer layers.

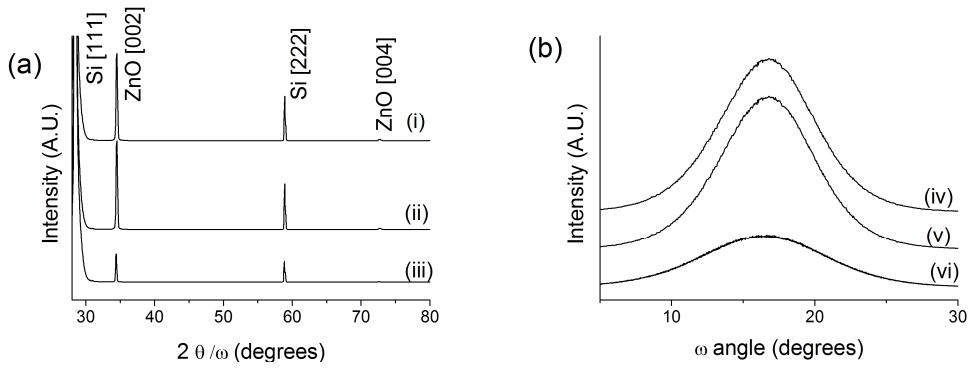

Figure 5.15: XRD 2 θ / ω scan of (a)(i) VPT grown patterned array on CBD buffer layer (ii) VPT grown patterned array on two CBD growths buffer layer (iii) ZnO buffer layer derived from zinc acetate. XRD rocking curve of the ZnO (002) peak for (b)(iv) VPT grown patterned array on CBD buffer layer (v) VPT grown patterned array on two CBD growths buffer layer (vi) ZnO buffer layer derived from zinc acetate.

5.5 Conclusions

In this chapter we have examined the use of nanosphere lithography for the deposition of honeycomb nanohole arrays and HCP ordered nanorod arrays. It was found that CBD deposition through the apertures created by the HCP nanosphere array was hampered by the build up of unwanted precipitates. Using the precipitateless NaOH-CBD resulted in the delamination of the spheres, most likely due to the disturbance of the hydrophobic charge shell surrounding the polystyrene spheres by the NaOH. Very uniform, clean and thin nanohole arrays could be deposited by CBD from zinc hydroxide by separating the weakly soluble hydroxide suspension from the substrate by a membrane filter and using fluid elevation to drive the dissolved hydroxide into the main reaction vessel. Whilst slow, this method could be particularly useful for photonic devices given that the thin film could easily be metalised using a simple displacement and reduction technique.[24]

Using the spheres to create a secondary template, i.e. inverse nanosphere lithography, was also investigated. It was found that the choice of material for the template was not a trivial task. The material has to have sufficiently different physical properties so that the spheres can be easily removed. In addition the choice of material has to be compatible with the underlying buffer layer, which in this case is sensitive to both acids and strong bases and during CBD depositions the template must be able to withstand the

reaction conditions. In this work we did not find any material that was particularly suited to CBD growth using basic conditions. However, we developed a method to deposit high quality HCP ordered arrays using a silica template in conjunction with CTR-VPT. As will be seen in the next chapter, when we examine the optical properties of ZnO, the growth of HCP ordered arrays by CTR-VPT is arguably much better than by CBD given the superior optical quality of the material deposited.

5.7 References

(1) Liu, D. F.; Xiang, Y. J.; Wu, X. C.; Zhang, Z. X.; Liu, L. F.; Song, L.; Zhao, X. W.; Luo, S. D.; Ma, W. J.; Shen, J.; Zhou, W. Y.; Wang, G.; Wang, C. Y.; Xie, S. S. *Nano Letters* **2006,** *6* (10) 2375-2378

(2) Kumar, R. T. R.; McGlynn, E.; Mcloughlin, C.; Chakrabarti, S.; Smith, R. C.; Carey, J. D.; Mosnier, J. P.; Henry, M. O. *Nanotechnology* **2007,** *18* (21) 215704

(3) Garry, S.; McCarthy, E.; Mosnier, J. P.; McGlynn, E. *Applied Surface Science* **2011,** *257* (12) 5159-5162

(4) Tsai, T. Y.; Chen, T. H.; Tai, N. H.; Chang, S. C.; Hsu, H. C.; Palathinkal, T. J. *Nanotechnology* **2009,** *20* (30) 305303

(5) Liu, D. F.; Xiang, Y. J.; Liao, Q.; Zhang, J. P.; Wu, X. C.; Zhang, Z. X.; Liu, L. F.; Ma, W. J.; Shen, J.; Zhou, W. Y.; Xie, S. S. *Nanotechnology* **2007,** *18* (40) 405303

(6) Zhang, X. X.; Liu, D. F.; Zhang, L. H.; Li, W. L.; Gao, M.; Ma, W. J.; Ren, Y.; Zeng, Q. S.; Niu, Z. Q.; Zhou, W. Y.; Xie, S. S. *J Mater Chem* **2009,** *19* (7) 962-969

(7) Fan, H. J.; Fuhrmann, B.; Scholz, R.; Syrowatka, F.; Dadgar, A.; Krost, A.; Zacharias, M. *Journal of Crystal Growth* **2006,** *287* (1) 34-38

(8) Cheng, C.; Lei, M.; Feng, L.; Wong, T. L.; Ho, K. M.; Fung, K. K.; Loy, M. M. T.; Yu, D.; Wang, N. *ACS Nano* **2008,** *3* (1) 53-58

(9) Kim, T.-U.; Kim, J.-A.; Pawar, S. M.; Moon, J.-H.; Kim, J. H. *Cryst Growth Des* **2010,** *10* (10) 4256-4261

(10) Wei, Y.; Wu, W.; Guo, R.; Yuan, D.; Das, S.; Wang, Z. L. *Nano Letters* **2010,** *10* (9) 3414–3419

(11) Yu, C. W.; Lai, S. H.; Wang, T. Y.; Lan, M. D.; Ho, M. S. *J Nanosci Nanotechno* **2008,** *8* (9) 4377-4381

(12) Zhou, H.; Fallert, J.; Sartor, J.; Dietz, R. J. B.; Klingshirn, C.; Kalt, H.; Weissenberger, D.; Gerthsen, D.; Zeng, H.; Cai, W. *Applied Physics Letters* **2008,** *92* (13) 132112

(13) Li, C.; Fang, G. J.; Yuan, L. Y.; Liu, N. S.; Li, J.; Li, D. J.; Zhao, X. Z. *Applied Surface Science* **2007,** *253* (20) 8478-8482

(14) Rybczynski, J.; Banerjee, D.; Kosiorek, A.; Giersig, M.; Ren, Z. F. *Nano Letters* **2004,** *4* (10) 2037-2040

(15) Li, C.; Hong, G. S.; Wang, P. W.; Yu, D. P.; Qi, L. M. *Chem Mater* **2009,** *21* (5) 891-897

(16) Burmeister, F.; Schäfle, C.; Matthes, T.; Böhmisch, M.; Boneberg, J.; Leiderer, P. *Langmuir* **1997,** *13* (11) 2983-2987

(17) Fu, Y.; Jin, Z.; Liu, Z.; Li, W. *Journal of the European Ceramic Society* **2007,** *27* (5) 2223-2228

(18) Prevo, B. G.; Velev, O. D. *Langmuir* **2004,** *20* (6) 2099-2107

(19) Ogi, T.; Modesto-Lopez, L. B.; Iskandar, F.; Okuyama, K. *Colloids and Surfaces A: Physicochemical and Engineering Aspects* **2007,** *297* (1-3) 71-78

(20) Rybczynski, J.; Ebels, U.; Giersig, M. *Colloid Surface A* **2003,** *219* (1-3) 1-6

(21) Gao, H.; Henzie, J.; Odom, T. W. *Nano Letters* **2006,** *6* (9) 2104-2108

(22) Sai, H.; Fujiwara, H.; Kondo, M. *Solar Energy Materials and Solar Cells* **2009,** *93* (6-7) 1087-1090

(23) Cui, X.; Tawa, K.; Kintaka, K.; Nishii, J. *Adv Funct Mater* **2010,** *20* (6) 945-950

(24) Takahashi, H.; Nakamura, H.; Izaki, M.; Katayama, J., *Method of forming a Cu interconnect pattern*, United States Patent Office, **2003**, NEC Corporation, Tokyo (Jp), Osaka Municiple Government, Osaka (Jp) United States.

Chapter 6: Optical Properties

6.1 Introduction

In this chapter we examine the optical properties of the ZnO nanorod arrays grown by the methods described in chapter 3, 4 and 5 using low temperature PL. As discussed in chapter 2, PL is often used to characterise the electronic properties of semconductors as it often allows one to identify important features such as deep level defects, impurities and other anomalies. However often the data obtained from PL measurements is inconclusive and other techniques such as absorption or electrical characterisation are necessary to supplement the PL results. In this chapter we demonstrate the power of PL by definitively identifying the origin of the structured green band (SGB) by single isotope doping of single crystal ZnO. This chapter also contains absorption data performed in the laboratory of Dr. Frank Herklotz of the Institut für Angewandte Physik, Dresden, Germany, and which is included in this work for the completeness of the discussion.

6.2 CBD versus CTR-VPT

One of the main attractions of chemical solution growth processes for ZnO nanostructure deposition is the simplicity and low costs associated with the various techniques. The large number of controllable parameters allows chemical synthesises to be tailored for specific applications, giving unprecedented control over the ZnO morphology and choice in terms of possible substrates. In addition, many groups report that their deposition techniques produce materials of high quality, both in terms of the crystallinity, as determined by measurements such as XRD and TEM, but also in terms of the materials

optical properties, as determined by PL and absorption experiments. [1-10] It should be noted that many of these reports include only room temperature PL spectra and conclude the quality of material from the absence of, or relative weakness of, any visible emission bands such as the green or yellow bands. During the course of this work, we were unable to produce any samples by CBD techniques that demonstrated good optical quality. Despite using three different methods, on all occasions we found that the optical quality of the nanorods deposited was extremely poor. Two criteria based on low temperature PL measurements, were used to judge the optical quality of the CBD grown nanorods in our work which were different to the often used criterion mentioned above. Firstly, we compared the emission intensity of the nanorods to those deposited by CTR-VPT methods. Secondly, we compared the near band edge (NBE) emission line widths, to those grown by CTR-VPT methods. Figure 6.1 (a) and (b) show typical low temperature PL spectra of samples deposited by the different CBD methods used in this work. In contrast, figure 6.1 (c) and (d) show typical low temperature spectra of ZnO nanorods deposited by CTR-VPT on a CBD buffer layer.

Before discussing these results there are a couple of brief points worth mentioning about the Fourier transform spectrometer. The position of the moving mirror is determined by two light sources, the first is the 633 nm line of a frequency stabilised HeNe laser which is used to determine the position of the mirror; the second is a white light source used to determine the zero path difference of the mirror. During our experiments the white light source was filtered to remove all wavelengths below 700 nm so as to prevent interference with the collection of the visible and near UV spectra. A second filter was placed directly in front of the photomultiplier tube. When obtaining spectra in the visible region, a 606HSP visible bandpass filter (cut on 380 nm, cut off 620 nm) was used. For UV data collection a BG25 Schott glass bandpass filter was used (cut on ~330 nm, cut off ~480 nm). The filters in this equipment set up have two important roles. First, they remove most of the stray light associated with the internal mirror positional control system, that is, the 633 nm and filtered white light source. Second, the FT system detector has a poor dynamic range. When a spectrum has intense spectral features, such as the NBE in the CTR-VPT samples, the frequencies associated with these features can drown out weaker spectral features. In order to detect the visible emission spectrum it was necessary to filter out the UV spectrum. This was particularly important for CTR-VPT samples as the intensity of the visible emission was too weak to be detected without removing the NBE emission.

Consequently, the green band emission looks quite strong for example in figures 6.1 (d) and 6.2 (b) (d) and (f) as compared to the NBE, but this effect is due to the NBE filtering. For consistency, the same filtering was used for CBD samples.

In general PL is considered a non-quantitative analysis technique, owing to possible variations in intensity due to variations in the collection optics, sample orientation, sample thickness, nanorod density, changes in relative efficiencies of radiative and non-radiative decay channels with defect concentration etc. since PL is not an internally intensity referenced technique such as optical absorption. However, in making judgement about relative emission intensities between samples where order of magnitude variations occur it is reasonable to draw some conclusions from such variations in emission intensity, as these go beyond any expected variations induced by the collection optics. Figure 6.1 (a) has been amplified approximately 10,000 times as compared to figure 6.1 (c). Both spectra were acquired using identical instrumental and software gain, temperature, sample orientation and filtering. The CBD samples prepared for this analysis were of similar thickness to the rod length in the CTR-VPT sample and the rod density was significantly higher than that of the CTR-VPT sample. Therefore if the quality of the sample was similar, one would expect that the emission intensities of the CBD grown material would be higher, due to the increased mass of ZnO being sampled by the laser spot. It was of course possible to significantly improve the CBD band edge and visible band spectra by judicious selection of the aperture size, instrumental gain and resolution, so as to acquire a clean spectrum without any visible noise. On all occasions, this resulted in detector saturation when attempts were made to measure the CTR-VPT spectra using the CBD optimised conditions. Therefore direct comparison was not possible unless the system was optimised for the CTR-VPT samples, i.e. a small aperture size and low gain settings.

As discussed in chapters 3 and 4 the structural characterisation of both the CBD and CTR-VPT grown nanorods indicate that the material is of good quality. However TEM analysis is nearly insensitive to point defects. These defects are more easily identified by PL measurements.[11] In a general sense the large variation between the optical properties of the CTR-VPT and CBD grown materials is entirely consistent with the fact that the former are grown at significantly higher temperatures, leading to better crystal quality and fewer native point defects during growth due to the annealing effects of the higher temperatures during the adatom incorporation into the growing crystal, ensuring these atoms reach correct lattice sites. By contrast the lower temperatures used for CBD grown material

means that adatoms can remain at non-equilibrium initial attachment sites, thus forming native point defects in the growing crystal. Previous studies comparing the optical properties of ZnO nanorods deposited at low temperature using the HMT CBD method against nanorods deposited by the high temperature techniques, have identified some other more specific important factors relating to the properties of CBD grown nanorods due to both growth conditions and chemistry. Firstly, when the CBD nanorods are short, they are in greater contact with neighbouring rods, which lead to structural defects and an associated emission line centred around 3.332 eV.[12] A similar peak was observed in our samples prepared by the HMT method, as seen in figure 6.1 (a)(iii). This peak is notably absent in the sample prepared by the acetate method, where the contact between neighbouring rods is substantially higher owing to the increased lateral growth of the rods induced by the acetate counter ion. This may indicate that these "contact defects" involve the trapped species related to the HMT / nitrate chemistry which are absent in the acetate CBD system. In both the HMT and acetate CBD samples individual bound excitons are unresolvable, being replaced by a single broad emission centred around 3.364 eV. This broad emission is associated with excessive donors creating a continuous band of donor states. [12, 13] As discussed in chapter 3 section 3.5.1 (page 83), during nanorod growth both homogeneous growth and orientated attachment is taking place. It is therefore possible that during the growth process a significant amount of hydroxide or sub-hydroxide type species become incorporated into the rod structures along with other donors specific to the CBD reaction chemistry. This broad emission is common to both the HMT and acetate techniques reported both here and elsewhere, implying a common origin across the various different CBD and low temperature aqueous ZnO growth techniques. Consequently the role of intermediate zinc hydroxides may prove to be a crucial aspect in optimising the optical properties of CBD grown ZnO nanorods.

The optical properties of the CBD nanorods also varied considerably between the different growth methods used. The strongest NBE emission was from the samples grown via the HMT method. The acetate grown samples were slightly weaker, whilst the NaOH method produced samples with no discernable band edge emission. The FWHM of the NBE emission at low temperatures of both the acetate and HMT derived samples is quite broad compared to the CTR-VPT sample. The narrowest FHWM, in samples grown by the acetate method, is ~74 meV, while the FWHM of the HMT grown sample is ~132 meV. In comparison the FWHM of the dominant NBE peak of the CTR-VPT grown sample is ~1 meV.

In the visible region of the spectrum, all three CBD samples show a similar band in the yellow orange region of the spectrum. However owing to the bandpass filtering it is difficult to determine where the maximum of this band lies and given that a number of different bands are known to occur in this region it not possible assign a specific cause. It has been suggested that many different factors, including excess oxygen, interstitial oxygen, Li dopants, dislocations and poor crystallinity, can result in bands in this spectral region.[14-19] It is interesting to note that the most intense yellow emission is from the sample deposited by the NaOH method, where Li is a very likely impurity. Heavy doping with Li and cross-contamination between growth methods may be responsible for the yellow emissions. Given the uncertainty surrounding the origin of this band(s) a definitive assignment is not possible. The CBD deposited samples showed no evidence of a structured or unstructured green band. Given the poor optical quality of the CBD samples, no further investigation of their properties was undertaken and work was primarily focused on samples prepared by CTR-VPT methods.

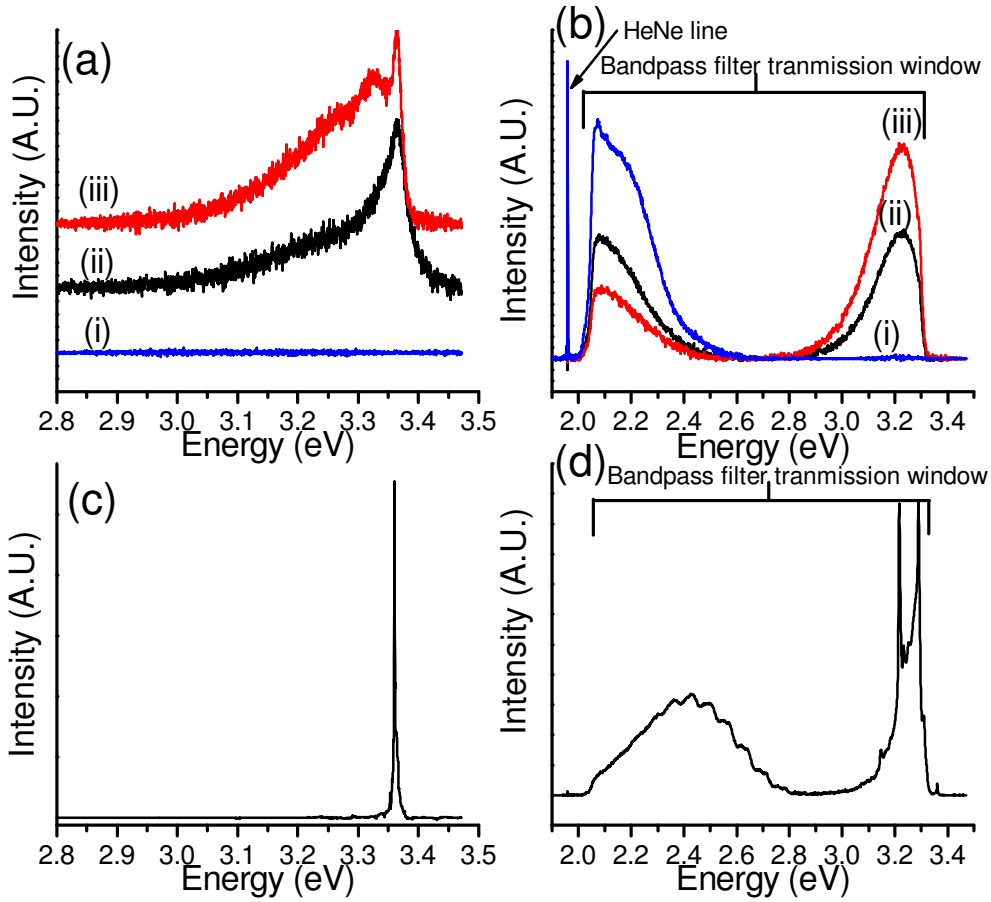

Figure 6.1: PL spectra take at 19.8 K of (a) NBE region (b) visible spectral region of (i) NaOH method (ii) acetate method (iii) HMT method CBD nanorod arrays and (c) NBE region (b) visible spectral region of a CTR-VPT nanorod array.

6.3 CTR-VPT deposited nanorods

The optical quality of nanorods grown by CTR-VPT using the process described in chapter 4 is clearly evident by the intensity of the emission and the narrow line widths. Examples of the NBE emission and visible luminescence from these structures are shown in figure 6.2. For most samples, the NBE emission is dominated by a single line centred around 3.360 eV corresponding to the I_6 / I_{6a} line.[20] This line is known to originate from aluminium (Al) and is a common impurity in CTR-VPT grown ZnO. The source of the Al is difficult to determine precisely. Give that the CTR reaction is carried out an alumina boat, it is likely that the growth equipment is at least a partial contributor to Al related signal. This signal may also be due in part to Al already present in the source powder. Figure 6.2 (a) also shows a weak secondary peak centred around 3.359 eV, corresponding to I_9. This peak has been positively identified as being due to Indium (In), another common impurity in ZnO.[21] While this impurity may also originate from the source powder, it is also very likely that it is due to equipment contamination as In has been used extensively in our laboratory and in our growth system. A broad emission centred around 3.364 eV is also present in some samples and can be seen in figure 6.2 (a) and (c). This emission is typical associated with nanostructures and is related to surface exciton recombinations. It is more commonly observed in nanorods with narrow diameters. More recently it has been identified that surface adsorbed species such as the hydroxide ion are most likely responsible for this emission.[22-23] The FWHMs for the dominant spectral feature, I_6 in figure 6.2 (a),(c) and (e) are 0.42 , 0.34 and 0.68 meV respectively, indicating that nanostructures are of good optical quality, as excessive doping concentrations are known to cause asymmetric peak broadening.[24] This suggests that the underlying CBD layer which was used to nucleate nanorod growth does not seem to affect the optical properties of the rods and no additional impurities are present. While the diffusion of dopants from the CBD layer into the CTR-VPT rods may occur, no detrimental effects that can be linked to the buffer layer has been observed and in particular no yellow luminescence was observed.

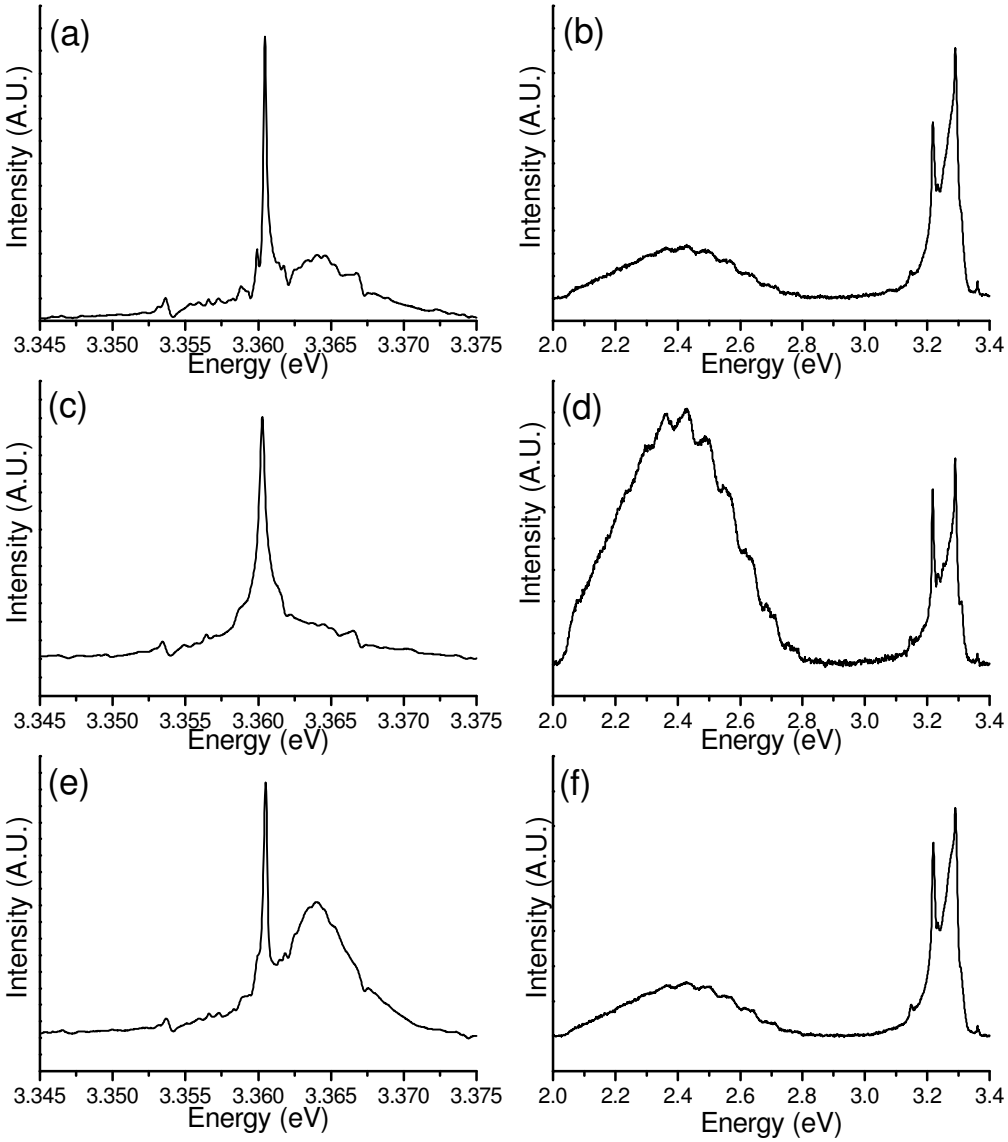

Figure 6.2: PL spectra take at 19.8 K of (a)(c)(e) NBE region (b)(d)(f) visible spectral region of various CTR-VPT nanorod array samples.

Figure 6.2 (b) (d) and (f) show the visible and part of the UV region emission spectra of the samples shown in figure 6.2 (a) (c) and (e). In all samples a prominent donor acceptor pair (DAP) is detected around 3.22 eV with a weaker peak at 3.148 eV.[20] The separation between the two lines is approximately 72 meV, suggesting that the weaker line is a LO-phonon replica of the DAP peak. The identity of the acceptor involved in this transition has yet to be identified but there are strong indications that nitrogen or nitrogen complexes are responsible, although other explanations such as other group elements or

stacking faults induced by dopants such as indium, have been suggested.[25-26] In all samples a weak SGB was detected, the origin of which has been the subject of much debate and is discussed in more detail in section 6.4. The peak intensity of this broad structure is located around ~2.43 eV and it has a FWHM of ~0.4 eV. On the high energy side of this broad band there are clearly defined steps with a ~72 meV spacing, again corresponding to the LO-phonon replicas of a zero phonon line located around 2.859 eV. In figure 6 (d) up to 10 phonon replicas can be observed, indicating that the emission centre is strongly coupled to the lattice structure, i.e. it has a large Huang-Rhys parameter (S) as discussed in chapter 2. The integrated intensity ratio of the SGB with respect to the integrated NBE emission for each of the three samples shown here was 0.06, 0.07 and 0.08 respectively. Similar ratios were found for most nominally undoped samples, indicating that VPT deposited samples were relatively free of deep level recombination centres and therefore, in conjunction with the narrow line widths and intense UV emission, we conclude that CTR-VPT growth deposits nanorods have an excellent optical quality. However, on occasion samples with substantially stronger SGB were observed. The unstructured green band was not detected in any samples grown by CTR-VPT.

The growth of ordered arrays using silica templates were also examined using low temperature PL, in order to determine if the silica templating process had any detrimental effects on the optical quality of the nanorods. Figure 6.3 shows a selection of band edge emission spectra, from samples where the nanorods were spaced 1 μm and 500 nm apart via nanosphere derived silica templates. As with the unordered arrays, the NBE spectra are dominated by the Al associated $I_{6/6a}$ line. Most samples also showed evidence of the indium associated I_9 line, whilst others had a strong surface exciton (SX) peak. The increased occurrence and intensity of the I_9 line is not associated with the patterning process. This impurity was more likely introduced by contaminated VPT growth system, as these samples were grown around the time other indium related experiments were taking place. An interesting feature to note is the variation in the SX peak between spectra in figure 6.3 (a) and (b) as compared to figure 6.3 (c) and (d). Previously it has been found that the SX emission is more intense in high aspect narrow nanorods and high surface area nanostructures.[27-28] In the spectra shown here, the SX peak is most intense in figure 6.3 (b), which corresponds to the positioned nanorod array shown in chapter 5, figure 5.12 (b). As was discussed in chapter 5, secondary nucleation which resulted in very thin high aspect ratio nanorods, were often observed to grow alongside “regular” sized nanorods. These

high aspect rods may in part explain the high intensity of SX peak observed in these PL measurements.

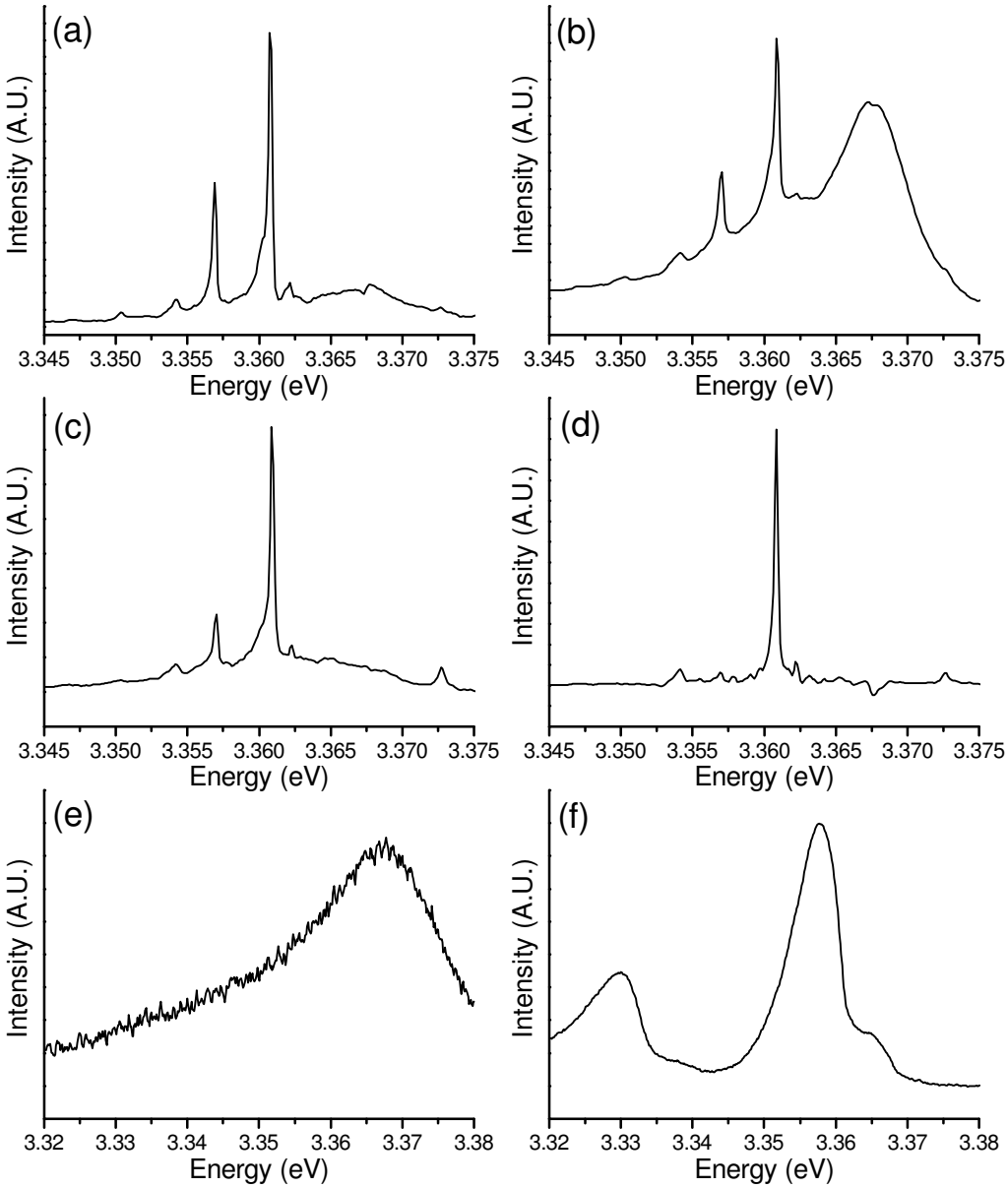

Figure 6.3: PL spectra taken at ~18-20K of (a) VPT grown 1 µm patterned nanorod array corresponding to the sample shown in figure 5.12a (b) 500 nm patterned array corresponding to figure 5.12b (c) 1 µm patterned array corresponding to figure 5.14a (d) 500 nm patterned array corresponding to figure 5.14b (e) CBD acetate buffer layer deposited from a zinc acetate solution. (f) CBD buffer layer deposited from a zinc acetate solution annealed using the same temperature profile as that used for the VPT deposition.

The variation in the SX intensity between figure 6.3 (a) (which corresponds to the sample shown in chapter 5 figure 5.12 (a) and figure 6.3 (b) can then be explained in terms of the nanorod density, given that the 500 nm patterned sample has a significantly higher density of nucleation sites as compared to that of the 1 μm patterned sample. In contrast, when the patterned growth technique was modified to reduce the number of secondary nucleated nanorods, the intensity of the SX peak is significantly attenuated. This can clearly be seen in the PL measurements shown figure 6.3 (c) and (d), which correspond to the samples shown in chapter 5 figure 5.14 (a) and (b) respectively. This is an important consideration, particularly for optoelectronic device fabrication, as the low temperature SX emission has been associated with non-radiative recombination processes at room temperature, which quench the UV optical emission.[27] The FWHM of the dominant $I_{6/6a}$ peak in each spectra was 0.34, 0.93, 0.34 and 0.25 meV corresponding to figure 6.3 (a) – (d) respectively. These values are similar to those obtained for the non-patterned nanorod arrays shown in figure 6.2, indicating the quality of the material deposited has been preserved as compared to non-patterned CTR-VPT arrays and that the silica template did not adversely affect the deposition process.

In order to determine the PL contribution from the underlying buffer layer, samples were prepared without the final VPT deposition. The PL spectra of these samples were measured before and after a thermal cycle identical to that of the final VPT deposition process. From this it was found that PL contribution from the underlying CBD buffer layer, as shown in figure 6.3 (e), is extremely weak and as expected, of similar intensity to that of the CBD samples discussed in section 6.2. After the thermal annealing cycle identical to the CTR-VPT growth process, some improvement in the buffer layer PL signal was observed, as can be seen in figure 6.3 (f). However the signal intensity is still approximately 100 times weaker than its CTR-VPT equivalent. Interestingly prior to the annealing step the only peak detected is a broad peak at ~3.368 eV. Post annealing this peak has been replaced with a feature close in energy to the I_9 line, which could indicate the incorporation of some indium impurities during the annealing cycle. This again points toward equipment contamination as the origin of the In peak observed in these and the other CTR-VPT samples discussed above.

The UV emission was by far the most intense emission in both the patterned and unpatterned samples and the spectra obtained were relatively typical of CTR-VPT grown ZnO. The dominant peaks observed in these samples are both well known and characterised, with detailed discussions of their origins being available in both

comprehensive review literatures and recent books on ZnO.[29-31] In the context of this work, these measurements were made in order to demonstrate that the ZnO nanorods deposited by CTR-VPT using both patterned and unpatterned substrates were of a high optical quality and that the patterning process does not impact on the overall quality of the rods. The NBE emission, while very important, did not yield any particularly unusual results and therefore was not the primary focus of this work.

6.4 The structured green band

Green emission from ZnO has been observed for a long time and has been the source of much debate. Figure 6.4 shows a cathodoluminescence spectra recorded in 1947 by Shrader *et al.*[32] This spectra illustrates two major features of ZnO, an intense UV emission peak centred around 380 nm and a broad green emission centred around 500 nm. While the origin of the UV emission and many of the factors that affect it has been well understood for sometime, the origins of the green emission and associated factors that affect it have been substantially more controversial.

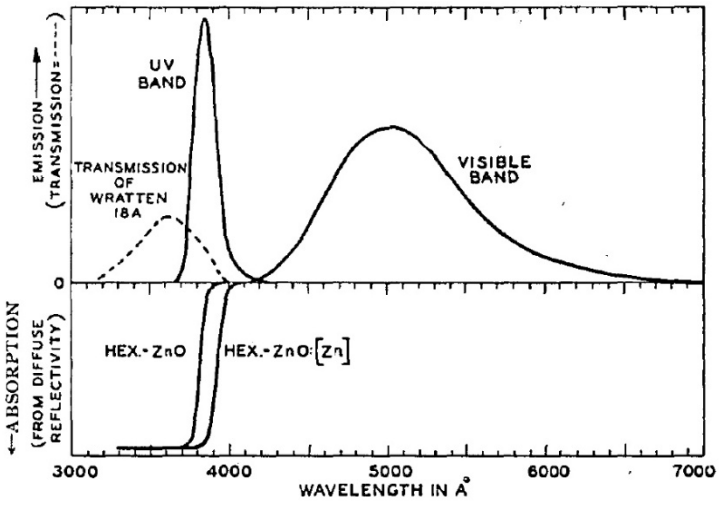

Figure 6.4: Cathode luminescence, absorption and emission spectra reproduced from reference 32. Copyright: (1947) The Optical Society of America

By the 1950's in Heiland, Mollwo and Stöckmann's review of ZnO, it was established that the green emission spectra depended on the method of production of the material and of how the material was treated.[33] In particular, they noted that the UV emission was maximised as compared to the green emission when ZnO was prepared in an oxidising atmosphere while the green emission was maximised by preparing the material or

heating it in a reducing atmosphere and that the green emission can either be maximised or completely eliminated by the addition of lead or manganese respectively. From this they reported that "It seems sure to conclude from the method of preparation that neither the ultraviolet or the green luminescence require foreign atoms as Activators."

A decade later R. Dingle published what would later become one of the most fundamental contributions to the ZnO green band debate.[34] In this work, Dingle assigned the origin of the SGB to copper impurities which result in a transition from a highly shielded localised level of the copper impurity to a level strongly perturbed by the valence band of the crystal. At low temperatures this transition leads to a sharp zero-phonon line with pronounced phonon coupled side bands. Furthermore, this zero phonon line was composed of a sharp doublet, the intensity of which corresponded to the natural isotopic ratio of copper, one of the principal contaminants found in Dingle's samples. Each of the lines of the doublet was found to behave in an identical fashion during PL studies in a magnetic field (Zeeman) and under uniaxial stress, leading Dingle to conclude that they originate from identical processes. In addition the anisotropic g-factor for one of the states involved in the transition obtained from Dingle's Zeeman spectroscopy were in close agreement with the g-factors of one of the states involved in a Cu^{2+} absorption transition as determined by both absorption spectroscopy and electron spin resonance (ESR) by Dietz *et al.*[35] Figure 6.5 show the zero-phonon doublet obtained by Dingle where the narrow line separation of 0.11 meV and sharp FWHM of 0.05 meV are indicated and the ratio of the peak emissions supposedly matches that of the natural isotopic ratio of Cu.[34]

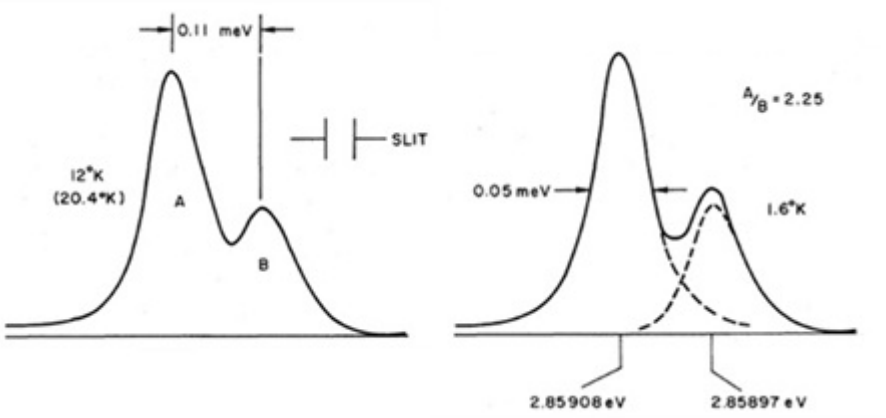

Figure 6.5: Low temperature PL showing the zero-phonon doublet reproduced from reference 34. Copyright: (1969) The American Physical Society.

It was therefore concluded by Dingle that the green emission from ZnO, as discussed by Heiland *et al.* was due to Cu^{2+} impurities. However, this can only be consider half the story as the green emission discussed by Heiland *et al.* was obtained at room temperature and was unstructured.[33] Consequently, some degree of disparity already existed between Heiland's summary of the green band and Dingle's proposed answer. Secondly, an unstructured green band has also often been detected at low temperature, where there is no indication of either the zero-phonon line or SGB. Therefore it is quite clear that there must be at least two green bands, one structured and one unstructured, whose origins are different.

The unstructured green band and its origins has been at least as controversial as the SGB, with many research groups proposing different origins and mechanisms, such as zinc interstitials, oxygen vacancies and zinc vacancies.[36-38] Some attempts were also made to link the unstructured green band to Cu^{1+}.[39] However the g-values obtained for the different green bands are different implying that the bands must be of different origin. More recently strong evidence has been presented that identifies the origin of the unstructured green band as oxygen vacancies.[36, 40] This assignment came about by assuming the unstructured green band was due to an intra-defect transition. By using a configuration coordinate model and fitting the experimentally determined temperature dependant FWHM, the Huang–Rhys factor and mean local mode phonon was determined. The mean phonon mode was then used to determine an energy for the fundamental absorption transition. Absorption and photoluminescence excitation were then used to confirm the presence of a weak absorption band in this region. Furthermore the absorption energy of this defect agreed extremely well with the model put forward for two electron F centres, that is anion vacancies. This convincing evidence confirms what Heiland had hypothesized some 45 years earlier, "that neither the ultraviolet or the green luminescence require foreign atoms as activators", at least in regard to the unstructured green band.[33]

The unstructured green band was not detected in our nanorod samples and so we must return our attention to the SGB and its origin. Dingle's assignment of copper as being responsible for the SGB was mainly based on two key factors. First, the similarity of the anisotropic g-factor to that of one of the states involved in an absorption line previously identified as Cu^{2+} and second, the intensity of the two peaks apparently matched that of the natural isotopic ratio of copper which he knew to be present in his samples. Whilst convincing, there are three important considerations that should be kept in mind. First, the

similarity in the anisotropic g-factor does not definitely identify the absorption transition as being of the same origin as the zero phonon emission. Second, the isotope shift of some of the electronic levels did not fit with the standard theories for isotope shift at the time.[41] This point was later addressed by Van Vechten who extended the model of Heine *et al.* to take account of the charge state of the Cu impurity.[42] More recent models put forward suggest that Van Vechten's approach and that of others was flawed and that a new approach which took into account the microscopic electronic structure was a more accurate approach.[43] While both these approaches were able to arrive at the energy separation between the two isotope lines and the unusual ordering of the isotope shift, these models and associated experiments still fail to provide direct experimental evidence that the ZPL doublet is due to the emission from the two different Cu isotopes with an isotope shift between them. Some notable attempts have been made to provide this missing link and in particular the doping of ZnO by nuclear transmutation of neutron irradiated ZnO.[44] When ZnO is irradiated by a neutron beam, some of the ^{64}Zn atom can absorb a neutron to form ^{65}Zn, which subsequently decays by the emission of γ-rays to leave ^{65}Cu.[45] An increase in the green luminescence yield was observed in irradiated samples, and as expected the EPR signal confirmed the presence of copper.[30, 44] However care should be taken in interpreting the increase in green luminescent yield given that the neutron absorption process emits high energy γ-rays which may induce lattice defects. Similar transmutation experiments in ZnSe estimated the γ-ray energy for the radiative capture of a neutron by ^{64}Zn as several MeV which in turn imparts a recoil energy in excess of 100 eV to the lattice.[46] This recoil energy is sufficient to dislodge O atoms from the lattice creating vacancies, thus increasing the green luminescence and creating copper interstitials.[47] It is unclear whether this aspect was taken into account and in addition, no PL spectra showing the growth of one ZPL peak associated with a particular Cu isotope over another was included in Broser's work, leaving us no option but to conclude that such measurements were not made.[44] Third, the extremely high resolution necessary to observe the ZPL doublet has limited the number of detailed investigations into this spectral feature and as far as we are aware nobody has successfully demonstrated control of the isotope doping, confirming the theoretical models put forward. Consequently, many published papers appear content to accept Dingle's explanation, without the availability of unambiguous and definitive proof of copper's involvement or direct evidence of the unusual isotope shift.

Deliberate doping of ZnO with Cu and specifically isotpically pure Cu would provide direct evidence of the ZPL shift and also unambiguously identify Cu as the species responsible for the SGB emission. Therefore if we could grow samples by CTR-VPT and deliberately introduce single isotopes of Cu, we should then be able to observe a distinctive variation in the ratio of the two ZPL peaks which would depend on the isotopes introduced. However, before attempting single isotope doping, it was necessary to find a method whereby the Cu isotopes could be introduced in a controlled manner. The first step of this approach was to introduce copper into the growth process in various quantities and find the conditions which would maximise the SGB intensity. We attempted to do this by pre-doping the ZnO powder with Cu using a rapid combustion process, which had been previously demonstrated to incorporate dopants in a controlled manner in other materials.[48] Copper nitrate and zinc nitrate in the desired ratios were dissolved in ethylene glycol and mixed for several hours. These mixtures were then rapidly combusted to produce fine ZnO powders with Cu concentrations of 1, 5, 10 and 20 ppm. The nitrate salts act as an oxidiser and the ethylene glycol as the fuel, which ensures that reaction proceeds extremely fast, preventing the formation of secondary CuO phases. Each copper doped powder was then mixed with an equal mass of the nominally undoped ZnO usually used for our CTR-VPT growth, yielding ZnO mixtures with a nominal doping concentration of 0.5, 2.5, 5 and 10 ppm. This concentration range was chosen as it was close to Dingle's reported Cu concentration.[34] Samples were then grown by CTR-VPT using these doped powders by our usual methods outlined in chapter 4. SEM analysis of the samples indicated that all bar one sample resulted in the expected nanorod morphology. For unknown reasons the sample grown using the second highest Cu doping concentration (5 ppm) resulted in shorter thicker nanostructures. Each CTR-VPT sample was then cleaved into two equal pieces. One piece of each sample was annealed at 900°C for 10 minutes. The annealing step was performed as previous studies in our lab and in the reported literature indicate that annealing at high temperatures increases the intensity of the SGB.[39, 49] PL measurements were made of each sample using identical conditions. For reference purposes three additional undoped samples were also included in the sample set, hereafter referred to as reference A, B and C.

Peak Emission Intensity	Near band edge	Green band	Near band edge (post annealing)	Green band (post annealing)
Weakest	10 ppm	Reference A	10 ppm	2.5 ppm
	2.5 ppm	0.5 ppm	Reference B	Reference A
	0.5 ppm	10 ppm	2.5 ppm	0.5 ppm
	5 ppm	2.5 ppm	Reference A	10 ppm
	Reference A	Reference C	5 ppm	Reference B
	Reference C	5 ppm	0.5 ppm	Reference C
Strongest	Reference B	Reference B	Reference C	5 ppm

Table 6.1: A summary of the observed emission intensities for a range of Cu doped and undoped CTR-VPT grown ZnO nanorod arrays.

A summary of the PL results can be seen in tables 6.1 and 6.2. First we consider the absolute intensities of the NBE emission and green band before and after annealing. Prior to annealing the undoped reference samples had the strongest NBE emission. The weakest emission was from that of the heaviest doped 10 ppm sample. The order of intensities did not follow any relationship with the doping concentration, as the 5 ppm sample had stronger band edge than all other doped samples. No specific relationship could be determined from the green band prior to annealing. The reference samples had both the strongest and weakest green band intensities with the doped samples randomly scattered in between. Post annealing, both the band edge and green band showed no discernable pattern linking the doping concentration to the emission intensity.

	Ratio of near band edge peak intensity to green band peak intensity prior to annealing	Ratio of near band edge peak intensity to green band peak intensity post annealing
Reference A	2196	4.0
Reference B	1629	0.5
Reference C	1031	4.5
0.5 ppm	977	9.3
2.5 ppm	414	3.4
5 ppm	401	2.0
10 ppm	181	0.1

Table 6.2: The ratio of peak NBE intensity to peak green band intensity for Cu doped and undoped CTR-VPT nanorod arrays prior to annealing and post annealing at 900°C

The ratio of the NBE intensity to the green band shows that prior to annealing, the relative intensity of the green band increases with respect to the band edge and follow the

doping concentration order. However, the increase does not appear to form a linear relationship with the doping concentration. After annealing, all samples show a dramatic decrease in the NBE intensity with respect to the green band. The increased doping concentration appears to quench the band edge emission, but surprisingly, the nominally undoped also samples show substantial quenching of the same magnitude as that of the doped samples. From the data contained in tables 6.1 and 6.2, no definitive conclusions can be drawn about the role of copper in the green emission. The distribution and randomness of the results suggest that the CTR-VPT growth process with doped ZnO powders may incorporate additional Cu, but that the quantity of Cu incorporated may not be uniformly related to the doping concentration. Alternatively, variations in the nanorod density, morphology and the collection optics and analysis may also contribute in part or in whole to the variability in results. Consequently no definitive conclusions may be drawn from this data.

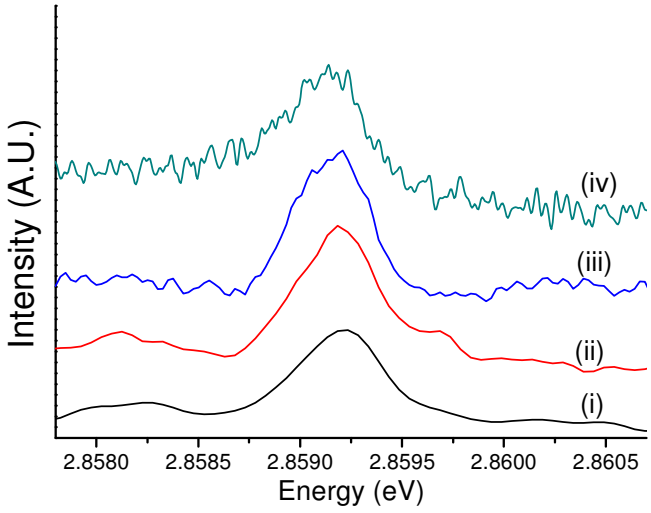

Figure 6.6: Low temperature (19.8 K) PL spectra of the ZPL region of the spectrum from a CTR-VPT grown sample at resolutions of (i) 0.24 meV (ii) 0.12 meV (iii) 0.06 meV (iv) 0.027 meV. The FWHM for the various spectra are (i) 0.46 meV (ii) 0.44 meV (iii) 0.40 meV and (iv) 0.34 meV.

Next, we examined the ZPL line for evidence of Cu involvement in the SGB. Given that the doping experiments were inconclusive, the sample chosen for this analysis were not those with the brightest green emission. Instead, the samples which had the sharpest line widths were chosen, as the resolution necessary to observe the two ZPL components is

extremely high. Figure 6.7 shows the ZPL region of the spectrum for the same sample acquired at increasing resolution, from 0.25 meV to 0.027 meV. In each case only one dominant peak was observed. Increasing the resolution by a factor of 10 resulted in a rapid drop of the signal intensity, resulting in more noisy spectra, where a weak secondary peak would be more difficult to detect.

Despite the factor of 10 increase in resolution the combined FWHM of the peaks only reduced by 0.12 meV, from 0.46 meV to 0.34 meV. Given that the separation of the ZPL lines is only 0.11 meV and the FWHM of a single line was estimated as 0.05 meV by Dingle, it was clear that the ZPL doublet would be unresolvable as the resolution was limited by the sample. Impurity induced band broadening or strain induced at the nanorod / buffer layer interface may have been responsible for this sample limitation. It was therefore clear that we would not be able to identify the origin of the SGB or examine the isotope shift using CTR-VPT grown samples and that another strategy would be required.

6.5 Single crystal ZnO and isotopic doping

Given our failure to conclusively identify the origin of SGB using high quality CTR-VPT grown samples, focus was then shifted to commercially available ZnO single crystals form the Tokyo Denpa company. These crystals are know to be of extremely high optical quality, with a low intrinsic background Cu concentration (1 x 10^{15} atoms /cc or 0.02 ppm).[50] PL spectra of the Zn terminated *c*-plane of an as received crystal (as shown in figure 6.7i) showed only weak evidence of a SGB. The crystal was then cleaved into 4 equal pieces. After annealing one piece at 900°C for ten minutes, the unstructured green band was converted into the same SGB (figure 6.7ii) observed in our CTR-VPT samples. This conversion was consistent with the report of Garces *et al*., who speculated that the annealing process converts Cu^{+} into Cu^{2+}, thus rendering the copper defect optically active.[39]

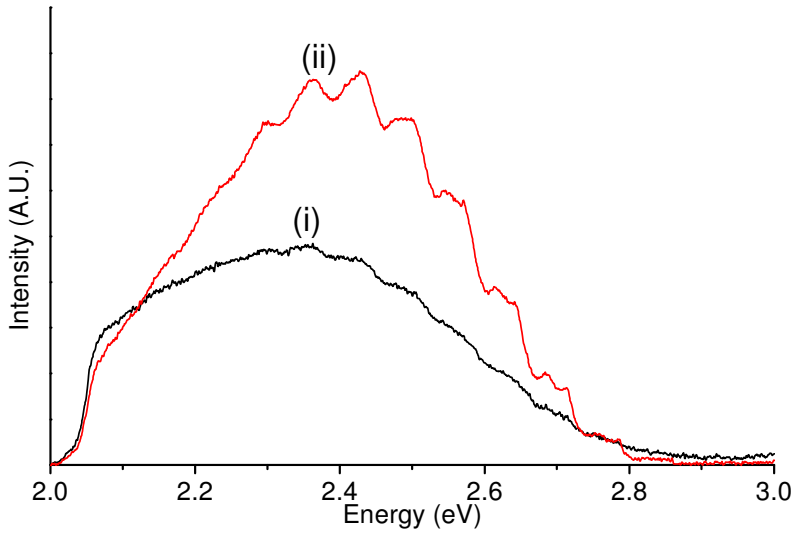

Figure 6.7: Low temperature PL spectra of the visible emission region for a Tokyo Denpa single crystal ZnO sample (i) as received (ii) after annealing at 900°C for ten minutes.

As was mentioned in chapter 5, a galvanic displacement reaction occurs between Cu^{2+} solutions and ZnO, which was detrimental to our patterning attempts. This technique was originally used by Takahashi *et al.* as a method of forming Cu interconnect patterns.[51] In their original patent they specified that the ZnO crystallite size of the polycrystalline ZnO films must be small (~50 nm) in order for the displacement reaction to form a continuous CuO film on the ZnO. While no reason was specified, this strongly suggested that the Cu / ZnO displacement reaction formed a self passivating CuO layer which inhibited further reaction. We concluded that this displacement reaction may prove to be a novel method for doping ZnO single crystals, without inducing the sort of damage associated with ion implantation. Therefore it may be possible to introduce isotopically pure Cu into the ZnO crystal and still be able to resolve the ZPL line, thereby obtaining direct evidence of the isotopic shift and the identity of the chemical species responsible for the SGB.

^{63}Cu and ^{65}Cu isotopes in the form of small metal flakes (with isotopic enrichments of 99.8% and 99.2%, respectively) were first obtained from Isoflex.[52] Flakes of ~15 mg were partially dissolved in 80 µl of hydrogen peroxide and 40 µl of acetic acid to produce copper acetate solutions. These solutions were allowed to react for several hours before being diluted to 20 ml with DI-H_2O. Only a small fraction of the Cu isotope flakes dissolved. ZnO single crystal samples were then submerged in these solutions for 40 seconds before being removed, washed with ethanol and dried using a gentle nitrogen stream. A third

solution consisting of equal parts of the ^{63}Cu and ^{65}Cu solution was also prepared, and used to co-dope a third ZnO sample with an approximately equally amount of each isotope. The samples were then annealed at 700°C for 16 hours. This temperature was chosen for two principal reasons. First it was hoped that a lower temperature would reduce the number of defects such as Zn_i, V_{zn}, V_o and O_i, and associated inhomogeneous strain, which may reduce our ability to resolve the ZPL doublet. Second, the Cu deposited on the substrate surface was in the form of CuO i.e. already in the 2+ state. Therefore in the absence of a reducing atmosphere, the Cu will be incorporated in the 2+ state. At higher temperatures CuO forms Cu_2O thereby rendering the Cu optically inactive. The Cu doped single crystal ZnO samples were then examined by low temperature PL, the results of which can be seen in figure 6.8.

In the visible region of the spectrum, (as shown in figure 6.8a) the familiar SGB was detected in all samples, including the nominally undoped sample annealed at 900°C for ten minutes. High resolution spectra of the ZPL region (figure 6.8b), shows a range of emission peaks depending on the sample treatment. The nominally undoped sample (i) has two peaks centred around at 2.8591 eV, with a separation of 0.11 meV. The ratio between the two peaks is ~2.2. These lines are clearly the Dingle lines given that both the position separation and intensity ratio match that of Dingles report.[34] The sample doped with ^{63}Cu (figure 6.8b ii) shows only one peak located at 2.85922 eV, while the sample doped with ^{65}Cu (figure 6.8b iii) also shows only one peak located at 2.85906 eV. Interestingly, the ^{65}Cu peak shape has a slight shoulder on the high energy side, which may correspond to a weak signal from the intrinsic ^{63}Cu. The co-doped sample (figure 6.8b iv) has two clearly resolved peaks located at 2.85913 and 2.85924 eV, again corresponding to an isotope shift of 0.11 meV, in direct agreement with Dingle's reported isotope shift. The intensity ratio of the two peaks is ~0.99 confirming the equal isotopic doping of the sample. The data in figure 6.8 (c) show the NBE region of the same samples, where multiple donor bound exciton features are present, and specifically shows the I_8 (3.3598 eV) line region.[29, 31] It can be seen that the shifts in the peak energy of the I_8 line is in all cases less than 0.03 meV, of a similar order of magnitude to the linewidths of the components of the SGB ZPL doublet (~0.11 meV) and less than the separation of the doublet components (~ 0.11 meV), which confirms the peaks and shifts observed in the ZPL region are not result of strain or drift in the spectrometer wavelength calibration. We must therefore conclude that the ZPL line and associated SGB result from a defect involving a single Cu atom.

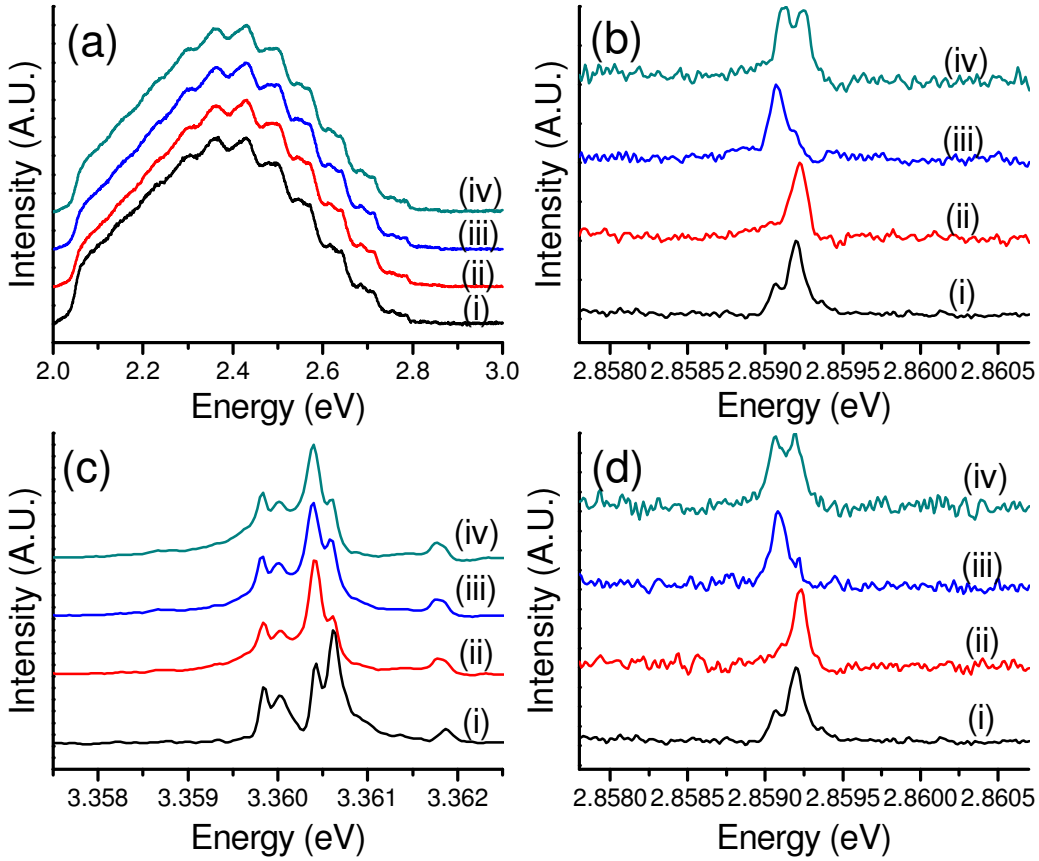

Figure 6.8: Low temperate PL spectra of (a) broad spectral range for (i) natural Cu isotope distribution (ii) ^{63}Cu doped sample (iii) ^{65}Cu and (iv) ^{63}Cu/^{65}Cu Co-doped sample (b) zero phonon region for (i) natural Cu isotope distribution (ii) ^{63}Cu doped sample (iii) ^{65}Cu and (iv) ^{63}Cu/^{65}Cu Co-doped sample (c) NBE region for (i) natural Cu isotope distribution (ii) ^{63}Cu doped sample (iii) ^{65}Cu and (iv) ^{63}Cu/^{65}Cu Co-doped sample (d) as per figure (b) after each sample was annealed at 900°C for 10 minutes (Spectra shown in all cases have been normalised and off-set for ease of comparison)

There are some intriguing points to note on the copper doping experiment. The most intense ZPL emission was observed for the undoped / intrinsically doped sample. The question then arises as to why the intrinsic Cu is undetected in the isotope doped samples and is this related to the annealing process, given that the undoped sample was annealed at 900°C for ten minutes and the doped samples were annealed at 700°C for 16 hours. To address this issue the doped samples were annealed a second time, at 900°C for ten minutes and the results shown in figure 6.8d (iv). The sample doped with ^{63}Cu showed no distinctive variation. Activating the intrinsic Cu would make the ^{63}Cu peak stronger with only a small increase in the ^{65}Cu (which is the less naturally abundant isotope), so no

observable variation is a likely outcome of the second annealing. A weak new peak appears in the ^{65}Cu doped sample, around the location of the shoulder observed prior to the second anneal, which is in good agreement with the ^{63}Cu peak position, indicating that the intrinsic Cu impurity has been activated during the second anneal. A slight change in the co-doped sample is observed, with the ratio of the two peaks shifting from ~0.99 (^{65}Cu slightly dominant) to ~1.01 (^{63}Cu slightly dominant). These results can be interpreted in one of two ways. The first interpretation is that the Cu was incorporated into the ZnO lattice, without significant activation of the intrinsic Cu. Or alternatively, the initial diffusion of Cu during the first anneal displaces much of the intrinsic Cu near the surface so that the doped Cu is the dominant species being sampled during the PL experiment, which tends to probe the near surface region (the penetration depth of the 325 nm HeCd laser is < 100 nm). During the second anneal the doped and intrinsic Cu begin to intermix leading to a mixed ZPL intensity ratio.

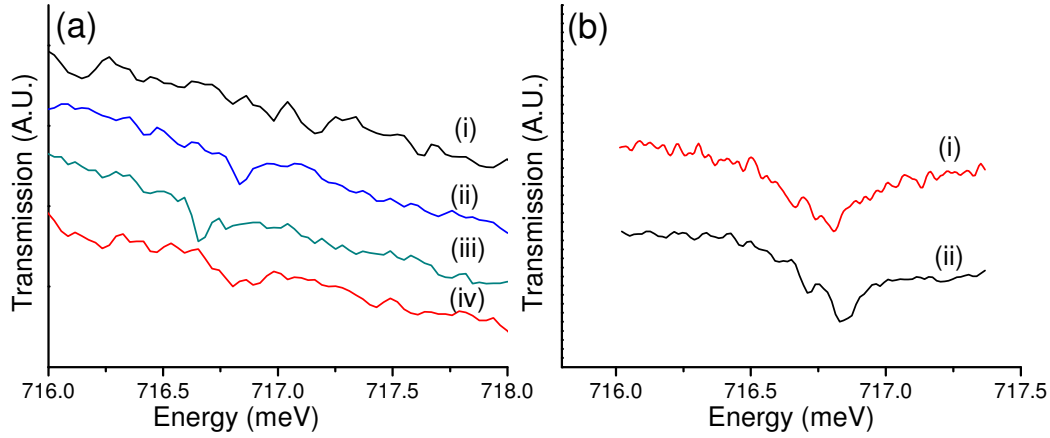

Figure 6.9: (a) Absorption measurements of the Cu related line in ZnO for (i) undoped sample (ii) ^{63}Cu doped sample (iii) ^{65}Cu doped sample and (iv) co-doped sample. (b) Absorption measurements of the Cu related line in ZnO for sample doped twice using (i) natural Cu isotopic ratio and (ii) co-doped ratio. These absorption measurements made by Dr. F. Herklotz of the Institut für Angewandte Physik, Dresden Germany. (Spectra shown in all cases have been normalised and off-set for ease of comparison)

The original assignment of Cu being responsible for the green emission in ZnO came in part from the similarity between the anisotropic g-factor of one of the states involved in an absorption line associated with Cu and that of the green band ZPL. Absorption measurements were made of our ZnO samples to determine if these lines could be observed and if they confirmed the isotopic doping. These absorption measurements

are shown in figure 6.9. No definitive conclusions can be drawn from the absorption spectra, as any peaks that are present in the region where the Cu isotope absorption lines are known to occur are of the same magnitude as the background noise. The two single isotope doped samples have what appears to be a single weak absorption line each, located at 716.8 meV and 717.7 meV corresponding to the ^{63}Cu and ^{65}Cu doped sample respectively. While this is in reasonable agreement with the position of the absorption lines associated with the individual copper isotopes,[53] the intensity of these possible peaks are not suitably strong enough so as to definitively identify them as (a) absorption lines as opposed to background noise and (b) the absorption lines due to the individual Cu isotopes. Further absorption and PL measurements (figure 6.9 (b)) were made on samples that were doped more heavily using both the natural Cu and the 50/50 Cu isotopic ratios. The increase in doping was achieved by doubling the concentration of the Cu salt solution, doubling the ZnO crystal immersion time and performing the whole doping process twice. No significant improvement in the absorption spectra was observed. The most likely explanation is that the region doped with isotopically enriched Cu is a rather thin layer close to the surface and thus contributes little to the absorption signal compared to the absorption due to the entire bulk crystal (0.3 mm thick). Consequently, the concentration of Cu required to achieve a reasonable absorption signal is far higher than that required for PL experiments, since the PL signal is mainly from the near surface region because the penetration depth of the 325 nm excitation is of the order of some hundreds of nm. However, as more Cu is incorporated the intensity of the ZPL obtained by PL measurements decreased. The nominally undoped sample had the most intense ZPL while the single isotope doped samples had a weaker ZPL. The samples that were doped twice using higher concentrations had the weakest ZPL signal. From this one could speculate that Cu may have more than one role in ZnO. In particular we note that previous studies have shown that during doping only ~50% of the Cu atoms occupy a Zn site and after annealing at 700°C a substantial reduction in the number of Cu atoms on Zn sites is observed.[54] The Cu atoms then occupy random lattice sites of very low symmetry or heavily distorted surroundings. Furthermore the ZPL line width also appears very sensitive to doping concentration. Figure 6.10 shows the effect of increasing the doping concentration on the ZPL emission. The FWHM of the combined peaks increase substantially and the two individual isotope peaks are no longer resolvable. The ZPL emission intensity was weaker than that of the single step co-doped sample, which suggests that the additional Cu may also be suppressing the ZPL emission. While the anisotropic g-factor and stress data available on the ZPL line are

consistent with the assignment of a single Cu^{2+} atom on the Zn site, the suppression of the ZPL emission and increase in the ZPL line width which occurs with increased doping suggests that the role of Cu in ZnO may be more complex.[34, 55]

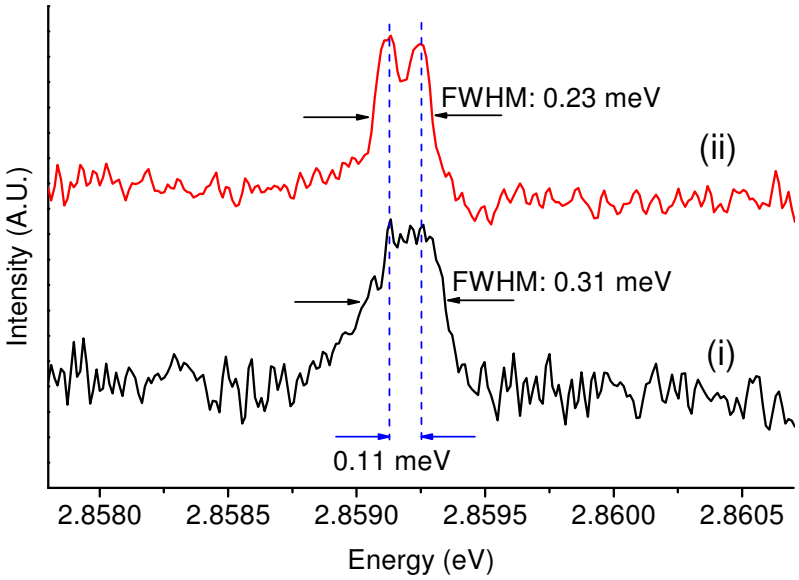

Figure: 6.10: Low temperature PL spectrum of the ZPL region of a (i) ZnO sample co-doped twice and (ii) a ZnO sample co-doped once with ^{63}Cu and ^{65}Cu

6.6 Conclusions

In this chapter we have examined the optical properties of ZnO nanorods grown by both CBD and CTR-VPT and of single crystal ZnO samples by low temperature PL. In general we found that, in our lab CTR-VPT deposition results in nanostructures of significantly higher quality than those produced by CBD methods. The origin of the dramatic differences in quality between CTR-VPT and CBD may well originate in an unintentional doping with excessive donors during the CBD growth process The CBD nanorods typically resulted in a single broad spectral feature with a large FWHM in the NBE region and a broad featureless yellow band emission. Qualitative assessment of the CTR-VPT and CBD grown samples indicate that CTR-VPT samples were significantly brighter than those grown by solution methods and in general had very sharp NBE features indicating that the material was of high quality. A more rigorous analysis, including a determination of the internal quantum efficiency from temperature and power dependent PL studies by methods outlined else

where, may be very useful in quantifying and perhaps identifying the cause of the large disparity between CBD grown and CTR-VPT grown samples.[56]

In most CTR-VPT samples two or three NBE features were observed, including $I_{6/6a}$, I_9 and SX bound excitons indicating the presence of aluminium, indium and surface bound exciton recombination channels in high aspect ratio nanorods. The CTR-VPT samples also had a SGB associated with Cu impurities. Whilst the prior evidence in the literature for the involvement of Cu in the SGB was strong, in our opinion this identification had not yet been unambiguously shown. Doping the CTR-VPT samples with Cu during growth resulted in ambiguous outcomes, from which a definitive identification of Cu involvement in the defect responsible for the emission could not be made. To address this shortcoming, a novel adaption of Takahashi's method for forming Cu interconnects was used to dope ZnO single crystals with specific isotopes and isotopic ratios of ^{63}Cu and ^{65}Cu, without inducing the structural damage associated with other methods such as ion implantation. This allowed us to both resolve the ZPL doublet of the SGB for both nominally undoped ZnO and for the ZnO samples doped with specific isotopes and isotope ratios. This allowed us to both definitively identify a single Cu atom as a constituent of the defect responsible for the SGB and confirm the previously assumed unusual ordering of the isotope shifts in certain electronic levels in Cu doped ZnO. As the work of Leiter *et al.* has shown some 45 years later that Heiland's conclusions regarding the origin of the unstructured green band were broadly correct, we too, some 43 years later, must conclude that the observations of Dingle regarding the origin of the structured green band were also correct.

6.7 References

(1) Hung, C. H.; Whang, W. T. *Journal of Crystal Growth* **2004,** *268* (1-2) 242-248

(2) Wang, M.; Ye, C. H.; Zhang, Y.; Hua, G. M.; Wang, H. X.; Kong, M. G.; Zhang, L. D. *Journal of Crystal Growth* **2006,** *291* (2) 334-339

(3) Xu, F.; Yuan, Z. Y.; Du, G. H.; Ren, T. Z.; Volcke, C.; Thiry, P.; Su, B. L. *Journal of Non-Crystalline Solids* **2006,** *352* (23-25) 2569-2574

(4) Uthirakumar, P.; Karunagaran, B.; Nagarajan, S.; Suh, E. K.; Hong, C. H. *Journal of Crystal Growth* **2007,** *304* (1) 150-157

(5) Wahab, R.; Ansari, S. G.; Kim, Y. S.; Seo, H. K.; Kim, G. S.; Khang, G.; Shin, H. S. *Materials Research Bulletin* **2007,** *42* (9) 1640-1648

(6) Yang, J.; Lang, J.; Yang, L.; Zhang, Y.; Wang, D.; Fan, H.; Liu, H.; Wang, Y.; Gao, M. *Journal of Alloys and Compounds* **2008,** *450* (1-2) 521-524

(7) Yang, L. L.; Zhao, Q. X.; Willander, M. *Journal of Alloys and Compounds* **2009,** *469* (1-2) 623-629

(8) Gao, S. Y.; Li, H. D.; Yuan, J. J.; Li, Y. A.; Yang, X. X.; Liu, J. W. *Applied Surface Science* **2010,** *256* (9) 2781-2785

(9) Sun, S.-N.; Marí, B.; Wu, H.-L.; Mollar, M.; Cui, H.-N. *Applied Surface Science* **2010,** *257* (3) 985-989

(10) Ting, C. C.; Li, C. H.; Kuo, C. Y.; Hsu, C. C.; Wang, H. C.; Yang, M. H. *Thin Solid Films* **2010,** *518* (15) 4156-4162

(11) Schlenker, E.; Bakin, A.; Weimann, T.; Hinze, P.; Weber, D. H.; Gölzhäuser, A.; Wehmann, H. H.; Waag, A. *Nanotechnology* **2008,** *19* (36) 365707

(12) Bekeny, C.; Voss, T.; Hilker, B.; Gutowski, J.; Hauschild, R.; Kalt, H.; Postels, B.; Bakin, A.; Waag, A. *Journal of Applied Physics* **2007,** *102* (4) 044908-044905

(13) Bekeny, C.; Voss, T.; Gafsi, H.; Gutowski, J.; Postels, B.; Kreye, M.; Waag, A. *Journal of Applied Physics* **2006,** *100* (10) 104317-104314

(14) Djurisic, A. B.; Leung, Y. H.; Tam, K. H.; Ding, L.; Ge, W. K.; Chen, H. Y.; Gwo, S. *Applied Physics Letters* **2006,** *88* (10) 103107

(15) Reshchikov, M. A.; Morkoç, H.; Nemeth, B.; Nause, J.; Xie, J.; Hertog, B.; Osinsky, A. *Physica B: Condensed Matter* **2007,** *401-402* (0) 358-361

(16) Kwok, W. M.; Djurisic, A. B.; Leung, Y. H.; Chan, W. K.; Phillips, D. L. *Applied Physics Letters* **2005,** *87* (9) 093108

(17) Radoi, R.; Fernández, P.; Piqueras, J.; Wiggins, M. S.; Solis, J. *Nanotechnology* **2003,** *14* (7) 794

(18) Djurisic, A. B.; Leung, Y. H. *Small* **2006,** *2* (8-9) 944-961

(19) Ohashi, N.; Ebisawa, N.; Sekiguchi, T.; Sakaguchi, I.; Wada, Y.; Takenaka, T.; Haneda, H. *Applied Physics Letters* **2005,** *86* (9) 091902

(20) Meyer, B. K.; Alves, H.; Hofmann, D. M.; Kriegseis, W.; Forster, D.; Bertram, F.; Christen, J.; Hoffmann, A.; Strassburg, M.; Dworzak, M.; Haboeck, U.; Rodina, A. V. *Physica Status Solidi B-Basic Research* **2004,** *241* (2) 231-260

(21) Strassburg, M.; Rodina, A.; Dworzak, M.; Haboeck, U.; Krestnikov, I. L.; Hoffmann, A.; Gelhausen, O.; Phillips, M. R.; Alves, H. R.; Zeuner, A.; Hofmann, D. M.; Meyer, B. K. *Physica Status Solidi B-Basic Research* **2004,** *241* (3) 607-611

(22) Biswas, M.; Jung, Y. S.; Kim, H. K.; Kumar, K.; Hughes, G. J.; Newcomb, S.; Henry, M. O.; McGlynn, E. *Phys Rev B* **2011,** *83* (23) 235320

(23) Biswas, M., *Growth and Characterisation of ZnO Nanostructures: Excitonic Properties and Morphology*, in *School of Physical Sciences*. 2010, Dublin City University: Dublin

(24) Morgan, T. N. *Physical Review* **1965,** *139* (1A) A343-A348

(25) Monteiro, T.; Neves, A. J.; Carmo, M. C.; Soares, M. J.; Peres, M.; Wang, J.; Alves, E.; Rita, E.; Wahl, U. *Journal of Applied Physics* **2005,** *98* (1) 013502

(26) Lin, S.; He, H.; Ye, Z.; Zhao, B.; Huang, J. *Journal of Applied Physics* **2008,** *104* (11) 114307

(27) Grabowska, J.; Meaney, A.; Nanda, K. K.; Mosnier, J. P.; Henry, M. O.; Duclere, J. R.; McGlynn, E. *Phys Rev B* **2005,** *71* (11) 115439

(28) Biswas, M.; Jung, Y. S.; Kim, H. K.; Kumar, K.; Hughes, G. J.; Newcomb, S.; Henry, M. O.; McGlynn, E. *Phys Rev B* **2011,** *83* (23) 235320

(29) Morkoç, H.; Özgür, Ü., *Zinc Oxide: Fundamentals, Materials and Device Technology*. Zinc Oxide. 2009: Wiley-VCH Verlag GmbH & Co. KGaA.

(30) Klingshirn, C. F.; Meyer, B. K.; Waag, A.; Hoffmann, A.; Geurts, J., *Zinc Oxide From Fundamental Properties Towards Novel Applications*. Springer Series in materials science, ed. R.Hull, et al. 2010, Heidelberg: Springer-Verlag.

(31) Ozgur, U.; Alivov, Y. I.; Liu, C.; Teke, A.; Reshchikov, M. A.; Dogan, S.; Avrutin, V.; Cho, S. J.; Morkoc, H. *Journal of Applied Physics* **2005,** *98* (4) 041301

(32) Shrader, R. E.; Leverenz, H. W. *J. Opt. Soc. Am.* **1947,** *37* (11) 939-940

(33) Heiland, G.; Mollwo, E.; Stöckmann, F., *Electronic Processes in Zinc Oxide*, in *Solid State Physics*, S. Frederick and T. David, Editors. 1959, Academic Press. p. 191-323.

(34) Dingle, R. *Physical Review Letters* **1969,** *23* (11) 579

(35) Dietz, R. E.; Kamimura, H.; Sturge, M. D.; Yariv, A. *Physical Review* **1963,** *132* (4) 1559-1569

(36) Leiter, F.; Alves, H.; Pfisterer, D.; Romanov, N. G.; Hofmann, D. M.; Meyer, B. K. *Physica B: Condensed Matter* **2003,** *340-342* 201-204

(37) Korsunska, N. O.; Borkovska, L. V.; Bulakh, B. M.; Khomenkova, L. Y.; Kushnirenko, V. I.; Markevich, I. V. *J Lumin* **2003,** *102-103* 733-736

(38) Yang, X.; Du, G.; Wang, X.; Wang, J.; Liu, B.; Zhang, Y.; Liu, D.; Liu, D.; Ong, H. C.; Yang, S. *Journal of Crystal Growth* **2003,** *252* (1-3) 275-278

(39) Garces, N. Y.; Wang, L.; Bai, L.; Giles, N. C.; Halliburton, L. E.; Cantwell, G. *Applied Physics Letters* **2002,** *81* (4) 622-624

(40) Leiter, F. H.; Alves, H. R.; Hofstaetter, A.; Hofmann, D. M.; Meyer, B. K. *physica status solidi (b)* **2001,** *226* (1) R4-R5

(41) Heine, V.; Henry, C. H. *Phys Rev B* **1975,** *11* (10) 3795-3803

(42) Van Vechten, J. A. *Phys Rev B* **1976,** *13* (2) 946-949

(43) Dahan, P.; Fleurov, V.; Thurian, P.; Heitz, R.; Hoffmann, A.; Broser, I. *Phys Rev B* **1998,** *57* (16) 9690-9694

(44) Broser, I.; Schulz, M. *Zeitschrift für Physik A Hadrons and Nuclei* **1972,** *254* (1) 35-45

(45) Selim, F. A.; Tarun, M. C.; Wall, D. E.; Boatner, L. A.; Mccluskey, M. D. *Applied Physics Letters* **2011,** *99* (20) 202109-202103

(46) Wheeler, E. D.; Boone, J. L.; Farmer, J. W.; Chandrasekhar, H. R. *Journal of Applied Physics* **1997,** *81* (1) 524-526

(47) Look, D. C.; Hemsky, J. W.; Sizelove, J. R. *Physical Review Letters* **1999,** *82* (12) 2552-2555

(48) Chen, W.; Li, F.; Yu, J. *Materials Letters* **2006,** *60* (1) 57-62

(49) Duignan, M., *Origin of the structured green photoluminescence band in ZnO crystals*, in *School of Physical Sciences*. **2010**, Dublin City University: Dublin.

(50) TEW Tokyo Denpa, High Quality ZnO Substrates for wide band gap applications, **2011**

(51) Takahashi, H.; Nakamura, H.; Izaki, M.; Katayama, J., *Method of forming a Cu interconnect pattern*, U.S.P. Office, Editor. 2003, NEC Corporation, Tokyo (JP), Osaka Municiple Government, Osaka (Jp) United States.

(52) Isoflex; **2011** Product catalogue, Available from: http://www.isoflex.com/isotopes/index.html.

(53) Broser, I.; Kaczmarczyk, G.; Thurian, P.; Heitz, R.; Hoffmann, A. *Journal of Crystal Growth* **1996,** *159* 889-892

(54) Wahl, U.; Rita, E.; Correia, J. G.; Agne, T.; Alves, E.; Soares, J. C. *Superlattice Microst 39* (1-4) 229-237

(55) Solbrig, C. *Zeitschrift für Physik A Hadrons and Nuclei* **1968,** *211* (5) 429-451

(56) Al-Suleiman, M. A. M.; Bakin, A.; Waag, A. *Journal of Applied Physics* **2009,** *106* (6) 063111

Chapter 7

7.1 Conclusions

In this thesis we have examined several aspects of ZnO nanorod growth, from the initial seed layer formation, to factors affecting CTR-VPT growth. We have demonstrated a method to grow high quality ZnO nanorods by combining CBD deposition with CTR-VPT and extended this method by developing a novel technique to control both the orientation and the positioning of the nanorods using an inexpensive nanosphere lithography technique. Finally, we have examined the optical properties of ZnO nanostructures using low temperature PL and absorption measurements. During the course of this latter work, it was necessary to develop a soft chemical solution doping technique that allowed us to definitively identify the role of Cu in an important defect related emission in ZnO. From this work, there are many conclusions drawn and issues identified which will now be briefly summarised.

CBD growth

The pioneering work of Greene *et al.* in developing a method to deposit ZnO seed layers on diverse non-epitaxially matched substrates using simple accessible reagents and methods has opened the door to a wide range of ZnO film and nanostructure research. However, their initial conclusions regarding the chemical pathways involved in this deposition method were incorrect. Our study has indicated that the formation of a ZnOH intermediate by a reaction with atmospheric water is critical to the deposition process confirming the chemical pathway first proposed by Lee *et al*. Consequently, if this method is to be adopted at larger industrial scales, attention will need to be paid to the atmospheric conditions during the deposition process. We have also identified edge effects, which are common to other film processes which will also need attention. While

the precise origin of these edge effects has not been identified, several possibilities have been proposed and in particular the possibility of a Marangoni type flow has been discussed.

We have examined the growth of ZnO nanorods by three different chemical solution methods and in each case found that that *c*-axis aligned growth was possible when using thin seed layers. While the seed layer orientation is important in controlling the alignment, we have also found that neighbouring rods and the rod density and spatial confinement all play an important role in controlling the orientation. We examined the use of surfactants during growth and that they can control and increase the aspect ratio of the rods and suppress the formation of films. However surfactants can impact significantly on the growth rates, thus requiring multiple bath changes and extended growth times. We have observed distinct variations due to the zinc counter ion, which lead to variations in the nanorod morphology and other factors such as rod coalescence, bubbles masking areas from growth etc. Characterisation of the CBD nanorods have shown that structurally they are of good quality with no evidence of planar defects or dislocations.

CTR-VPT

During the course of this work we have developed a facile method to grow high quality *c*-axis aligned nanorods by CTR-VPT using thicker buffer layers prepared by CBD. This method is particularly advantageous as it eliminates the need for expensive deposition processes such as PLD and sputtering to deposit initial nucleation layers. We have undertaken a detailed analysis of the growth process and have identified important reactions between the interface of the buffer layer and substrate which leads to secondary phase formation. This is particularly important if the substrate is expected to act as an electrical contact in a device application. We have also identified thermally induced structural changes in the buffer layer which affect the final nanorod morphology and we have proposed a method of controlling these changes. We have also identified reasons why CTR-VPT deposition on thin seed layers on a silicon substrate close to the source powder leads to non-uniform growth at the edges and a near complete absence of growth at the sample centre. From this we conclude that when depositing ZnO nanorods at high temperatures, there is a critical particle size / buffer layer thickness necessary to overcome the growth in the silicon thermal oxide which envelops smaller, thinner seed layers.

Nanosphere lithography

For many proposed ZnO applications, not only is the nanostructure morphology important but also the density and/or position of the nanostructures. It is therefore important to not only be able to deposit the desired morphology but also control the position / density. In this work we have developed a method that allows us to control both the position and orientation of the ZnO nanorods, while still maintaining the high quality of the material. This was achieved using a combination of nanosphere lithography in conjunction with silica templating, which eliminated the need for catalysts such as Au and was suitable for growth at high temperatures. In addition by using a silica template, a permanent insulating layer is deposited between the underlying buffer layer / substrate and that of the emerging nanorods, which may be of particular use for applications such as LEDs and field emission devices where the substrate needs to be electrically isolated from the rods.

Optical characterisation

In this work we also examined the optical properties of ZnO nanorods grown by various different chemical solution methods and by the combined CBD CTR-VPT deposition technique developed in our lab. Distinct differences were observed between the CBD and the CTR-VPT samples and in general it was found that the CBD samples were of a much poorer optical quality than the CTR-VPT samples, despite our previous work showing that the structural quality was good. PL examination of the ordered arrays grown by CTR-VPT showed that the novel positioning method did not appear to interfere with the optical properties of the nanorods and that they were of similar quality to unordered CTR-VPT arrays. The CTR-VPT growth process resulted in optically bright ZnO nanorods, which were dominated by a strong, narrow line, near band edge emission. High resolution PL of this region indicated that Al was the dominant impurity along with a smaller contribution from In as well as features related to the high surface to volume ratio associated with the nanostructure morphology. All CTR-VPT grown samples had a weak deep level structured green band emission, which has been traditionally associated with Cu. Deliberate doping of the nanorods with Cu resulted in inconclusive results, which could not definitively identify Cu as the source of the deep level defect. To conclusively identify Cu as a chemical constituent of the deep level defect, we developed a novel solution based soft doping technique, which allowed us to dope ZnO single crystals with single isotopes and specific

isotope ratios. From this we were able to conclusively identify the involvement of a single Cu atom in the defect responsible for the deep level emission and confirm the unusual ordering of the isotope shift for Cu in ZnO. However variations between the absorbance data and the PL data hint at a more complex role for Cu in ZnO.

7.2 Outlook

ZnO has been subject of intensive research for the last 10 years and given the large number of potential applications, will undoubtedly be of interest for some time to come. However, despite the apparent versatility of ZnO, many challenges still remain. The bottle neck in reliably producing p-type ZnO has limited the prospects of ZnO being a viable technology for UV optoelectronic devices in the near future. In addition, ZnO is an amphoteric oxide being damaged by both acid and bases and the reactivity of ZnO surfaces and the anisotropic nature of these surface means that many of the proposed applications such as dye sensitised solar cells and solid state gas sensors may not be possible in their present proposed form, e.g. following the design of TiO_2 dye sensitised solar cells.

Despite these uncertainties, great strides are being made in overcoming many of the limitations associated with ZnO with focus shifting towards novel heterostructures. ZnO optoelectronic devices with UV emission spectra have been demonstrated using ZnO in conjunction with materials such as PEDOT and $CuAlO_2$. Dye sensitised solar cells with improved chemical stability and enhanced dye loading have been produced using ZnO nanorod arrays with a TiO_2 outer shell. These examples demonstrate that while ZnO may not be suitable by itself, by judicious selection of secondary materials and clever device design many of the limitations of ZnO can be overcome, while many advantages of the material and/or its nanostructured morphology can still be effectively utilised. To facilitate this next generation of research and device design much work still needs to be done, particularly in understanding the interaction between ZnO and other materials. The importance of interfaces in ZnO heterostructures and core-shell type structures, especially given surface reactivity of ZnO, will be an important aspect of ZnO device research.

In this work, we have demonstrated a method of growing ZnO nanostructures by combining two existing growth methods, taking advantage of the benefits of each. However the CTR-VPT growth system, which is ideal for laboratory scale research, may be unsuited to larger wafer scale depositions. This is in part due to the variation in Zn vapour

production from the carbothermal reduction. Variations in contact between the graphite and the ZnO powders along with variations in the ZnO source powder particle size, while not investigated in this work, are believed to have had an impact on the morphology of the samples produced. At larger size scales these variations may prove to be too unreliable to give suitable device yield levels. Therefore a method which can produce the Zn vapour necessary for growth in a uniform and well distributed manner both spatially and temporally without adding excessive complexity maybe a fruitful direction for future research. This extra level of control may help avoid many of the difficulties encountered in this work. In this regard, methods such as CVD or MOCVD may be ideal for this task. As has been discussed through out this work, growth by CBD is advantageous because the chemical environment can be tailored to produce many different and novel morphologies. In this work we concentrated on the growth of ordered and aligned nanorod arrays using just one CBD morphology. Another interesting area of research would be to examine a range of different CBD morphologies such as nanoflowers and nanotubes and what would be the outcome of using these morphologies as buffer layers for subsequent CTR-VPT growth.

Given the expected importance of the optical properties of ZnO in terms of optoelectronic devices, methods of introducing dopants without damage such as the soft solution based method described in chapter 6 may provide an ideal platform for examining optical properties of a range of different dopants. Specifically those elements lower in the metal reactivity series such as mercury, silver, lead, tin, nickel and cobalt which may also undergo a galvanic displacement reaction with ZnO, given their matching charge state, could be of interest. If these materials are found to undergo a displacement reaction with ZnO then solution doping may prove ideal for investigating the properties of ZnO doped with these impurities. Finally, the CBD growth technique has a number of distinct potential advantages over high temperature growth. Despite this, the optical properties of the ZnO deposited are generally poor as compared to high temperature growth techniques. Identifying the factors which limit the optical properties and in particular the internal quantum efficiency is therefore of significant importance. A detailed study of CBD grown ZnO which identifies the deposition parameters which influence the quantum efficiency would undoubtedly yield interesting results, and may provide insights into how the optical properties of CBD grown nanostructures could be improved, paving the way for low cost, high quality ZnO optical devices.